Cranfield University

Pierre Casaubieilh

Fibre Optic Fizeau Interferometer For Optical Coherence Tomography

School of Engineering

PhD

Cranfield University

School of Engineering

PhD Thesis

2006

Pierre Casaubieilh

Fibre Optic Fizeau Interferometer For Optical Coherence Tomography

Supervisor: Prof. Ralph P. Tatam

Academic Year 10/2002 to 2006

ABSTRACT

The aim of the project was to develop the Fizeau interferometer configuration to take advantage of the benefits derived from its “downlead insensitivity” to temperature and polarisation fading. This sensing interferometer was investigated and implemented in conjunction with various processing interferometers with the view to achieve optimised performances for Optical Coherence Tomography (OCT) application.
A comprehensive theoretical analysis has been carried for Signal-to-Noise ratio of these OCT systems.

Balanced detection indenting two detectors with anti-phase signals was also investigated to improve further the SNR. The analysis showed that the SNR (67 dB) of the balanced Fizeau interferometer improved by 30 dB from that of standard Fizeau interferometer implementing a single detector. Experimentally, the best SNR for this configuration was achieved by adding an electronic rectifier based demodulation system for the signal after balanced detection.

The OCT systems investigated in this project were developed based on a broadband source operating in the 1550 nm wavelength-band to facilitate improvement in the depth of penetration of light directed into imaged samples. The coherence length or axial resolution in air of the system was 21 μm while the transverse resolution was 18 μm and focusing depth was 340 μm.

ACKNOWLEDGEMENTS

The author wishes to acknowledge the supervision of Prof. Ralph P. Tatam throughout the duration of this PhD work at Cranfield University. Significant thanks are given to Dr. Helen D. Ford for her guidance and valuable help. The author also thanks Dr. Stephen W. James for the interesting discussions he had with him.

The author specially acknowledges Mr Stephen Staines for making opto-mechanical devices that were used in this work and he was of great help.

Of course, students and staffs of the Optical Sensors Group cannot be forgotten. The author thanks Dr. Edmon Chehura for his advices and his help. Dr. Samuel Cheung is a really good cook and the author had the privilege to taste, on several occasions, Chinese food and teas and he was very helpful.

Finally, special acknowledgments are given to my family, Papar'Oc and friends for their support during my PhD studies.

TABLE OF CONTENTS

TABLE OF FIGURES

TABLE OF TABLES

Abbreviation and Symbols

OCT	Optical Coherence Tomography
2-D OCT	2-Dimensional Optical Coherence Tomography
OTDR	Optical Time Domain Reflectometry
LCI	Low-Coherence Interferometry
SNR	Signal-to Noise Ratio
MI	Michelson Interferometer
MZI	Mach-Zehnder Inteferometer
MPI	Michelson Processing Interferometer
MZPI	Mach-Zehnder Processing interferometer
FPPI	Fabry-Perot Processing Interferometer
HR	High-Resolution
SLD	Super-Luminescent Diode
OPD	Optical Path Difference
IR	Infrared
NIR	Near-Infrared
UV	Ultra-violet
L_c	Coherence Length
λ	Wavelength
$\Delta\lambda$	Wavelength Bandwidth
NA	Numerical Aperture
PS-OCT	Polarisation Sensitive Optical Coherence Tomography
SD-OCT	Spectral Domain Optical Coherence Tomography
FD-OCT	Fourier Domain Optical Coherence Tomography
DOCT	Doppler Optical Coherence Tomography
RSOD line	Rapid Scanning Optical Delay Line
E_1, E_2, E_{11}, E_{12}, E_{21}, E_{22}, E	Electric fields
E_1^*, E_2^*, E_{11}^*, E_{12}^*, E_{21}^*, E_{22}^*	Complex conjugate electric fields
I_1, I_2, I_3, I_4	Intensities of E_{11}, E_{12}, E_{21} and E_{22}
X_1, X_2	Optical path difference in the sensing and processing interferometer
$\langle\ \rangle$	Time averaging

1 Introduction

1.1 Overview

For centuries, the human body has been of interest to scientists attempting to understand the different functions of the organs and its constitution. Histology is frequently used, being the science of sectioning samples to characterize the structures and comparing diseased with normal tissue. It is generally applied to *post-mortem* detection.

From the discovery of X-rays (Goodman, 2006) properties passing through the body and enabling to check the skeletal or bone structure, research has been focused on developing devices to image through the body, without requiring histology.

One big concern of our society is cancer and techniques to detect and cure it. There are many forms or types of cancer that occur in various parts or organs of the human body. Cancer cells can develop from normal cells that undergo mutations, which then regroup and grow, and after spread in the organs. Skin cancer for example, primarily results from the DNA mutation of cells when exposed to ultra-violet light.

Several devices have been developed for medical applications in order to detect malignant tissues. All the devices available in the market have the advantage, for most of them, to image through the body, but they suffer from low resolution. Cancer can efficiently be cured at an early stage of its development if an instrument able to detect it at this early stage is available. Interferometry is of interest for medical imaging techniques because of the high resolution that it can achieve.

1.2 Histology

Methods like histology and “simple visualization” of tissue can be used to detect the presence of cancer.

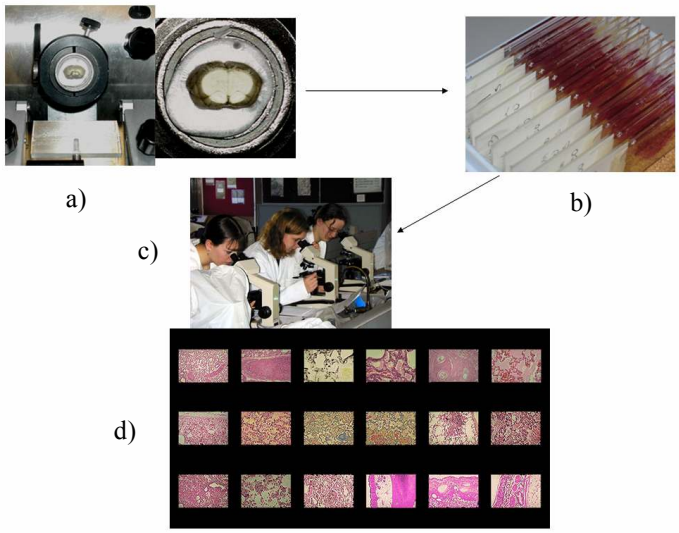

Figure 1-1: Histology principle; a): (Leon and Johnson, 2005), b): (www.mrpath.com/slidevault.html, 2005), c): (The Royal (Dick) School Veterinary Studies, 2005), d): (http: and numbat.murdoch.edu.au/histology/hystology_imagebase_1.html, 2005)

Histology consists of sectioning thin layers of samples to view the microscopic structures inside the sample (School Of Anatomy And Human Biology - The University Of Western Australia, 2003): it is a destructive technique. The sample is put in a gel and, after having hardened, it is positioned in a histology system (figure (1-1 a)). Several thin layers are sectioned and prepared between microscope slides (figure (1-1-b)) with dyes to identify microstructures (figure (1-1-c)). Figure (1-1-d) presents examples of coloured histology images of samples.

A simple visualization technique, comprised of a system of viewing lenses and light illumination, may be used for skin cells for example to observe whether the underlying cells show the presence of cancer development. This method is generally not accurate, especially where the cancerous cells are not yet well-developed and further diagnostics are required. Histology may be used to provide more detailed analysis but can be applied only to elements where biopsy samples can readily be taken. Taking sample of tissue, used regularly e.g. on oesophageal cancer, is more often used in post-mortem examinations rather than as a diagnostic tool.

These techniques are therefore only applicable where the cancerous cells are well developed, in which case a cure may be too late. In this case treatments such as

chemotherapy and *radiotherapy* may be used to slow down cell growth to prolong life, though other side effects or complications may occur (e.g. loss of the hair, decreasing spermatozoid production).

1.3 Clinical imaging systems

Research and development needs to focus on developing diagnostic techniques that are capable of precancerous cell detection. Such a technique would be an enormous contribution to the medical fraternity for early detection and then a treatment may be more effective. Medical techniques have been developed for applications like viewing veins and organs.

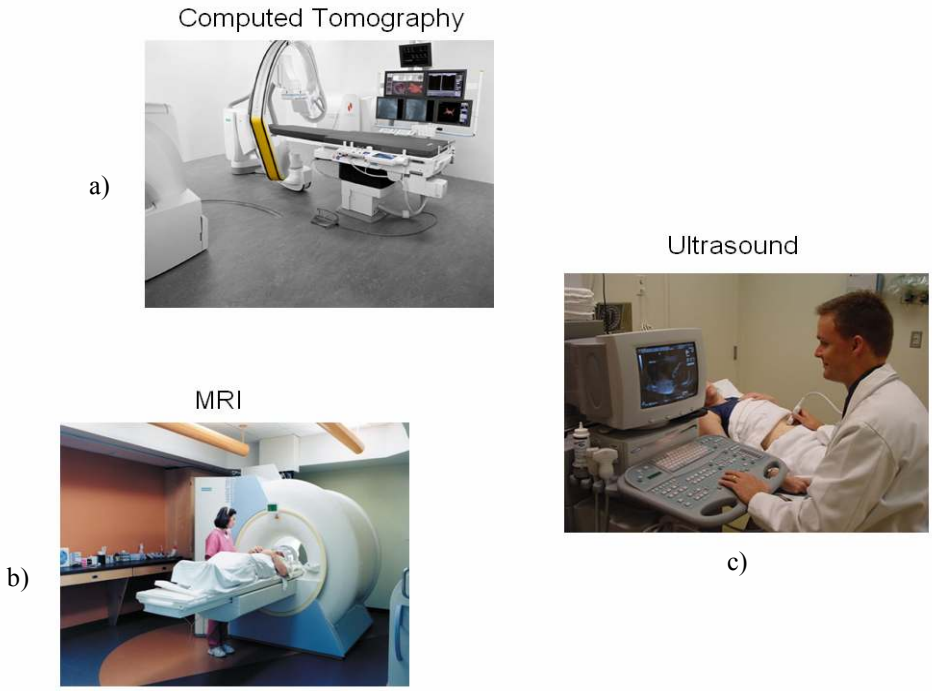

Figure 1-2: Clinical imaging systems; a): (Siemens, 2005), b): (William Osler Health Center, 2003), c): (Univesity Of Virgina Health System, 2005)

Most medical imaging systems used in hospital can image through the body, e.g. Computed Tomography and MRI (Magnetic Resonance Imaging) figures (1-2-a) and (-b).

Ultrasound, figure (1-2-c), is a technique that measures the time delay between an initial acoustic impulse and the reflected sound from tissue boundaries. It is a contact method requiring the application of a gel between the source-sensor and the body to increase the transfer of the sound through the body. Most of these systems, e.g. CT or MRI, require a room for their special use and have a low resolution of about 1 mm.

Comparisons of medical imaging techniques are available in reference (Department Of Physics: University Of Maryland,) and most of the medical imaging techniques are summarised in table 1-1.

Table 1-1: medical imaging techniques

Technique	Imaging source	Resolution	Image depth	Comments	References
X-ray	Large radiation field	0.5 cm	Through body	Ionising radiation	
CT	x-ray beam	0.5-1 mm	Through body	Ionising radiation, Functional imaging	(Garcia-Ramirez et al. 2002)
SPECT	Gamma rays (typically 140 keV)	0.5 cm	Through body	Ionising radiation, Functional imaging	(Loudos et al. 2003)
PET	Gamma rays 511 keV	1 mm	Through body	Ionising radiation, Functional imaging	(Joung et al. 2002)
MRI	Typically 1.5 T External magnetic field combined with radio frequency pulses	0.5 mm (commonly) (but also 117 μm)	Through body	Strong external magnetic field required	(Columbia University, 2004)
Ultrasound	Sound (high frequency)	1 mm (commonly) (but also 50 μm)	30 cm	Contact gel necessary	(Foster et al. 2000)
OCT	Light: 0.8-1.5 μm	1—15 μm	2-3 mm	Strongly attenuated in scattering tissue	(Fujimoto, 2001)

There is a necessity to develop techniques to detect normal and abnormal tissues. In the body the cell size is about 10 to 40 μm. Problems: cancers develop due to abnormalities differentiating in the top sub-layers of tissues. Current medical imaging techniques do not have the necessary resolution to differentiate the state of cancer.

When the cells begin to develop into cancer they grow and differentiate from the normal cells, forming a new layer or losing normal tissue organisation; the system used has to be able to detect the cancerous tissue.

1.4 Optical Coherence Tomography

Optics has been shown to be an efficient tool applied to many fields e.g. in communication, in sensors (temperature, pressure), and interferometric techniques offer the highest resolution.

A technique called Optical Coherence Tomography (OCT) has been proposed and is the subject of current research. The technique is still relatively new and is based on Optical Low-Coherence Reflectometry (OLCR) and shows great promise in medical imaging. The technique has already been demonstrated on most of the important parts of the body such as the eye (Hoerauf et al. 2000), the skin (Welzel, 2001) and the gastro-intestines (Rollins et al. 2002), which are susceptible to deterioration due to e.g. the sun or the smoke.

Most of the systems used to date are based on a fibre optic Michelson interferometer.

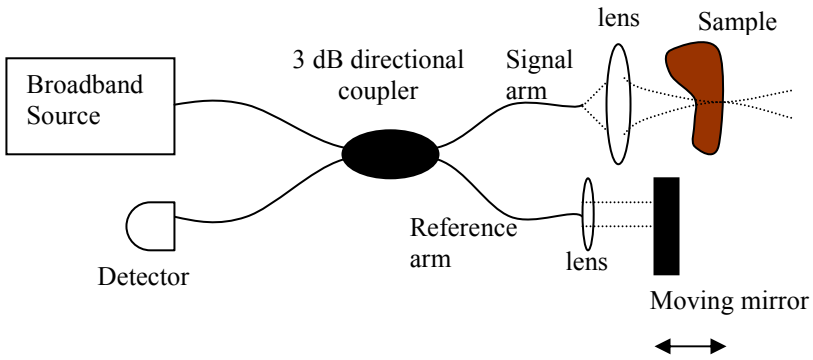

Figure 1-3: In-fibre Michelson configuration

The light from the broadband source passes through the 3 dB directional coupler and is split in two parts. One part of the light passes through one arm of the coupler and is reflected at the mirror (the reference arm), and the other part passes through the other arm and is reflected, transmitted and scattered by the sample (the sample arm). Both the

backscattered and reference light mix in the coupler and the signal is detected by the detector. Interference will be observed in the detector only if the optical path difference between the two arms is within the coherence length of the source.

The intensity at the detector I_d (developed in section 3-2) can be written as:

$$I_d = I_1 + I_2 + 2\sqrt{I_1 I_2}\,\gamma(x)\cos\left(\frac{2\pi}{\lambda}x\right) \qquad \textbf{(1-1)}$$

Where I_d is the intensity at the out put of the detector, I_1 and I_2 are the dc intensities, x is the optical path difference, $\gamma(x)$ is the mutual coherence function normalised, and λ is the wavelength

The detected signal, when the reference mirror is scanned, is illustrated by the figure 1-4:

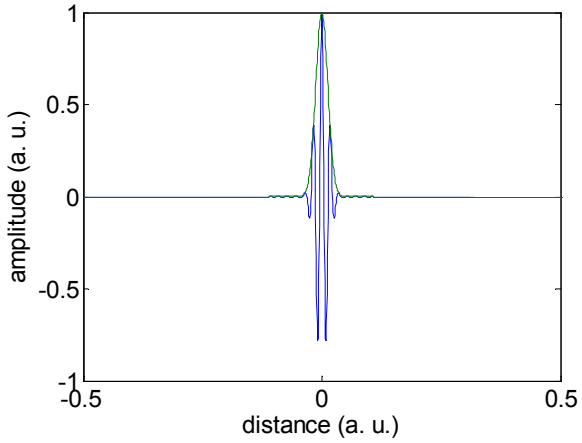

Figure 1-4: Interference signal observed at the output of a detector in a Michelson interferometer, assuming a Gaussian spectral bandwidth. A Gaussian signal will be observed modulated by interference fringes

A practical application of the Michelson configuration is illustrated in figure 1-5.

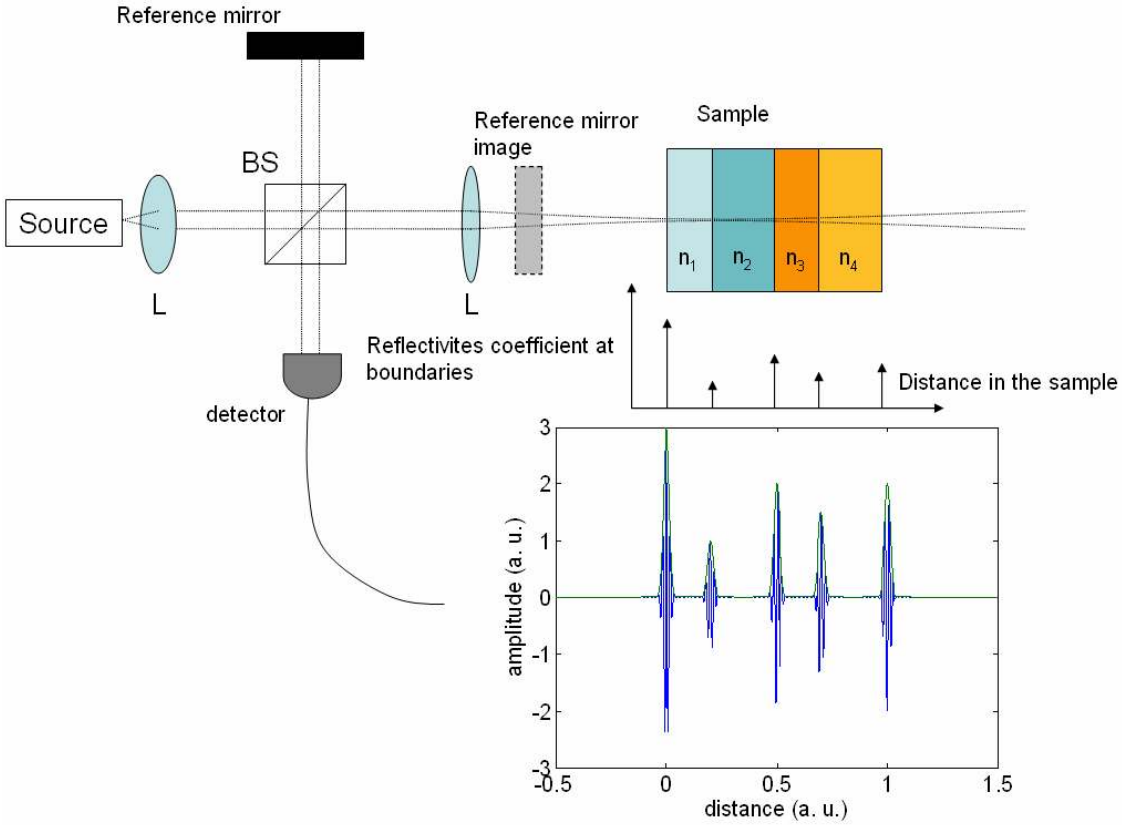

Figure 1-5: Free space Michelson interferometer; SLD: super-luminescent diode, BS: beam splitter, L: lens, n_1, n_2, n_3 and n_4: refractive indices of the layers

The observed interferometric signal can be explained as the cross-correlation between the reflectivity map of the sample as a function of depth, and the auto-correlation characteristic to the source.

High resolution images have been obtained using this approach, however it suffers from a number of disadvantages for general development and use by non-optical specialists. The problem with this device is that it suffers from signal fading due to relative polarisation changes in the light propagation in the two arms, for example, if the fibres are bent or twisted. Thermal fluctuations between the two fibre paths will result in fringe movement leading to difficulty in finding the position of the maximum fringe intensity. To remove these problems, polarisation controllers are required to maximise the detected signal.

To avoid polarisation controllers, which should be tuned depending on the application (especially with endoscopy) and this polarisation dependence for an OCT system, a Fizeau configuration is investigated, the most basic form shown below:

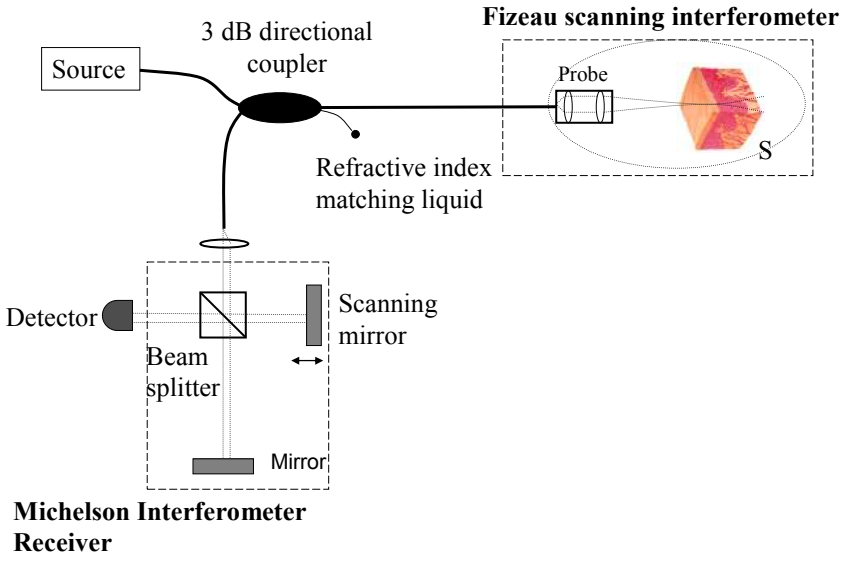

Figure 1-6: Standard Fizeau configuration; S: sample

The light passes through the 3dB coupler and is sent to the Fizeau scanning interferometer. One part of the light is reflected at the end of the optical fibre and the other part is reflected, transmitted and scattered by the different boundaries of the sample. Both the reflected light at the end of the fibre and the backscattered light pass through the same optical fibre. The advantage of such a system over the Michelson interferometer is that both light signals will pass through the same optical fibre and suffer from the same polarisation changes. This offers downlead insensitivity. The light then passes through the 3-dB coupler and is sent to the Michelson processing interferometer. Both beams will be split by the beam splitter and reflected by the mirrors and mix at the beam splitter. The signal is then detected. Interference is obtained when the optical path in the Michelson processing interferometer matches the optical path difference in the Fizeau scanning interferometer.

More information of this configuration and development will be provided through the thesis.

The subject of this research project is the development of an OCT system that is capable of imaging to a depth of 1-2 mm in a range of different media. An affordable, compact and portable system that is easily transportable to hospital environments for measurement purposes is required. The system was developed around data acquisition operating using the Labview^{TM} platform that processes the information and displays the image.

For *in-vivo* medical imaging applications and to avoid artefacts introduced by movement of the patient, the acquisition has to be done as fast as possible. Many of the systems are based on the use of a Fourier rapid scanning optical delay line (RSOD line), enhanced using a grating, a lens and a galvanometer (Tearney et al. 1997).

1.5 Contents of the thesis

Chapter 2 will first illustrate the type of results that have been obtained from previous research. An OCT system, being essentially an interferometer, is composed of a source, interferometer and the detector. The instrumentation for this technique is detailed in this section.

The system developed in this project was based on the Fizeau interferometer, chapter 3 will deal with the explanation of the expected signal from the system.

Due to scattering and absorption in the samples, an OCT system has to be able to detect low back-reflected intensity and it is therefore important to reduce noise in the system. In optics, a way to do so is to employ a balanced detection. In chapter 4, the SNR of the most used Michelson interferometer optical configurations is compared theoretically to the Fizeau configuration, to investigate the potential and improvements required for the Fizeau configuration.

Chapter 5 provides the experimental steps that have been carried out to improve the sensitivity and the SNR of the Fizeau configuration. This comes with the comparison of different kinds of detectors and the application on several samples. The process of the experimental investigation of the SNR efficiency is provided.

The results are then presented in chapter 6 with a discussion. This will demonstrate that the Fizeau configuration has a great potential in OCT applications.

Reference List

1. Columbia University. About Functional MRI (General): The Future Role Of Functional MRI In Medical Applications, www.fmri.org/fmri.htm. 2004.

2. Department Of Physics: Univeristy Of Maryland. http://www.physics.umd.edu/lecdem/honr228q/notes/imaging.jpg.

3. Foster, F.S., Pavlin, C.J. and Harasiewicz, K.A. (2000) Advances In Ultrasound Biomicroscopy. *Ultrasound In Med & Biol.* **26**, 1-27.

4. Fujimoto, J.G. (2001) Optical And Acoustical Imaging Of Biological Media. *Compte Rendu De L'Academie Des Sciences* **t. 2**, 1099-1111.

5. Garcia-Ramirez, J.L.M.S., Mutic, S.M.S., Dempsey, J.F.Ph.D., Low, D.A. and Purdy, J.A. (2002) Performance Evaluation Of An 85-cm-Bore X-Ray Computed Tomography Scanner Designed For Radiation Oncology And Comparison With Current Diagnostic CT Scanners. *Int. J. Radiation Oncology Biol. Phys.* **52**, 1123-1131.

6. Goodman, Philip C. http://www.xray.hmc.psu.edu/rci/ss1/ss1_2.html: Roentgen And The Discovery Of X-rays. 2006.

7. Hoerauf, H., Wirbelaurer, C. and Scholz, C. (2000) Slit-Lamp-Adapted Optical Coherence Tomography Of Anterior Segment. *Graefe Archive for Clinical and Experimental Ophthalmology* 238, 8-18.

8. http: and numbat.murdoch.edu.au/histology/hystology_imagebase_1.html (2005)

9. Joung, J., Miyaoka, R.S. and Lewellen, T.K. (2002) cMICE: A high Resolution Anima PET Using Continuous LSO With A Statistical Based Positioning Scheme. *Nuclear Instruments And Methods In Physics Research* **Section A 489**, 584-598.

10. Leon, Michael and Johnson, Brett A.

http://leonserver.bio.uci.edu/about/ourMethods/histology.jsp. 2005.

11. Loudos, G.K., Nikita, K.S. and Uzonoglu, N.K. (2003) Improving Spatial Resolution In SPECT Based Detector And Iterative Reconstruction Algorithms. *Computerized Medical Imaging And Graphics* **27**, 307-313.

12. Prahl, S.A., Keijzer, M., Jacques, S.L. and Welch, A.J. (1989) A Monte Carlo Model Of Light Propagation In Tissue. *SPIE Institute Series: Dosimetry Of Laser Radiation In Medicine And Biology* **IS**, 102-110.(Abstract)

13. Rollins, A.M., Sivak, M.V., Radhakrishnan, S., Lass, J.H., Huang, D., Cooper, K.D. and Izatt, J.A. (2002) Emerging Clinical Applications Of Optical Coherence Tomography. *Optics & Photonics News, Optical Society of America*

14. School Of Anatomy And Human Biology (2003) - The University Of Western Australia. Blue Histology - A Brief Introduction To Stereology, http://www.lab.anhb.uwa.edu.au/mb140/

15. Siemens.
http://www.medical.siemens.com/siemens/en_US/rg_marcom_FBAs/images/press_room_images/2005/061.05_MagNav_dBC_Purchase.jpg. 2005. 2005.

16. Tearney, G.J., Bouma, B.E. and Fujimoto, J.G. (1997) High-Speed Phase- And Group-Delay Scanning With A Grating-Based Phase Control Delay Line. *Optics Letters* **22**, 1811-1813.

17. The Royal (Dick) School Veterinary Studies (2005) www.vet.ac.uk/photos.htm.

18. Univesity Of Virgina Health System.
http://www.healthsystem.virginia.edu/internet/women/tours/primarycare/ultrasound.jpg. 2005.

19. Welzel, J. (2001) Optical Coherence Tomography In Dermatology: A Review. *Skin Research And Technology* **7**, 1-9.

20. William Osler Health Center. http://www.williamoslerhc.on.ca/Patient_Services/MRI.jpg. 2003. 2003.

21. www.mrpath.com/slidevault.html (2005)

2 Optical Coherence tomography: a review

2.1 Introduction

Optical Coherence Tomography (OCT) is a non-invasive imaging technique based on low-coherence interferometry, providing sub-surface information. This method has low penetration depth (1-2 mm) but it has high resolution (HR) (about 1-10 μm) compared to conventional medical imaging techniques (table 1-1).

Interference fringes occur only when the optical path difference (OPD) between the reference and the sample arms is within the coherence length of the source. This technique has been used for clinical examination of many tissue types including non-transparent samples. Several interferometer configurations are available and these are compared in this chapter.

The instrumentation used (source, interferometer, scanners…) developed for this technique are reviewed and discussed. In order to remove artefacts from the image due to the movement of the patients or their organs, improvement of the data acquisition rate is necessary. Different systems have been employed, where the most important are discussed here.

With the development of this technology, extensions have been proposed and produced for more applications: flow measurement (blood), spectroscopy, and polarisation sensitive imaging.

2.1.1 White light and Low-Coherence interferometry

To detect faults in systems, e.g. broken optical fibres, ultrashort pulses are used. The pulse is reflected at the faults and using the time delay between the initial pulse and the reflected pulse, the position of the fault is determined. This technique is called optical time domain reflectometry (OTDR) and the instrumentation has been reviewed by Healey (Healey, 1986). The resolution of this technique is 0.5 m over 125 km. In

terms of biomedical application such resolution is not very practical because millimetre thickness have to be measured. With the development of low-coherent sources, detecting faults in optical waveguides was possible with a spatial resolution of 17 μm (Takada et al. 1987).

Optical coherence domain reflectometry (OCDR, another name for low-coherence interferometry (LCI) technique) measurements were performed by Fercher *et al.* (Fercher et al. 1988) obtaining one-dimensional profiles of the reflecting sites within eye tissue. Taking a series of adjacent, longitudinal profiles and combining them in order to create a tomogram produces two-dimensional images of OCDR. This technique is nowadays called Optical Coherence Tomography (OCT).

Schmitt *et al.* (Schmitt et al. 1997) demonstrated that OLCR can have a high potential for applications in medical diagnostics based on the correlation of the optical properties with the functional state of the tissue.

Masters (Masters, 1999) reviewed the applications of LCI in OLCR for biomedical application and provided information on the development of Optical Coherence Tomography (OCT).

Coupling OLCR and transverse scanning enables cross-sectional imaging of samples.

2.1.2 First Applications of OCT

OCT was first demonstrated by Huang *et al.* in 1991 (Huang et al. 1991) using a Michelson Interferometer set-up to obtain two-dimensional, micron-resolution images of the human eye showing detailed structure of the retina, optical disk and images of the coronary artery. Outstanding comparisons were published between the OCT images and the histology specimens under examination.

Most early work using OCT was carried out using transparent tissue, exhibiting little scattering properties, like in the eye. This was a prime example for presenting the exceptional performance of OCT. A more turbid sample will degrade the images and prevent measurements to greater depths.

Since the first reports of OCT, the number of medical applications has increased significantly and OCT can now be used for most tissue types. Improvements in image performance have been made to increase resolution and signal to noise ratio, and faster scanning techniques have also been developed, the progress of which is outlined below, along with other areas of OCT applications.

2.2 Sample types investigated

2.2.1 Eye

OCT was first applied to the eye. Figure 2-1 provides some details of the eye which has a well defined morphology.

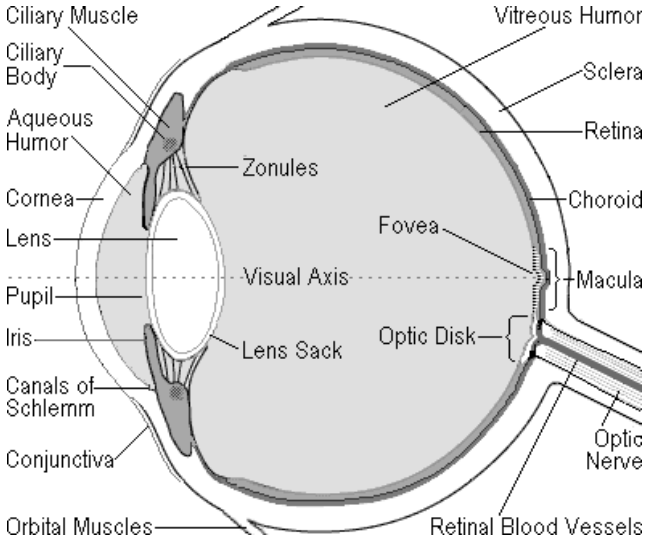

Figure 2-1: Structure of the eye (99Main, 2005)

The light is refracted by the lens and focused on the retina, where there are photoreceptors converting the intensity of the light to an electrical impulse which is sent to the brain via the optical nerve.

Several eye diseases (MD Support: The Eyes Of The Macular Degeneration Community, 2005) give discomfort to the vision or bringing blindness. Essentially, areas around the lens, the macula, the retina and the optical disk are the elements where checking is necessary.

The first images of OCT (Huang et al. 1991) have been obtained from the cornea, where the imaging depth was about 1-2 mm with high resolution. An 830 nm SLD was used.

Since then, OCT applications in Ophthalmology have been well investigated and developed to examine the structure of the cornea and the retina (Hee et al. 1995b). This has been possible because OCT is a non-invasive optical technique employing low power source.

With the growing interest in OCT, clinical approaches have been developed (Hee et al. 1995a), (Hoerauf et al. 2000) based on a Michelson interferometer. The light from the superluminescent diode passes through the directional coupler (figure 2-2).

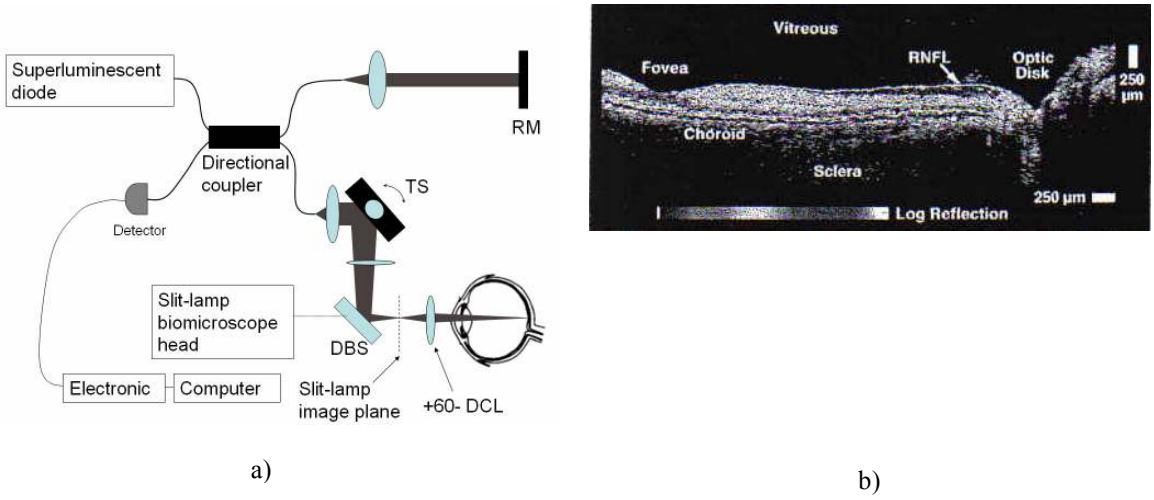

a) b)

Figure 2-2: a) Michelson interferometer arrangement mounted with a slit-lamp, b) OCT image of the back of the eye; RM: reference mirror, TS: transverse scanning, DCL: dioptre condenser lens, BS: beam splitter; DBS: dichroic beam-splitter; RNFL: retina nerve fibre layer. (Hee et al. 1995a)

The light is split in two parts: the reference beam is collimated at the output of the fibre and is reflected at a mirror. The sample beam passes through a probe composed of 2 lenses (the former collimating and the later focusing) and the light is reflected by the beam splitter to be sent to the sample. A mirror, mounted on a galvanometer, is placed between the two lenses to allow focusing at different transverse positions. A slit lamp was incorporated in order to track the region of observation. In figure (2-2-b), a cross-sectional image of the tissue enables to distinguish the different layers. Different parallel cross-sectional images were taken of the optical disk, in figure (2-3-a) by the

arrows, have been carried out and the results are presented in figure (2-3-b). They manage to produce different scans at different angles. The slit lamp enables to know where the light is sent.

Figure 2-4 summarises the possible applications of OCT on ophthalmology (Rollins et al. 2002).

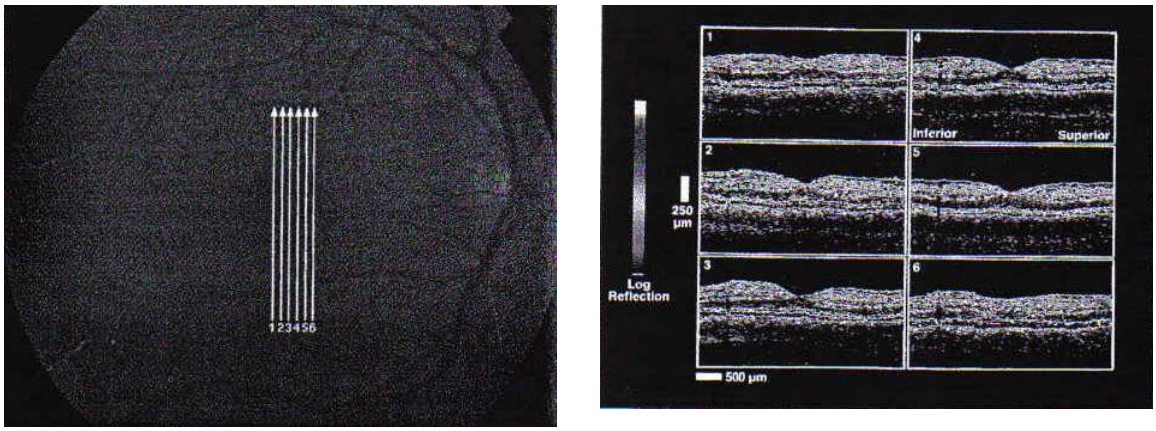

a) b)

Figure 2-3: a) picture of the eye under investigation, b) cross-sectional image of the back of the eye as indicated in a). (Hee et al. 1995a)

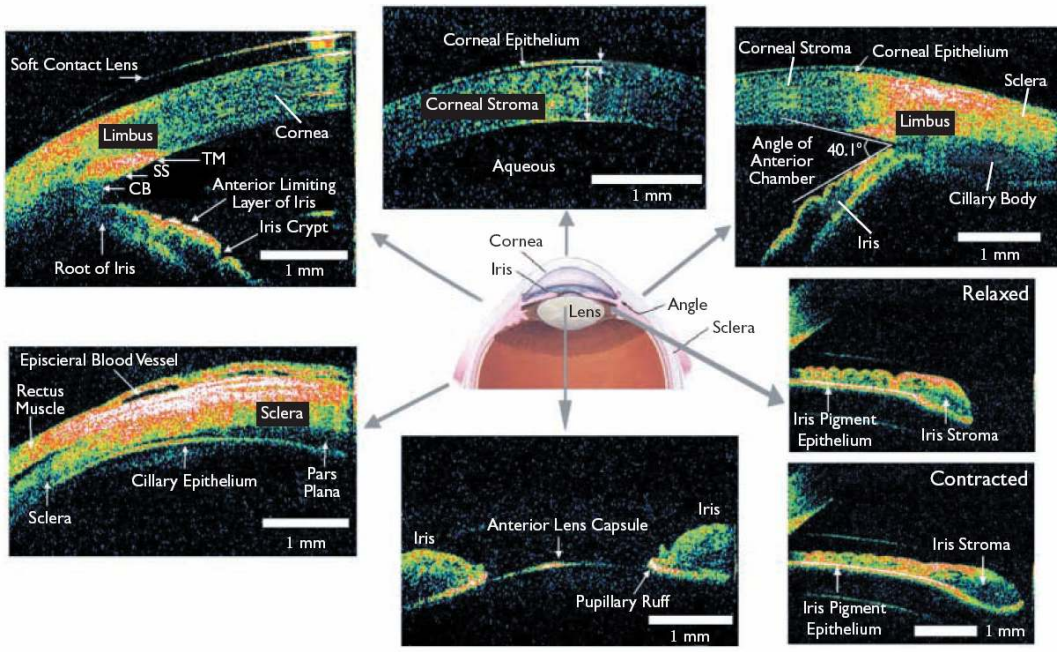

Figure 2-4: Real-time OCT imaging of the anterior segment of a normal eye (Rollins et al. 2002)

Finally with the development of charged-coupled devices (CCD's), *en-face* imaging became possible. Fast CCDs enabled OCT to be employed extensively in ophthalmology where real-time volume scans is possible (Wiesauer et al. 2005). Aberrations due to the retina influence imaging in the eye. Similar observations were obtained with the observation of stars from Earth with telescopes due to the atmosphere; adaptive optics (AO) has been demonstrated, compensating the influence of the atmosphere. This technique has been successfully applied on the eye (Zhang et al. 2005), (Zawadzki et al. 2005), (Merino et al. 2006).

The first OCT applications have shown a potential and strong interest for the use in ophthalmology, the next steps were to investigate other parts of the body which were much less transparent. Previous results have been provided in 1996 (Brezinski et al. 1996) on the feasibility of generating a 2-D OCT image of a coronary artery.

2.2.2 Gastrointestinal tissue

The gastrointestinal tract is an important organ of the body which is sensitive to acid and alcohol abuse, deteriorating the tissue where ulcer and cancers can develop. It was suggested that early stage cancer can be identified by observing changes in the squamous cell structure close to the tissue surface. The respiratory and the gastrointestinal (GI) tract have been investigated with OCT.

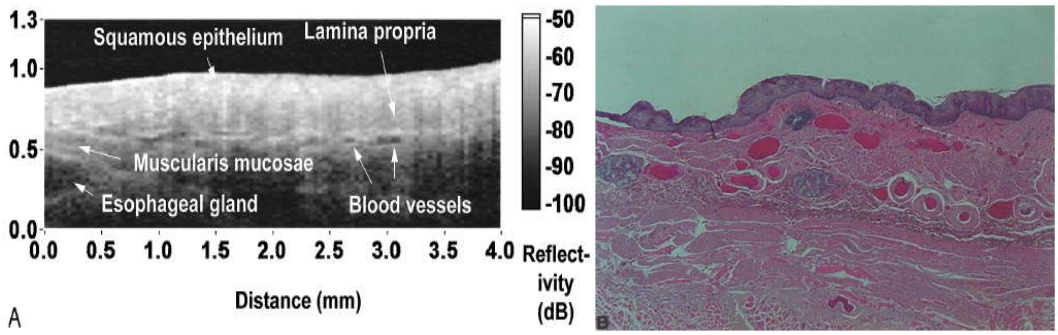

Figure 2-5: A and B are the OCT image and the corresponding histological section (horizontal axis is 4 mm) obtained from oesophagus and corresponding histological section. Squamous epithelium is identified as a layer that is brighter than the lamina propria. Oesophageal gland and blood vessels in the submucosa are clearly visualized. (Kobayashi et al. 1998)

In 1998 (Kobayashi et al. 1998) high resolution cross-sectional images of the GI tract were obtained in an experiment to investigate the possibility of the implementation of an endoscope for endoscopic OCT. Results showed clear definition of the mucosa and submucosa layers within the tissue. A 1270 nm SLD (superluminescent diode) was used to obtain 19.2 μm resolution longitudinal images to a depth of 1.2 mm – blood vessels (0.5 mm in diameter) (figure 2-5), crypts (60-70 μm) (figure 2-6) and other microstructures were clearly identified.

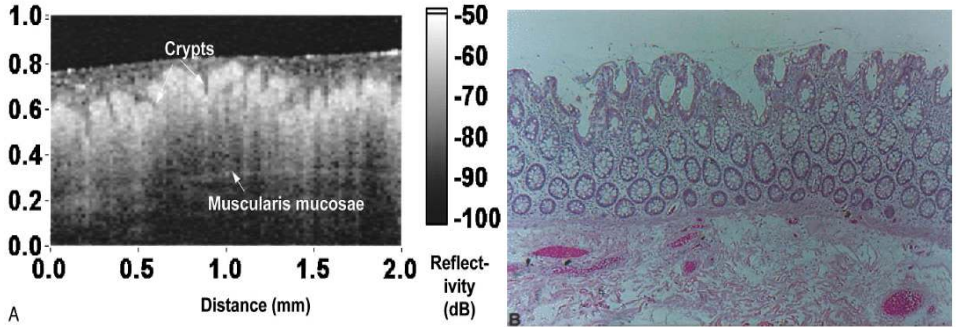

Figure 2-6: A and B are the OCT image and corresponding histological section (horizontal axis is 2 mm) obtained from colon. Crypts and muscularis mucosae are demonstrated. (Kobayashi et al. 1998)

During this period, work was being carried out to use OCT to image the skin (Welzel et al. 1998). An SLD, 830 nm, was used to give 15 μm resolution. Accurate images of the superficial layers within the skin were presented. Patients with certain skin conditions volunteered to be scanned and results were obtained showing how OCT can detect eczema tissue, blisters, malignant melanoma and even scabies mites.

Results have been published on the comparison between OCT and ultrasound (US) on the gastrointestinal (GI) cancer. It was shown that US enables information now deeper in the tissue than OCT, but OCT, because its high resolution, can distinguish cancerous tissue from normal tissue from the first five layers of GI (Mac Neill et al. 2002).

Figure 2-7 illustrates the endoscopy application of OCT throughout the body. It shows results obtained from many parts of the body, e.g. oesophagus, stomach and colon, being sensitive to cancer development.

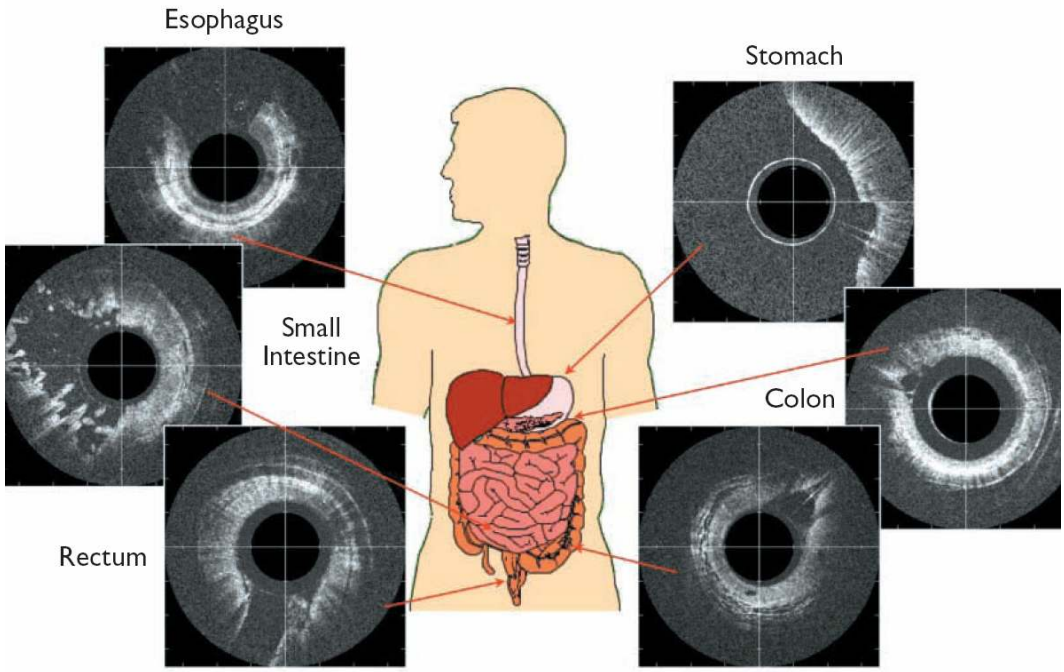

Figure 2-7: Endoscopic OCT images of normal tissue throughout the GI tract (Rollins et al. 2002)

2.2.3 Dental imaging

With increasing interest in the applications of OCT, Colston *et al.* (Colston et al. 1998) in 1998 were able to image the hard and soft tissue structure of the oral cavity. OCT was now progressing into dentistry. Subsurface imaging is important in this area to identify tooth fractures, demineralised enamel and other indications of tooth decay. A 1310 nm SLD was used to image premolar, 5-6 month old pig's teeth using a conventional OCT scanner. The images showed definition of the oral mucosa, the enamel-dentin interface and the tooth-mucosa interface down to a depth of 1 mm.

2.2.4 Skin imaging

Optical coherence tomography has also been applied on the skin. The skin, which enables regulation of the temperature of the body, is a complex tissue, composed of three layers that have different functionalities: the epidermis, the dermis and the hypodermis (figure 2-8).

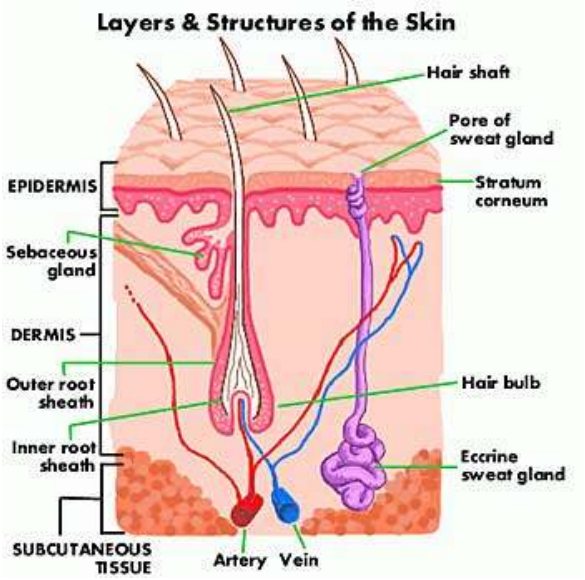

Figure 2-8: Skin layers (Quaker Chemical, 2005).

These layers can have different thicknesses depending on the observation point on the body. Krishnaswamy *et al.* (Krishnaswamy and Baranoski, 2004) review the thickness of the layers and provide information on the absorbing constituent in each which can be found in table 2-1.

Table 2-1: thicknesses of layers in the skin

Layer	Thickness	Absorption due to
Stratum corneum	0.01 - 0.02 mm	-
Epidermis	0.027-0.15 mm	Melanin
Dermis	0.6-3 mm	Haemoglobin in blood
Hypodermis	Up to 3 cm (abdomen)	White fat → light is totally reflected at this point

In dermatology, researchers are essentially concerned with the three first layers where cancer development is observed in the epidermis and dermis.

There are different kinds of skin cancers, which are grouped essentially in carcinoma and melanoma types that may be caused by e.g. sun exposure. Melanoma cancer comes from the differentiation and change of the melanocytes giving the colour of the skin, eye and hair (concentrated in moles and present in the epidermis (Skin Surgery Center, 1998-2006)). Carcinoma cancers arise from the development of the

basal cells (cells being at the bottom of the epidermis) (Risingsun Health Alternatives, 1999).

In 1998, Boppart *et al.* (Boppart et al. 1998) assessed the feasibility to identify intra-cortical melanomas where other lower resolution imaging modalities had been unsuccessful. A 1300 nm-broadband source was employed in a Michelson interferometer (figure (2-9-a)) and images of a specimen from the outer human cerebral cortex were taken which contained an intra-cortical melanoma located near the surface of the cortex. The images showed a definite increase in backscatter within the tumour tissue (figures (2-9-b)) (because of the refractive index of the tumour) and even smaller lesions (<500 μm) were identified.

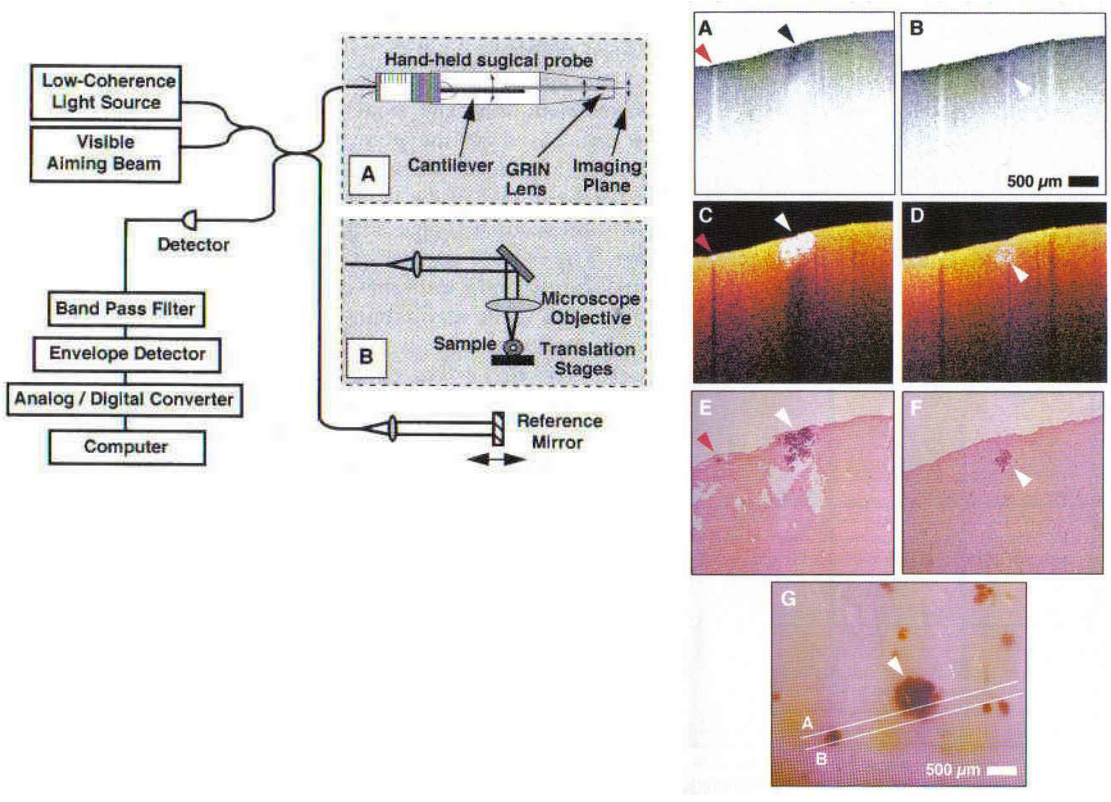

a) b)

Figure 2-9: a) Michelson interferometer set-up employed and b) the results obtained for the neurosurgical application; figure G is the image from the top of the surface, A and B are the OCT images as indicated in the en-face image in G; C and D are the figures if a threshold is applied; E, F: corresponding histology

There is a good correlation between the histological samples and the OCT images. They produce their OCT pictures from a *post-mortem* sample where the intracortical

melanoma is situated near the top surface (it is visible), which helps for the prediction. In the general application of OCT, the sample is not chosen because it is easy to detect but more because it is necessary to check if a tissue is normal or developing a disease.

Welzel reviewed the application of OCT in the dermatology (Welzel, 2001). Figure 2-10 and figure 2-11-a show a normal and abnormal skin. Figure 2-11-b corresponds to the histology of the abnormal tissue.

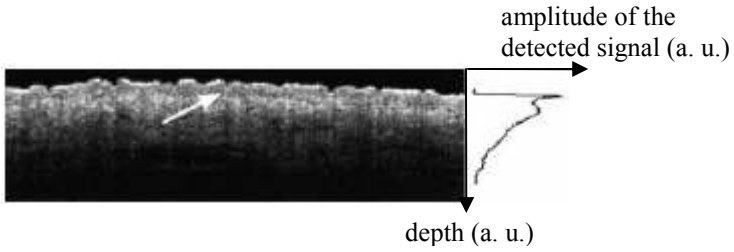

Figure 2-10: OCT image of healthy skin of the forearm. On the right side, the averaged A-scan is represented. The thickness of the epidermis is 195 mm; the relationship between the entrance signal and the second intensity peak on the border to the dermis is 1.7; the light attenuation coefficient in the upper dermis is 1.8/mm. (830 nm OCT, 4 mm×1.3 mm)

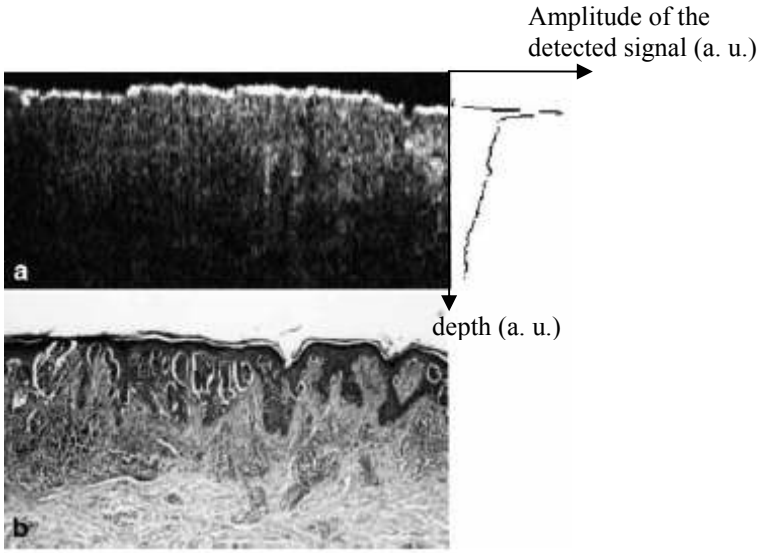

Figure 2-11: (a) OCT and (b) histology of a malignant melanoma. On the averaged A-scan (right), no second intensity peak at the level of the basal membrane is detectable. (OCT 4 mm×1.8 mm; histology ×50)

The two 1-D graphs on the right hand side of each OCT image are the reflected intensity profile, and it can clearly be noticed in the OCT image (figure (2-11-a) or the histology

(figure (2-11-b) that the dermis-epidermis boundary is gone in the abnormal tissue. A cancer having spread tends to break the boundaries between the layers.
Some medical applications are summarised in table 2-2.

Table 2-2: Summary of some OCT applications in medicine

Application	Year of application	Centre wavelength of the source (nm)	Axial resolution (μm)	Imaging depth
Retina (Huang et al. 1991)	1991	830	17	1-2 mm
Coronary artery (Huang et al. 1991)	1991	830	17	150-200 μm
Blood vessels (Brezinski et al. 1996)	1996	1300	20	1 mm
Gastrointestinal tissue (Kobayashi et al. 1998)	1996	1270	19.2	1-2 mm
Skin (Welzel et al. 1998)	1998	830	15	1 mm
Dental studies (Colston et al. 1998)	1998	1310	20	1 mm
Neurology (Boppart et al. 1998)	1998	1300	23	1.8-2 mm

2.2.5 Industrial applications

Duncan *et al.* (Duncan and Bashkansky, 1998) used an OCT system, with a 1.3 μm source, to image defects in materials like ceramics, paints and coatings. OCT is a non-invasive technique and this application shows as well that this technique can be used to check several material qualities without damaging the samples.

In 2001, OCT was compared with two other techniques, X-rays CT and laser scanning confocal microscopy, to image cracks in matrix composites (Dunkers et al. 2001). OCT resolved the depth of the cracks that both other techniques failed to identify.

The OCT application on materials has been extended to the stress measurement. Oh *et al.* map stress distribution and damage due to tensile loading, using polarisation sensitive OCT (Oh and Kim, 2003).

In order to produce an OCT image from a sample *in-vivo* it is necessary for the instrumentation to be adapted for fast acquisition in order to minimise artefacts due to the movement of the patient and to improve comfort.

2.3 Instrumentation

OCT uses LC interferometric signals to detect changes in the refractive index between different layers in samples. The instrumentation is based on a broadband source, an interferometer and a detection system:

Details of the investigated interferometers and types of source employed are provided. Different scanning devices are indexed with a discussion.

2.3.1 Interferometer configurations of OCT

People have investigated OCT using different interferometer configurations; here the different interferometers set-ups employed in OCT are explained.

The Michelson interferometer (MI) is one of the most implemented configurations, because it is easy to implement and it requires few components. Figure 2-12 provides the free space and in-fibre configuration set-ups.

In the first version the light from the broadband source is split into two parts by the 3-dB directional coupler. One part of the light passes through one arm of the fibre and undergoes reflection, transmission and scattering by the sample (the sample arm). The other part of the light passing through the other fibre is reflected at the mirror (the reference arm). Both the backscattered light and the reflected light at the mirror recombine at the 3-dB directional coupler, and the signal is detected at the detector. Interferences occur when the optical path difference between the reference and sample arms is within the coherence of the source. By analogy, a similar explanation applies for the free-space configuration.

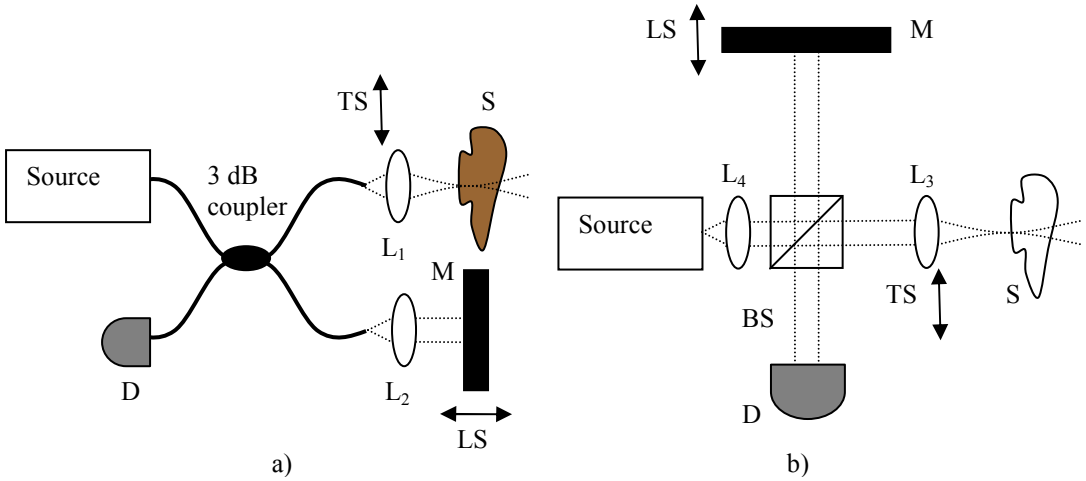

Figure 2-12: a) In-fibre and b) free-space Michelson interferometers; TS: transverse scan, LS: longitudinal scan, L_1, L_2, L_3, L_4: lenses, BS: beam splitter, D: detector, S: sample, M: mirror

The second configuration (in free-space), figure (2-12-b), is now generally used mainly for full-field OCT systems, where a CCD is used as a detector (Egan et al. 1930). This set-up has been well developed for ophthalmology application (Yazdanfar et al. 2003). Point OCT is mostly applied with the in-fibre MI.

Because it is easy to implement, most improvements and extensions described to date use this configuration. However, the in-fibre configuration suffers from fringe drift which may be due to fibre stretching or a different temperature in one of the arms of the interferometer. Polarisation changes also arise from induced birefringence due to fibre deployment such as bending. A maximum of 50 % of the light reaches the detector. The other 50 % returns towards the source, as feedback, and may result in deterioration of source performance. In order to reduce the polarisation fading, polarisation controllers are often used to maximise the visibility of the fringes.

In many systems, the MI has been slightly modified, incorporating another coupler (Yang et al. 2004) (figure (2-13-a)) or an optical circulator (Zara et al. 2002), (Huber et al. 2005), (Yang et al. 2006) (figure (2-13-b)) to carry out balanced detection and improve the signal-to- noise ratio (SNR).

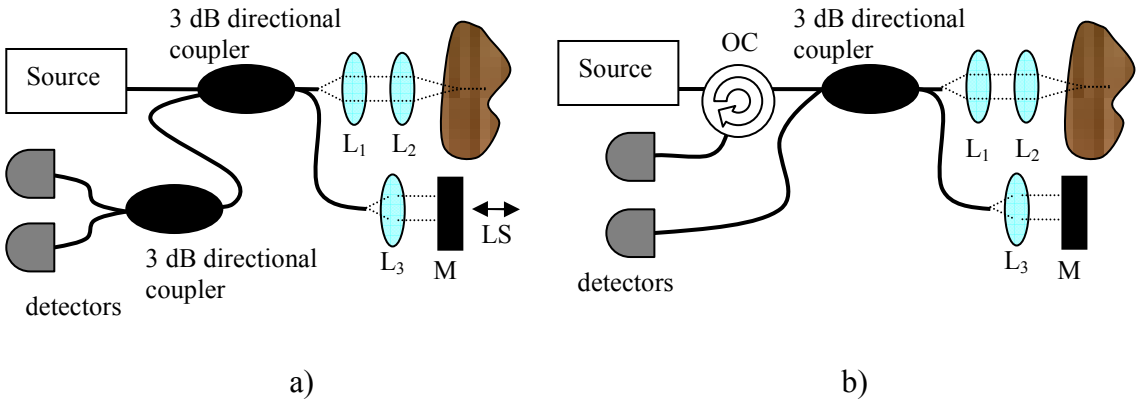

Figure 2-13: Balanced Michelson interferometer employing a) a directional coupler and b) and optical circulator; OC: optical circulator

After the first OCT images of biological structures using a MI (Huang et al. 1991), other interferometer configurations were investigated in order to achieve optimal performance (Schmitt Joseph M., 1999) (Rollins and Izatt, 1999). An in-fibre Mach-Zehnder interferometer (MZI) has been used to investigate phase-drift suppression using harmonics in heterodyne detection created by piezoelectric elements placed in the reference arm (Sato et al. 2000).

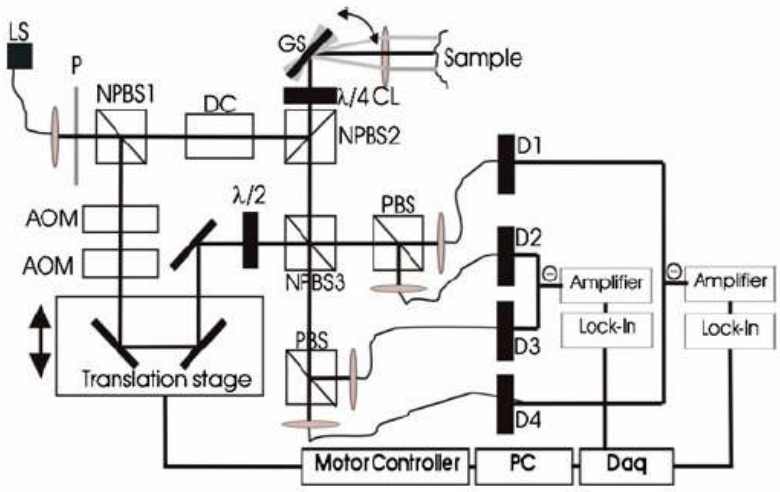

Figure 2-14: Experimental set-up of the transversal phase resolved polarization sensitive optical coherence tomography technique (for the *in vitro* measurements the dual balanced detection unit was not implemented, only the signals from D1 and D2 were recorded). LS: light source, P: polarizer, NPBS: non-polarizing beam splitters, GS: galvo-scanner, DC: dispersion compensation, AOM: acousto-optic modulators, λ/4: quarter wave plate, λ/2: half wave plate, PBS: polarizing beam splitters, D1, D2, D3, D4: detectors, PC: personal computer, DAQ: data acquisition board. (Pircher et al. 2004)

In 2004, a free space MZI has been demonstrated for the application of polarisation sensitive OCT (Pircher et al. 2004). The experimental arrangement is shown below in figure 2-14.

Surface birefringence of the cornea was shown where the signal was demodulated via a lock-in system: acousto-optic modulators were placed in the reference arm to produce a carrier frequency which was used as a reference.

Due to the change in the environment where the system is placed, Michelson and Mach-Zehnder interferometers suffer from phase fluctuations because e.g. the reference and the sample arms do not have the same temperature or the same polarisation (minimising the visibility of the fringes). The signal fading is due to random fluctuations in the state of polarization of the interfering beams propagating in the optical fibre (Kersey et al. 1988). The effect of temperature changes is to modify the refractive index of the optical fibre via the thermo-optical effect and also causes fibre expansion. The overall temperature effect therefore leads to phase change which can be of the order of 35.8 fringes.m^{-1}.K^{-1} (White et al. 1987).

In order to match the polarisation and increase the visibility of the fringes polarisation controllers are used. *In-vivo* applications using endoscopic technology suffer from temperature and stress changes along the fibre when the endoscope is inserted in the body.

Schmitt (Schmitt Joseph M., 1999) did a comparison between the Michelson and Mach-Zehnder interferometers in free-space or in fibre. The use of fibre is convenient but it is not essential for *ex-vivo* applications. There are far fewer problems in polarisation change and dispersion employing a free-space configuration.

The disadvantages of the Michelson and Mach-Zehnder interferometer can be overcome by the used of a Fizeau-based interferometer. A basic Fizeau interferometer is shown in figure 2-15.

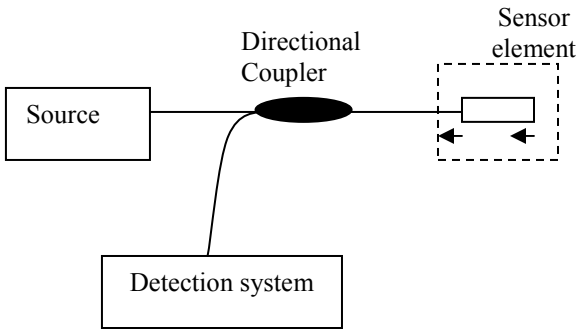

Figure 2-15: Basic Fizeau configuration concept

The light from the source passes through the directional coupler and is transmitted to the sensor element where the light suffers an optical phase change due to the measurand. The light passes back through the coupler and is detected. The sensing element, composed of two parallel reflectors, is called a Fizeau interferometer.

It has been considered for the development of optical sensors for displacement (Bosselmann and Ulrich, 1984), strain measurement and temperature sensing (Boheim, 1986) (Beheim, 1986)). A necessary requirement was to have stability of the system used which was achieved by employing a broadband source, providing low coherence interferences, and combined with a second interferometer, called as a processing interferometer. The second interferometer is used to match the optical path difference in the sensing interferometer.

This interferometer is much used in its bulk optic configuration for checking the profile of optical components (lenses, mirror) (Sigma Koki Co., 2004-2005) because with white light, interferences are only seen for path-length imbalances within the coherence length of the source.

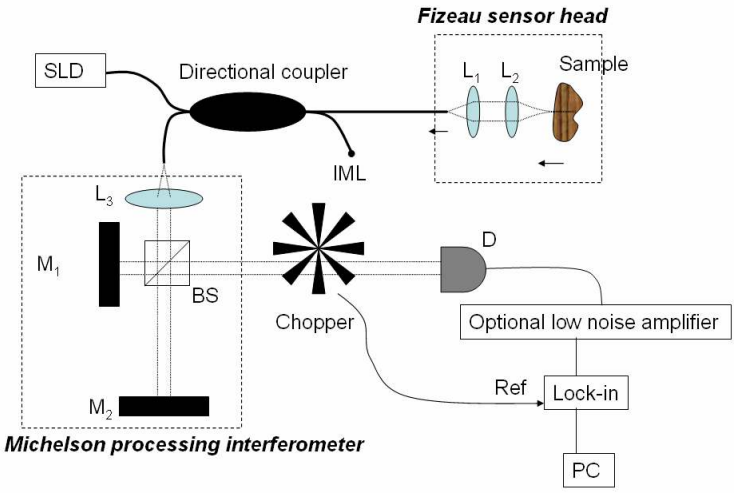

Figure 2-16: Standard Fizeau configuration for OCT investigation; L1, L2 and L3: lenses; BS: beamsplitter; M1, M2: mirrors; D: detector (Bamford, 2000)

The standard Fizeau configuration has been investigated in OCT for the detection of precancerous bronchial tissue (Bamford, 2000) (figure 2-16). The system employed used a lock-in amplifier: the optical signal was modulated with a chopper and an electrical reference signal was used at the same frequency of modulation; this technique reduces noise, because the detection is done only at the modulating frequency (it acts as a filter). In this configuration interference occurs only when the optical path difference between the sensing interferometer and the processing interferometer is within the coherence length of the source.

Bamford's (Bamford, 2000) experiments achieved a SNR that was capable of resolving a relative permittivity difference of 0.14 at a boundary between two layers. Thus it was shown that this configuration was suitable for Epithelium/submucosa measurements of the skin. In this thesis, the work is focused on the development of the Fizeau configuration.

Table 2-3 summarises the advantages and disadvantages of the interferometers.

Table 2-3: Advantages and disadvantages of the interferometers

Interferometers	Disadvantages	Remedies	Advantages
Michelson	Polarisation-sensitive Temperature-sensitive Maximum 50 % of the power of the light source reaches the detector	Polarisation controller to maximise the fringes.	Easy to implement
Mach-Zehnder	• Polarisation-sensitive Temperature-sensitive • difficult to implement compare to Michelson interferometer	Polarisation controller to maximise the fringes	_
Fizeau interferometer	• Not straight forward alignment • Maximum 12.5 % of the light source reach the detector	Processing interferometer needed	Downlead insensitivity No polarisation- and temperature-sensitive

The advantages of such a configuration are that the interferometric signal depends on essentially the combined optical path difference of both the sensing and the processing interferometers. Any change in the fibre leading to the sensing interferometer will change the reference and sample beams in the same way. This is known as “downlead insensitivity”. This also means the sensing fibre can have a length as long as required, without affecting the measurement.

The main problem of this standard configuration is that due to the 3 dB coupler a maximum of 50 % of the available light from the source goes to the sensing interferometer, and a maximum of 25 % of the light from the source reaches the processing interferometer. This is an inefficient use of the available light which will affect the SNR of the configuration.

This type of interferometer is key to the stability of an OCT system; another important issue is the centre wavelength and bandwidth of the source.

2.3.2 Source wavelength

Absorption and scattering of the wavelength due to chromophores are essentially both phenomena limiting imaging in tissue, the former being important at short wavelength, and the latter at longer wavelength.

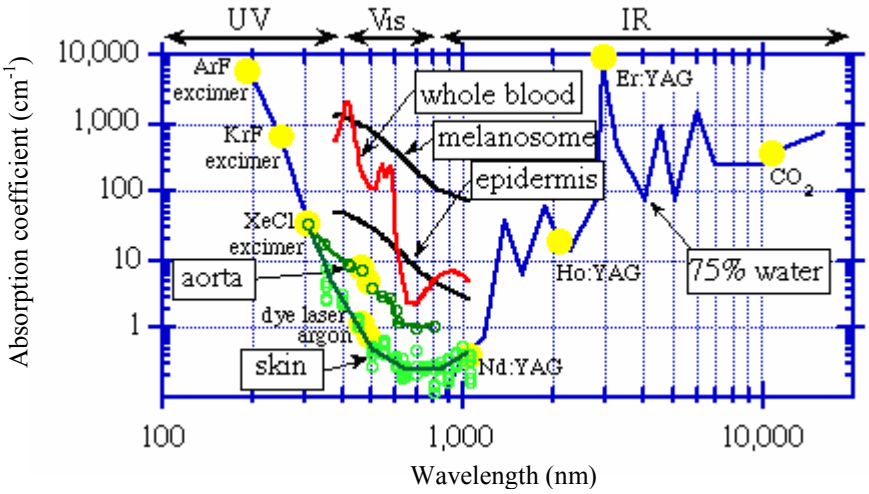

Figure 2-17: Spectral absorbance of some constituents of the human tissue (Jacques and Prahl, 1998)

As shown in figure 2-17, the imaging window in the optical spectrum is around 800 nm (infrared (IR)) as the absorption is low. Treatments against cancer have been possible using lasers that emit in the UV to near visible (figure 2-17). Tissues being good absorbers, the idea behind the treatment is that the cancer will absorb the radiation, until the moment it will not be able to absorb more energy. There is a risk with this technique to irradiate the normal tissue.

As well on this figure it is noticed that in the UV and in the infrared, the absorption of the skin tissue is high. In the IR, absorption is mainly due to water.
Oxyhemoglobin and deoxyhemoglobin are the principal constituents and chromophores in the human tissues (e.g. skin). The absorption spectrum shows a minimum around 800 nm. This is one reason why broadband sources centred around this wavelength are in common use.

OCT, as was explained earlier, has been applied to transparent tissue for ophthalmologic imaging. The first OCT systems were used to examine transparent

tissue such as optical tissue, and the depth of imaging was not a major consideration. The wavelength of the low coherent SLD sources used was centred around 830 nm (Huang et al. 1991).

OCT imaging through non-transparent tissue requires greater light penetration than transparent tissue. This is achieved by using a light source emitting in the Near Infrared (NIR) region of the spectrum (the only limitation is water, being a good absorber in the IR region).

Even with the newly developed, high resolution Ti:Al_3O_2 (Drexler et al. 1999) sources the wavelength used stayed initially around 780 nm, although these allowed a high power output. Now the interest in OCT imaging has spread to examining non-transparent tissue such as skin (Lazar et al.) or the lining of the gastrointestinal tract (Brezinski and Fujimoto, 1999), and imaging to a greater depth is therefore more relevant. Izatt *et al.* (Liu et al. 1993) used a 1300 nm SLD with a coherence length of 15 μm to look at gastrointestinal tissue. Microstructures <30 μm were identified to a depth of 600 μm.

Using two wavelengths (Brezinski and Fujimoto, 1999), 850 and 1300 nm, the human epiglottis has been imaged and their results are shown in Figure 2-18. Comparing the histology and the OCT images obtained at these wavelengths, shows that at 1300 nm the tissue is imaged deeper and the centre cell begins to be seen. At 850 nm, the top surface is just distinguished whereas at 1300 nm, microstructures are observed in the OCT image, including the cartilage (as shown in the histology).

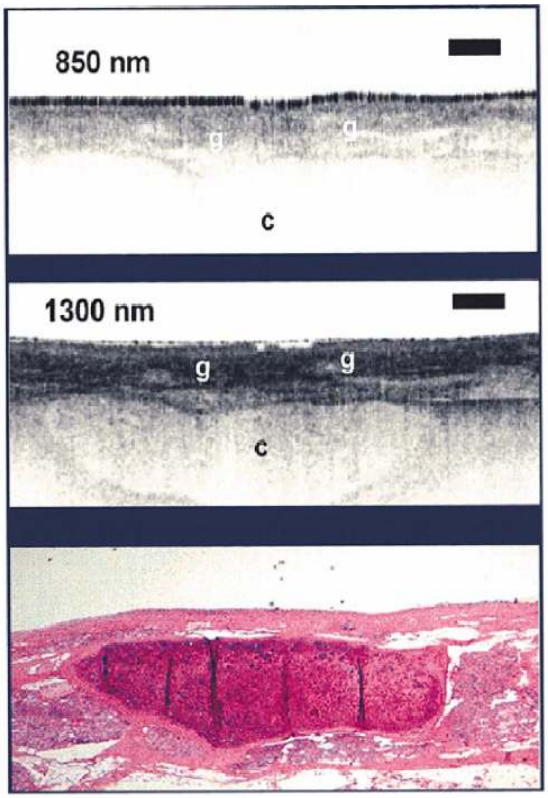

Figure 2-18: OCT images at the wavelength of 850 nm and 1300 nm and histology of the area under study (c: cartilage, g: gland) (Brezinski and Fujimoto, 1999)

Less scattering and absorption are, in practice, achieved for slightly longer wavelengths in the near-IR. Comparing different results obtained with different wavelengths (Bouma et al. 1998), at 1300 nm and 1800 nm, it has been found that the visibility is good and the depth of imaging is about 2-3 mm at 1300 nm; at 1800 nm, it is the contrary: visibility is reduced but depth is increased. The 1300-1800 nm window appears to be appropriate for improvement of the penetration of the light for OCT applications on tissue.

Schmitt (Schmitt Joseph M., 1999) pointed out that the deepest penetration was obtained for a range of wavelength between 1200 and 1800 nm.

To support the justification for use of the wavelength, several OCT images have been produced for a range of wavelength from 475 to 1375 nm (figure 2-19). The higher the wavelength, the deeper the structure information observed from the tissue.

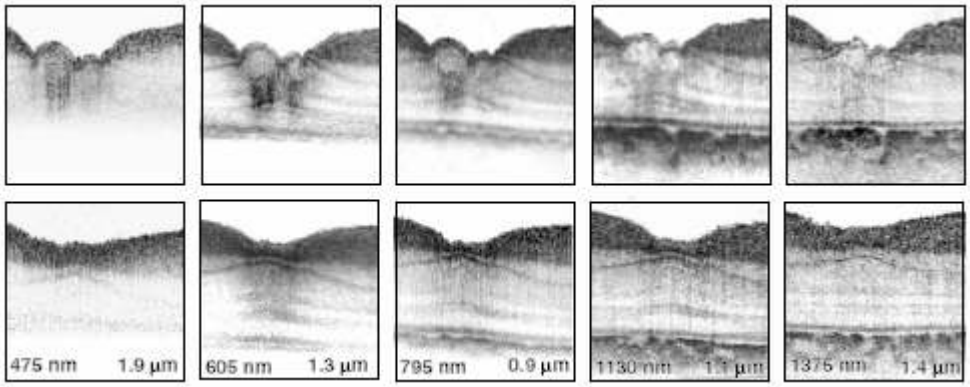

Figure 2-19: *Ex vivo* UHR OCT images (500×500 µm) of a perfusion fixed monkey retina at multiple wavelengths demonstrating enhanced penetration into the choroids using longer wavelengths (Unterhuber et al. 2004)

OCT has also been used with 1550 nm (Yu-Lung et al. 2006). 1550 nm wavelength has several advantages:

- firstly it is in the near IR and the depth of imaging can be high because of less scattering and absorption;
- secondly this wavelength is a telecommunications wavelength. Due to its application in communications, electro-optical components are available and widely used, and therefore their price is relatively low.

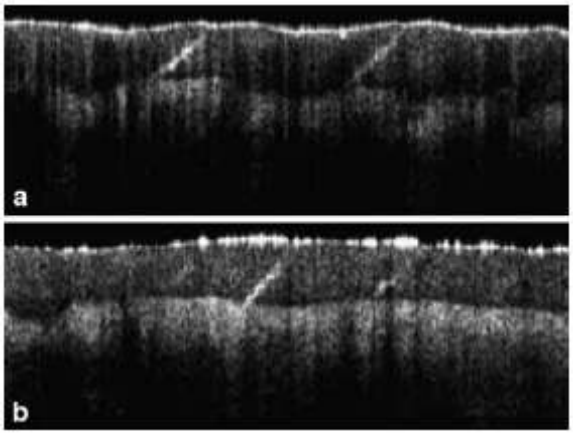

Figure 2-20: Healthy skin of the finger tip before (a) and directly after application of glycerol (b). The treatment leads to an increase in the depth of detection and to an attenuation of the entrance signal. (4 mm by 1.1mm) (Welzel, 2001).

Water and chromophores are good absorbers and are the limiting factors on imaging the depth of tissue. Chemical solutions have been considered to minimise the reflection and scattering from the first layer and then to observe deeper layers (Welzel,

2001). Glycerol has been used in dermatology to improve depth information (figure 2-20).

Solutions have been compared to evaluate the potential of improvement when they are applied. Wang *et al.* (Wang et al. 2003) compared glycerol and dimethyl sulfoxide in the optical clearing of gastric tissue showing that there is not a significant difference between both results.

2.3.3 Improving resolution

The axial resolution of OCT images is primarily dependent on the temporal coherence length of the light source used in the system – the shorter the coherence length, the higher the resolution. The lateral resolution is dependent on the beam diameter of the focussed light on the tissue sample.

For accurate, high-resolution imaging it is necessary to use an extremely broad bandwidth source in order to determine the location of the microstructures within the tissue and gain a higher quality image.

The axial resolution (Schmitt Joseph M., 1999) is defined by the coherence length of the source:

$$L_c = \frac{2\ln 2}{\pi}\frac{\lambda^2}{\Delta\lambda} \qquad \textbf{(2-1)}$$

where λ and $\Delta\lambda$ are the source wavelength and the spectral bandwidth of the source respectively. This is the resolution in air. When applied in tissue it has to be divided by the refractive index of the medium. From equation 2-1, it may be observed that the coherence length is inversely proportional to the bandwidth.

Early studies of OCT made use of the broad bandwidth SuperLuminescent Diodes (SLD) sources, developed in the 1980's, and the first OCT image that was obtained used an 830-nm SLD with a 30-nm bandwidth (Huang et al. 1991). This allowed an axial resolution of 17 μm to be achieved along with a beam diameter of 9 μm for the lateral resolution. Since then, with the development of broader bandwidth sources, the axial resolution has improved considerably.

In 1992 Clivaz *et al.* (Clivaz and Salathè, 1992) used the fluorescence light of a Ti:Al_2O_3 crystal as a light source to obtain 1.9 μm resolution measurements with Optical Low Coherence Reflectometry (OLCR). The spectrum from the fluorescent light emitted (after excitation with an argon laser) showed a maximum output at 780 nm with an extremely large bandwidth of 180 nm. The power of this particular source was low (4.8 μW) and inadequate for biological imaging.

In 1995, Bouma *et al.* (Bouma et al. 1995) published a paper showing 3.7 μm resolution OCT images of onion cells. The high resolution was achieved using a kerr-lens mode-locked Ti: Al_2O_3 laser source, generating low coherent light with power levels above 100mW which is more than required for biological imaging.

In order to produce high quality images, the transverse resolution has to be as high as the axial resolution. Transverse resolution depends upon the imaging quality of the probe. This device will focus the light going out of the fibre on an area of the sample; from the Gaussian beam theory a spot size and depth of focus can be determined.

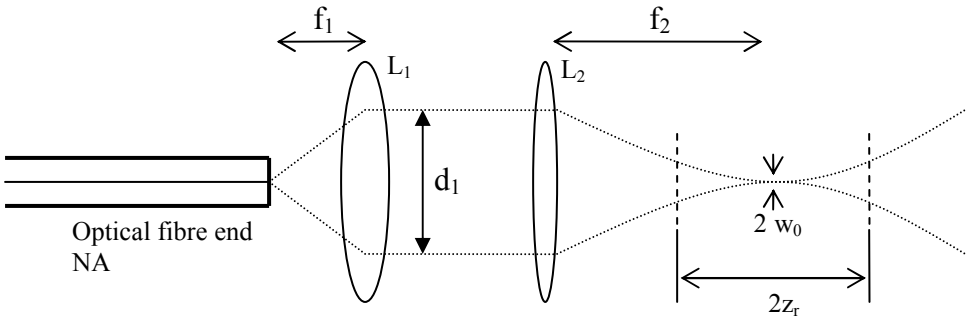

Figure 2-21: Probe design; l_1 and l_2 are two lenses, and w_0 is the radius of the $1/e^2$ irradiance contour at the plane where the wavefront is flat, f_1 and f_2 are the focal lengths of L_1 and L_2; D is the diameter of the fibre core; z_r is the Rayleigh range

A simple biconvex lens could be used to focus the light in the sample. However, to reduce aberrations paired achromates are preferable. An optical achromat lens L_1 is used to collimate the light at the output of the fibre (because of diffraction effects produced by the fibre end the light exiting the fibre diverges at the angle being the

numerical aperture (NA) of the optical fibre) and another L_2 to focus the light on the sample (figure 2-21).

The probe, as described above, has to be moved in a transverse direction, with a step by step distance at least equal to the transverse resolution. Probes have been developed to minimise the mechanical displacement required and to increase the transverse beam displacement, as shown in figure 2-22.

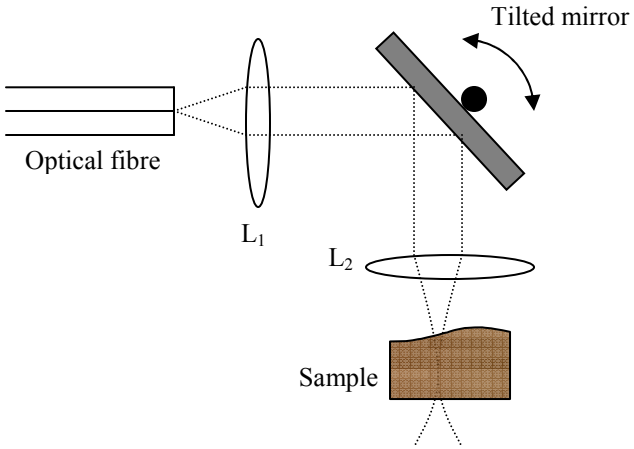

Figure 2-22: Probe configuration using one galvanometer

Light at the output of the optical fibre is collimated by a lens (L_1) and using a rotating mirror and a lens (L_2), light is focused on different areas of the sample.

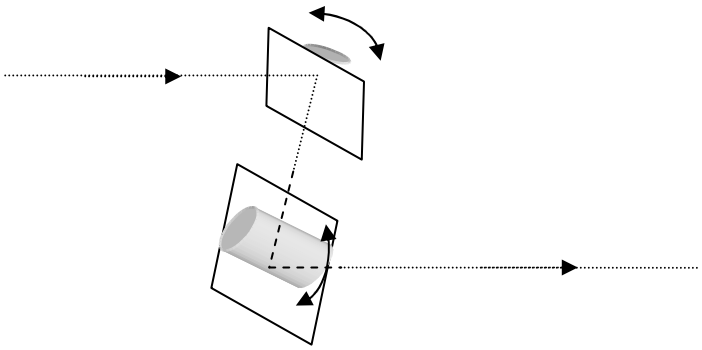

Figure 2-23: Transverse scan using two galvanometers

In particular, set-ups have been proposed and applied using two galvanometers, as shown in figure 2-23, which provides the capability to generate a 3-D image (Yeov et

al. 2005). It was first applied to OCT ophthalmic measurements, and since then miniaturised versions have been described (Xie et al. 2003a).

Endoscope/catheter devices have been developed for industrial applications (Karl Storz - Endoskope, 2005), e.g. to check the surface of pipes without easy access.

This kind of device uses a lens to focus light from a rotating prism onto the sample. The transverse scan traces out radii of the pipe. The diameter of these devices have been minimised to about 1 mm and has been proposed for medical imaging (Patwari et al. 2000). A coronary artery was imaged employing OCT and ultrasound technique enabling comparison. More details are obtained with the endoscopic OCT system where the vessel wall is observed.

The main problem with medical applications is that, due to the movement of the tissue, the system requires a high speed scanning device to freeze the image and produce near real-time imaging. It has been applied on colon tissue, gastrointestinal tissue, and some results are shown in figure 2-6. Endoscope devices have been developed to produce fast acquisition using micro-electronic mirror scanners (MEMS) (Pan and Huikai Xie, 2001), (Xie et al. 2003), (Xie et al. 2003a), (Xie et al. 2003b).

2.3.4 Increasing scanning speed

It is important that OCT images are acquired as quickly as possible in order to reduce motion artefacts that blur images and to retain image quality which is particularly important for micrometer accuracy. It is also important for patient comfort and faster scanning is more bearable for the patient under examination.

Increasing longitudinal and lateral scanning speeds are both important, however more longitudinal scans are acquired to improve the accuracy of the images and so the speed of these scans are the limiting factor to the overall acquisition rate.

Longitudinal scanning time is limited by the speed of the moving reference arm used to vary the path length in the interferometer. The first OCT system (Huang et al. 1991) used a translating reference mirror to vary the path length, moving at a speed of 1.6 mms^{-1}. For many years afterwards other researchers took this approach using a translating mirror or piezoelectric (PZT) fibre stretching (Swanson et al. 1992). The

maximum speed of the translation mirror (Swanson et al. 1993) reached 160 mms^{-1} and the PZT fibre stretching (Tearney et al. 1996b) 3 ms^{-1}.

In 1997 a new method for increasing the scanning speed was presented, using a rotating glass cube to vary the path length (Ballif et al. 1997). The cube was placed between the end of the fibre and a fixed reference mirror. The light beam is internally reflected within the cube onto an external prism. This directs the beam back to the cube and onto the reference mirror where it is reflected back. The cube rotates at 96 Hz and a longitudinal scan speed of 21.3 ms^{-1} was achieved.

Continued development of the rotating cube led to increased speeds of up to 96 ms^{-1} for longitudinal scanning (Delachenal et al. 1997) by placing the rotating cube in the path of the reference arm and the sample arm.

In 1998 (Szydlo et al. 1998) longitudinal scan speeds of up to 176 ms^{-1} were achieved using a rotating glass cube spinning at 427000 rpm driven by a high speed air turbine. The rotating cube arrangement has proven to be the most successful for attaining fast scanning speeds but the set-up involves a great deal of precision and the system requires high electrical powers to run on. A summary of the scanning speeds achieved using various techniques is shown in table 2-4.

However these techniques all have inconveniences: some of them have a problem with the duty cycle; the reference arm is also subject to dispersion, because the light passes through a glass in the reference arm and, interfering with the sample arm, it worsens the resolution. This can be reduced placing a prism between the rotating cube and the reflecting mirror.

Minimising wavelength dispersion can be achieved employing two parallel mirrors on a rotating plate as proposed by Fercher (Fercher, 2001). Light does not pass through the glass anymore.

Any non-linearity in the scan speed induces a varying signal centre frequency and bandwidth and warping of the image unless processing for compensation is included.

Table 2-4: Comparison of high-speed scanning systems

Techniques	Scan rate delay line	Maximum speed	Inconveniences
Galvanometer based translation retroreflector system (Liu et al. 1993), (Swanson et al. 1992), (Swanson et al. 1993)	100 Hz	160 mms^{-1}	Low speed method
Rotation cube (Ballif et al. 1997; Delachenal et al. 1997; Su, 1997)	384 Hz	96 ms^{-1}	• Duty cycle, very low • Scan non-linear with time
Piezoelectric actuated fibre stretchers (Tearney et al. 1996b), (Gelikonov et al. 1996)	600 Hz	3 ms^{-1}	Static and dynamic: birefringence effects Requirement: extra component to compensate the instability due to the temperature dependence
High speed resonant mirror (Windecker et al. 1997)	1200 Hz (3 mm scan length)	176 ms^{-1} (Szydlo et al. 1998)	Not capable of higher repetition rate
• Rotating mirrors (Yasa and Amer, 1981) • Rotating roof prisms (Harde and Burggraf, 1981), (Xinan et al. 1988) • Loudspeakers (Sala et al. 1980)	They have not achieved the scan rate necessary for real time OCT		Some suffer from low duty cycle

Several other delay line systems have been developed in order to reduce the data acquisition time of the signal coming from the OCT system.

The RSOD Line is an optical delay line previously used in femtosecond pulse shaping (Weiner, 2000). An example of the general set-up is given in figure 2-24.

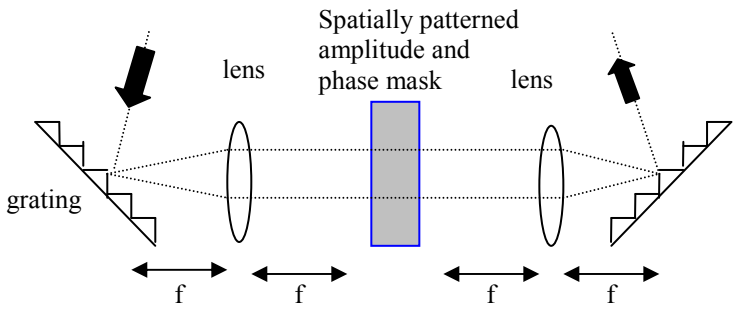

Figure 2-24: Pulse Shaping

The light is dispersed by the grating; it is collimated by the lens; a spatially patterned amplitude and phase mask is positioned at the focal point of the lens where a Fourier transform occurs. Using a second lens, the light is focused onto another grating to recompose at the output of this device the collimated beam. By defining different types of mask different kind of pulses can be produced. Femtosecond pulse shaping is a well-known and well-established technique. It has been shown that the femtosecond pulse shaping device may be used as an optical delay line. It is based on the well known property of the Fourier transform, for which a linear change in the Fourier domain corresponds to a phase change in the time- or space-domain. It was first used for checking of pulse shaping (Kwong et al. 1993).

In 1997 (Tearney et al. 1997), a high–speed phase- and group-delay scanning was presented where a grating-based phase control delay line has been used. The scanning rate was 6 ms^{-1} and the frequency repetition rate was 2 kHz. The experimental arrangement is shown in Fig 2-25.

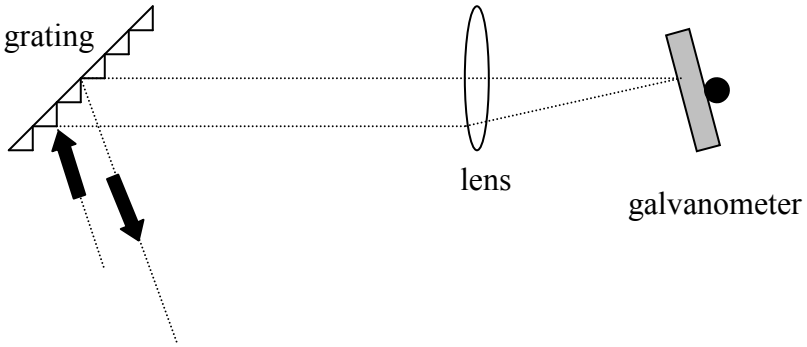

Figure 2-25: Rapid-scanning optical delay line

It utilizes a property of the Fourier domain: a linear modulation of the phase in the Fourier frequency domain produces a group delay in the time domain.

The light is dispersed by the grating and focused by a lens onto a rotating mirror positioned at the focal plane where the spectral Fourier components appear. By tilting the mirror (typically using a galvanometer), a wavelength-dependent phase change $\Phi(\lambda, t)$ is produced, equal to:

$$\Phi(\lambda, t) = \frac{4\pi f \gamma(t)}{\lambda}\left\{\theta_o - \arcsin\left[\frac{\lambda}{d} - \sin(\theta_i)\right] + \frac{x_0}{f}\right\}, \qquad \textbf{(2-2)}$$

where f is the focal length of the lens, $\gamma(t)$ is the galvanometer angle, λ is the wavelength, x_0 is the offset position to the rotation axis of the galvanometer, θ_i and θ_o are the incident and the diffracted beams on the grating and d is the groove spacing of the diffraction grating; the group delay produced (Tearney et al. 1997) is expressed by:

$$l_g(\gamma) = 2\frac{f\lambda_0\gamma}{d\cos(\theta_0)}. \qquad \textbf{(2-3)}$$

The carrier fringe frequency is dependent on the offset position of the galvanometer to the optical axis but is independent of the group delay (Tearney et al. 1997). The light is then refocused on the grating producing a collimated beam, parallel to the incident beam.

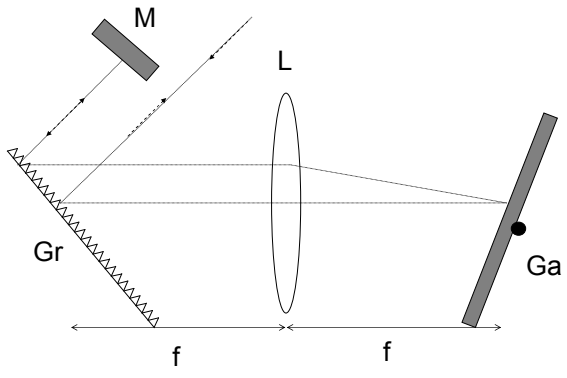

Figure 2-26: High-speed phase and group-delay scanning with a grating phase control delay line and a double pass mirror

A double path configuration may also be considered as shown in figure 2-26, where a mirror is used to couple back the light to its initial point. This reduces the generation of group delay dispersion (GGD). It has been employed to image disease in the eye and skin in real-time (Rollins et al. 1998).

The retroreflecting mirror also enables minimisation of the phase dispersion, produced by a delay in the average wavelength arrival time at the grating, where recombination of the collimated beam takes place.

This system has been implemented in different application in OCT systems (Rollins et al. 1998).

In table 2-5, an example of the experimental values for the set-up is given for the two references cited.

Table 2-5: Example of the characteristics of the RSOD lines

		RSOD line	Double RSOD line
Grating	Number of grooves/mm	150	600
	Incident Angle (degrees)	15	-
	Output Angle (degrees)	-27	-
Focal length (mm)		100	50
Galvanometer/ scanner	Frequency of rotation (kHz)	1	4
	Scan Angle (degrees)	3.6	-
Wavelength (nm)		1280	1310
Remarks		There is no specification on the grating-lens distance, but the lens-galvanometer distance has to be equal to the focal length	The grating-lens and lens-galvanometer distances are equal to the focal length.
Optical path length delay (mm)		3	3
Reference		(Tearney et al. 1997)	(Izatt et al. 1997)

Table 2-5 shows that while different parameters are considered, similar scan depths are achievable, but the advantage of double-pass configuration is to reduce the dispersion.

The RSOD line has been used to produce 2-D images, permitting imaging *in vivo*, of samples such as the gastrointestinal tissue (Rollins and Ung-Arunyawee, 1999).

Some patents have suggested similar set-ups employing different shapes for the moving mirror (Tearney et al. 2001a), (Tearney et al. 2001b). At the focal plane different mirror shapes can be used, with different geometry, such as a cube or a polygonal mirror array. With the polygonal mirror array (Oldenburg et al. 2003) 15 kHz rotating rate might be obtained. But this system suffers from stability problems; using a cube, the system will suffer from inertia force that prevents a suitable linearity.

Many of the papers do not explain explicitly the method of alignment or the kind of signal observed at the output of the RSOD line.

Systems have been modified to permit the double pass. A double pass was introduced in an RSOD line to create a linear delay of about 2.3 cm using a double-pass polarizing reflector (Silva et al. 1999). The scheme of the employed system is shown in figure 2-27-a):

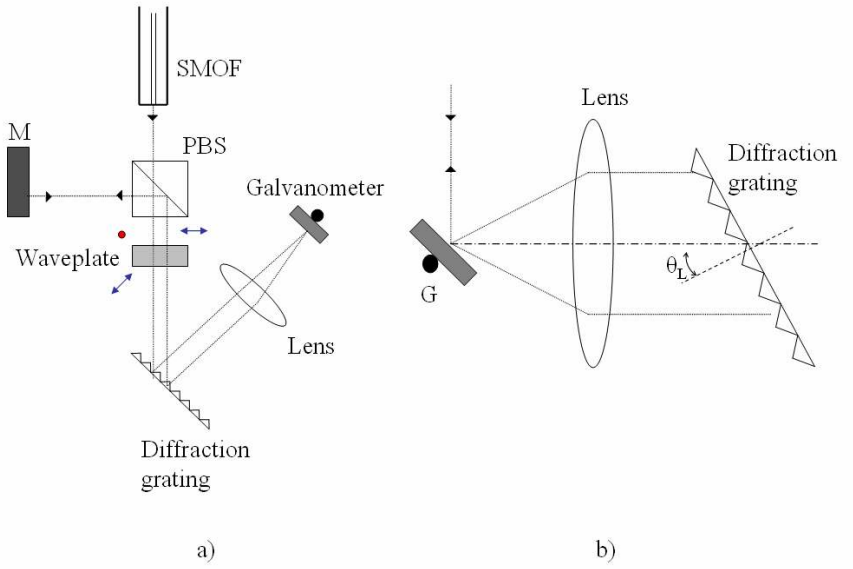

Figure 2-27: a) Double pass RSOD for linearly polarised light (Piao and Zhu, 2004). b) time domain optical delay line (Silva et al. 1999); SMOF: single mode optical fibre, M: mirror, PBS: polarisation beam splitter, G: galvanometer, θ_L: Littrow-mount angle

The light at the output of the fibre, being linearly polarised, passes through the polarisation beam splitter, the half-waveplate where the polarisation is rotated at 45º, the grating-lens-galvanometer. The return light polarisation is rotated by a further 45º (vertical polarisation) by the waveplate, reflected by the PBS and the mirror. The light passes back the optical path to the optical fibre.

Another configuration is the time domain rapid scanning optical delay line. The configuration is shown in the figure (2-27-b). This system uses the Littrow-mount of the grating θ_L (the diffracted beam is collinear with the incident). It should improve the SNR by about 4 dB because the light is diffracted only once and improve the induced group delay (Piao and Zhu, 2004). The collimated beam is reflected at the mirror mounted on a galvanometer that is placed at the focal point of the lens. After the lens the light beam is parallel for all different angles of rotation of the galvanometer. Placing the diffraction grating at the Littrow angle for the incident light, the light is then reflected and sent back to the interferometer.

All the devices presented here require at least one moving element. Some people have investigated the possibility of scanning by changing the frequency of the source. Sources have been developed, where the wavelength may be swept. This technique applied to OCT is known as swept source OCT, a similar technique to Spectral-Domain OCT (SD-OCT).

The principle of SD-OCT is illustrated in figure 2-28:

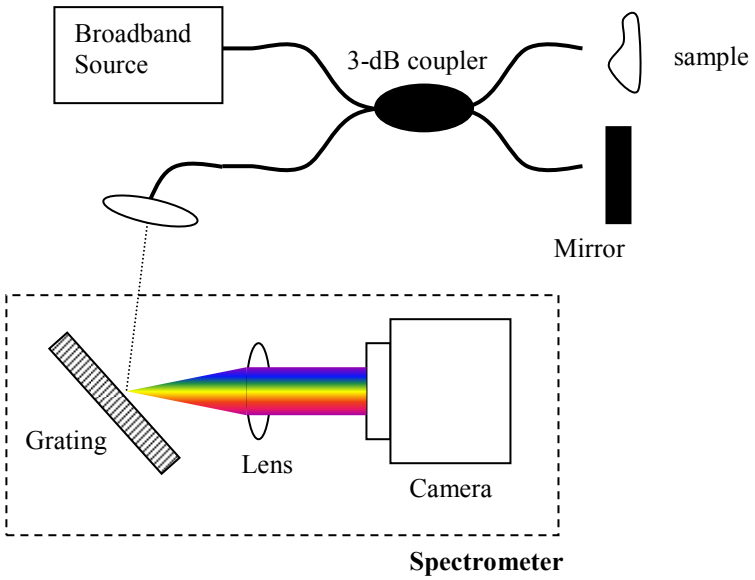

Figure 2-28: SD-OCT using spectrometer

The output of the Michelson interferometer is transmitted to a spectrometer (it is basically composed of a grating, a lens and a camera at the focal point in order to obtain the spectral information). A discrete-Fourier transform is carried out on the displayed signal and the depth information is obtained.

Another version has been investigated to carry out a similar application; the main difference is that instead of using a broadband source and a spectrometer, a tuneable source is employed and a single detector is used to detect the spectral information. The concept is illustrated in figure 2-29.

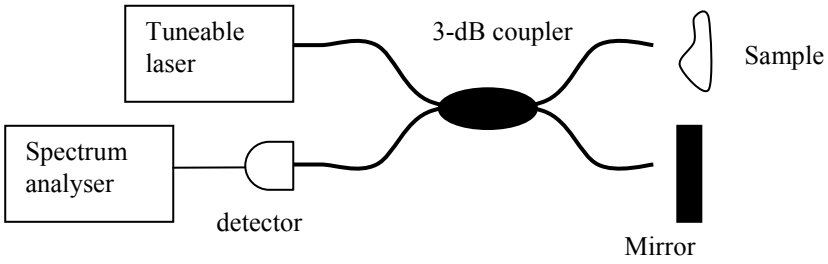

Figure 2-29: SS-OCT using a tuneable laser

The wavelength of the tuneable laser (or swept source) is changed rapidly, and from the signal detected, a spectrum is obtained. A Fourier transform is again required to obtain the result. Optical paths in both arms have to be closely similar, but a small offset is required between both arms to separate the correlogram and the wanted signal (Andretzky et al. 1999).

The SNR of the SS-OCT and SD-OCT techniques have been compared with TD-OCT (Choma et al. 2003) for SS-OCT systems employing a balanced detection. A significant improvement is obtained with the SD-OCT and SS-OCT of about 20-30 dB. The improvement of SNR of SD-OCT over TD-OCT has also been reported and demonstrated elsewhere.

The good advantage of this technique is that no-moving elements are required and as a complex Fourier signal is used, phase information can also be provided, which then can be used for polarisation sensitive-SD-OCT (Yasuno et al. 2002) and Doppler SD-OCT (Zhang and Chen, 2005).

2.4 Extensions to the OCT technique

2.4.1 Introduction

As discussed previously, OCT is an imaging technique which has been applied to both transparent and turbid tissue (Schmitt Joseph M., 1999), (Zvyagin et al. 2003).

OCT, with its attractive high resolution imaging of biological tissue and local small optical path difference, can be used in conjunction with other imaging techniques and also be used for measuring other optical properties, which may enhance contrast or supply additional information about the biological tissue.

It has been shown that some tissues, like cartilage, have birefringent properties and different tissue types have different spectral absorption that can provide additional information (Madden et al. 2004), (Savage, 2001).

Additionally in fluid mechanics applications, techniques have been developed in order to provide information on the flow velocity, which is used, for example, in the determination of the blood velocity.

The following section discusses additional capabilities of OCT.

2.4.2 Polarisation-Sensitive OCT (PS-OCT)

A combination of OCT and polarisation sensitive detection have been used to produce two dimensional image maps showing the changes in polarisation as a function of depth (de Boer et al. 1997), (Schoenenberger et al. 1998), (de Boer et al. 1999b).

Two-dimensional maps of birefringence of biological tissue are useful in revealing structural information, which may not be displayed using other imaging techniques. It has been proposed that PS-OCT may be used to detect thermal damage by identifying areas of partial loss in birefringence (Schoenenberger et al. 1998).

Figure 2-30 shows an example of free-space PS-OCT system. Light from an SLD passes through a polarizer selecting a linear and vertically polarised input state. This is split 50/50 by a polarisation insensitive beam splitter into a reference and sample arm. Light in the reference arm passes through a Quarter Wave Plate (QWP) orientated

at 22.5° to the incident polarisation. After reflection on the reference mirror, mounted on a translation stage, the light emerges with a linear polarisation state oriented at 45° with respect to the incident plane of polarisation.

Light in the sample arm passes through a QWP orientated at 45° to the incident light so that circularly polarised light is incident on the tissue sample. After passing through the lens system and tissue sample, the backscattered light is in an arbitrary polarisation state depending on the birefringence of the reflection site.

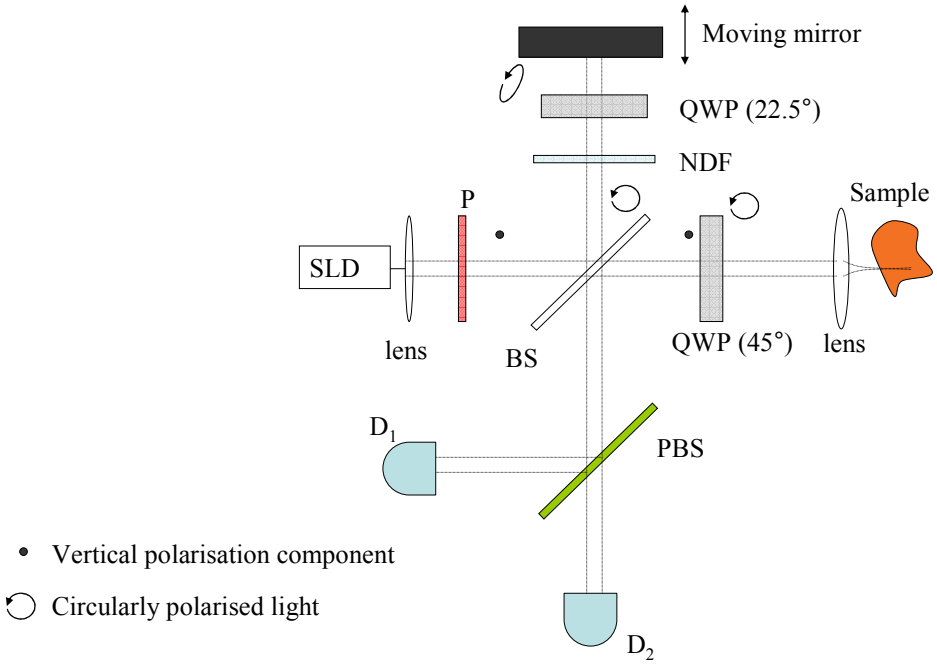

Figure 2-30: PS-OCT system; SLD: superluminescent diode, P: polarizer, NDF: neutral density filter, QWP: quarter waver plate (angle to incident light), BS: beam splitter, and PBS: polarised beam splitter

The reference and sample beams recombine at the BS and are split into their horizontal (A_H) and vertical (A_V) polarised field amplitude components of intensity, by a polarising beam splitter (PBS). Each polarisation state is calculated using equations 2-4 (horizontal) and equation 2-5 (vertical) (de Boer et al. 1999b).

$$A_H = \sqrt{R_{(z)}}\cos(2k_0\Delta z + 2\alpha)\, e^{-\left(\frac{\Omega\Delta z}{c}\right)^2} \sin(k_0 z\delta) \quad \textbf{(2-4)}$$

$$A_V = \sqrt{R_{(z)}}\cos(2k_0\Delta z) e^{-\left(\frac{\Omega\Delta z}{c}\right)^2} \cos(k_0 z\delta) \quad \textbf{(2-5)}$$

Where Δz is the path length difference between the two interferometer arms, z is the depth of the light reflected from the sample, $R_{(z)}$ is the reflectivity at depth z, c is the free space speed of light, $k_0 = \frac{2\pi}{\lambda_0}$ is the attenuation of the coherent beam by scattering, $\delta = n_s - n_f$ is the tissue birefringence, α is the angle of the fast optical axis measured with respect to the vertical and $\Omega = \frac{\Delta\lambda\, c}{\lambda_0^2\sqrt{\ln 2}}$ ($\Delta\lambda$ is the bandwidth of the source, λ_0 is the centre wavelength and n_s and n_f are the refractive indices along the fast and slow axes of the tissue respectively).

From the vertical and horizontal components detected, the signal is filtered at the carrier frequency [$\cos(2k_0\Delta z)$], leaving a signal oscillating as a function of birefringence and depth. The OCT image may be reconstituted by summing signals from both components:

$$I_{s(z)} = I_{H(z)} + I_{V(z)} \quad \textbf{(2-6)}$$

Where:

$$I_{H(z)} = R(z)\sin^2(k_0 z\delta) \quad \textbf{(2-7)}$$

$$I_{V(z)} = R(z)\cos^2(k_0 z\delta) \quad \textbf{(2-8)}$$

The phase retardation, giving birefringence details, is then:

$$\Phi = \arctan\left(\sqrt{\frac{I_H(z)}{I_V(z)}}\right) = k_0 z\delta \quad \textbf{(2-9)}$$

This technique gives an idea of the birefringence property of the samples.

To define the full birefringence properties of the tissue, the Stokes parameters may be determined (de Boer et al. 1999a). This may be done by use of appropriate

combinations of polarisation incident light (Quaker Chemical, 2005), (Yasuno et al. 2002).

The first PS-OCT results were obtained by De Boer *et al.* in 1997 (de Boer et al. 1997), using the Michelson Interferometer as shown in figure 2-28. A 862 nm SLD with 21 nm-bandwidth was used to image fresh bovine tissue, with results demonstrating changes in birefringence up to 700 μm deep. Results were displayed for normal and thermally damaged tissue and there was a clear indication of where the tissue was irradiated due to the loss of birefringence (figure 2-31). This is not observable on the OCT image.

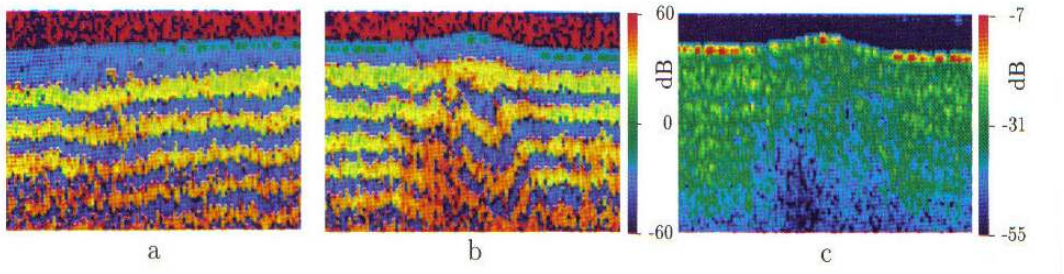

Figure 2-31: image of fresh bovine tendon (1 mm (wide) by 700 μm (depth)); a: birefringence image of fresh bovine tissue, b: birefringence of bovine tendon following exposure, c: OCT image of the bovine tissue (de Boer et al. 1997)

In 1998 Everett *et al.* (Everett et al. 1998) employed a similar PS-OCT system as De Boer *et al.*. The main differences are that a 1310 nm-SLD was used to improve the depth penetration of the light and the polarisation components were coupled to the single-mode optical fibre in the detection system. Impressive depth maps of the birefringence of porcine myocardium were published. Evidence showing how PS-OCT could eliminate artefacts found in conventional OCT was displayed by producing an OCT image using only one of the detectors and this was compared to a conventional OCT image. A layer of reduced scattering was displayed on the PS-OCT image approximately 200 - 450 μm depth, this was not visible on the conventional OCT scan and was shown to be a birefringence induced artefact eliminated by PS-OCT.

In 1999 (de Boer et al. 1999b) OCT was extended to map the birefringence of skeletal muscle, bone, skin and brain tissue (figure 2-32).

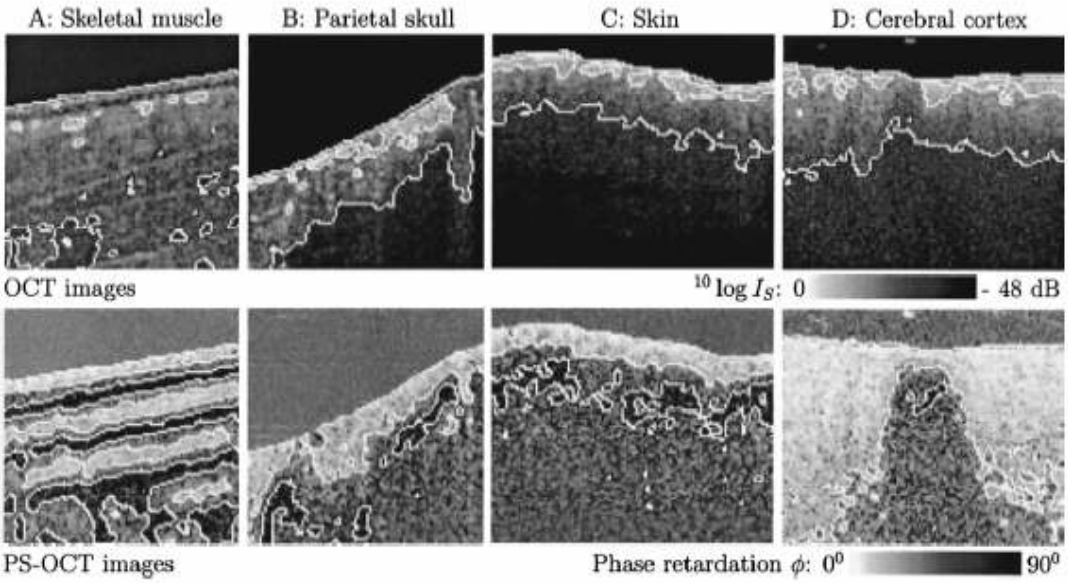

Figure 2-32: OCT (upper) and PS-OCT images (lower) of different tissues (de Boer et al. 1999b)

It has been employed and compared with the microscopy technique to demonstrate its efficiency in the case of bone reconstruction (Drexler et al. 2000). The cartilage is a birefringent tissue (Herrmann et al. 1999); it is shown that if the bone is not properly rebuilt, the bone loses its birefringent property.

2.4.3 Spectroscopic OCT

This technique uses the fact that many samples exhibit an absorption spectrum for light in the visible and near infrared. The same method as in astronomical detection is employed. For different wavelengths it is possible to provide a 2-D image of the sample and, by summing the different "pictures", some information about the issue is obtained. This extension of OCT employs the same principle as space imaging, in which spectral information of the image is observed, providing an image for each wavelength, and they are "superposed". It has been used in oxymetry (measurement of the oxygen rate) to detect the problem of diabetic retinopathy (Owen et al. 2004).

The spectral information is obtained by measuring the full interference signal and gaining the corresponding spectral content. Spectroscopic detection is performed

using a Morlet Wavelet transformation (equation 2-10) this calculates an entire spectrum $W(\Omega,\tau)$ for each point (x,τ) on the OCT image.

$$W(\Omega,\tau) = \left| FT\left\{ \int I_d(t+\tau)\exp^{-\left(\frac{t}{t_0}\right)^2} \right\} \right|^2 , \qquad \textbf{(2-10)}$$

where $\Omega(x,z)$ is the centre of mass of the spectra, FT is the Fourier transform, I_d is the resulting interferogram, t is the scanning time and τ is the time delay between mirror movements.

In standard OCT only the envelope of the interference signal is detected and the image consists of a two dimensional array representing the backscattered light intensity.

Spectroscopic detection using information from an OCT signal has recently come under investigation due to the availability of sufficiently broad bandwidth sources. This technique measures the spectral content of the back-scattered light over the entire optical bandwidth in order to obtain additional information about the properties of tissue. In January 2000, Morgner *et al.* (Morgner et al. 2000) reported the highest OCT resolution to date using spectroscopic OCT in conjunction with conventional OCT. Longitudinal resolutions of 1 μm and lateral resolutions of 3 μm were achieved using a Ti: Al_2O_3 ultra-broad bandwidth femtosecond laser over the range 650-1000 nm. Absorption features due to the presence of oxyhemoglobin and deoxyhemoglobin could be identified within the spectral range, and may enable functional imaging or identification of certain tissues. Presently however, spectroscopic OCT has only been used to enhance the resolution and contrast of conventional OCT images. Broadband sources, such as Ti: Al_2O_3, could be useful if they were not too expensive, because the optical spectrum goes from the visible to infrared. Of course, knowledge of the optical spectrum shape of the source is required.

Alder et *al.* (Adler et al. 2004) investigated spectroscopic OCT using a chirped z-transform algorithm (Rabiner et al. 1969) instead of a discrete Fourier transform. Smoother results were obtained and spectroscopic images were obtained with spectral autocorrelation. The system is insensitive to noise due to Doppler frequency shift.

2.4.4 Doppler OCT

Doppler OCT (DOCT), also called Colour Doppler Optical Tomography (DOCT) is a technique that combines the flow measurement method of Doppler velocimetry with OCT.

The DOCT technique is based on the fact that the phase of the detected signal is a function of the velocity of the fluid flow. All development of this technique is based on the detection of the phase, relating the frequency to the velocity. Ultrasonic Doppler velocimetry has been used extensively for measuring blood flow by determining the Doppler shift induced in the returning signal after being reflected from flowing blood, either towards or away from the transducer.

In 1997 Chen *et al.* (Chen et al. 1997) used DOCT to look at the velocity of polystyrene beads in suspension in a tissue phantom. They used a single detector Michelson configuration with a superluminescent diode (λ = 850 nm, $\Delta\lambda$ = 25 nm, power = 1 mW). The configuration used is given in figure 2-33.

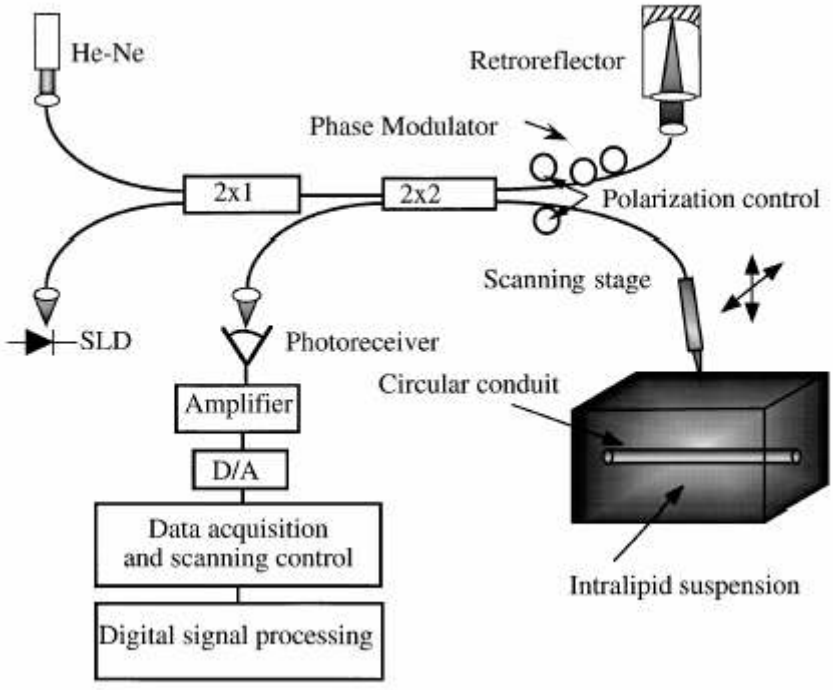

Figure 2-33: In-fibre Michelson configuration for DOCT.; the He-Ne laser is coupled with the SLD to illuminate the sample (Chen et al. 1997)

Izatt *et al.* (Izatt et al. 1996) showed improvements in accuracy, speed and sensitivity and presented impressive results within rat arteries achieving a resolution of approximately <50 μm and a velocity uncertainty of <0.6 mms^{-1}.

At present the difficulty associated with Doppler OCT is the depth penetration of the optical signals and only vessels near the surface of the body are accessible using this technique.

Observation on blood vessels, made before and after treatment using irradiation from a pulse dye laser at 585 and 532 nm, has been reported by Barton *et al.* (Barton et al. 1998). In this paper, the magnitude of the detected signal both as amplitude image and the Doppler image that is obtained from the coherent demodulation of the signal.

DOCT has also been applied to a "U" tube in which water is circulated (Rollins et al. 1999). On the Doppler image the positive and negative velocities of the flow were observed. The technique was also employed using a balanced in-fibre Michelson configuration (Wang, 2004) (with an SLD: λ = 1298 nm, $\Delta\lambda$ = 52 nm, P = 0.5 mW, SNR = 98 dB, Doppler angle = 75°) on a hydrodynamic phantom in which a converging flow occurs. For different positions in the sample the velocity information may be obtained, showing different flow regime along the sample. The OCT image shows that there is some turbulence at the junction of the sample, and using the Doppler shift, the velocity of the flow may be quantified.

The extraction of the phase and spectral information can be processed by different methods:

• Applying a Fourier transform: due to the small shifts induced by the flow, high resolution detection of the phase is required. This is achieved by applying a short-time Fourier transform to the signal. Demodulating the signal at its frequency can be applied;

• Use of Rapid Scanning Optical Delay properties in DOCT: in the RSOD line based on the properties of the grating with the linear phase change in the Fourier domain, the galvanometer may be placed at different positions to get fringes on the obtained signal (Tearney et al. 1997), and there is one position for which there is no phase modulation of the signal (Tearney et al. 1997). Using this property, the signal can be demodulated and, as the Doppler phenomena will add an extra component in the fringes, the fringes in the corresponding demodulated signal will correspond to the moving fluid. In this extension it is noted that the probe is placed at an angle to

maximise the detected Doppler shift and to obtain optimum sensitivity (Chen et al. 1999) from the fluid.

2.4.5 Determination of the refractive index

Most of these extensions use the phase information obtained from the sample to determine some of its optical properties, such as the birefringence. Employing just the amplitude information of the detected signal of the OCT systems has been developed to determine the refractive index of some tissue. OCT measures the optical thickness which is equal to the physical thickness multiplied by the refractive index of the layer considered. This property has been employed to determine the refractive index of transparent and turbid samples (Tearney et al. 1995), (Stifter et al. 2005). A substrate surface is taken as a reference. A liquid or solid layer is deposited on the top. The uncovered substrate surface will have the light passing through the same physical thickness as the sample under study. The refractive index of the sample under investigation is found by dividing the optical thickness by the physical thickness.

All the above techniques are summarised in Table 2-6.

Table 2-6: Summary of OCT

Technique	Information provided	Comments
Conventional OCT (Huang et al. 1991)	Map of structural feature	2-D images of tissue structure
Doppler OCT (Chen et al. 1997), (Izatt et al. 1997)	Measures velocity of blood flow	It requires to detect the interference signal, which may require a high scan rate Limited by depth penetration through vessel walls
Polarisation sensitive OCT (Schoenenberger et al. 1998), (de Boer et al. 1997)	Measures birefringence of tissue	Additional image contrast for conventional OCT. It also identifies birefringence properties of tissue
Spectroscopic OCT (Morgner et al. 2000)	Measures spectral information from the interferogram	Improves resolution of OCT images and identifies spectral properties of tissue

Also a system has been built enabling to focus the two polarisation components on two planes. Their separation distance is known by moving a mirror in the sample arm (Zvyagin et al. 2003). Focusing in the layer under study, the optical thickness is found, and, dividing by the separation distance, the refractive index is then found. This requires, of course, that the distance between the focusing planes is small compared to the layers.

2.4.6 Multiparameters OCT Systems

This consists of producing an OCT system where birefringence, Doppler shift, spectroscopic and OCT images may be displayed together (Hyle Park et al. 2003). In the case of the determination of the thickness, it is important to know the refractive index of the media under investigation. It is assumed that the refractive index of the sample layers is about 1.4-1.5. Using histology, the refractive index may be deduced.

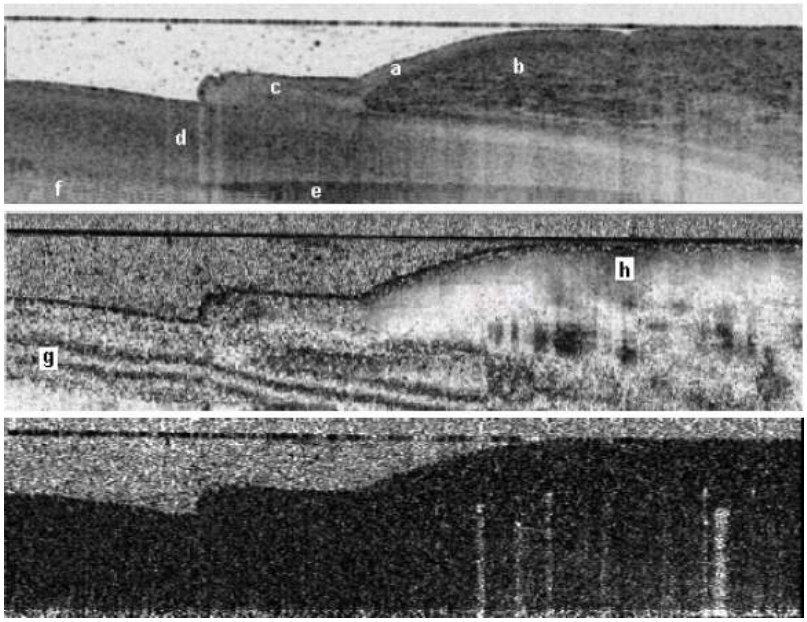

Figure 2-34: Intensity, birefringence, and flow (phase variance) images of the proximal nail fold of a human volunteer (upper, middle, and lower images respectively). (a) and (b): The epidermal and dermal areas of the nail fold, (c): cuticle, (d): nail plate, (e): nail bed, (f): and nail matrix are all identifiable in the intensity image. Images size: 5 mm · 1.2 mm (Hyle Park et al. 2003)

The birefringence image (figure 2-34, middle) shows the phase retardation of the epidermal-dermal boundary (g) as well as the lower half of the nail plate (h). Small transverse blood vessels in the nail fold are distinguishable in the flow image by their lighter colour. It has to be noted that, although polarisation maintaining optical fibre is required to ensure known input states of polarisation, ordinary single-mode optical fibre was used in this case employing polarisers and polarisation controllers to control the polarisation of the light. PS-OCT with single-mode fibre has also been demonstrated by Saxer et *al.*(Saxer et al. 2000).

The extension of OCT used the phase information of the acquired signal, providing useful information on birefringence, velocity and structural information of the sample.

As it was noted previously, the phase information may be directly obtained using a fully demodulated RSOD line set-up. At the same time, a compromise is made when the RSOD line is used. It will improve the acquisition speed, but it does not tend to improve the SNR.

2.4.7 Endoscopic OCT imaging

In 1996 Tearney *et al.* (Tearney et al. 1996a) designed a fibre-optic catheter endoscope, 1.1 mm in diameter, for *in-vivo* imaging of blood vessels. For in-vivo measurements, e.g. in vessels or to check gastrointestinal track, circular scans are necessary. Tearney employed a right-angle prism fixed to the fibre to send the light incident to the sample, the optical fibre is rotated to then map vessels.

In 1997 Boppart *et al.* (Boppart et al. 1997) discussed three possible designs for OCT surgical probes. A single fibre was used for the sample arm and in each instance the lateral scanning was performed with piezoelectric cantilevers.

In 1997 (Sergeev and Gelikonov, 1997) the first in-vivo OCT images of the human mucosa in the respiratory and gastrointestinal (GI) tract were performed using a single-fibre endoscope 1cm in diameter. Lateral scanning was performed using an electromechanical unit within the sample head to move the fibre known lateral distances. Methods for lateral scanning can be improved to decrease the scanning

speed, but the over all determination of faster scanning is the longitudinal acquisition rate and most endoscopic sample heads are used in conjunction with faster longitudinal scanning methods to improve their performance.

2.4.8 SNR and other improvements

Other improvements with OCT systems have suggested using directional couplers and circulators to improve the SNR. A number of trials using combinations of these has been carried out (Bouma and Tearney, 1999), (Rollins and Ung-Arunyawee, 1999) and in 1999 (Rollins and Izatt, 1999) a paper was published determining the optimal interferometric design to achieve the highest power-conserving set-up. This configuration consisted of an unbalanced coupler and a circulator, which improved the sensitivity by a 4.1-dB advantage over the standard Michelson.

Recently there has been an interest in OCT scanners, which require no moving parts. This is an attractive feature for faster scanning techniques and endoscopic applications. One such system was presented in 1999 (Zuluaga and Richards-Kortum, 1999) using an imaging spectrograph as an alternative to a detector within a Michelson Interferometer. The reference mirror and the sample arms are stationary and the interferogram (spectrum of interference output) is analysed instead. The Fourier Transform (FT) of the interferogram contains depth information. The spectrograph images a line along the sample surface onto the entrance slit of the imaging spectrograph. At the output plane of the spectrograph it is possible to obtain depth information (from the spectral content) along each point in that line, which can then be processed into a two-dimensional, depth-by-surface image captured using a CCD camera. The disadvantage of using this technique is that it is computationally intensive since the FT of each of the acquired spectra must be taken in order to retrieve all the depth-resolved reflectance.

Finally Full field imaging has recently been demonstrated using an imaging fibre bundle implemented in a mainly free-space Fizeau interferometer (Ford and Tatam, 2005). The reflection at the distal end of the bundle was taken as a reference. A CCD camera acquires the different depth scans in parallel to reconstruct a 3-D image of a sample. In a related publication, instead of using a CCD and illuminating all the fibres,

a probe focused the light on one fibre(Xie et al. 2005). By scanning across the fibre bundle, a 2-D image was produced. The advantage is that a better SNR should be obtained with such a configuration. Fibre bundle technologies offer potential advantages for endoscopic OCT applications.

2.4.9 Summary

Since the early days of OCT, this optical imaging technique has received strong interest from many researchers. Most of all configurations to date have been based on the Michelson interferometer configuration because it is easy to implement. Researchers used this arrangement to implement new ways of obtaining faster longitudinal and transverse scans in order to acquire at near real-time for patient comfort and to avoid artefacts due to the movement of the patient.

However, considering the endoscopic application, there are disadvantages in employing the Michelson interferometer, because of the signal fading experienced when each arm of the interferometer does not suffer from the same temperature changes and polarisation state fluctuation.

A way to reduce this problem, and to get a multi-purpose system, is to implement a Fizeau interferometer: the reference and the sample beams pass through the same fibre providing “downlead” insensitivity. The basic form of this configuration, however, is not efficient in terms of the amount of light arriving at the detector. Improvement in telecommunication and optical components should now provide methods to improve the signal-to-noise ratio of the system, and an investigation of these developments forms the basis of the work presented in this thesis.

Reference List

1. 99Main. http://www.99main.com/~charlief/theeyebg.gif. 2005.

2. Adler, D.C., Ko, T.H., Herz, P.R. and Fujimoto, J.G. (2004) Optical Coherence Tomography Contrast Enhancement Using Spectroscopic Analysis With Spectral Autocorrelation. *Optics Express* **12**.

3. Andretzky, P., Lindner, M.W., Hermann, J.M., Schultz, A. and Kiesewetter, F. (1999) Optical Coherence Tomography By Spectral Radar, Dynamic Range Estimation And In-Vivo Measurements Of Skin. *Proceedings Of SPIE: Optical And Imaging Techniques For Biomonitoring IV* **3567**.

4. Ballif, J., Gianotti, R. and Chavanne, R. (1997) Rapid And Scannable Scans At 21m/s In Optical Low-Coherence Reflectometry. *Optics Letters* **21**, 757-759.

5. Bamford, K.J. (2000) An Investigation Of Optical Radar And Low Coherence Interferometry For The Detection Of Precancerous Tissues. *Ph. D., Cranfield University, School Of Engineering.*

6. Barton, K.J., Izatt, J.A. and Welch, A.J. (1998) Investigating Laser-Blood Vessels Interaction With Color Doppler Optical Coherence Tomography. *SPIE* **3251**.

7. Boheim, G. (1986) Fibre Optic Thermometer Using Semiconductor Etalon Sensor . *Electronical Letters* **22**, 238-239.

8. Boppart, S.A. , Bouma, B.E. and Pitris, C. (1997) Forward-Imaging Instruments For Optical Coherence Tomography. *Optics Letters* **22**, 1618-1620.

9. Boppart, S.A. , Brezinski, M.E. and Pitris, C. (1998) Optical Coherence Tomogrraphy For Neurosurgical Imaging Of Human Intracortical Melanoma. *Neuro surgery* **43**, 834-841.

10. Bosselmann, T. and Ulrich, R. High-Accuracy position-Testing With Fibre-

Coupled White-Light Inrterferometry. Proc. 2nd Int.Conf. Optical Fibre Sensors. 361-364. 1984.

11. Bouma, B.E. and Tearney, G.J. (1999) Power Efficient Non-Reciprocal Interferometer And Linear Scanning Fiber Optic Catheter For Optical Coherence Tomography. *Optics Letters* **24**, 531-533.

12. Bouma, B.E., Tearney, G.J. and Boppart, S.A. (1995) High-Resolution Optical Coherence Tomography Using A Mode-Locked Ti: Al_2O_3 Laser Souce. *Optics Letters* **20**, 1486-1488.

13. Bouma, B.E., Nelson, L.E., Tearney, G.J., Jones, D.J., Brezinski, M.E. and Fujimoto, J.G. (1998) Optical Coherence Tomographic Imaging Of Tissue at 1.55 μm And 1.81μm Using Er- and Tm- Doped Fibre Sources. *Journal Of Biomedical Optics* **3**, 76-79.

14. Brezinski, M.E., Tearney, G.J. and Bauma, B.E. (1996) Imaging Of The Coronary Artery Microstructure (*In Vivo*) With Optical Coherence Tomography. *The American Journal Of Cardiology* **77**, 92-93.

15. Brezinski, M.E. and Fujimoto, J.G. (1999) Optical Coherence Tomography: High-Resolution Imaging In Non-transparent Tissue. *IEEE Journal Of Selected Topics In Quantum Electronics* **5**, 1185-1192.

16. Chen, Z., Zhao, Y., Srivinas, S.M., Nelson, J.S., Prakash, N. and Frostig, R.D. (1999) Optical Doppler Tomography. *IEEE Journal Of Selected Topics In Quantum Electronics* **5**, 1134-1142.

17. Chen, Z., Milner, T. and Dave, D. (1997) Optical Doppler Tomographic Imaging Of Fluid Flow Velocity In Highly Scattering Media. *Optics Letters* **22**, 64-66.

18. Choma, M.A., Sarunic, M.V., Yang, C. and Izatt, J.A. (2003) Sensitivity Advantage Of Swept Source And Fourier Domain Optical Coherence Tomography. *Optics Express* **11**, 2183-2189.

19. Clivaz, F. and Salathč, R.P. (1992) Optical Coherence Reflectometry With 1.9 μm Spatial Resolution . *Electronics Letters* **28**, 1553-1555.

20. Colston, B.W., Everett, M.J. and Dasilva, L.B. (1998) Imaging Of Hard- And Soft-Tissue Structure In the Oral Cavity By Optical Coherence Tomography. *Applied Optics* **37**, 3582-3585.

21. de Boer, J.F., Milner, T.E. and Gernet, B.W. (1997) Two-Dimensional Birefringence Imaging In Biological Tissue By Polarisation-Sensitive Optical Coherence Tomography. *Optics Letters* **22**, 934-936.

22. de Boer, J.F., Milner, T.E. and Nelson, J.S. (1999a) Determination Of The Depth-Resolved Stokes Parameters Of Light Backscattered From Turbid Media By Use Of Polarization-Sensitive Optical Coherence Tomography. *Optics Letters* **24**, 300-302. (Abstract)

23. de Boer, J.F., Srinivas, S.M., Park, B.H., Pham, T.H., Chen, Z., Milner, T.E. and Nelson, J.S. (1999b) Polarisation Effect In Optical Coherence Tomography Of Various Biological Tissues . *IEEE Journal Of Selected Topics In Quantum Electronics* **5**, 1200-1203.

24. Delachenal, N., Gianotti, R. and Walti, R. (1997) Constant High-Speed Optical Low-Coherence Reflectometry Over 0.12 m Scan Range. *Electronics Letters* **33**, 1159-1162.

25. Drexler, W., Morgner, U. and Kartner FX (1999) In-Vivo Ultra-High Resolution Optical Coherence Tomography. *Optics Letters* **24**, 1221-1223.

26. Drexler, W., Stamper, D., Jesser, C., Li, X., Pitris, C., Saunders, K., Fugimoto, J.G. and Brezinski, M.E. (2000) Correlation Of Polarization-Sensitive Optical Coherence Tomography With Early Osteoarthritis And Collagen Disorganization. *CLEO 2000*.

27. Duncan, M.D. and Bashkansky, M. (1998) Surbsurface Defect Detection In Materials Using Optical Coherence Tomography. *Optics Express* **2**, 540-545.

28. Dunkers, J.P., Phelan, F.R., Sanders, D.P., Everett, M.J., Green, W.H., Hunston, D.L. and Parnas, R.S. (2001) The Application Of Optical Coherence Tomography To Problems In polymer Matrix Composites. *Optics and Lasers in Engineering* **35**, 135-147.

29. Egan, P., Aguanno, M.V., Lakestani, F., Whelan, M.P. and Connelly, M.J. (1930) Optical Coherence Tomography Using A Programmable CMOS Camera. *ISSC, Belfast*h

30. Everett, M., Schoenenberger, K. and Colston, B. (1998) Birefringence Characterization of Biological Tissue By Use Of Optical Coherence Tomography. *Optics Letters* **23**, 228-230.

31. Fercher, A.F. inventor GmbH, C.Z.J., (Jun 5, 2001) Optical Path Length Modulator. US 6,243,191 B1.

32. Fercher, A., Mengedoht, K. and Werner, W. (1988) Eye-Length Measurement By Interferometry With Partially Coherent Light. *Optics Letters* **13**, 186-188.

33. Ford, H. D. and Tatam, R. P. Full-Field Optical Coherence Tomography. SPIE Optical Metrology Symposium (Micro- And Nano-Technology Conference), Proc SPIE **5858-19**. 2005.

34. Gelikonov, V.M., Sergeev, A.M., Gelikonov, G.V., Feldchtein, F.I., Gladkova, N.D., Iovannovich, J., Fragia, K. and Pirza, T. (1996) Compact Fast-Scanning OCT Device For In Vivo Biotissue Imaging. *Conference On Lasers And Electro Optics, OSA Technical Digest Series, Optical Society of America* **9**, 58-59.

35. Harde, H. and Burggraf, H. (1981) Rapid Scanning AutoCorrelator For Measurement Of Picosecond Laser Pulses. *Opt. Comm.* **38**, 211-215.

36. Healey, P. (1986) Instrumentation Principles For Optical Time Domain Reflectometry. *J. Phys. E: Sci. Instrum.* **19**, 334--341

37. Hee, M.R., Izatt, J.A. and Swanson, E.A. (1995a) Optical Coherence

Tomography Of The Human Retina. *Archives Of Ophthalmology* **113**, 325-332.

38. Hee, M., Izatt, J. and Swanson, E. (1995b) Optical Coherence Tomography For Ophthalmic Imaging: New Technique Delivers Micron-Scale Resolution. *IEEE In Medecine And Biology* **113**, 67-76.

39. Herrmann, J.M., Pitris, C., Bouma, B.E., Boppart, S.A., Fujimoto, J.G. and Brezinski, M.E. (1999) High Resolution Imaging Of Normal And Osteoarthritic Cartilage With Optical Coherence Tomography. *Journal Of Rheumatology* **26**, 627-635.

40. Hoerauf, H., Wirbelaurer, C. and Scholz, C. (2000) Slit-Lamp-Adapted Optical Coherence Tomography Of Anterior Segment. *Graefe Archive for Clinical and Experimental Ophthalmology* **238**, 8-18.

41. Huang, D., Swanson, E.A. and Lin, P.C. (1991) Optical Coherence Tomography. *Science* 1178-1181.

42. Huber, R.H., Wojtkowski, M., Fujimoto J. G., Jiang, J.Y. and Cable, A.E. (2005) Three-Dimensional And C-Mode OCT Imaging With A Compact, Frequency Swept Laser Source At 1300 nm. *Optics Express* **13**, 10523-10538.

43. Hyle Park, B., Pierce, M.C., Cense, B. and de Boer, J.F. (2003) Real-Time Multi-Functional Optical Coherence Tomography. *Optics Express* **11**, 782-793.

44. Izatt, J., Kulkarni, M. and Yazdanfar, S. (1997) In-Vivo Color Doppler Imaging Of Picoliter Blood Volumes Using Optical Coherence Tomography. *Optics Letters* **22**, 1439-1441.

45. Izatt, J.A., Kulkarni, D., Wang, H.-W., Kobayaski, D. and Sivak, M.V.J. (1996) Optical Coherence Tomography And Microscopy In Gastrointestinal Tissues. *IEEE Journal Of Selected Topics In Quantum Electronics* **2**, 1017-1028.

46. Jacques, S.L. and Prahl, S.A. (1998) Absorption Spectra For Biological Tissues. *http://omlc.ogi.edu/classroom/ece532/class3/muaspectra.html.*

47. Karl Storz - Endoskope. http://www.karlstorz.com/. 2005.

48. Kersey, A.D. , Marrone, M.J., Dandridge, A. and Tveten, A.B. (1988) Optimization And Stabilization Of Visibility In Fiber-Optic Sensors Using Input-Polarization Control. *Journal Of Lightwave Technology* **6**, 1599-1609.

49. Kobayashi, K., Izatt, J. and Kularni, M. (1998) High-Resolution Cross-Sectional Imaging Of The Gaestrointestinal Endoscopy: Preliminary Results. *Gastrointestinal Endoscopy* **47**, 27-37.

50. Krishnaswamy, A. and Baranoski, G.V.G. (2004) A study On The Skin Optics.

51. Kwong, K.F., Yankelevich, D., Chu, K.C., Heritage, J.P. and Dienes, A. (1993) 400-Hz Mechanical Scannind Delay Line. *Optics Letter* **18**, 558-560.

52. Lazar, R., Brunner, H. and Steiner, R. Optical Coherence Tomography (OCT) Of Human Skin With A Slow CCD-Camera. *SPIE* **2925**, 143-151.

53. Liu, H.H., Ceng, P.H. and Wang, J.P. (1993) Spatially Coherent White-Light Interferometer Based On A Point Fluorescent Source. *Optics Letters* **18**, 678-680.

54. Mac Neill, B.D., Hayase, M. and Jang, I.-K. (2002) The Comparison Between Optical Coherence Tomography And Intravascular Ultrasound. *Minerva Cardioangiologica.*

55. Madden, S., Zamora, G., Truitt, P., Fournier, P., Russel, S. and Otten, L.J. (2004) A Hyperspectral Image Retinal Imager For Non-Morphological Tissue Classification. *Imaging In The Eye II: Technologies And Clinical Application, Institute Of Physics.*

56. Masters, B.R. (1999) Early Development Of Optical Coherence Reflectometry

And Some Recent Applications. *Journal Of Biomedical Optics* **4**, 236-247.

57. MD Support: The Eyes Of The Macular Degeneration Community. Eye diseases & Conditions, http://www.mdsupport.org/diseases.html. 2005.

58. Merino, D., Dainty, C., Bradu, A. and Podoleanu, A.Gh. (2006) Adaptive Optics Enhanced Simultaneous *En-Face* Optical Coherence Tomography And Scanning Laser Ophthalmoscopy. *Optical Express* **14**, 3345-3353.

59. Morgner, U., Drexler, W. and Kartner, F.X. (2000) Spectroscopic Optical Coherence Tomography. *Optics Letters* **25**, 111-113.

60. Oh, J.-T. and Kim, S.-W. (2003) Polarization-Sensitive Optical Coherence Tomography For Photoelasticity Testing Of Glass/Epoxy Composites . *Optics Express* **11**, 1669-1676.

61. Oldenburg, A.L., Reynolds, J.J., Marks, D.L. and Boppart, S.A. (2003) Fast-Fourier-Domain Delay Line For *In Vivo* Optical Coherence Tomography With A Polygonal Scanner. *Applied Optics* **42**, 4606-4611.

62. Owen, C.G., Ellis, T.J., Rudnicka, A.R. and Woodward, E.G. (2004) Towards Quantitative Analysis Of Biochemical Signatures In The Retina Using Hyperspectral Imaging. *Imaging In The Eye II: Technologies And Clinical Applications, The Institute Of Physics*.

63. Pan, Y. and Huikai Xie, F.G.K. (2001) Endoscopic Optical Coherence Tomography Based On A Microelectromechanical Mirror. *Optics Letters* **26**, 1966-1968.

64. Patwari, P., Weissman, N.J., Boppart, S.A., Jesser, C., Stamper, D., Fujimoto, J.G. and Brezinski, M.E. (2000) Assessment Of Coronary Plaque With Optical Coherence Tomography And High-Frequency Ultrasound . *The American Journal of Cardiology* **85**, 641-644.

65. Piao, D. and Zhu, Q. (2004) Power-Efficient Grating-Based Scanning Optical

Delay Line: Time-Domain Configuration. *Electronics Letters* **40**, (Abstract)

66. Pircher, M., Goetzinger, E., Leitgeb, R. and Hitzenberger, C.K. (2004) Transversal Phase Resolved Polarization Sensitive Optical Coherence Tomography. *Institute Of Physics Publishing: Physics In Medecine And Biology* **49**, 1257-1263.

67. Quaker Chemical.

http://www.quakerchem.com/safety/white_papers/skin_layers.gif. 2005.

68. Rabiner, L.R., Schafer, R.W. and Rader, C.M. (1969) The Chirp Z-Transform . *IEEE Transactions On Audio And Electroacoustic* **AU-17**,

69. Risingsun Health Alternatives. www.bloodrootproducts.com. 99. 2005.

70. Rollins, A.M. and Izatt, J.A. (1999) Optimal Interferometer Designs For Optical Coherence Tomography. *Optics Letters* **24**, 1484-1486.

71. Rollins, A.M., Kulkarni, M.D., Yadzanfar, S., Ung-Arunyawee, R. and Izatt, J.A. (1998) *In-Vivo* Video Rate Optical Coherence Tomography. *Optics Express* **3**,

72. Rollins, A.M., Sivak, M.V., Radhakrishnan, S., Lass, J.H., Huang, D., Cooper, K.D. and Izatt, J.A. (2002) Emerging Clinical Applications Of Optical Coherence Tomography. *Optics & Photonics News, Optical Society of America*

73. Rollins, A.M. and Ung-Arunyawee, R. (1999) Real-Time *In-Vivo* Imaging Of Human Gastrointestinal Ultrastructure By Use Of Endoscopic Optical Coherence
Tomography With A Novel Efficient Interferometer Design . *Optics Letters* **24**, 1358-1360.

74. Rollins, A.M., Yazdanfar, S., Ung-Arunyawee, R. and Izatt, J.A. (1999) Real

Time Doppler Optical Coherence Tomography Using An Autocorrelation Technique. *SPIE Conference On Coherence Domain Optical Methods In Biomedical Science And Clinical Applications III, San Jose, California* **3598**,

75. Sala, K.L., Kennedy-Wallace, G.A. and Hall, G.E. (1980) CW Autocorrelation Measurement Of Picosecond Laser Pulses. *IEEE. Quant. Elect.* **QE-16**, 990-996.

76. Sato, M., Seino, K., Onodera, K. and Tanno, N. (2000) Phase-Drift Suppression Using Harmonics In Heterodyne Detection And Its Application To Optical Coherence Tomography. *Optics Communications* **184**, 95-104.

77. Savage, N. (2001) Hyperspectral Imaging. *OPN TRENDS: BIOPHOTONICS* **1**.

78. Saxer, C.E., de Boer, J.F., Hyle Park, B., Zhao, Y., Chen, Z. and Nelson, J.S. (2000) High-Speed Fiber–Based Polarization-Sensitive Optical Coherence Tomography Of In Vivo Vuman Skin. *Optics Letters* **25**.

79. Schmitt, J.M., Knüttel, A. and Bonner, R.F. (1997) Measurement Of Optical Properties Of Biological Tissues By Low-Coherence reflectometry. *Applied Optics* **22**, 757-759.

80. Schmitt Joseph M. (1999) Optical Coherence Tomography: A Review . *IEEE Journal Of Selected Topics In Quantum Electronics* **5**, 1205-1215.

81. Schoenenberger, K., Colston, B.W. and Maitland, D.J. (1998) Mapping Of Birefringence And Thermal Damage In Tissue By Use Of Polarisation-Sensitive. *Applied Optics* **37**, 6027-6037.

82. Sergeev, A.M. and Gelikonov, G.V. (1997) In-Vivo Endoscopic OCT Imaging Of Precancer And Cancer States Of Human Mucosa. *Optics Express* **1**, 432-440.

83. Sigma Koki Co.

http://www.sigma-koki.com/english/A/Interferometers/Fezeau.html. 2004-2005. 2005.

84. Silva, K.K.M.B.D., Zvyagin, A.V. and Sampson, D.D. (1999) Extended Range, Rapid Scanning Optical Delay Line For Biomedical Interferometric Imaging . *Electronics Letters* **35**, 1404-1406.

85. Skin Surgery Center.

http://www.skinsurgerycenter.com/dictionary/melanocytes.html. 98-2006. 2004.

86. Stifter, D., Sanchis Dufau, A.D., Breuer, E., Wiesauer, K. , Burgholzer, P., Höglinger, O., Götzinger, E., Pircher, M. and Hitzenberger, C.K. (2005) Polarisation-Sensitive Optical Coherence Tomography For Material Characterisation And Testing. *The British Institute Of Non-Destructive Testing* **47**, 209-212.

87. Su, C.B. (1997) Achieving Variation Of The Optical Coherence Path Length By A Few Millimeters At Millisecond Rates For Imaging Of Turbid Media And Optical Interferometry: A New Technique. *Opt. Lett.* **22**, 665-667.

88. Swanson, E.A., Huang, D. and Hee, M.R. (1992) High-Speed Optical Coherence Domain Reflectometry. *Optics Letters* **17**, 151-153.

89. Swanson, E.A., Izatt, J.A. and Hee, M.R. (1993) In-Vivo Retinal Imaging Using Optical Coherence Tomography. *Optics Letters* **18**, 1864-1866.

90. Szydlo, J., Bleuer, H., Walti, R. and Salathč, R.P. (1998) High Speed Measurement In Optical Low-Coherence Reflectometry. *Measurement In Science And Technology* **9**, 1159-1162.

91. Takada, K., Yokohama, I., Chida, K. and Noda, J. (1987) New Measurement System For Fault Location In Optical Waveguide Devices Based On An Interferometric Technique. *Applied Optics* **26**, 1603-1606.

92. Tearney, G.J., Boppart, S.A. and Bouma, B.E. (1996a) Scanning Single-Mode Fiber Optic Catheter-Endoscope For Optical Coherence Tomography. *Optics Letters* **21**, 543-545.

93. Tearney, G.J., Bouma, B.E. and Boppart, B. (1996b) Rapid Acquisition Of *In-Vivo* Biological Images By Use Of Optical Coherence Tomography. *Optics Letters* **21**, 1109-1111.

94. Tearney, G.J., Bouma, B.E. and Fujimoto, J.G. (1997) High-Speed Phase- And Group-Delay Scanning With A Grating-Based Phase Control Delay Line. *Optics Letters* **22**, 1811-1813.

95. Tearney, G.J., Brezinski, M.E., Southern, J.F., Bouma, B.E., Hee, M.R. and Fujimoto, J.G. (1995) Determination Of The Refractive Index Of Highly Scattering Human Tissue By Optical Coherence Tomography. *Opt. Lett.* **20**, 2258-2260.

96. Tearney, G., Bouma, B.E. and Fujimoto, J.G. inventors Massachusetts Institute Of Technology, (Jun 13, 2001a) Interferometric Imaging With A Grating Based Phase Control Optical Delay line. United States. US 6,421,164 B2.

97. Tearney, G., Bouma, B.E. and Fujimoto, J.G. inventors Massachusetts Institute Of Technology, (Aug 28, 2001b) Grating Based Phase Control Optical Delay Line. US 6,421,164 B2.

98. Unterhuber, A., Provažay, B., Bizheva, K., Hermann, B., Sattmann, H., Stingl, A., Le, T., Seefeld, M., Menzel, R., Preusser, M., Budka, H., Schubert, Ch., Reitsamer, H., Ahnelt, P.K., Morgan, J.E., Cowey, A. and Drexler, W. (2004) Advances In Broad Bandwidth Light Sources For Ultrahigh Optical Coherence Tomography. *Institute Of Physics Publishing: Physics In Medecine And Biology* **49**, 1235-1246.

99. Wang, R.K. (2004) High-Resolution Visualiszation Of Fluid Dynamics With Doppler Optical Cohrence Tomography. *Measurement Science And Technology* **15**, 725-733.

100. Wang, R.K., Xu, X., He, Y. and Elder, J.B. (2003) Investigation Of Optical Clearing Of Gastric Tissue Immersed With Hyperosmoic Agents. *IEEE Journal Of Selected Topics In Quantum Electronics* **9**.

101. Weiner, A.M. (2000) Femtosecond Pulse Shaping Using Spatial Light Modulators. *Review Of Scientific Instruments* **71**, 1929-1960.

102. Welzel, J., Lankenau, E. and Birngruber, R. (1998) Optical Coherence Tomography Of The Skin. *Skin Bioengineering Techniques And Application* **26**, 27-37.

103. Welzel, J. (2001) Optical Coherence Tomography In Dermatology: A Review. *Skin Research And Technology* **7**, 1-9.

104. White, B.J. , Davis, J.P., Bobb, L.C., Krunboltz, H.D. and Larson, D.C. (1987) Optical-Fiber Thermal Modulator. *Journal Of Lightwave Technology* **LT-5**, 1169-1175.

105. Wiesauer, K., Pircherb, M., Götzingerb, E., Bauer, S., Rainer, E., Ahrens, G., Grützner, G. , Hitzenberger, C.K. and Stifter, D. (2005) En-Face Scanning Optical Coherence Tomography With Ultra-High Resolution For Material Investigation. *Optics Express* **13**.

106. Windecker, R., Fleischer, M., Franze, B. and Tiziani, H.J. (1997) Two fast Methods For Fast Coherence Tomography And Topometry. *J. Mod. Optics* **44**, 967-977.

107. Xie, H., Pan, Y. and Fedder, G.K. (2003) Endoscopic Optical Coherence Tomographic Imaging With A CMOS-MEMS Micromirror. *Sensors and Actuators A* **103**, 237-241.

108. Xie, T., Mukai, D., Guo, S., Brenner, M. and Chen, Z. (2005) Fibre-Optic-Bundle-Based Optical Coherence Tomography. *Optics Letters* **30**, 1803-1805.

109. Xie, T., Xie, H., Fedder, G.K. and Pan, Y. (2003a) Endoscopic Optical Coherence

Tomography With New MEMS Mirror. *Electronics Letters* **39**.

110. Xie, T., Xie, H., Fedder, G.K. and Pan, Y. (2003b) Endoscopic Optical Coherence Tomography With A Modified Microelectromecanical Systems Mirror For Detection Of Bladder Cancers . *Applied Optics* **42**, 6422-6426.

111. Xinan, G., Lambsdorff, M., Kuhl, J. and Biachang, W. (1988) Fast Scanning Autocorrelator With 1ns Scanning Range For Characteriztion Mode-Locked Ion Lasers. *Rev. Sc. Inst.* **59**.

112. Yang, Y., Dubois, A., Qin, X., Li, J.L., El Haj, A. and Wang, R.K. (2006) Investigation Of Optical Coherence Tomography As An Imaging Modality In Tissue Engineering. *Physics In Medecine And Biology* **51**, 1649-1659.

113. Yang, Y., Whiteman, S., van Pittius, D.G., He, Y., Wang, R.K. and Spiteri, M.A. (2004) Use Of Optical CoherenceTomography In Delineating Airways Microstructure: Comparison Of OCT Images To Histopathological Sections. *Institute Of Physics Publishing, Phys. Med. Biol.* **49**, 1247-1255.

114. Yasa, Z.A. and Amer, N.M. (1981) A Rapid-Scanning Autocorrelation Scheme For Continuous Monitoring Of Picosecond Pulses. *Opt. Comm.* **36**, 406-408.

115. Yasuno, Y., Makita, S., Sutoh, Y., Itoh, M. and Yatagai, T. (2002) Birefringence Imaging Of Human Skin By Polarization-Sensitive Spectral Interferometric Optical Coherence Tomography. *Optics Letters* **27**, 1803-1805.

116. Yazdanfar, S., Rollins, A.M. and Izatt, J.A. (2003) In Vivo Imaging of Human Retinal Flow Dynamics By Color Doppler Optical Coherence Tomography. *Archives Of Ophthalmology* **121**, 235--239

117. Yeov, J.T.W., Yang, V.X.D., Chahwan, A., Gordon, M.L. , Qi, B., Vitkin, I.A., Wilson, B.C. and Goldenberg, A.A. (2005) Micromachined 2-D Scanner For 3-D Optical Coherence Tomography . *Sensors And Actuators* **117**,

331-340.

118. Yu-Lung, L. , Chih-Chung, Y. and Shean-Jen, C. (2006) Fiber Type Of Optical Coherence Tomography With An Auto-Focus Device. *Optics Communications* **259**, 70-77.

119. Zara, J.M., Izatt, J.A., Divakara Rao, K., Yazdanfar, S. and Smith, S.W. (2002) Scanning Mirror For Optical Coherence Tomography Using An Electrostatic Mems Actuator. *IEEE*.

120. Zawadzki, R.J., Jones, S.M., Olivier, S.S., Zhao, M., Bower, B.A., Izatt, J.A., Choi, S., Laut, S. and Werner, J.S. (2005) Adaptive-Optics Optical Coherence Tomography For High-Resolution And High-Speed 3D Retinal In Vivo Imaging. *Optics Express* **13**, 8532-46.

121. Zhang, J. and Chen, Z. (2005) In Vivo Blood Blow Imaging By A Swept Laser Source Based Fourier Domain Optical Doppler Tomography. *Optics Express* **Vol. 13**, 7449-7457.

122. Zhang, Y., Rha, J., Jonnal, R.S. and Miller, D.T. (2005) Adaptive Optics Parallel Spectral Domain Optical Coherence Tomography for Imaging The Living Retina. *Optics Express* **13**, 4792-4811.

123. Zuluaga, A.F. and Richards-Kortum, R. (1999) Spatially Resolved Spectral Interferometry For Determination Of Sub-Surface Structure. *Optics Letters* **24**, 512-519.

124. Zvyagin, A.V., Silva, K.K.M.B.D., Alexandrov, S.A., Hillman, T.R. and Armstrong, J.J. (2003) Refractive Index Tomography Of Turbid Media By Bifocal Optical Coherence Refractometry. *Optics Express* **11**, 3503-3517.

3 Fibre-based Fizeau Configuration OCT system

3.1 Introduction

OCT has been widely used with a Michelson interferometer. The study of the localisation of the microstructures in samples is achieved by the application of the principle of low-coherence interferometry (LCI). Interference signals are obtained when the optical path difference between the sample and reference arms is within the coherence length of the source.

This chapter provides an understanding of how LCI is employed in OCT technology. In chapter 2, an alternative configuration has been introduced that could be of interest, being the subject of this thesis: the Fizeau interferometer. It employs two interferometers in tandem. This system enables downlead insensitivity. By analogy to the Michelson interferometer a similar study is carried out on the Fizeau interferometer to establish the interference signal observed. This also gives information on the experimental set-up.

3.2 Low-coherence interferometry and white light interferometry

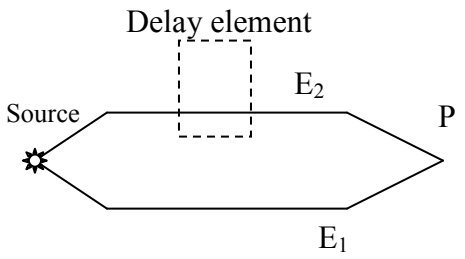

Figure 3-1: Interferometer principle

Considering two electric fields E_1 and E_2 from the same point source, having travelled different optical path lengths will recombine at the point P. There is a delay τ between the two beams, $E_2 = E_1(t+\tau)$ illustrated in figure 3-1.

The total electric field at P is equal to:

$$E_t = E_1 + E_2 \tag{3-1}$$

And the intensity of the signal P is obtained by:

$$\begin{aligned}\left\langle E_t E_t^* \right\rangle &= \left\langle (E_1 + E_2)(E_1 + E_2)^* \right\rangle \\ &= \left\langle E_1 E_1^* \right\rangle + \left\langle E_2 E_2^* \right\rangle + \left\langle E_1 E_2^* \right\rangle + \left\langle E_1^* E_2 \right\rangle\end{aligned} \tag{3-2}$$

Where $\left\langle E_1 E_1^* \right\rangle$ and $\left\langle E_2 E_2^* \right\rangle$ are the intensities I_1 and I_2 of the electric fields E_1 and E_2 contributing to the dc intensity; <> represents time-averaging.

The mutual coherence function (Brass et al. 1995) is given by:

$$\Gamma_{12}(\tau) = \left\langle E_1(t+\tau) E_2^*(\tau) \right\rangle \tag{3-3}$$

$$\text{and } \Gamma_{12}(\tau) + \Gamma_{12}^* = 2\,\mathrm{Re}\{\Gamma_{12}(\tau)\}, \tag{3-4}$$

and the normalisation of the mutual coherence function by gives:

$$\gamma_{12}(\tau) = \frac{\Gamma_{12}(\tau)}{\sqrt{\Gamma_{11}(\tau)\Gamma_{22}(\tau)}} = \frac{\Gamma_{12}(\tau)}{\sqrt{|E_1(t)|^2 |E_2(t)|^2}} = \frac{\Gamma_{12}(\tau)}{\sqrt{I_1 I_2}} \tag{3-5}$$

Remembering that it is a complex function in terms of amplitude and phase it can be written:

$$\begin{aligned}\gamma_{12}(\tau) = |\gamma_{12}(\tau)| e^{i\Phi_{12}} &= |\gamma_{12}(\tau)| e^{i(\alpha_{12}(\tau) - \Delta\Phi(\tau))} \\ &= e^{-\left(\frac{\pi \Delta\upsilon \tau}{2\sqrt{\ln 2}}\right)^2} e^{-j2\pi\upsilon_0\tau}\end{aligned} \tag{3-6}$$

where $\alpha_{12}(\tau)$ is the phase associated with the source.

Taking the real part:

$$\begin{aligned}\mathrm{Re}\{\gamma_{12}(\tau)\} &= 2|\gamma_{12}(\tau)| \cos(\Phi_{12}(\tau)) \\ &= 2 e^{-\left(\frac{\pi \Delta\upsilon \tau}{2\sqrt{\ln 2}}\right)^2} \cos(\Phi_{12}(\tau))\end{aligned}, \tag{3-7}$$

(assuming that the source has a Gaussian spectral distribution).

Considering Φ_{12}, being the optical phase difference between the two beams, being simply equal to the expression given in equation 3-8.

$$\Phi_{12} = kX\,, \tag{3-8}$$

Then applying this:

$$\frac{\left\langle E_{11}E_{12}^{*}\right\rangle + \left\langle E_{12}E_{11}^{*}\right\rangle}{\sqrt{I_1 I_2}} = 2\,\mathrm{Re}\{\gamma(X_1)\} = 2|\gamma(X)|\cos(kX) \tag{3-9}$$

$$= 2\,e^{-\left(\frac{\pi\Delta\upsilon X}{2v\sqrt{\ln 2}}\right)^2}\cos(kX)$$

Then the detected intensity I_d expression is:

$$I_d = I_1 + I_2 + 2\sqrt{I_1 I_2}\;\; e^{-\left(\frac{\pi\Delta\upsilon X}{2v\sqrt{\ln 2}}\right)^2}\cos(kX) \tag{3-10}$$

The Michelson interferometer is a useful model to explain how the technique of low-coherence interferometry is used in order to extract the depth of the tissue sample. However, the Michelson interferometer suffers from a number of points (polarisation fading due to temperature difference in both arms and stretching of the optical fibre in one arm). The Fizeau interferometer is therefore considered as an alternative configuration to overcome these disadvantages (the reference and sample light pass through the same optical fibre and both suffer from the same fluctuations).

3.3 Fizeau Interferometer

3.3.1 Principle

The principle of the Fizeau configuration is given in figure 3-2.

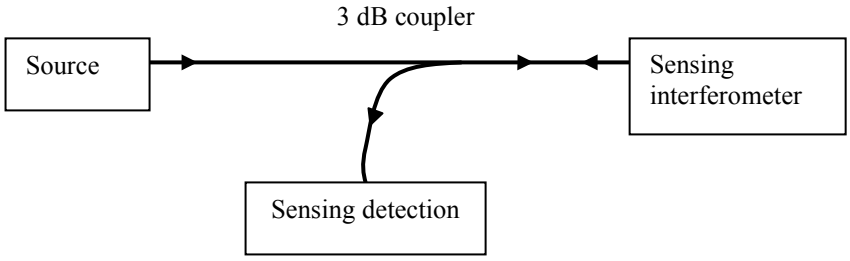

Figure 3-2: Fizeau configuration principle

The light from the source passes through the 3 dB-coupler and is sent to the sensing element; reflections occur and the backscattered light again through the 3-dB coupler and goes to the sensing detection. In this configuration, the reflection at the end of the fibre is typically taken as reference (Murphy et al. 1995).

Similar configurations have been previously applied in fibre sensing for strain measurement. The sensing interferometer was a Fabry-Perot interferometer, which was used in transmission or reflection modes (Zuliani et al. 1991), (Rao et al. 1993). Application of strain changes the optical phase in the sensing FP interferometer, and is related to the displacement of fringes.

In OCT, the system employed uses the back-scattered light from the sample. The sensing element is formed between the end of the fibre and the different boundaries in the sample. For simplicity and just to develop the general expression of the interference pattern of the Fizeau configuration, instead of considering boundaries in a tissue, a simple mirror is taken into account. The sensing interferometer is shown in figure 3-3.

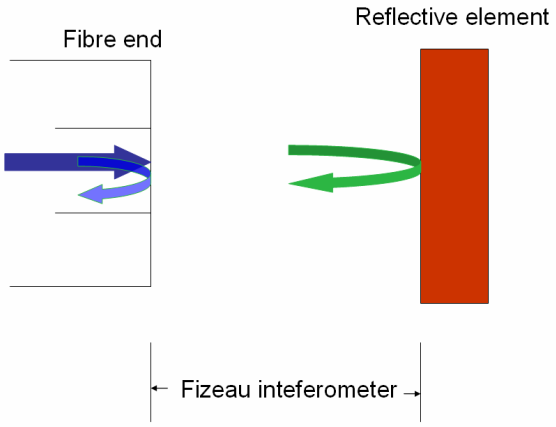

Figure 3-3: Sensing Fizeau interferometer

For initial discussions of the system, a Michelson processing interferometer will be considered. Later a discussion will be provided concerning the optimal processing interferometer to use.

3.3.2 Theory of the Fizeau Interferometer

In order to explain the theory of the Fizeau configuration, the most basic form of the system will be considered, as given in figure 3-4:

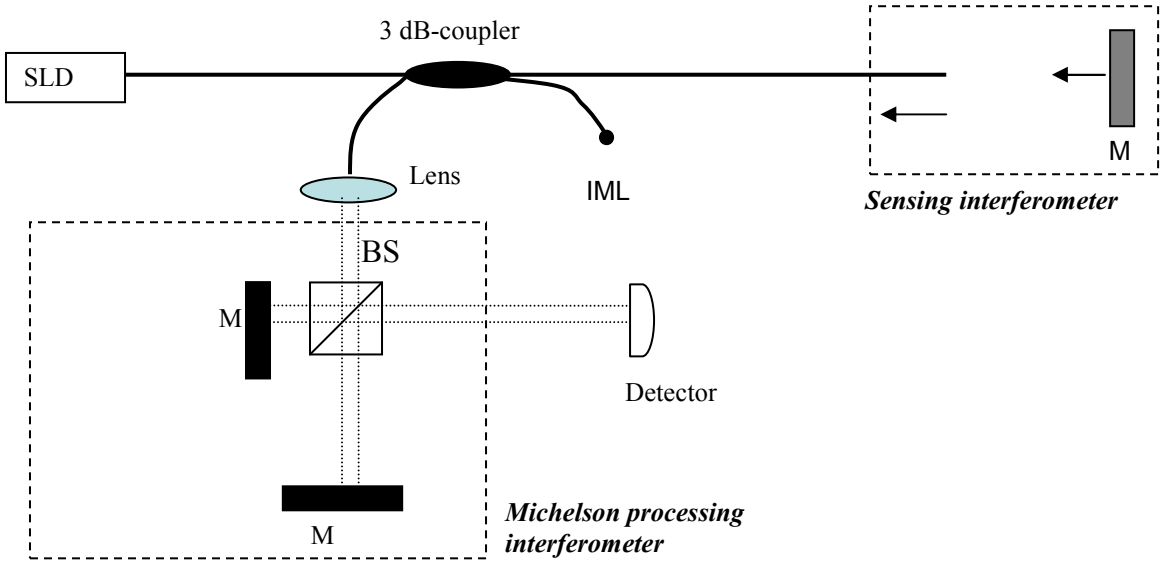

Figure 3-4: Standard Fizeau configuration; IML: index matching gel, M: Mirror, BS: beam splitter

The light passes through a 3 dB-coupler. 50 % of the light from the source goes to the sensing interferometer where two reflections occur: one at the end of the fibre and the other at the boundary (mirror). The backscattered light, from the end of the fibre and from the mirror, pass back through the 3 dB-coupler and a maximum of 25 % of the light from the source is sent to the processing Michelson interferometer, where each component suffers from two reflections on the mirrors after having been split by the cubic beam splitter. Four electric fields are detected by the detector, and a maximum of 12.5 % of the light is detected. The other 12.5 % of light, anti-phase signal, passes back through the fibre. This makes a poor use of the available light. In chapter 4, the improvement of the available light use will be discussed, improving the SNR of the configuration.

To find the transfer function of this tandem interferometer arrangement, the electric fields at the output of the processing Michelson interferometer are expressed as given in equation 3-11.

$$E = E_{11} + E_{12} + E_{21} + E_{22} \quad \textbf{(3-11)}$$

where E_{ij} is the component of the electric field at the output arising from propagation via the j[th] arm of the sensing arm interferometer and the i[th] arm of the Michelson interferometer.

It can be written as:

$$E_{11} = A_{11} e^{i\Phi} \quad \textbf{(3-12)}$$

$$E_{12} = A_{12} e^{i(\Phi + kX_1)} \quad \textbf{(3-13)}$$

$$E_{21} = A_{21} e^{i(\Phi + kX_2)} \quad \textbf{(3-14)}$$

$$E_{22} = A_{22} e^{i(\Phi + k(X_1 + X_2))}, \quad \textbf{(3-15)}$$

where A_{ij} is wave amplitude of each electric field E_{ij}, k and Φ are the wavenumber and the optical phase of E_{11} respectively; X_1 and X_2 are the Optical Path Difference (OPD) of the sensing interferometer and of the processing Michelson interferometer respectively. The optical output intensity I is defined taking the time average of eq. (3-11) given by:

$$\begin{aligned} I &= \langle E E^* \rangle \quad \textbf{(3-16)} \\ &= \left\langle \left(E_{11} + E_{12} + E_{21} + E_{22}\right)\left(E_{11}^* + E_{12}^* + E_{21}^* + E_{22}^*\right) \right\rangle \\ &= \left\langle E_{11}E_{11}^* \right\rangle + \left\langle E_{12}E_{12}^* \right\rangle + \left\langle E_{21}E_{21}^* \right\rangle + \left\langle E_{22}E_{22}^* \right\rangle \\ &+ \left\langle E_{11}E_{12}^* \right\rangle + \left\langle E_{12}E_{11}^* \right\rangle + \left\langle E_{11}E_{21}^* \right\rangle + \left\langle E_{21}E_{11}^* \right\rangle \\ &+ \left\langle E_{11}E_{22}^* \right\rangle + \left\langle E_{22}E_{11}^* \right\rangle + \left\langle E_{12}E_{21}^* \right\rangle + \left\langle E_{21}E_{12}^* \right\rangle \\ &+ \left\langle E_{21}E_{22}^* \right\rangle + \left\langle E_{22}E_{21}^* \right\rangle + \left\langle E_{12}E_{22}^* \right\rangle + \left\langle E_{22}E_{12}^* \right\rangle \end{aligned}$$

By analogy as for the Michelson configuration, equations 3-17 to 3-22 are obtained.

$$\frac{\langle E_{11}E_{12}^{*}\rangle + \langle E_{12}E_{11}^{*}\rangle}{\sqrt{I_1 I_2}} = 2|\gamma(X_1)|\cos(kX_1) \quad \textbf{(3-17)}$$

$$\frac{\langle E_{11}E_{21}^{*}\rangle + \langle E_{21}E_{11}^{*}\rangle}{\sqrt{I_1 I_3}} = 2|\gamma(X_2)|\cos(kX_2) \quad \textbf{(3-18)}$$

$$\frac{\langle E_{11}E_{22}^{*}\rangle + \langle E_{22}E_{11}^{*}\rangle}{\sqrt{I_4 I_1}} = 2|\gamma(X_1 - X_2)|\cos(k(X_1 - X_2)) \quad \textbf{(3-19)}$$

$$\frac{\langle E_{12}E_{21}^{*}\rangle + \langle E_{21}E_{12}^{*}\rangle}{\sqrt{I_2 I_3}} = 2|\gamma(X_1 + X_2)|\cos(k(X_1 + X_2)) \quad \textbf{(3-20)}$$

$$\frac{\langle E_{12}E_{22}^{*}\rangle + \langle E_{22}E_{12}^{*}\rangle}{\sqrt{I_2 I_4}} = 2|\gamma(X_2)|\cos(kX_2) \quad \textbf{(3-21)}$$

$$\frac{\langle E_{21}E_{22}^{*}\rangle + \langle E_{22}E_{21}^{*}\rangle}{\sqrt{I_3 I_4}} = 2|\gamma(X_1)|\cos(kX_1) \quad \textbf{(3-22)}$$

and so replacing in equation 3-16:

$$\begin{aligned} I = I_0 &+ 2\left(\sqrt{I_1 I_3} + \sqrt{I_2 I_4}\right)|\gamma(X_2)|\cos(kX_2) + 2\left(\sqrt{I_1 I_2} + \sqrt{I_3 I_4}\right)|\gamma(X_1)|\cos(kX_1) \\ &+ 2\sqrt{I_2 I_3}\,|\gamma(X_1 + X_2)|\cos(k(X_1 + X_2)) + 2\sqrt{I_1 I_4}\,|\gamma(X_1 - X_2)|\cos(k(X_1 - X_2)) \end{aligned} \quad \textbf{(3-23)}$$

$$I = I_0\left[\begin{aligned} &1 + 2\frac{\sqrt{I_1 I_3} + \sqrt{I_2 I_4}}{I_0}|\gamma(X_2)|\cos(kX_2) + 2\frac{\sqrt{I_1 I_2} + \sqrt{I_3 I_4}}{I_0}|\gamma(X_1)|\cos(kX_1) \\ &+ 2\frac{\sqrt{I_2 I_3}}{I_0}|\gamma(X_1 + X_2)|\cos(k(X_1 + X_2)) + 2\frac{\sqrt{I_1 I_4}}{I_0}|\gamma(X_1 - X_2)|\cos(k(X_1 - X_2)) \end{aligned}\right] \quad \textbf{(3-24)}$$

3.3.3 Interference pattern signal

When one of the mirrors in the processing Michelson interferometer is moved, the detected ac signal is shown on figure 3-5.

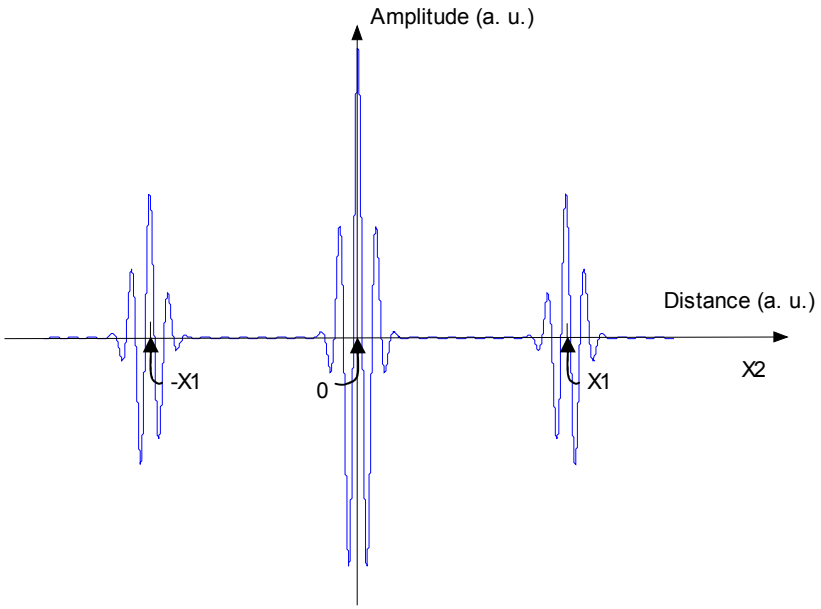

Figure 3-5: Interference pattern for different values of X_2

The case $X_1 = 0$ does not need to be considered in practice because the optical path difference in the sensing interferometer is much larger than the coherence length of the source and therefore no interference is produced.

The central peak, for $X_2 = 0$, corresponds to the condition where the optical path difference in the processing interferometer is zero, i.e. the two paths in this interferometer are matched in length. The others peaks, at $X_2 = -X_1$ and $X_2 = X_1$, are due to the optical path in the processing interferometer matching the sensing interferometer. In the Fizeau interferometer, one of these two cases is considered, allowing depth information to be obtained from the sample when the stage is moved. Murphy *et al.* (Murphy et al. 1995) noted that, as expected, in a system with two-Fabry-Perot interferometers there was no signal if the cavity length in the processing Fabry-Perot interferometer was not equal to the sensing cavity.

Therefore a processing interferometer is necessary to detect interference signals from refractive index change boundaries in the sample. By moving the mirror, or simply

by changing the optical path in the processing interferometer, the true optical path length for layers from the sample can be detected.

3.3.4 Sensing interferometer

For OCT applications, a probe, as described in chapter 2, is employed in the sensing interferometer in order to collimate the light going out of the fibre and to focus the light in the sample. The set-up is shown in figure 3-6.

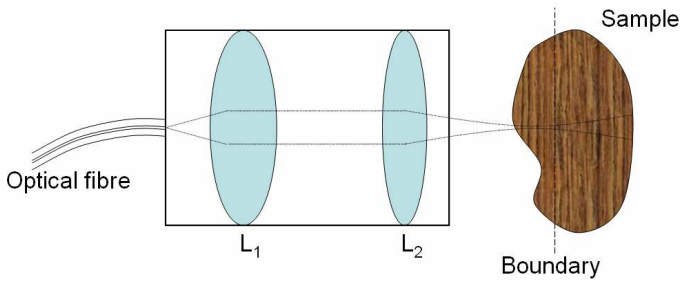

Figure 3-6: Fizeau head sensing interferometer; L_1, L_2: lenses

As explained in section 2-3-3, different probes can be considered for the OCT application, however in order to prove the feasibility of the Fizeau arrangement for OCT, the probe presented in the figure 3-6 is considered.

As explained in chapter 2, OCT is similar to the ultrasound (US) technique, but instead of using sound, light is used. US technique requires straightforward electronic detection of the time delay for reflected sound from boundaries. In OCT a low-coherence interferometry technique is used in order to detect the different boundary. The speed of the light is much faster than US and detectors cannot directly detect small time delays involved.

3.3.5 Processing interferometers

The standard Fizeau configuration is presented employing a processing Michelson interferometer. Other processing interferometers may be employed e.g. a Fabry-Perot or Mach-Zehnder processing interferometer as shown in the figure 3-7.

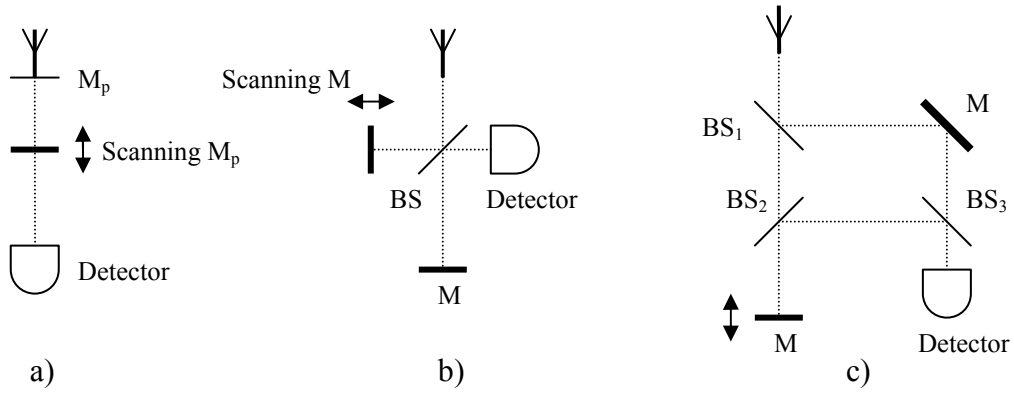

Figure 3-7: a) Fabry-Perot, b) Michelson and c) Mach-Zehnder processing interferometers; M_p: partial-reflective mirror; BS, BS_1, BS_2 and BS_3: Beam splitter; M: mirror

The visibility of the fringes using two Fabry-Perot cavities (one in the sensing interferometer and the other in the processing interferometer) in tandem has been investigated for strain measurement. A better efficiency was obtained with the FP processing interferometer rather than the Michelson processing interferometer (Rao et al. 1993).

The next chapter will provide a discussion of the fringe visibility in terms of Signal-Noise-Ratio (SNR) for OCT applications. This will also consider the different processing interferometers from which a better efficiency of the system can be obtained.

Reference List

1. Brass, M., Van Stryland, E.W., Williams, D.R. and Wolfe, W.L. (1995) Handbook Of Optics: Fundamentals, techniques and design. Second Edition. pp. 4.4-4.9.

2. Murphy, K.A., Bhatia, V. and Claus, R.O. (1995) Multiplexed Extrinsic Fabry-Perot Interferometers And Applications. *SPIE* **2507**.

3. Rao, Y., Webb, D. and Jackson, D. (1993) Design Study Of Fibre-Optic Based Fabry-Perot Type Interferometric Sensors Using Low-Coherence Signal Recovery. *SPIE: Fiber Optic And Laser Sensors XI* **2070**.

4. Zuliani, G., Hogg, D., Liu, K. and Measures, R.M. (1991) Demodulation Of A Fibre Fabry-Perot Strain Sensor Using White Light Interferometry. *SPIE: Fibre Optic Smart Structures And Skins IV* **1588**.

4 Signal-to-Noise Ratio for OCT configurations

4.1 Introduction

The most widely used configuration for fibre-optic based OCT is a Michelson interferometer formed from a directional coupler (figure 4-1), in which either an external mirror or the polished (and sometimes coated) end of one coupler output fibre generates the reference reflection (Izatt et al. 1996), (Schmitt Joseph M., 1999).

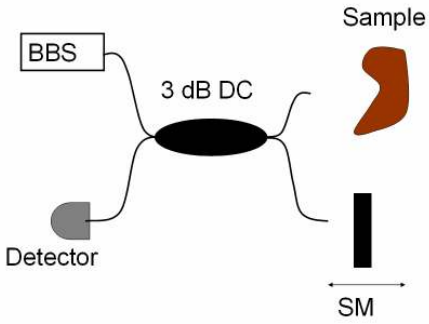

Figure 4-1: Michelson interferometer; SM: scanning mirror, DC: directional coupler

This is mixed, using appropriate lenses at the fibre output, with light backscattered from a sample positioned close to the other coupler output arm. The path length difference between the interferometer arms is scanned linearly with time.

When a source of low temporal coherence is used to illuminate the system, interference fringes are observed only when the path length difference at any point in time is less than the coherence length of the source. Thus a plot of the variation in fringe magnitude seen during a scan represents the variation of the backscattered signal from different depths within the sample. The spatial resolution perpendicular to the sample surface is of the order of the coherence length. A single scan produces a one-dimensional map of refractive-index variation as a function of sample depth. By repeating the depth scan over a grid of positions on the sample surface, a two- or three-

dimensional map of subsurface structure is obtained (Podoleanu et al. 2000). Various types of rapid scanning techniques have been investigated to reduce the time taken for acquisition of a three-dimensional image (Ballif et al. 1997), (Tearney et al. 1997).

The Michelson arrangement for OCT is widely used. Other configurations based on Mach-Zehnder interferometers have been suggested, all resulting in very similar values of SNR to the Michelson configuration, when used with balanced detection (Rollins and Izatt, 1999). However, both the Michelson and Mach-Zehnder configurations have disadvantages. The signal and reference beams travel in different arms of the directional coupler. They therefore experience differential polarisation state changes as a result of physical perturbation of the fibre introducing birefringence, and differential phase changes caused by variations in ambient temperature around the fibre arms. Periodic fading or loss of the interference signal is experienced if the states of polarisation are mismatched in the region where interference occurs (Kersey and Dandridge, 1987). Under laboratory conditions, such changes are typically slow and can be reduced by the inclusion of polarisation-state controllers in the system (Hui et al. 2003), although regular adjustment of the relative polarisation states is likely to be necessary.

When an OCT system is required to make clinical measurements including internal investigations, control over ambient conditions is much more difficult and polarisation mismatches can become more troublesome. Several approaches to reducing the problem are possible: it is possible under favourable circumstances simply to make measurements only when the polarisation states are well matched. However, this can lead to measurement artefacts being missed if ambient conditions change significantly during the course of a measurement. Another alternative is to construct the interferometer using polarisation-preserving fibres and fibre components (Hui et al. 2003). This is a satisfactory solution when the sample is non-birefringent. For linearly polarised light, coupled into an eigenmode of the interferometer fibre, the state of polarisation (SOP) is preserved throughout. However, if the sample itself causes depolarisation, then the SOP of the backscattered light will no longer be preserved within the fibres and, once again, signal fading will occur.

A more robust solution is to employ a completely different interferometer configuration, which is insensitive to changes in ambient conditions.

For a birefringent sample, variations in signal intensity will occur, but these are now a function only of the sample birefringence, and are no longer connected with random polarisation drifting in the fibres. They can be made use of to extract information about the magnitude and orientation of sample birefringence (Everett et al. 1998).

The basic form of the Fizeau–based OCT system shown in figure 4-2 makes poor use of the available light; it can be seen from the figure that 87.5 % of the power from the source is lost in the system.

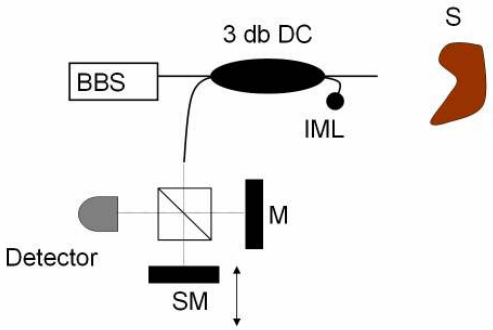

Figure 4-2: Standard Fizeau interferometer; DC: directional coupler, S: sample, SM: scanning mirror, M: mirror, IML: index matching gel

This configuration also suffers from the severe drawback that the maximum theoretical signal-to-noise ratio for a given source and detector is much lower than that for the Michelson–based system (Beddows et al. 2002). This may be the reason why Fizeau-based OCT has not been previously investigated. However she has theoretically shown that, as discussed below, the use of optical circulators and novel processing configurations can improve the theoretical SNR with the added advantage of "downlead insensitive" operation.

The maximum SNR of an OCT system is defined as the ratio of the mean square signal photocurrent $\left\langle I_s^{\,2} \right\rangle$ from the detector, under path-matched conditions, to the total photocurrent variance $\sigma_i^{\,2}$.It is given on equation 4-1 (Rollins and Izatt, 1999).

$$\mathrm{SNR} = 10\log_{10}\left(\frac{\left\langle I_s^2 \right\rangle}{\sigma_i^2}\right) \qquad \textbf{(4-1)}$$

The SNR calculation makes use of the optical power P_r in the reference beam, power P_s in the sample beam and the optical power P_x of stray incoherent light at the detector. Corresponding power reflectivities R_r, R_s and R_x are also used and the responsivity ρ of the detector is required. For maximum fringe visibility, the states of polarisation of the interfering beams must be identical, or reductions in SNR will occur. It is assumed that the light from the source is unpolarised. Although this is not always the case experimentally, it is a valid assumption for the purpose of comparing the maximum expected SNR for a range of proposed interferometer configurations. $\left\langle I_s^2 \right\rangle$ is a function of the optical powers in the reference and signal beams and of the detector responsitivity.

4.2 Noise

Noise is by definition "A disturbance, especially a random and persistent disturbance, that obscures or reduces the clarity of a signal" (Hawker et al. 2001). A number of sources of noise could be considered due to the environment. In optical systems, the sources of noise come from the source and the detectors (if a standard source-system-detector is considered). The elements in the system can contribute or not to increase the noise which degrades the SNR of the system. This will be discussed in comparing the efficiency of the interferometers.

There are three sources of noise to be considered in calculating the SNR of any OCT system.

The first is receiver noise, which arises due to the random thermal motion of electrons within the PIN photodetector. As the detector is normally followed by an electronic circuit in order to amplify the signal, a receiver noise component due to the amplification has normally to be taken in account. For commercial photodetectors, the receiver noise is usually specified by the manufacturer (in terms of NEP (Noise

Equivalent Power ($W/\sqrt{Hz}$))), it is usually expressed by (Rollins and Izatt, 2000), (Frosz et al. 2001):

$$\sigma_{re}^2 = \rho\left(NEP\right)^2 B, \tag{4-2}$$

where *B* is the detection bandwidth (Oliver, 1961). The NEP is defined as the signal power required to obtain a unity signal to noise ratio in the presence of some known (detector or background) noise (Benford et al. 1998). The two other sources of noise are both dependent upon the average photocurrent I_{dc} at the detector or, in the case of balanced detection, detectors.

Shot noise arises as a result of the random distribution in arrival times of photons at the detector from a monochromatic light source. The shot noise photocurrent variance $\sigma_{sh}{}^2$ that results from this Poisson process is given by:

$$\sigma_{sh}{}^2 = 2qI_{dc}B, \tag{4-3}$$

where *q* is the electronic charge.

The final source of noise to be considered is excess photon noise, which arises due to the random arrival of photons from a broad band light source. This is a Bose-Einstein process, with different statistics from shot noise, and the photocurrent variance for the excess noise is given by:

$$\sigma_{ex}{}^2 = I_{dc}{}^2 \frac{B}{\Delta\nu}. \tag{4-4}$$

Here, $\Delta\nu$ is the frequency linewidth of the source.

When a balanced receiver can be used, much of the excess noise has identical time dependence in both detectors, and is therefore cancelled. The dominant remaining noise contribution at moderate optical powers is often shot noise, and the resulting improvement in SNR can be as much as 40 dB.

However, in some configurations there can be a phase difference between the beams arriving at the two detectors for stray, incoherent beams arising from unwanted reflections (Takada, 1998). In this situation, the beating that occurs between non-coherent spectral components of the broadband source gives rise to a form of noise called beat noise. The beat noise is given in equation 4-5.

$$\sigma_{be}{}^2 = \rho^2 P_x P_r B / \Delta\nu \,. \qquad \textbf{(4-5)}$$

The beat noise may appear in the Michelson interferometer due to scattering at the end of the fibre.

A second detector can be considered to pick-up the antiphase signal and to carry out the subtraction between both signals. By this the amplitude is doubled and most of the noise is eliminated.

In the next section, the SNR of the Michelson and Fizeau configurations is derived for comparison in the unbalanced and balanced configurations, with I_{dc} and I_s provided for each configuration.

4.3 SNR calculation for different configurations

4.3.1 Assumptions in the analysis

The SNR is calculated for selected optical fibre OCT configurations, using a constant set of assumed values for the required parameters as given in table 4-1.

Table 4-1: Values of parameters used for calculation

	Symbol	Value
Power of the source (mW)	P_0	20
Wavelength (nm)	λ	1300
Source bandwidth (nm)	$\Delta\lambda$	50
Responsitivity (A/W)	ρ	0.95
Noise Equivalent Power* ($pW.Hz^{0.5}$)	NEP	2
Electronic Bandwidth (MHz)	B	1
Reflectitvity of the mirror	Rr	$0 \rightarrow 1$
Reflectitivity of the sample	Rs	$0 \rightarrow 1$
Unwanted reflection	Rx	0.0005
Splitting ratio of the coupler	α	$0 \rightarrow 1$

These parameters have been selected to be identical with those chosen by Rollins *et al.* (Rollins and Izatt, 1999), to allow comparison with the SNR analysis that they used for their in-fibre Michelson and Mach-Zehnder interferometer configurations. However, in calculating the average photocurrent, Rollins *et al.* assumed that the power P_s backscattered from the sample is negligible compared with the reference power, even though the sample reflectivity $R_s = 1$ is an order of magnitude higher than the reference reflectivity $R_r = 0.1$. The P_s term makes a significant contribution in the calculations of shot noise and excess noise. Therefore, in the following part, it is asserted it should be included, and then lower theoretical values of SNR are obtained than Rollins *et al.* did for the same configurations. However, the general conclusions about the benefits of balanced detection are unaffected, as can be seen from the analysis below.

In each case, a program written in Matlab is used. R_s, R_r, α and P can be variables varying from 0 to 1 for the reflectivities and the splitting ratios, and from 0 to 20 mW for the power. It is pointed out on the graphs that the maximum SNR found when the sample reflectivity is $R_s = 1$ (which corresponds to a 100% reflectivity mirror as a sample). Another point is also considered for a more realistic application. As an example, values of relative permittivity have been published for bovine bronchus tissue, giving 1.96 for the submucosa and 2.1025 for the epithelium at 1550 nm (Qu et al. 1995), leading to a reflectivity of 0.000 31 (Bamford et al. 2000). For simplicity, a value of $R_s = 0.001$ is used here in the sample calculations.

R_r is considered as a potential variable from 0 to 1, ranging from 0 % to 100 % reflectivity.

R_x, being due to the unwanted reflection, occurs in-fibre systems and it appears at the end of the fibres. For a normally cleaved fibre-in air $R_x \approx 0.04$, and in order to reduce this unwanted reflection, the fibre end can be polished at an angle but it must not exceed Brewster's angle (Utzinger and Richards-Kortum, 2003), where only one polarisation state could be reflected inside the fibre and no light is going on the reference mirror. Another possibility is to employ index matching liquid gel (IMLG), but still as the RI of the IMLG may not perfectly match the refractive index of the fibre and the light at the output of the fibre will be refracted, then it is not always helpful. An example of IMLG application is when a 3 dB coupler is used and just three ports of the 3 dB coupler are necessary and to reduce the light reflection from the last port IMLG

can be applied. For the same purpose, the fibre can be wrapped with small buckles: this implies that the light will be sent to the cladding and will be lost.

4.3.2 Michelson Interferometer with a single detector

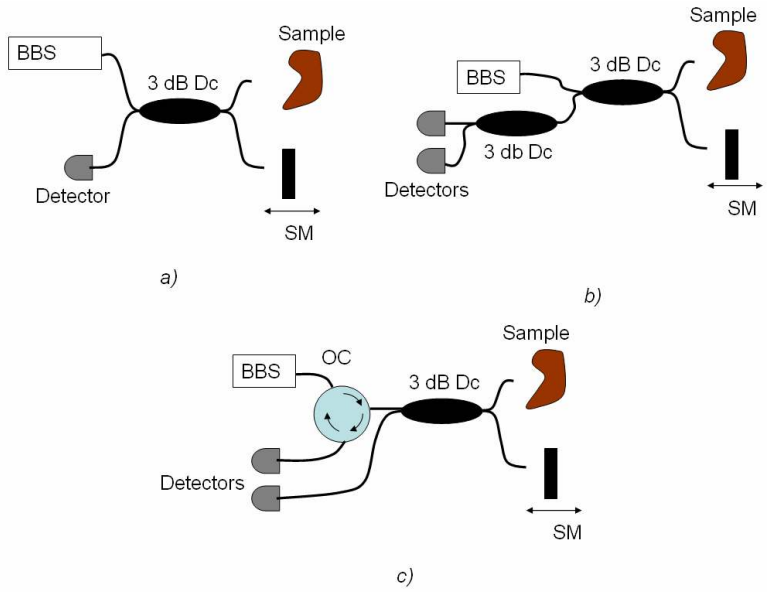

Figure 4-3: In-fibre Michelson configurations: a) with single detector, b) implementing balanced detection with second coupler, c) implementing balanced detection adding an optical circulator; Dc: directional coupler, OC: optical circulator

The most widely used optical-fibre configuration for OCT measurements is still the Michelson interferometer. The sample is positioned at the output of one interferometer path, and the reference surface at the output of the other. Consider first a system using a single detector, as shown in figure (4-3-a). The calculation here assumes that the splitting element is a directional coupler with a split ratio of $\alpha/(1-\alpha)$. This is also a possible variable which is varied from 0 to 1. Ignoring losses in the system, the powers received at the detector from the sample arm, reference arm and unwanted reflections respectively are given in equations 4-6, 4-7 and 4-8.

$$P_s = P_0 \alpha R_s (1-\alpha)(1-R_x)^2 \quad \textbf{(4-6)}$$

$$P_r = P_0 (1-\alpha) R_r \alpha \quad \textbf{(4-7)}$$

$$P_x = P_0 (1-\alpha) R_x \alpha \quad \textbf{(4-8)}$$

The interference term produces a periodic signal photocurrent I_s, which varies cosinusoidally as the interferometer phase θ is scanned linearly,

$$\begin{aligned} I_s &= \rho 2\sqrt{P_r P_s}\cos(\theta) \\ &= 2\rho\left[P_0^2 \alpha^2 (1-\alpha)^2 R_r R_s (1-R_x)^2\right]^{1/2}\cos(\theta) \end{aligned} \quad \textbf{(4-9)}$$

and the average photocurrent is given by I_{dc}, where

$$\begin{aligned} I_{dc} &= \rho(P_r + P_s + P_x) \\ &= \rho P_0 \alpha(1-\alpha)\left[R_s(1-R_x)^2 + R_r + R_x\right] \end{aligned} \quad \textbf{(4-10)}$$

The SNR expression for the unbalanced Michelson Configuration is given by:

$$\begin{aligned} &SNR_{(dB)} = 10\ \log\left(\frac{\langle I_s\rangle^2}{\sigma_{re}^2 + \sigma_{sh}^2 + \sigma_{ex}^2}\right) \\ &\text{with}: \langle I_s\rangle^2 = 4\rho^2\left[P_0^2\alpha^2(1-\alpha)^2 R_r R_s (1-R_x)^2\right] \\ &\sigma_{re}^2 = \rho(NEP)^2 B \\ &\sigma_{sh}^2 = \rho P \alpha(1-\alpha)\left[R_s(1-R_x)^2 + R_r + R_x\right] 2qB \\ &\sigma_{ex}^2 = \rho^2 P_O^2 \alpha^2 (1-\alpha)^2\left[R_s(1-R_x)^2 + R_r + R_x\right]^2 \frac{B}{\Delta\nu} \end{aligned} \quad \textbf{(4-11)}$$

Figure 4-4 presents the evolution of the SNR as a function of the sample and reference reflectivities (figure (4-4-a)), when α = 0.5 and P = 20 mW, and as a function of the split ratio and the power (figure (4-4-b)), when R_s = 1 and R_r = 0.1.

When R_s = R_r, a maximum visibility is obtained and this translates to a maximum SNR value of 65 dB. Since signal and reference intensities are matched at this value, all signal light contributes to the generation of interference fringes.

The SNR turns out to be almost independent of the split ratio α over a very wide range, for values of α between about 0.05 and 0.95. The maximum SNR is found for α = 0.5. This is a typical result; it turns out that for all configurations examined below, the optimum split ratio is 0.5 and there is generally a rather weak dependence of SNR on the split ratio.

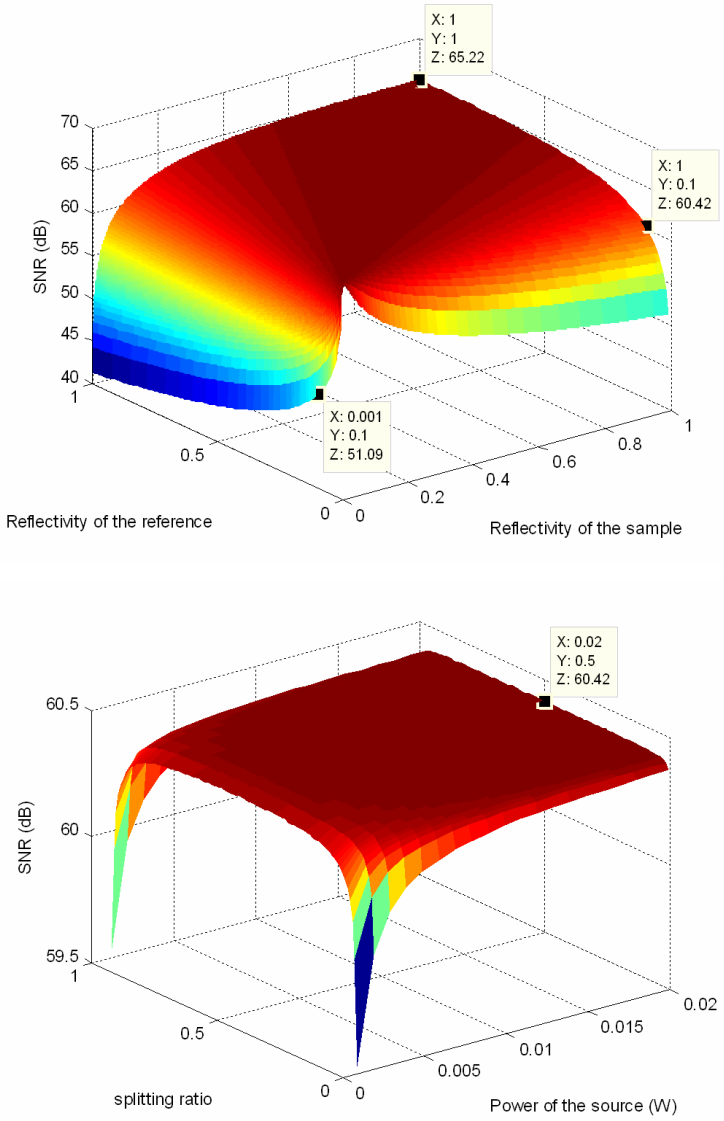

Figure 4-4: SNR (Z-axis) for unbalanced Michelson configuration OCT system as a function of the sample (X-axis) and reference (Y-axis) reflectivities (curves (a)) and as a function of the split ratio (Y-axis) and the power of the source (X-axis) (curves (b)). The colour grade from blue to red represents the change from low to high SNR values. The labelled points enable the comparison of the different configurations.

4.3.3 Michelson Interferometer with balanced detection

Consider now the modified configuration shown in figure (4-3-c), with an optical circulator included between the source and the directional coupler to allow balanced detection. By that the magnitude of the interference signal is doubled figure (4-5-b) and much of the noise is suppressed (figure (4-5-d)).

The use of balanced detection in this configuration has three important effects:

- The magnitude of $<I_s^2>$ increases by a factor of 4;
- The total noise variance is doubled, as the noise appears on each of the two Detectors;
- The excess noise is cancelled, although this term must be replaced in the calculations by the beat noise term, which corresponds to the component of excess noise not removed by the balanced detector.

Figure 4-5 illustrates the effect of balanced detection for the best SNR case, that is when the two detector signal levels are equal.

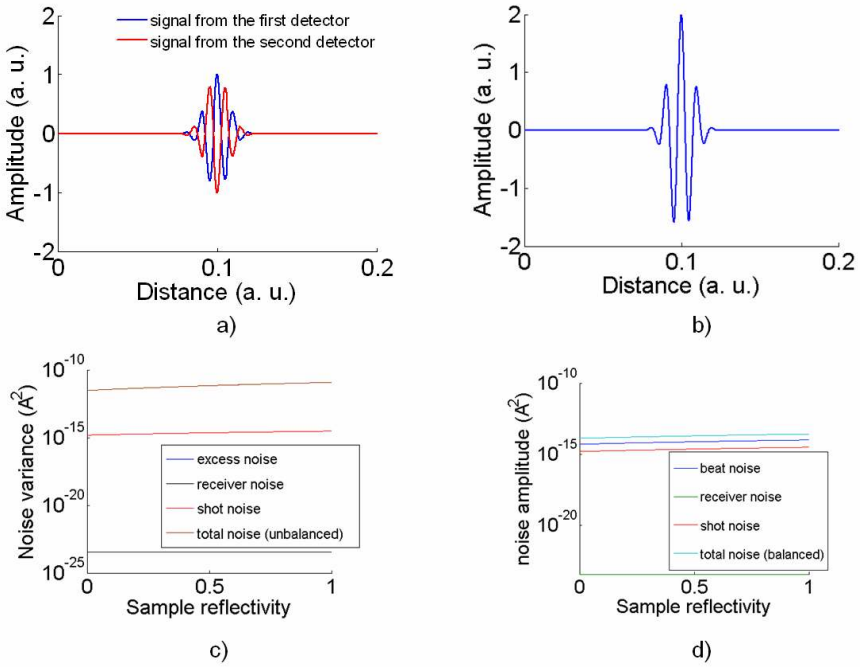

Figure 4-5: a) signals in anti-phase at the detectors; b) signal obtained after subtraction of the signals in anti-phase; c) noise considered at each detector (excess noise curve coincidental with the total noise curve); d) noise after balanced detection

If both signals in anti-phase did not have the sample intensity, the amplitude will not be doubled (figure (4-6-b)) and the excess noise will not be diminished completely (figure (4-6-c)), implying that the SNR will be reduced.

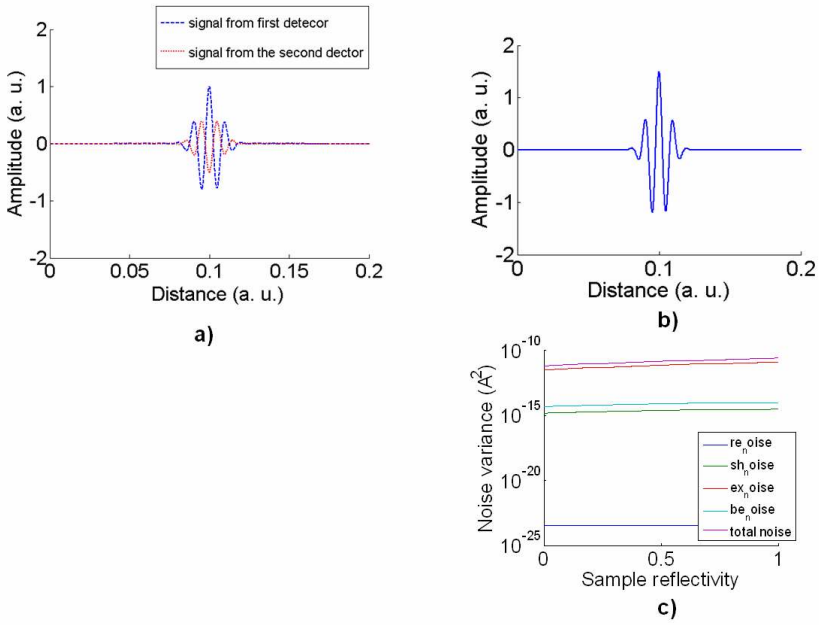

Figure 4-6: a) signals in anti-phase and different amplitude; b) subtraction of both signals in anti-phase; c) noise considered when the signals have different intensities. The noise at each detector is the same as in figure (4-5-c)

The SNR expression for the balanced Michelson is given by:

$$\mathrm{SNR}_{(\mathrm{dB})} = 10\ \log\left(\frac{\langle \mathrm{I_s}\rangle^2}{2\left(+\sigma_{\mathrm{re}}^2+\sigma_{\mathrm{sh}}^2+\sigma_{\mathrm{ex}}^2\right)}\right)$$

$$\text{with}: \langle \mathrm{I_s}\rangle^2 = 16\rho^2\left[\mathrm{P}^2\alpha^2(1-\alpha)^2\mathrm{R_r}\mathrm{R_s}(1-\mathrm{R_x})^2\right] \qquad \textbf{(4-12)}$$

$$\sigma_{\mathrm{re}}^2 = \rho(\mathrm{NEP})^2\,\mathrm{B}$$

$$\sigma_{\mathrm{sh}}^2 = \rho\,\mathrm{P}\,\alpha(1-\alpha)\left[\mathrm{R_s}(1-\mathrm{R_x})^2+\mathrm{R_r}+\mathrm{R_x}\right]4\,\mathrm{q}\,\mathrm{B}$$

$$\sigma_{\mathrm{be}}^2 = \rho^2\,\mathrm{P}^2\,\alpha^2(1-\alpha)^2\,\mathrm{R_r}\,\mathrm{R_x}\,\frac{\mathrm{B}}{\Delta\nu}$$

When these modifications are introduced, the calculated values of SNR increase significantly as shown in figure 4-7 (by analogy to the previous calculation, the SNR is plotted as a function of the same parameters). This is largely due to the cancellation of the excess noise. Shot noise now makes the dominant contribution to the overall noise

variance, although the beat noise component also becomes more important for values of R_s lower than about 0.01.

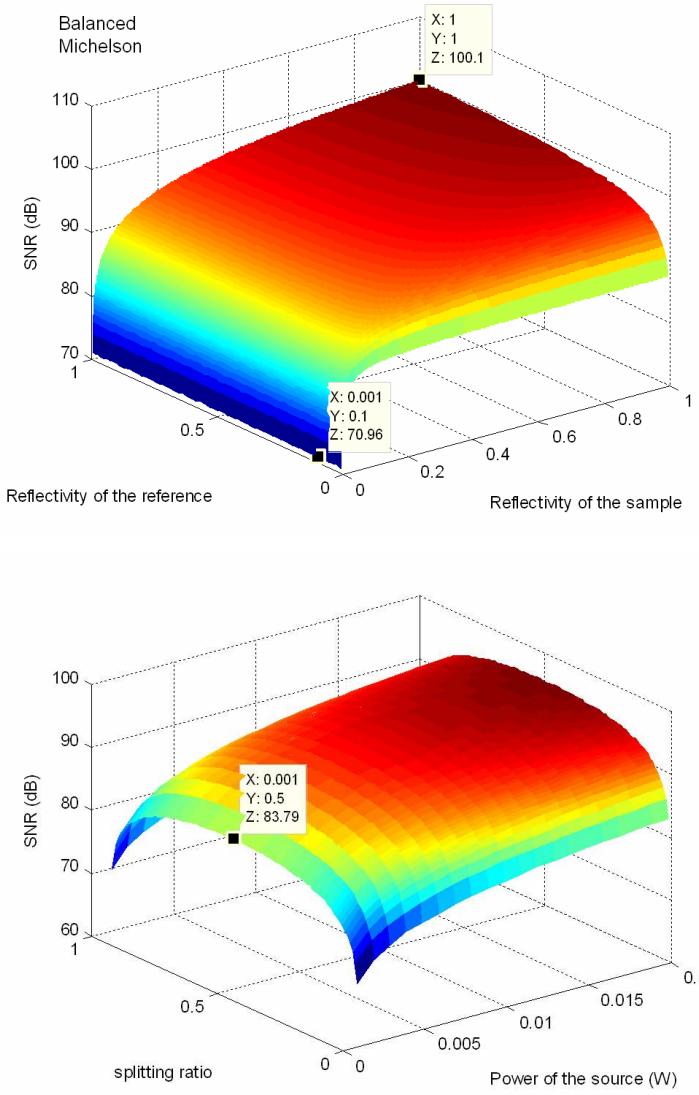

Figure 4-7: SNR (Z-axis) of balanced Michelson configuration as a function of a) Rr (Y-axis) and Rs (X-axis) (P= 20 mW), and b) split ratio (Y-axis) and power of the source (X-axis) (R_s = 1; R_r =0.1). The colour grade from blue to red represents the change from low to high SNR values. The labelled points enable the comparison of the different configurations

The maximum SNR of 100 dB for this system is obtained for $R_s = R_r = 1$ and $\alpha = 0.5$. The SNR remains above 90 dB for $0.1 < \alpha < 0.9$ for P = 20 mW.

When the lower value of R_s = 0.001 is taken, a maximum SNR of 71 dB is obtained, again for α = 0.5. Varying the reference reflectivity now has little effect; the balanced detection arrangement reduces the sensitivity of the system to differences between signal and reference power.

4.3.4 *Fizeau configuration using a directional coupler, with Michelson processing interferometer and a single detector*

The simplest form of Fizeau-based OCT system, shown in figure (4-8-a), uses a single directional coupler (Bamford et al. 1999), (Bamford, 2000), (Beddows et al. 2002). Calculation of the interference term is now more complicated, as interference can only occur between beams that are path-matched (to within the source coherence length) after their passage through both Fizeau and processing interferometers. The previous chapter provides expressions of I_{dc} and I_s for the configuration.

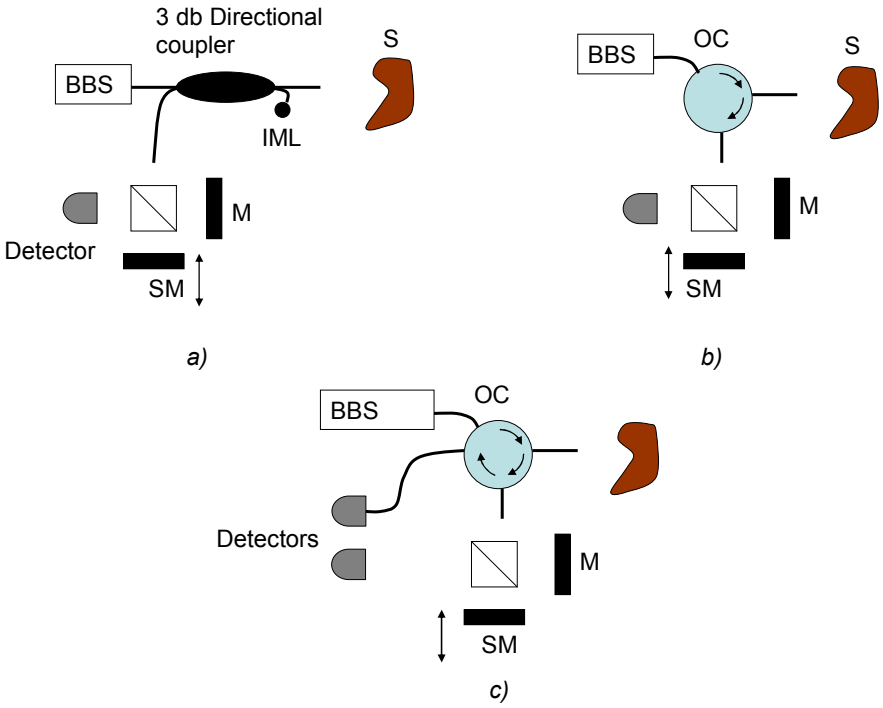

Figure 4-8: Fizeau configurations a) standard, b) with optical circulator single detector; c) using fourth port of the circulator for balanced detection; IML: index matching gel, OC: optical circulator, S: sample, M: mirror, SM: scanning mirror

Assuming that a split ratio α/(1- α) of the directional coupler and a split ratio β/(1-β) of the beam splitter are variables varying from 0 to 1, the powers at the detector are then given by the equations 4-13 and 4-14.

$$P_{12} = P_{22} = P(1-R_r)^2 R_s \alpha(1-\alpha)\beta(1-\beta) \quad \textbf{(4-13)}$$

$$P_{11} = P_{21} = P R_r \alpha(1-\alpha)\beta(1-\beta) \quad \textbf{(4-14)}$$

Only two of these four components, P_{11} and P_{12}, are path matched at the detector; therefore the interference term is given by:

$$I_s = 2\rho(P_{11} P_{12})^{1/2}\cos(\theta) = 2\rho P(1-R_r)\alpha(1-\alpha)\beta(1-\beta)(R_s R_r)^{1/2}\cos(\theta) \quad \textbf{(4-15)}$$

The average photocurrent is:

$$I_{dc} = 2\rho P \alpha(1-\alpha)\beta(1-\beta)\left[R_s(1-R_r)^2 + R_r\right] \quad \textbf{(4-16)}$$

The SNR expression of the standard Fizeau interferometer is then given by:

$$\begin{aligned} &SNRdB = 10\log\left(\frac{\langle I_s\rangle^2}{\sigma_{re}^2 + \sigma_{sh}^2 + \sigma_{ex}^2}\right) \\ &\text{with:}\quad \langle I_s\rangle^2 = 4\left[\rho P(1-R_r)^2\alpha(1-\alpha)\beta(1-\beta)\right]^2 (R_r R_s) \\ &\qquad \sigma_{re}^2 = \rho(NEP)^2 B \\ &\qquad \sigma_{sh}^2 = 4\rho P\alpha(1-\alpha)\beta(1-\beta)\left[R_s(1-R_r)^2 + R_r\right] q B \\ &\qquad \sigma_{ex}^2 = 4\left[\rho P\alpha(1-\alpha)\beta(1-\beta)\right]^2\left[(1-R_r)^2 R_s + R_r\right]\frac{B}{\Delta\nu} \end{aligned} \quad \textbf{(4-17)}$$

Figure (4-9-a) presents the results of the calculation of the SNR as a function of the sample reflectivity and the reference reflectivity. Calculation of the SNR for this configuration leads to values of 65 dB when $R_s = 1$ ($R_r = 0.1$) and 50 dB when $R_s = 0.001$.

The α and β split ratios change the SNR in the same way (figure (4-9-b)), and similar to the Michelson configuration. The maximum SNR 50 dB is for $\alpha = \beta = 0.5$. This was done taking $R_s = 0.001$ and $R_r = 0.1$ to get a realistic result. With $\alpha = \beta = 0.5$ and P = 20 mW (figure (4-9-b)), the SNR increases when R_s increases and decreases when R_r increases (this is due to less light reaching the sample). It can be observed that for $R_r \approx 0.4$, the maximum SNR 65 dB can be achieved. It is noted that for small values of R_r there is not a big change in SNR when R_s increases. The SNR changes linearly

with the power (figure (4-10-a)) and the maximum for each power is for $R_r \approx 0.36$. This is also seen in figure (4-10-b), which enables to show again that the SNR is maximal for $\alpha = \beta = 0.5$.

The influence of the change of SNR due to the reflectivies R_s and R_r is not the same as for the Michelson configuration.

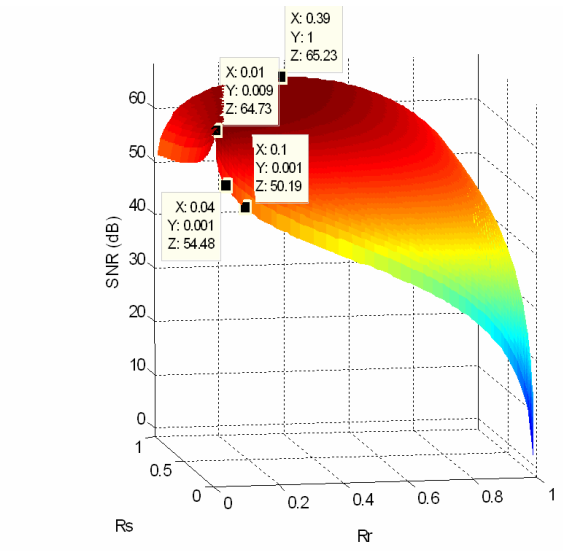

a)

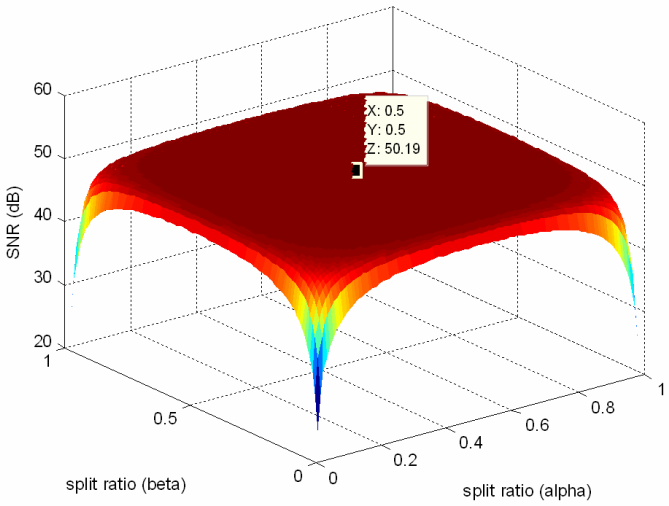

b)

Figure 4-9: SNR (Z-axis) plots of standard Fizeau configuration as a function of a) the sample (X-axis) and reference (Y-axis) reflectivities (P=20 mW, α=0.5, β=0.5), b) α (X-axis) and β (Y-axis) (P=20 mW, R_r=0.1, R_s=0.001); The colour grade from blue to red represents the change from low to high SNR values. The labelled points enable the comparison of the different configurations

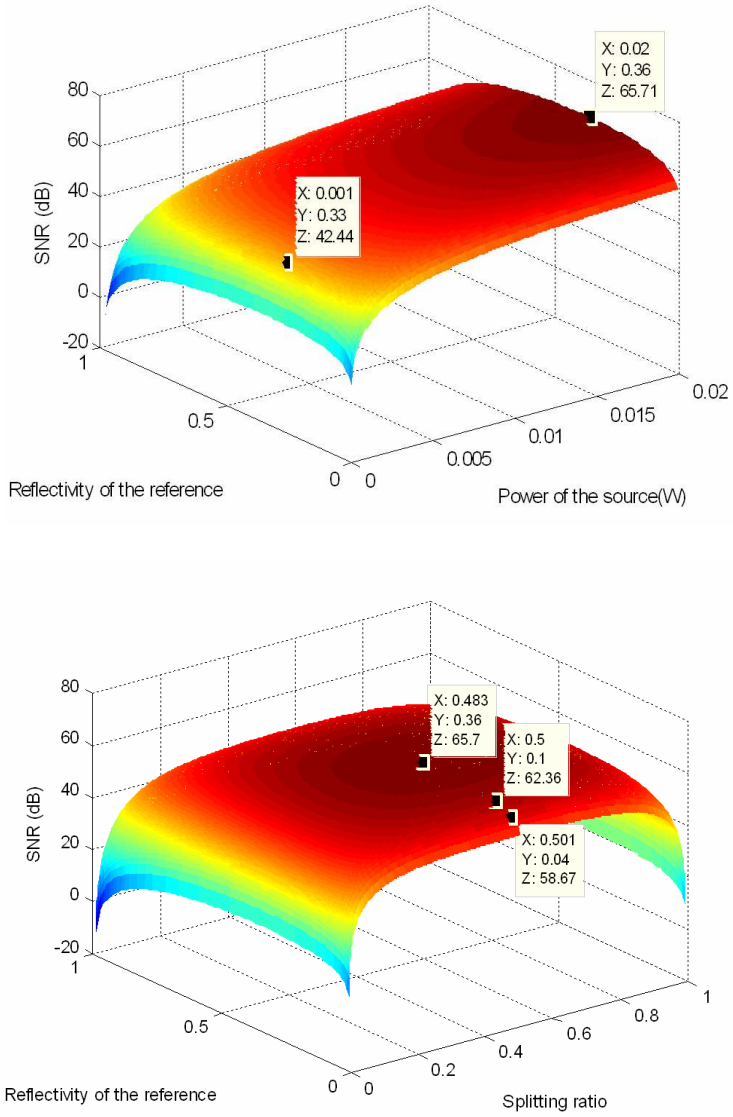

Figure 4-10: SNR (Z-axis) plots of standard Fizeau configuration as a function of a) R_r (Y-axis) and P (X-axis) (α=0.5, β=0.5, R_s=1) and b) R_r (Y-axis) and a split ratio α or β (X-axis) (P=20 mW, Rs=1). The colour grade from blue to red represents the change from low to high SNR values. The labelled points enable the comparison of the different configurations

4.3.5 Fizeau configuration using an optical circulator, with Michelson processing interferometer and a single detector

This is very similar to the case in section 4-3-4 above, the only difference being the improvement of the use of optical power. The use of an optical circulator, as shown in figure (4-8-b), allows all the light from the source to be transmitted to the sample and all backscattered light from the sample to be transmitted to the processing interferometer.

If losses in the circulator are ignored, then

$$P_{12} = P_{22} = P(1-R_r)^2 R_s \beta(1-\beta) \tag{4-18}$$

$$\text{and } P_{11} = P_{21} = P R_r \beta(1-\beta). \tag{4-19}$$

The SNR expression for the unbalanced Fizeau interferometer with an optical circulator is given by:

$$\begin{aligned} SNR_{(dB)} &= 10 \log\left(\frac{\langle I_s \rangle^2}{\sigma_{re}^2 + \sigma_{ex}^2 + \sigma_{sh}^2}\right) \\ \text{with: } \langle I_s \rangle^2 &= 4[\rho P \beta(1-\beta)(1-R_r)]^2 R_r R_s \\ \sigma_{re}^2 &= \rho (NEP)^2 B \\ \sigma_{ex}^2 &= 4\left[\rho P \beta(1-\beta)\left(R_s(1-R_r)^2 + R_r\right)\right]^2 \frac{B}{\Delta\nu} \\ \sigma_{sh}^2 &= 4\rho P \beta(1-\beta)\left(R_s(1-R_r)^2 + R_r\right) q B \end{aligned} \tag{4-20}$$

The SNR values are 6 dB-higher than in the case in section 4-3-4 and is limited by the dominant excess noise term which is proportional to the mean square signal. For R_s = 0.001, the SNR max is 38 dB at R_r = 0.1 (figure 4-11).

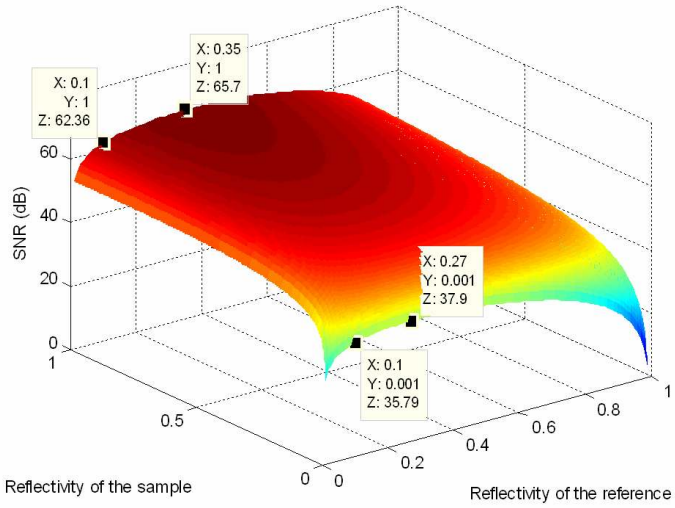

Figure 4-11: SNR of single detector Fizeau configuration with an optical circulator. The colour grade from blue to red represents the change from low to high SNR values. The labelled points enable the comparison of the different configurations

4.3.6 Fizeau configuration using a four-port optical circulator, with a Michelson processing interferometer and balanced detection

The use of balanced detection in this configuration, shown in figure (4-8-c), has two main effects:

• the magnitude of $\langle I_s^2 \rangle$ increases by a factor of being less than 4;

• the total noise variance is doubled, as the noise appears on each of the two detectors.

In that case the excess noise is not cancelled. At the first detector the expressions of the powers are:

$$P_{12} = P_{22} = PT_c^2 (1 - R_r)^2 R_s \beta (1 - \beta) \quad \textbf{(4-21)}$$

$$P_{11} = P_{21} = P T_c^2 R_r \beta (1 - \beta), \quad \textbf{(4-22)}$$

where T_c is the transmission factor of the optical circulator and R_e is the reflectivity at the end of the optical fibre from the third port of the optical circulator. The reflectivity R_e is 0.0005 (being a value when the optical fibre is polished at an angle). At the second detector, the expressions of the powers are:

$$P'_{12} = P'_{22} = P\,T_c^3\,R_s\,(1-R_r)(1-R_e)^2\,\beta(1-\beta) \quad \textbf{(4-23)}$$

$$P'_{11} = P'_{21} = P\,T_C^3\,R_r\,(1-R_e)^2\,\beta(1-\beta), \quad \textbf{(4-24)}$$

The SNR for the balanced Fizeau interferometer employing an optical circulator and its fourth port is given by:

$$\begin{aligned}
&SNR_{(dB)} = 10\,\log\left(\frac{\langle I_s\rangle^2}{2\left(\sigma_{re}^2+\sigma_{ex}^2+\sigma_{sh}^2\right)+\sigma_{be}^2}\right)\\
&\langle I_s\rangle^2 = 4\left[\rho\,P\beta(1-\beta)(R_rR_s)^{0.5}(1-R_r)(1-R_e)(2-R_e)\right]^2\\
&\sigma_{re}^2 = \rho\,(NEP)^2\,B\\
&\sigma_{ex}^2 = 4\rho^2P^2\beta^2(1-\beta)^2\left[R_r+R_s(1-R_r)^2\right]^4(1-R_e)^4\,\frac{B}{\Delta\nu}\\
&\sigma_{sh}^2 = 2\rho\,P\beta(1-\beta)\left[R_r+R_s(1-R_r)^2\right]^2(1-R_e)^2\,qB\\
&\sigma_{be}^2 = \rho^2P^2\beta^2(1-\beta)^2\left[R_rR_e+R_sR_e(1-R_r)\right]R_r(1-R_e)^2\,\frac{B}{\Delta\nu}
\end{aligned} \quad \textbf{(4-25)}$$

The results are found in figure 4-12. The form of the SNR dependence on R_s, shown as in figure (4-12-a), is similar to that was shown for the standard Fizeau arrangement. The maximum SNR 44 dB is obtained when $R_s = 1$ and declines rapidly when this reflectivity falls below 0.1. For a more practical sample, for $R_s = 0.001$, and $R_r = 0.1$ the SNR is 10 dB and at $R_r \approx 0.34$ the SNR is 14 dB. These values demonstrate that the inclusion of an optical circulator and balanced detection in the system design using the MPI decreases the theoretical SNR of the Fizeau-based OCT system. This is due to non-cancelled excess noise and the presence of beat noise. Also when a more realistic R_s value is used there is not a significant change on the SNR for $0.02 < R_r < 0.35$.

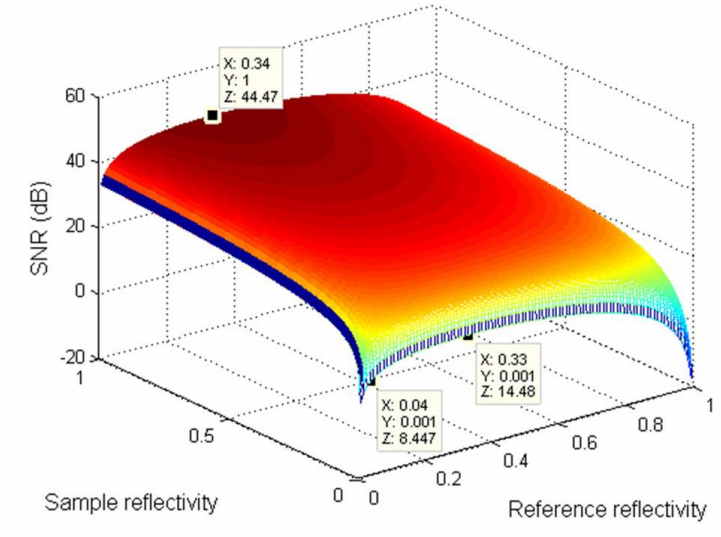

a)

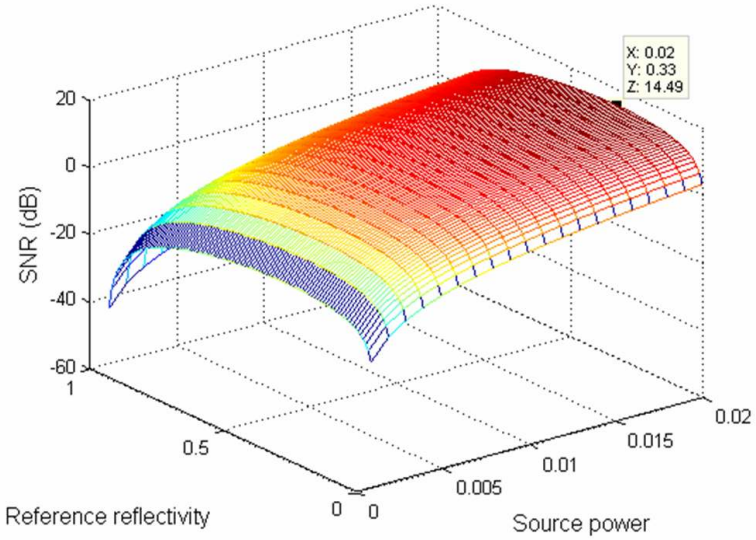

b)

Figure 4-12: SNR plot (Z-axis) of balanced detection Fizeau configuration with a four-optical circulator in function of a) R_r (X-axis) and R_s (Y-axis) (R_e = 0.0005, splitting ratio (β) = 0.5, P = 20 mW), b) R_r (Y-axis) and P (X-axis) (R_s = 0.001, splitting ratio (β) = 0.5, R_e = 0.0005). The colour grade from blue to red represents the change from low to high SNR values. The labelled points enable the comparison of the different configurations

In practice, the configuration of figure (4-6-c) is not easy to align. Because both beams from the interferometer must be recoupled into the 3rd optical fibre port of the circulator, there tends to be a large loss factor at this point in the system, which degrades the SNR severely. There is still some part of the light that is lost due to the

reflected light from the fibre end. It can then be understood that the beat noise is not negligible in this configuration. The substitution of a Mach–Zehnder processing interferometer eases practical alignment problem and provides immediate access to the complementary interferometer outputs for balanced detection.

4.3.7 *Fizeau configuration using an optical circulator, with Mach-Zehnder processing interferometer and a single detector or balanced detection*

The use of a Mach-Zehnder processing interferometer, as shown in figure 4-11, allows all the light to be transmitted through the processing interferometer.

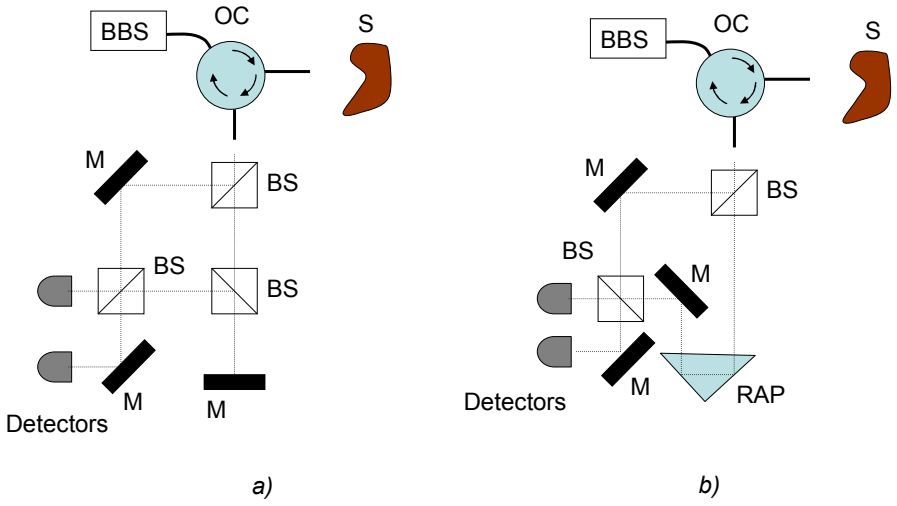

Figure 4-13: Fizeau interferometer arrangement with optical circulator and two possible implementations of the Mach-Zehnder processing interferometer; BS: beam splitter, M: mirror, RAP: right angle prism; configuration b) is more efficient because all the light at the output of the third port of the optical circulator is split in two beams that recombine at the second beam splitter. In configuration a), the two beams recombining do not have the same power (due to one beam suffering two splits), reducing the efficiency

The configuration in figure (4-13-a) will not be discussed because light is lost in the scanning arm of the processing interferometer and it does not make use of all the light, affecting the SNR. In figure (4-13-b) a right angle prism (with total internal reflection) replaces the mirror and the beam splitter. If the split ratios of the first BS in the system is α/(1-α) and of the second BS β/(1-β), 4 components of electric field reach each detector, and similar to the configuration with the Michelson processing interferometer, if losses in the circulator are ignored, then, on each detector:

$$P_{12} = P_{22} = P(1-R_r)^2 R_s\,\alpha(1-\beta) \tag{4-26}$$

$$\text{and } P_{11} = P_{21} = P\,R_r\,(1-\alpha)\beta\,. \tag{4-27}$$

Only two of these four components, P_{11} and P_{12}, are path matched at the detector; therefore the interference term is given by:

$$I_s = 2\rho(P_{11}P_{12})^{1/2}\cos(\theta) = 2\rho P(1-R_r)[\alpha(1-\alpha)\beta(1-\beta)R_s R_r]^{1/2}\cos(\theta) \tag{4-28}$$

The average photocurrent is:

$$I_{dc} = 2\rho P\left[R_s(1-R_r)^2\beta(1-\alpha) + R_r\beta(1-\alpha)\right] \tag{4-29}$$

The SNR expression for the balanced Fizeau interferometer employing an optical circulator and a Mach-Zehnder interferometer is given by:

$$\begin{aligned} SNR_{(dB)} &= 10\log\left(\frac{\langle I_s\rangle^2}{2\left(\sigma_{re}^2+\sigma_{ex}^2+\sigma_{sh}^2\right)}\right) \\ \text{with: } \langle I_s\rangle^2 &= 4\left(\rho P(1-R_r)\right)^2\alpha(1-\alpha)\beta(1-\beta)R_s R_r \\ \sigma_{re}^2 &= \rho\,(NEP)^2\,B \\ \sigma_{ex}^2 &= 4\rho^2P^2\left[R_s(1-R_r)^2\beta(1-\alpha)+R_r\beta(1-\alpha)\right]^2\frac{B}{\Delta\nu} \\ \sigma_{sh}^2 &= 2\rho P\left[R_s(1-R_r)^2\beta(1-\alpha)+R_r\beta(1-\alpha)\right]qB \end{aligned} \tag{4-30}$$

Considering this set-up, figure (4-13-b), the configuration with a single detector will provide similar results as for the standard Fizeau inteferometer or the Fizeau configuration with a single detector and an optical circulator. Some results are shown in figure (4-14-a) and (-b). The SNR values as a function of the reference and sample reflectivities (figure (4-14-a)) are similar to those presented for the unbalanced configurations. The maximum SNR of 58 dB is still at R_s = 1 and R_r = 0.36 and for

reference reflectivities from 0 to 0.36 the SNR does not change too much.the Mach-Zehnder processing interferometer with a single detector does not improve the SNR of the Fizeau arrangement.

In the balanced configuration, figures (4-16-a) and (-b) show that a maximum peak is observed at $R_r = 0.36$ for all R_s (which is the same in most of the results). The noise is the highest for the same R_r. There is a slight falling off of the SNR for an asymmetric split ratio of the beam splitter, but for α and β between 0.1 and 0.9, the value does not fall by more than 4 dB, showing that the same efficiency can be got for $\alpha = \beta = 0.5$ (figure (4-15-b)). The usual differences in the terms are seen, and the SNR values are much higher, at 67 dB for $R_s = 1$ and 64 dB for $R_s = 0.001$. These are lower than the values obtained using a Michelson interferometer (figure 4-3).

Table 4-2: Comparison of the calculated SNR values for the Michelson and Fizeau configurations for OCT considering $R_r = 0.1$

OCT configuration		SNR (dB)	
		$R_s = 1$	$R_s = 0.001$
Michelson Interferometer			
unbalanced		65	52
Balanced		96	75
Fizeau Interferometer			
Standard		56	46
With optical circulator and Michelson processing interferometer	*unbalanced*	62	36
	balanced	40	10
With optical circulator and Mach-Zehnder processing interferometer	*unbalanced*	61	50
	balanced	67	64

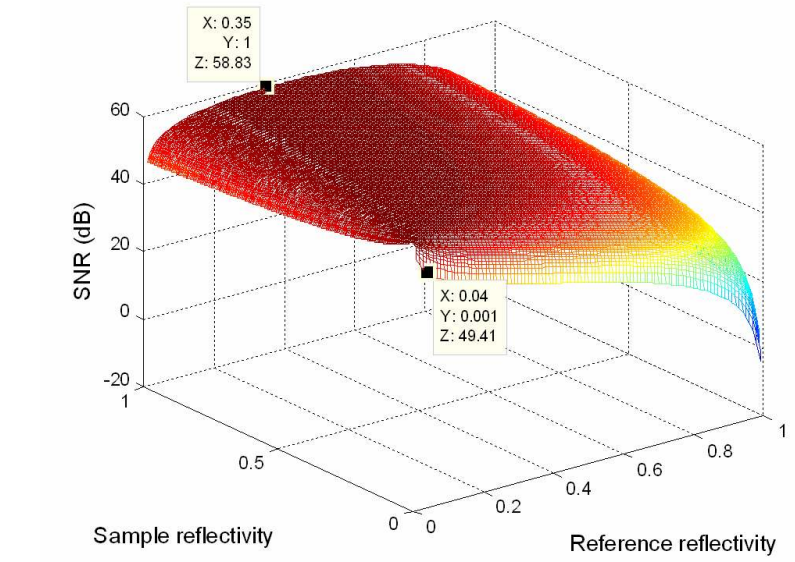

a)

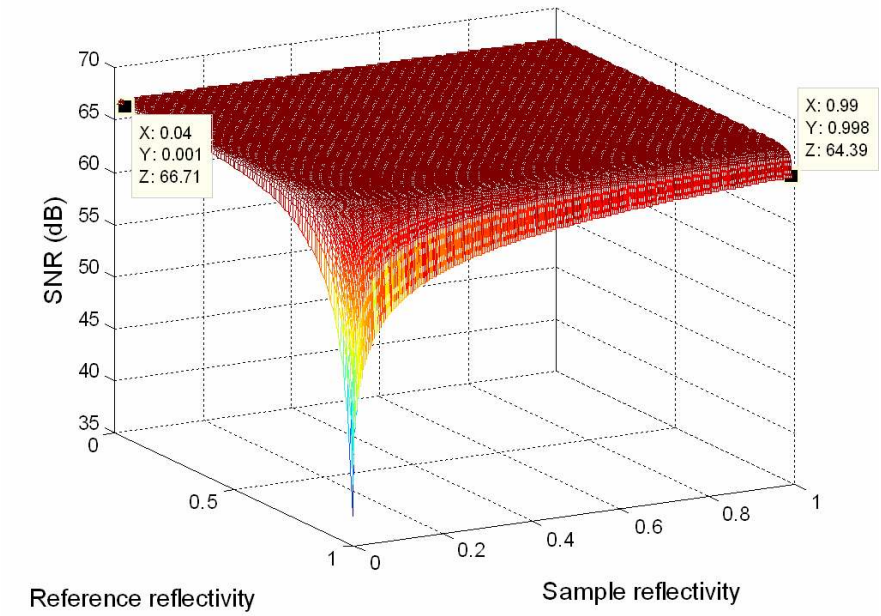

b)

Figure 4-14: a) SNR (Z-axis) of the unbalanced Fizeau configuration with optical circulator (OC) and Mach-Zehnder processing interferometer (MZPI) as a function of the reference (X-axis) and the sample reflectivities (Y-axis) (α = β = 0.5, P= 1 mW); b) SNR (Z-axis) of the balanced Fizeau configuration with OC and MZPI as a function of R_s (Y-axis) and R_r (X-axis) (P = 1 mW, α = β = 0.5).The colour grade from blue to red represents the change from low to high SNR values. The labelled points enable the comparison of the different configurations

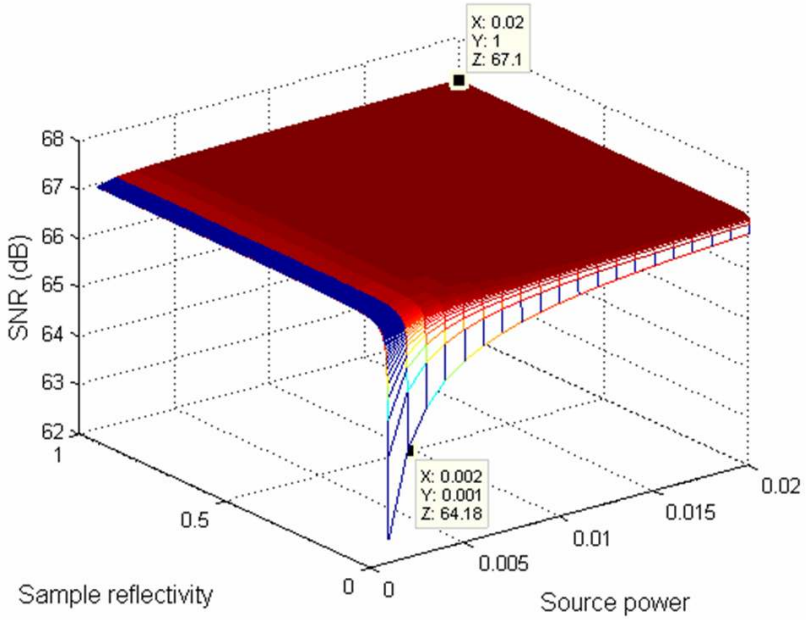

a)

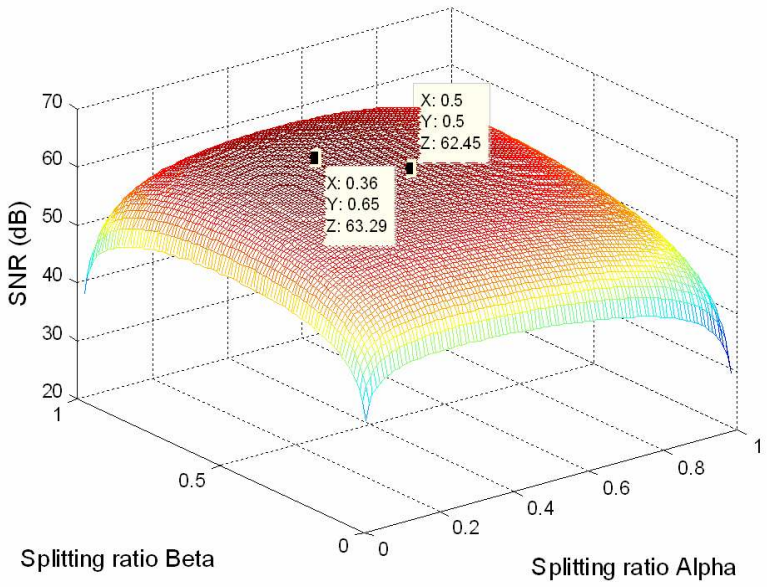

b)

Figure 4-15: a) SNR (Z-axis) of the balanced Fizeau configuration with OC and MZPI as a function of P (X-axis) and R_s (Y-axis) (R_r = 0.04, α = β = 0.5); b) SNR (Z-axis) of the balanced Fizeau configuration with OC and MZPI as a function of α (Y-axis) and β (X-axis) (P = 1 mW, R_r = 0.04, R_s = 0.001. The colour grade from blue to red represents the change from low to high SNR values. The labelled points enable the comparison of the different configurations

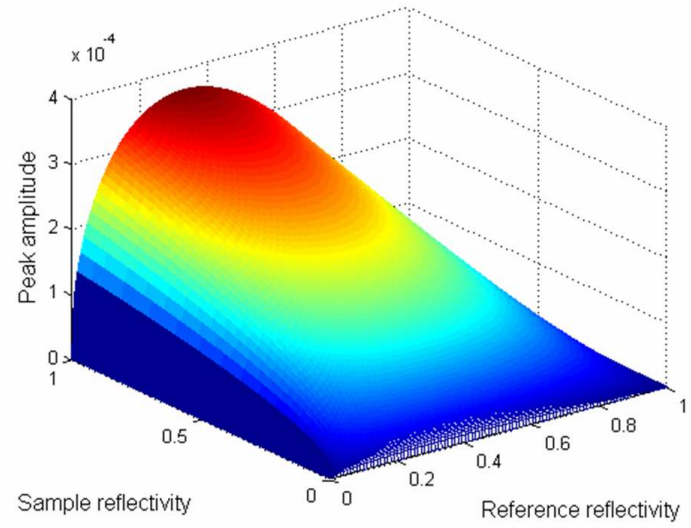

a)

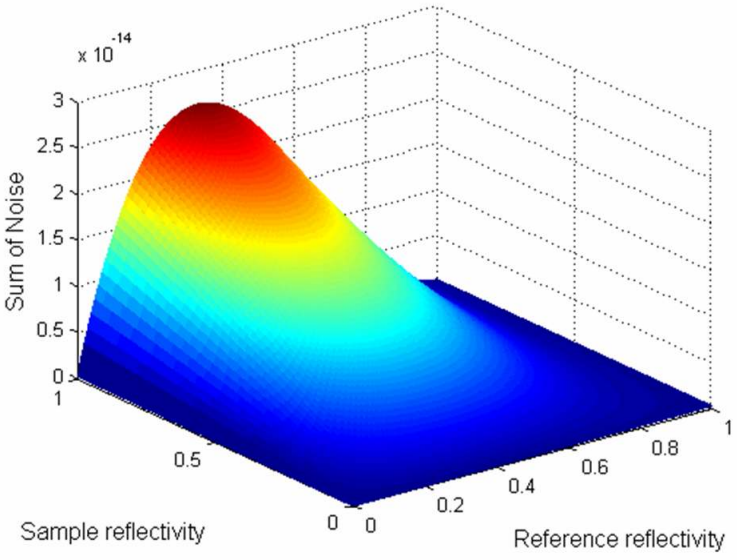

b)

Figure 4-16: a) Peak magnitude in function of the reference and sample reflectivities (P = 1 mW, α = β = 0.5); b) noise magnitude in function of the reference and sample reflectivities (P = 1 mW, α = β = 0.5). The colour grade from blue to red represents the change from low to high peak amplitude and sum of noise

4.4 Discussion

The theoretical SNR values for the basic form of Michelson-based system are slightly higher than the standard Fizeau OCT system, using a directional coupler and a single detector. The experimental difficulty in recoupling beams from the processing interferometer into the fibre for the Fizeau configuration tends to reduce the SNR still further in practice, and the Michelson configuration is therefore to be preferred when polarisation problems are not severe.

It is interesting that the use of a circulator alone does not, for moderate source powers, improve significantly the SNR of the Fizeau configuration, since the mean square signal photocurrent and the noise variance are approximately proportional.

However, the experimental problem with the Fizeau configuration persists, and the calculated SNR is likely to be an overestimate in this case.

The unbalanced Michelson is optimised when $R_r = R_s$, and the result is similar for the balanced detection. Considering the Fizeau configuration, an optimum is nearly always obtained for $R_r \leq 0.35$.

The reference reflectivity $R_r = 0.1$, chosen to match that in the set of parameters used by Rollins *et al.*, is higher than the value of 0.04 expected for the glass–air interface at a cleaved fibre end. However, it is possible to obtain values of reflectivity up to about 0.3 at a fibre end by the application of a titanium dioxide coating to the cleaved face (Naci Inci et al. 1992), so the value of $R_r = 0.1$ used is readily achievable.

The use of a Mach–Zehnder processing interferometer in the Fizeau configuration greatly eases alignment. The two complementary outputs are automatically available from this type of interferometer, facilitating the use of balanced detection and avoiding the requirement to recouple from the processing interferometer into fibre.

The theoretical SNR for this configuration is in fact lower than for the Michelson configuration with balanced detection, at 67 dB for $R_s = 1$, and similar when realistic values are used, 64 dB for $R_s = 0.001$. The SNR of the system is saturated when P increases due to the presence of the beat noise. The additional advantage of down-lead insensitivity obtained with this version of the Fizeau OCT system makes it a good candidate for measurements when polarization variation might otherwise be a problem.

The trends arising from this analysis follow a very similar pattern to those obtained by Rollins *et al.*, although the inclusion of the additional term leads us to obtain SNR values about 10 dB lesser than theirs for identical Michelson configurations.

4.5 Conclusions

4.5.1 Analysis of theoretical SNR

A number of optical-fibre Fizeau-based OCT configurations have been proposed and the theoretical maximum SNR value for each configuration has been calculated under a standard set of assumed illumination and detection conditions. Comparison of the various designs shows that, although the basic Fizeau OCT system has poor SNR compared with the more usual Michelson configuration, the use of optical circulators and balanced detection can ensure an SNR comparable with that of the corresponding Michelson interferometer.

The possibility of constructing a Fizeau-based system with good SNR is relevant in clinical OCT, since this configuration offers the advantage of "downlead insensitivity", giving it immunity to environmental perturbations, which are likely to occur during in-vivo measurements. The widely used Michelson configuration, can suffer from polarization-induced signal fading under similar conditions.

4.5.2 Analysis of practical issues with processing interferometers for balanced detection

Even though in-fibre configurations can provide very compact and portable systems, they can suffer from dispersion in the fibre and phase changes due to temperature fluctuations and fibre stretching. Free space configurations enable to minimise these and they can be compact employing micro-bench elements to hold the optical components.

An alternative to the MZPI is the Fabry-Perot processing interferometer (FPPI) is shown in figure (3-10-a). The light is reflected and transmitted inside the cavity made by two semi-reflecting mirrors, and the light is detected at the output of the cavity. One of the mirrors is moved to change the optical path difference. The anti-phase signal goes through the Optical circulator (OC). Its efficiency is low, compared to the Michelson processing interferometer (MPI) (Rao et al. 1993), and the best efficiency is obtained for a specific partial reflective mirror.

It requires the use of the fourth port of the OC to implement balanced detection, similar as for the Michelson processing interferometer. In theory, similar SNR should be found for the various balanced Fizeau interferometers. But The FPPI and MPI are not so good in practice for two reasons:

- firstly it is not easy to carry out the alignment, especially recoupling properly the light in the fibre to provide the best efficiency of the balanced detection;
- secondly there are still the beat noise limiting the SNR efficiency and some unwanted reflections or losses from the third port of the circulator in reflection (when the light is sent to the processing interferometer) or in transmission (when the light is focused back in the circulator port).

The optical power incident on both detectors is then not equal and most of the noise is not removed, which means that the system will not be as sensitive as predicted by the theory. The interesting points with the Mach-Zehnder processing interferometer (MZPI) are that the light is sent in transmission through the interferometer and there are two outputs that can be directly sent to the balanced detector.

Table 4-3 summarises the comparison of the characteristics of different PI's.

Table 4-3: Comparison of processing interferometers for the balanced detection implementation

Free space processing interferometers	Fizeau system Detection			
	Single detector		Balanced detection	
	Advantage	Disadvantage	Advantage	Disadvantage
MPI	Easy to set-up	Low SNR	It does not need a lot of components	Not proper balanced detection And not easy to align
FPPI		Lowest efficiency	It does not need a lot of components	Not proper balanced detection
MZPI	Same efficiency that with MPI		Best efficiency	Not straightforward to align

Reference List

1. Ballif, J., Gianotti, R. and Chavanne, R. (1997) Rapid And Scannable Scans At 21m/s In Optical Low-Coherence Reflectometry. *Optics Letters* **21**, 757-759.

2. Bamford, K., James, J., Barr, H. and Tatam, R.P. (2000) Optical Radar Detection Of Precancerous Bronchial Tissue. *Laser Med. Sci.* **15**, 188-194.

3. Bamford, K.J. (2000) An Investigation Of Optical Radar And Low Coherence Interferometry For The Detection Of Precancerous Tissues. *Ph. D., Cranfield University, School Of Engineering*

4. Bamford, K.J. , James, S.W., Barr, H. and Tatam, R.P. (1999) Optical Coherence Tomography Of Bronchial Tissue. *SPIE* **3858**, 1185-1191.

5. Beddows, R., James, S.W. and Tatam, R.P. (2002) Improved Performance Interferometer Designs For Optical Coherence Tomography. *Optical Fiber Sensors Conference Technical Digest, OFS 2002* **1**, 527-530 .

6. Benford, D.J. , Hunter, T.R. and Phillips, T.G. (1998) Noise Equivalent Power of Background Limited Thermal Detectors at Submillimeter Wavelengths. *International Journal of Infrared and Millimeter Waves* **19**,

7. Everett, M., Schoenenberger, K. and Colston, B. (1998) Birefringence Characterization of Biological Tissue By Use Of Optical Coherence Tomography. *Optics Letters* **23**, 228-230.

8. Frosz, M.H., Juhl, M. and Lang, M.H. (2001) Risø National Laboratory, Roskilde, Denmark.

9. Hawker, S., Soanes, C. and Spooner, A. (2001) Oxford Dictionary, Thesaurus, and WordPower Guide. 2Rev Edition edn, 978-0-19-860573-3.

10. Hui, R., Thomas, J., Allen, C., Fu, B. and Gao, S. (2003) Low-Coherent WDM Reflectometry For Accurate Fiber Length Monitoring. *IEEE Photonics*

Technology Letters **15**.

11. Izatt, J.A., Kulkarni, D., Wang, H.-W., Kobayaski, D. and Sivak, M.V.J. (1996) Optical Coherence Tomography And Microscopy In Gastrointestinal Tissues. *IEEE Journal Of Selected Topics In Quantum Electronics* **2**, 1017-1028.

12. Kersey, D. A. and Dandridge, A. Dual-Wavelength approach To Interferometric Sensing. Proc. SPIE. 798, 176-181. 87.

13. Naci Inci, M., Kidd, S.R., Barton, J.S. and Jones, J.D.C. (1992) Fabrication Of Single-Mode Fibre Optic Fabry-Pérot Interferometers Using Fusion Spliced Titanium Dioxide Optical Coatings. *Meas. Sci. Technol.* **7**, 678-684.

14. Oliver, B.M. (1961) Signal-To-Noise Ratios In Photoelectric Mixing. *Proc. IRE* **49**.

15. Podoleanu, A.Gh., Rogers, J.A. and Jackson, D.A. (2000) Three Dimensional OCT Images From Retina And Skin. *Optics Express* **7**, 292--298

16. Qu, J., MacAulay, C., Lam, S. and Palcic, B. (1995) Laser Induced Fluorescence Spectroscopy At Endoscopy: Tissue Optics; Monte Carlo Modelling And *In Vivo* Measurements. *Journal Of Optical Engineering* **34**, 3334-3343.

17. Rao, Y., Webb, D. and Jackson, D. (1993) Design Study Of Fibre-Optic Based Fabry-Perot Type Interferometric Sensors Using Low-Coherence Signal Recovery. *SPIE: Fiber Optic And Laser Sensors XI* **2070**.

18. Rollins, A. and Izatt, J.A. (2000) SNR Analysis of Conventional and Optimal Fiber-Optic Low-Coherence Interferometer Topologies. *Proceedings of SPIE* **3915**, 60-67.

19. Rollins, A.M. and Izatt, J.A. (1999) Optimal Interferometer Designs For Optical Coherence Tomography. *Optics Letters* **24**, 1484-1486.

20. Schmitt Joseph M. (1999) Optical Coherence Tomography: A Review . *IEEE Journal Of Selected Topics In Quantum Electronics* **5**, 1205-1215.

21. Takada, K. (1998) Noise In Optical Low-Coherence Reflectometry. *IEEE Journal Of Quantum Electronics* **34**,

22. Tearney, G.J., Bouma, B.E. and Fujimoto, J.G. (1997) High-Speed Phase- And Group-Delay Scanning With A Grating-Based Phase Control Delay Line. *Optics Letters* **22**, 1811-1813.

23. Utzinger, U. and Richards-Kortum, R.R. (2003) Fiber Optic Probes For Biomedical Optical Spectroscopy. *Journal Of Biomedical Optics* **8**, 121-147.

5 Experimental investigation of fibre Fizeau OCT

5.1 Introduction

The basic Fizeau interferometer configuration for OCT application, figure 2-13, has been reported by Bamford (Bamford, 2000), employing a 3 dB directional coupler, a Michelson processing interferometer, a lock-in amplifier and a low noise amplifier (LNA). The advantages and disadvantages have been discussed in section 2.3.1. The efficiency of the use of light can be improved by incorporating an optical circulator: it is a passive component enabling light to pass with low power loss from a first port (Port 1) to a second port (Port 2), the light going in port 2 to port 3, and so on, as shown in figure 5-1, and minimising losses between consecutive ports.

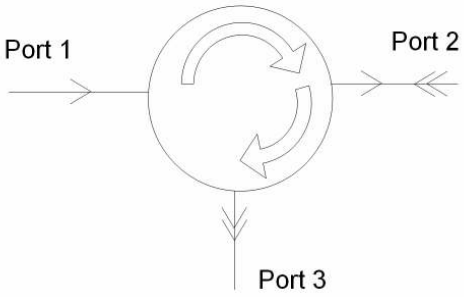

Figure 5-1: general optical circulator: an optical circulator is a passive non-reciprocal device in which light from port 1 is directed to port 2 and light coming in port 2 is directed to port 3 and so on

This chapter describes the preliminary experimental set-up and processes that have been used to investigate the feasibility of the unbalanced Fizeau configuration with an optical circulator. Preliminary experimental results are provided showing that the Fizeau configuration with an optical circulator can be used as an OCT system. This configuration is shown to have a similar SNR to the standard Fizeau configuration, but lower than the Michelson interferometer (chapter 4). It may be improved by implementing a balanced detection arrangement.

Chapter 4 has shown that no significant improvement would be obtained in the Standard Fizeau configuration by replacing the directional coupler with the optical circulator. The Fizeau configuration requires a processing interferometer (or remote interferometer): the optical path in the sensing interferometer (8.5 cm in the system) is much longer than the coherence length of the source and it is not possible to perform direct detection (a too large electronic bandwidth would be necessary). The processing interferometer has a path length imbalance matching the optical path difference in the sensing interferometer. In this chapter, the implementation of a suitable processing interferometer to carry out balanced detection is discussed in order to optimise the SNR. The chapter deals also with the choice of the optical components to get the best efficiency.

Then a discussion is provided giving reasons for the choice of the processing interferometer. The electronic instrumentation applied to the Fizeau configuration is also described and discussed to investigate the best efficiency. Finally transparent and turbid samples have been imaged using the system.

5.2 Configuration using single detector

5.2.1 Experimental arrangement

The experimental set-up is given in figure 5-2.
A 4-port polarisation insensitive optical circulator from AOC technologies, Inc (CIR-4-155-09-FC/UPC) is employed and only ports 1 to 3 are used as depicted in figure 5-2. Light from a broadband source from an SLD (model: Opto Speed SLED1550D5A, λ = 1550 nm, $\Delta\lambda$ = 40 nm, Maximum power: 2.5 mW) is directed to the sensing interferometer made by the cavity between the end of the fibre and the interfaces within the sample.

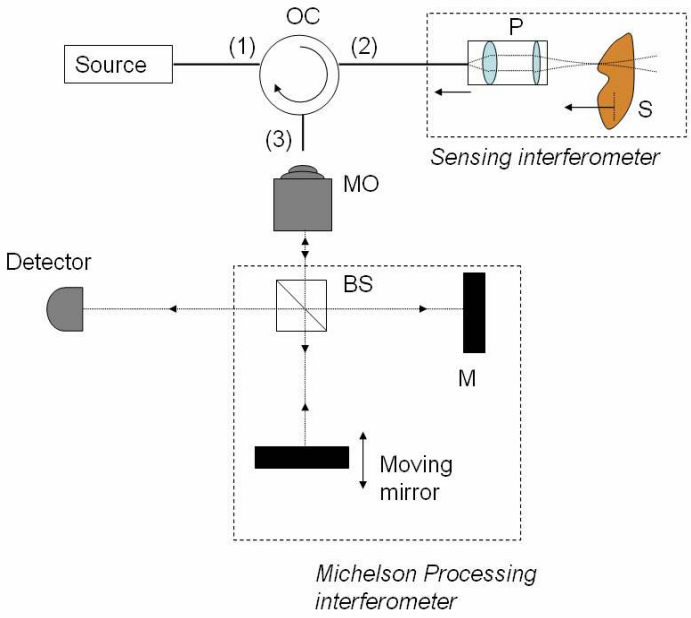

Figure 5-2: single detector Fizeau-based optical coherence tomography system; OC: optical circulator, P : probe, S: sample, MO: microscope objective, BS: beam splitter, M: mirror; (1), (2) and (3) are the ports of the optical circulator

Both reflections, at the end of the fibre and from the different refractive index discontinuities, are directed to the Michelson processing interferometer where each component is split into two further components, and after reflection at the mirrors they will recombine at the beam splitter, and the signal is detected by the detector (Hamamatsu G8376-03 PIN InGaAs photodiode) (Hamamatsu photonics K. K., 2004).
A probe was designed and employed to focus the light onto the sample. The aim was to achieve a transversal resolution of the order of the coherence length. Its principle and design is shown in figure 5-3.

The diameter d_1 of the collimated beam is equal to:

$$d_1 = 2\,NA \cdot f_1 \qquad \textbf{(5-1)}$$

Having NA = 0.11 and f = 2 cm, the diameter of the collimated beam is 4.4 mm.

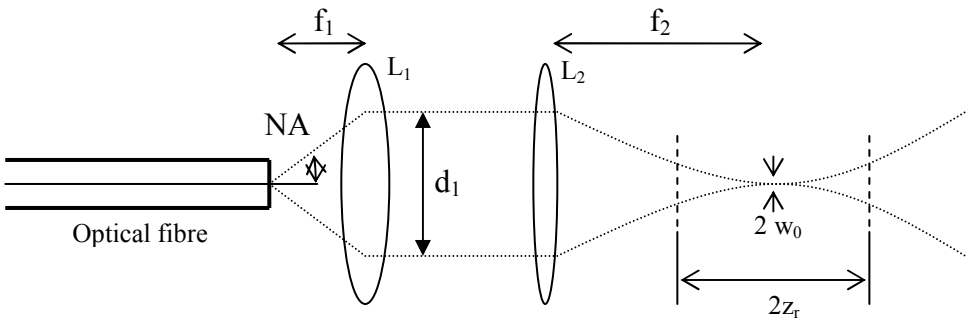

Figure 5-3: Probe design; L_1 and L_2 are two lenses, and w_0 is the is the radius of the $\frac{1}{e^2}$ irradiance contour at the plane where the wavefront is flat, f_1 and f_2 are the focal lengths of L_1 and L_2, z_r: the rayleigh range, NA: the numerical aperture, d_1: diameter of the collimated beam

Melles Griot group (Melles Griot, 1999) provides information for the design considering a Gaussian source. The principal expressions are the diameter and the depth of the focus point. The $\frac{1}{e^2}$ contour radius w(z) after the wave has propagated a distance z:

$$w(z) = w_0 \left(1 + \left(\frac{\lambda z}{\pi w_0^{\,2}} \right)^2 \right)^{0.5}, \qquad \textbf{(5-2)}$$

w_0 is the $\frac{1}{e^2}$ irradiance contour radius at the plane where the wavefront is flat.

From the expressions of the spot size and focal position, it can be found that the diameter of the spot size ($2\,w_0$) at the focus at the focal lens will have a diameter of:

$$\begin{aligned} 2w_0 &= \frac{\lambda f_2}{\pi \omega} \\ &= \frac{\lambda f_2}{\pi d_1} \end{aligned}, \qquad \textbf{(5-3)}$$

w being the radius of the collimated beam.

With f_2 = 4 cm, d_1= 4.4 mm and λ = 1550 nm, the spot size is equal to 4.5 µm.

The transversal resolution Δx (Brezinski and Fujimoto, 1999) is defined as:

$$\Delta x = \frac{4\lambda}{\pi} \cdot \frac{f_2}{d_1}, \quad \textbf{(5-4)}$$

where d_1 is the diameter of the beam on the L_2 lens and f is its focal length. The transverse resolution is equal to 18 μm. Combining equations 5-1 and 5-4, the focal lengths f_1 and f_2 can be found.

Finally, the definition of the depth of focus varies between users. A typical expression is:

$$\Delta z = 2 z_r = \frac{\pi (\Delta x)^2}{2\lambda} \quad \textbf{(5-5)}$$

With Δx = 18 μm and λ = 1550 nm, the depth is equal to 0.34 mm.

A standard microscope objective collimated the beam at the output of the third port of the OC. In chapter 2, results have been shown on the improvement of the depth imaging with near-IR wavelength. 1550 nm-wavelength is a telecommunication wavelength and is the wavelength used in the project. The optical path in the interferometer is changed by mounting one of the mirrors on a translation stage driven by a Physik Instrumente step-by-step positioning motor PI M-155.11 at 0.2 mms^{-1} and the acquisition is carried out every 50 nm. The movement of the motor is controlled by means of a C842.20 board and a Labview™ program. The frequency of the detected signal was 200 Hz.

This C842.20 card does not allow data acquisition and the control of the stage at the same time: the clock in the card essentially gives the priority to the movement of the stage and acquisition takes place during the time that the stage is stationary. This implies that the stage is moved for the required distance, and the signal observed is just corresponding to one point and not a scan. This explains why a step-by-step acquisition was done and this takes longer.

This was overcome by replacing the C842.20 card by a C843.20 card: it enabled to carry out the acquisition and the movement of the stage simultaneously.

5.2.2 Instrumentation

An InGaAs photodiode is inserted in an amplifier electronic circuit; the gain is adjusted to ensure that the detector does not saturate when a mirror is used as a sample and to give the maximum voltage when a longitudinal scan is carried out.

In order to reduce noise in the detected signal, a band pass filter is applied to the signal, before digitisation by the acquisition card, by means of a low-noise amplifier (LNA) (Stanford 560). The band pass setting is 100-300 Hz (encompassing the expected frequency of the signal).

5.2.3 Experimental samples

OCT produces localised interferences, with a resolution depending on the properties of the source. The coherence length or axial resolution was found by placing a mirror as a sample at the focal plane of the probe. Scanning the mirror in the processing interferometer, interference fringes are observed when the optical path (OP) difference in the processing interferometer is equal to the OP in the sensing interferometer. The properties of the source can also be determined with an optical spectrum analyser.

As for most of the OCT developments described in this thesis, the Fizeau interferometer (FI) with a Michelson processing interferometer (MPI) has first been employed on a microscope-slide refractive-index microscope-slide (MS-RIO-MS) sample. The microscope slides (MS) have a thickness of 1 mm and a small gap is created by gluing a tape between both MS. Several MS-RIO-MS samples are made with oils of different refractive index from Cargille Industry. Refractive index oils (RIO) are available from a range of 1.4 to 1.7, with an accuracy of ± 0.0002. The sample is then positioned and clamped by a sample holder. This experiment is similar to Bamford's (Bamford, 2000). Scans on the different samples are carried out. The low-noise amplifier (LNA) is not used in these experiments. Other examples of samples used are given in the next chapter.

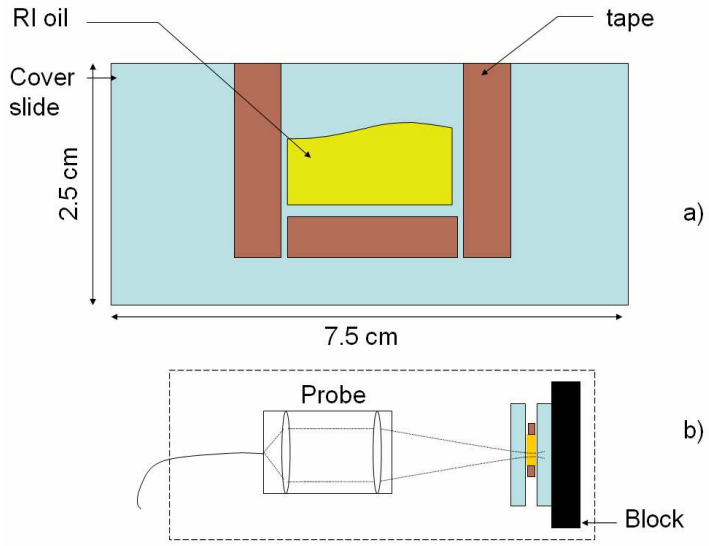

Figure 5-4: Glass-oil-glass sample

The analysis of the SNR has shown that balanced detection improve the SNR (chapter 4), however it is limited due to the presence of beat noise. The next section will discuss a preliminary test using a Fizeau interferometer with an optical circulator and MZPI.

The MZPI, as presented in figure (3-7-c), does not make use of all the light, and this degrades the SNR of the system. This can be improved by replacing the beam splitter by a right angle prism element and mirror, as shown in figure 5-5.

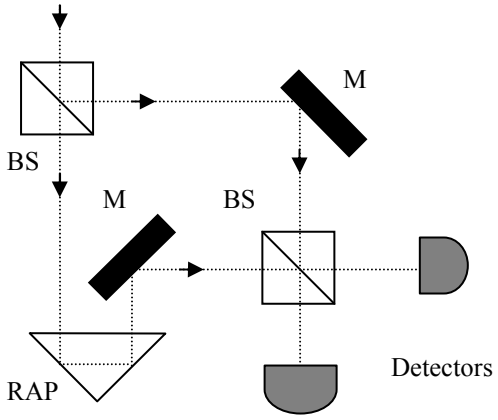

Figure 5-5: Modified MZPI; BS: beam splitter, M: mirror, RAP: right angle prism

The light is split by the beam splitter and both beams pass through each arm of the interferometer.

5.3 Preliminary balanced Fizeau configuration with MZPI

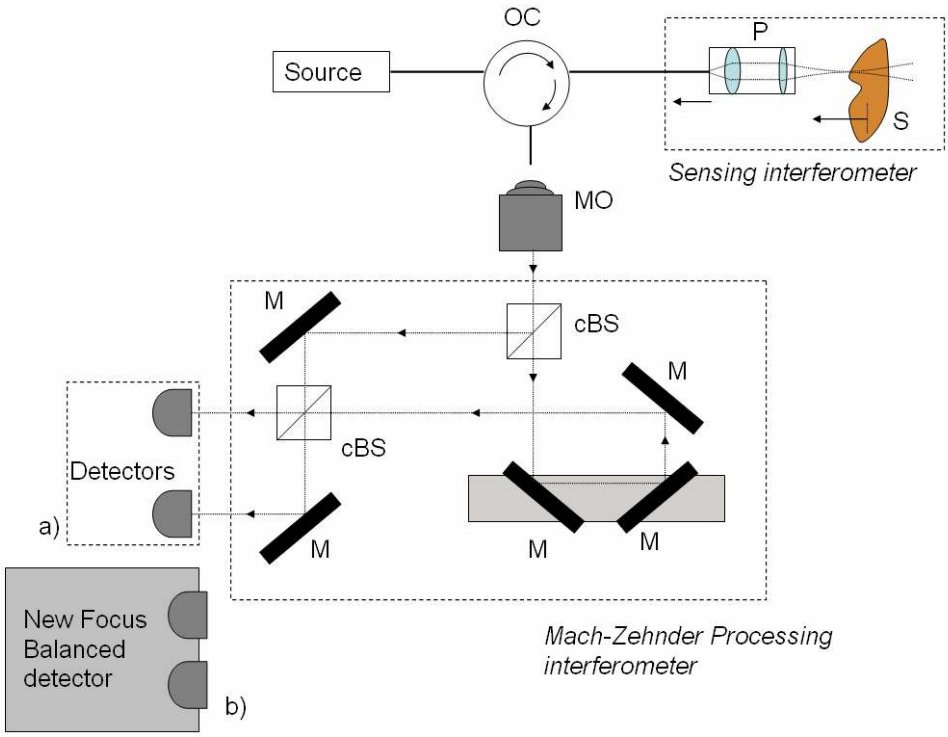

Figure 5-6: Experimental balanced Fizeau configuration with an optical circulator; OC: optical circulator, P: probe, S: sample, MO: microscope objective, cBS: cubic beam splitter, M: mirror

5.3.1 Set-up

To carry out balanced detection correctly, the same amount of power must reach both detectors. From the previous analysis the MZPI enables two anti-phase signals when applied to the Fizeau interferometer with conventional components (standard microscope objectives (MO) and cubic beam splitter (cBS)).

The light from the source is directed to the sensing interferometer and both the reference and the sample beams are directed to the MZPI. The light is collimated by means of MO and each component is split in two parts by the cBS which follow each arm of the MZPI and recombine at the second cBS. Two mirrors are mounted on the stage to carry out a similar action as the right angle prism.

5.3.2 Instrumentation

By analogy to the Fizeau interferometer with the Michelson processing interferometer (MPI), a none continuous acquisition was used. The only modification comes by using a New Focus model-2017 125 kHz balanced photoreceiver to collect both output of the MZPI. The balanced photoreceiver carries out the subtraction between the two signals that are in anti-phase: excess noise is reduced and signal amplitude is doubled. The LNA has the same settings and the stage is moved at the same speed.

5.3.3 Experimental test

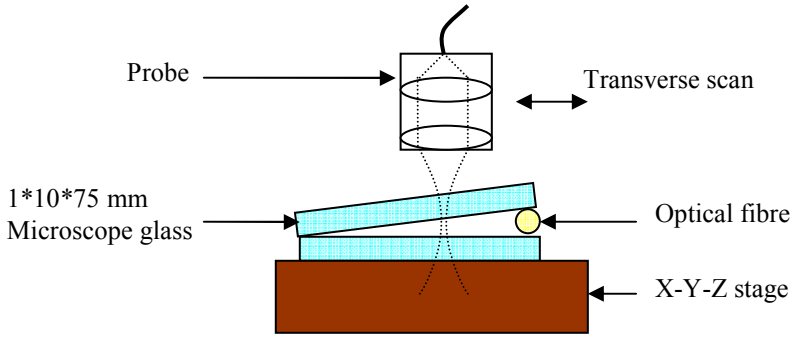

Figure 5-7: Air corner made of microscope slides

An air gap is produced by positioning an optical fibre between two clean 1 mm-thickness microscope glass slides creating a wedge angle of 0.8º (figure 5-7).
The probe design provides 30 µm transverse resolution and it was moved transversally every 30 µm after each longitudinal scan to create a cross-sectional image of the sample.

The MO contains anti-reflection coatings on its optics that may not be suitable for near-IR operation. The cubic beam splitters (cBSs) are polarisation-dependent broadband components. The source wavelength components may not be split by the same ratio. Podoleanu *et al.* has shown that the SNR can be affected by the spectral splitting efficiency of the components (Carmelo Rosa and Podoleanu, 2004).

5.4 Optimisation of the balanced Fizeau configuration

5.4.1 System components

The MO is replaced by a fibre-connected GRIN (Gradient Index) lens (LPC-01-1300/1550-9/125-S-0.4-1.81GR-40-3S-3-1) from Ozoptics, which provides a 0.4 mm diameter collimated beam.

The system is mounted on Micro-bench elements for good mechanical stability. This eliminates the use of bench components and minimises the size of the system.

The cBSs are replaced by plate BS which are much less polarisation-dependent with an antireflection coating for 1550 nm on one of the facets to reduce potential "ghost" effects (illustrated in figure 5-8).

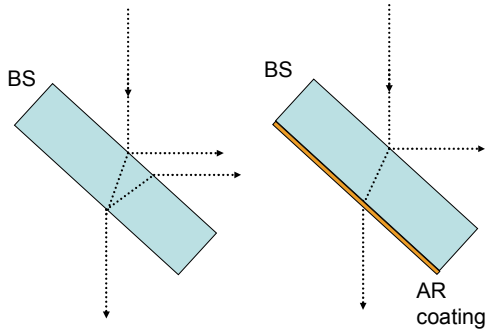

Figure 5-8: Plate beam splitter; without the anti-reflection coating, the light will be first reflected and the transmitted light will be also reflected at the second surface and will be transmitted; the AR coating helps removing the second reflection

The plate beamsplitters and the aluminium and gold mirrors are from Crystran Ltd.

5.4.2 Experimental Set-up

A photograph of the experimental system, incorporating the above modifications, is given in figure 5-9. Figure 5-10 shows the schematic of the experimental arrangement.

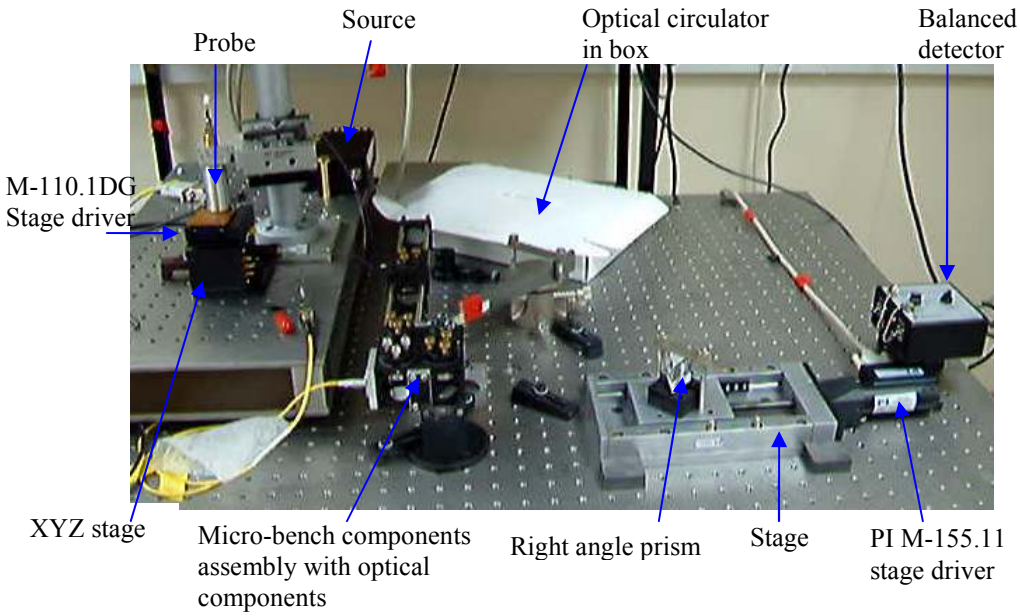

Figure 5-9: experimental system

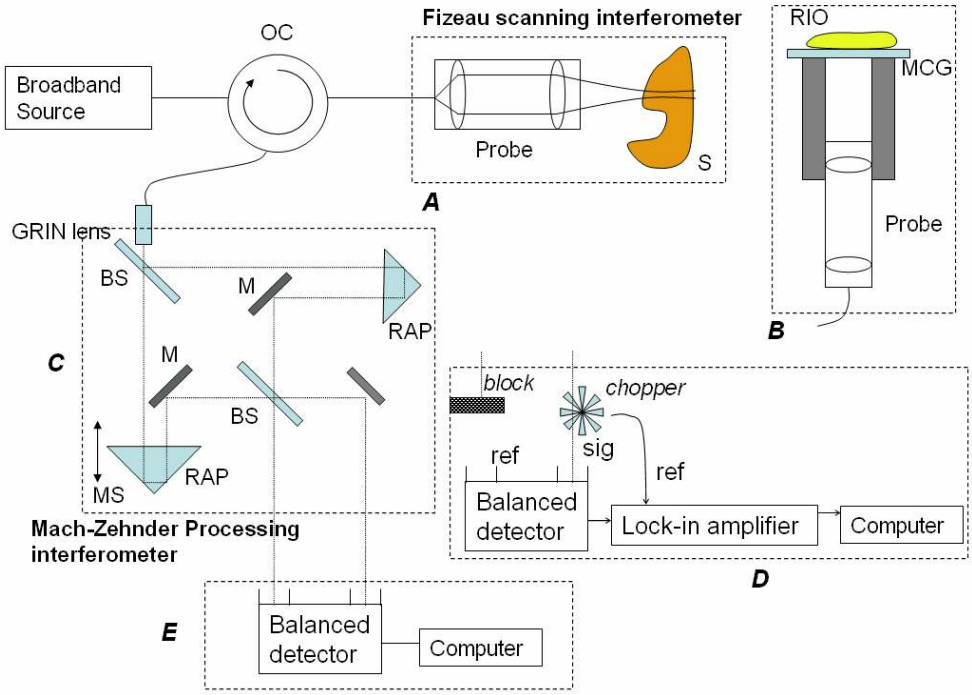

Figure 5-10: Balanced Fizeau configuration; A: sensing interferometer, B: experimental arrangement for SNR investigation, C: Mach-Zehnder processing interferometer, D: set-up when used lock-in detection lock-in amplifier, E: balanced detection carried out with balanced detector; BS: beam splitter, OC: optical circulator, RAP: right angle prism, MS: moving stage, S: sample, RIO: refractive index oil, MCG: microscope cover glass

Light from the source is directed to the Fizeau sensing interferometer. Both reflections, from the end of the fibre and from the different interfaces of the sample, are directed to the MZPI where each component is split in two parts which pass through both arms of the MZPI and recombine at the second BS. The signal is then detected.

5.4.3 Instrumentation

The SNR of a system depends on several parameters. One is the electronic detection bandwidth B. Two balanced detectors, Models-2017 and -1817 from Newfocus, were compared together and also compared with balanced detection carried out with standard InGaAs detectors connected to the two inputs of the LNA (and using a function that enables subtraction of the input signals). Adding a LNA after the model-1817 BP is also investigated.

The lock-in amplification technique can also be used to reduce the noise and should give similar results to the balanced detection (BD). The light beam is chopped at a frequency of 5 kHz. The system is shown in figure (5-10-D). The chopper modulates the signal and, connecting the output voltage of the chopper to the lock-in amplifier reference input allows the signal to be demodulated. This technique removes the DC component of the noise. To allow possible comparison with BD, the Signal photodiode of the model-2017 balanced photoreceiver is employed for the detection. Instead of using both inputs of the balanced photoreceiver, it is set to Signal input and the reference detector is blocked. This means, as the same detector is used in balanced detection and in the lock-in detection, the SNR can be compared.

If the time constant is high, the SNR is high. The problem with such detection is that it requires a low speed scan for a good performance. The time constant was set to 300 ms, and the sensitivity to 300 mV. No additional filtering was applied. The scan speed was 0.2 mms^{-1} for the OCT system.

The detected signal can be acquired directly and displayed on a graph on a PC. This requires a high sampling rate in order to observe most of or all the fringes, and then determine the peak maximum to identify reflecting sites. This takes time and the final results may take a lot of space in memory (especially if 2-D imaging is then carried out). The SNR is achieved by taking the maximum of a range in the interferometric

signal and dividing by the noise floor. If the sampling rate is not properly chosen, or if the acquisition is not fast enough, the maximum value, that the calculation determines, may not be the correct value. A way to reduce the sampling rate and the number of samples is to demodulate the signal. This enables also to reduce the place taken on the PC by each OCT image produced.

5.4.4 Rectifier Based Demodulation

The rectifier-based demodulation of the detected signal consists of removing the carrier fringes to leave only the low frequency envelope. A bulk electronic demodulation system is preferable to a software demodulation in order to carry out a fast acquisition and for the convenience of the OCT system user.

A first order high-pass filter, figure 5-11, is designed to have a cut-off frequency of 8 Hz with a resistor R = 1.2 MΩ and a capacitor C = 0.1 μF. It removes the DC background, while retaining the AC signal for the demodulation.

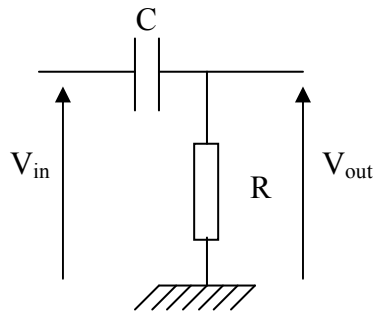

Figure 5-11: high-pass filter

A gain in the range from 100 to 1000 increases the amplitude of the signal (and the noise) before rectification (the rectifier needs a voltage of the order of 0.6-1 V to rectify properly).

The rectification converts negative signals to positive values. The frequency of the signal is then twice the initial frequency. The envelope has a lower frequency and, employing a low-pass filter with a cut-off frequency of 10 Hz, high frequencies are removed from the signal and the fringes disappear, leaving the envelop function.

The SNR of these different techniques were compared to determine which instrumentation would be more appropriate for the OCT application.

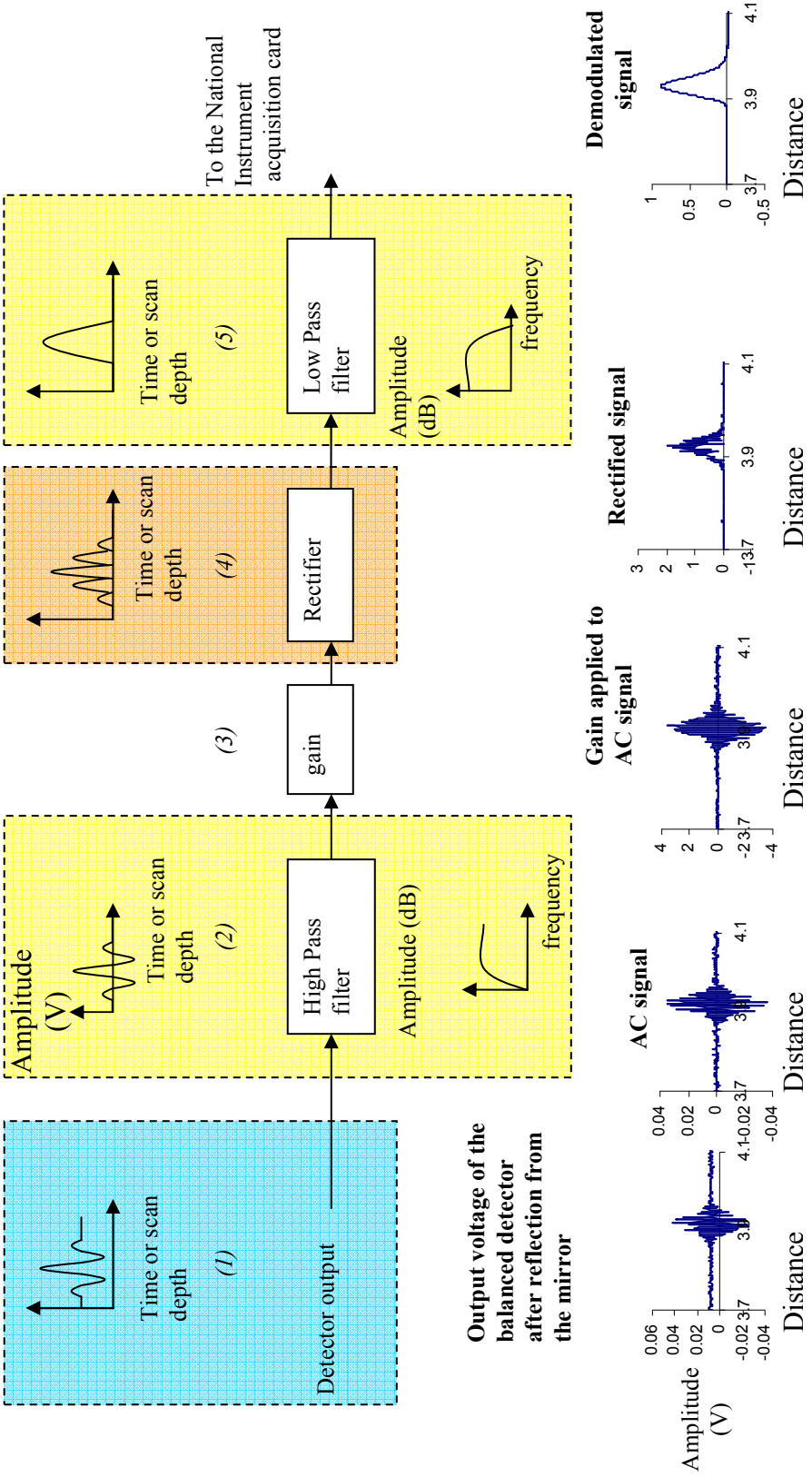

Figure 5-12: Steps in the electronic rectifier demodulation process

5.4.5 Efficiency and SNR of the system

Many studies of SNR have considered values for the reflectivity of the sample (Rollins and Izatt, 2000), (Ford et al. 2005) between 0 and 1. System SNR is usually measured by taking the amplitude of the fringes obtained from the reflection of a mirror, the noise being obtained by blocking the reference arm.

Reference mirror reflectivities are difficult in practice because the optical components required can be expensive: these devices require adapted coatings and anti-reflection coatings.

Bamford (Bamford, 2000) employed several samples made of two 1 mm-thickness microscope slides with a few droplets of oil of known refractive index (Cargille Industry) between them. To ensure accurate measurements all the microscope slides have to have the same amount of RI, the space between the two slides must be equal for all the measurements and the sample must be set-up normal to the incident light within the Rayleigh range of the probe. Finally the thickness between the microscope slides has to be greater than the coherence length of the source and the microscope slides have to be parallel.

In summary, this is another method to check the system sensitivity but it is difficult to make sure that the measurements will be repeatable and reproducible.

A simpler sample employing the same concept is considered as shown in figure 5-13; the probe is vertically positioned and a cylindrical block (in aluminium) is fixed in such way that if a microscope cover slide (MCS) is put on the top it is positioned in the focusing depth (Rayleigh range) of the probe.

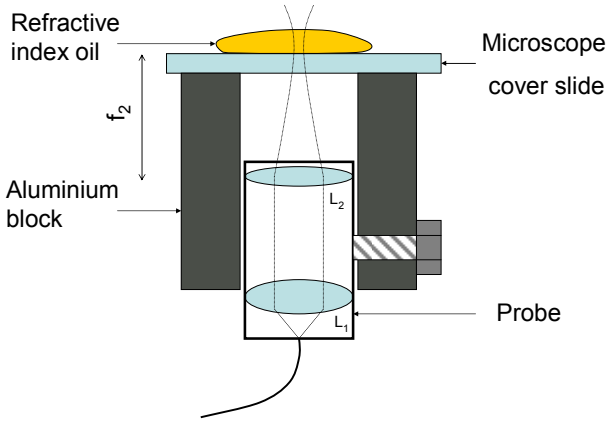

Figure 5-13: sensing interferometer arrangement for sensitivity measurement

The probe has a focusing depth of 0.34 mm, a 0.2 mm thick microscope cover slide (MCS) comprises an appropriate sample. The probe was positioned vertically. The slide is properly set-up when, after having carried out a longitudinal scan, the same peak amplitude is measured for the air-glass and glass-air interfaces.

Droplets of each refractive index oil in the range of 1.400 to 1.700 are deposited in turn on the top of the glass slide.

The glass-oil interface Fresnel reflectivity R_b for nomal incidence is:

$$R_b = \left(\frac{n_g - n_{oil}}{n_g + n_{oil}} \right)^2 \quad \textbf{(5-6)}$$

Where n_g is the refractive index of the glass and n_{oil} is the refractive index of the oil, and the total reflectivity of the sample is the sum of the air-glass and glass-oil interfaces reflectivities (the oil-air reflection is neglected: it is out of the Rayleigh range and the contribution of the specula reflection is small compared with the two others):

$$\begin{aligned} R_s &= R_{air-glass} + R_{glass-oil} \\ &= \left(\frac{n_a - n_g}{n_a + n_g} \right)^2 + \left(\frac{n_g - n_{oil}}{n_g + n_{oil}} \right)^2 \end{aligned} \quad \textbf{(5-7)}$$

In order to compare the experimental measurements and the theory, R_b is used for the determination of the boundary reflectivity under study, which provides I_s (being the mean square photocurrent at the boundary under study), and R_S contributes to I_{dc} (being DC component of the detected signal).

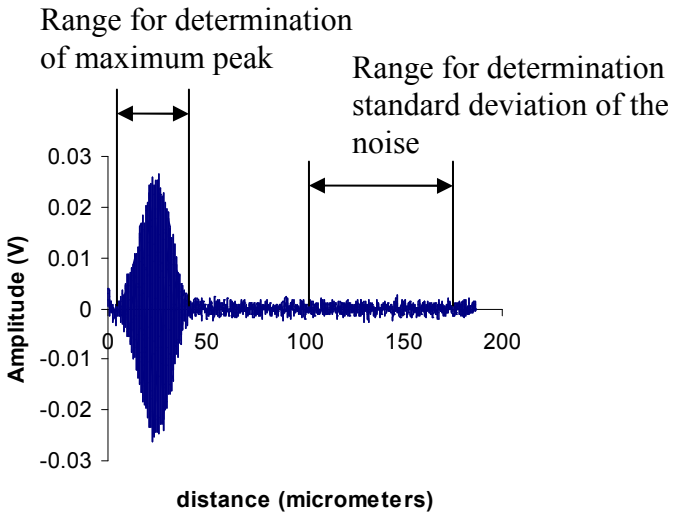

Figure 5-14: Illustration of the measurement of the SNR

After having carried out several scans, a Labview^{TM} program calculates the SNRs from the scans, averages them and the standard deviation is provided. The program also takes an average value of the peak amplitude and its associated standard deviation. The principle of the program is illustrated in figure 5-14. The peak intensity is detected from a selected range including the peak, and the standard deviation of the noise is taken, away from any potential sample boundaries.

The first step for the sensitivity measurement consists of determining the RI of the MCS. The optical thickness OT of the glass is linked to the physical thickness T by:

$$OT = T \cdot n_g, \tag{5-8}$$

Where n_g is the refractive index of the glass. The refractive index is equal to:

$$n_g = \frac{OT}{T}, \tag{5-9}$$

The physical thickness is determined by means of a vernier and, carrying out several scans along the thickness, the optical thickness is found.

Before every measurement of a new RI oil, the cleaning steps for the glass are as follows: most of the oil is removed with distilled water, isopropanol is used to clean the glass, further distilled water, and the MCS is dried employing a lens cleaning tissue.

For each measurement, an RI oil droplet is deposited on the top surface of the MCS as illustrated on figure 5-13 and several scans are taken along the interface, SNR value calculated and its repeatability and uncertainty assessed.

5.4.6 Imaging a variety of experimental samples

Transparent and semi-transparent samples have been considered. A first sample was a droplet of a liquid resin (OG 134) (that is cured under UV irradiation) deposited on a MCS, placed on a second stage. The probe, positioned above the sample, was moved in 30 μm steps for a total length of 4 mm, and by combining the longitudinal scans a 2-D image can be produced.

The same procedure has also been applied to less transparent samples (spring onion and red onion) to characterise the sub-layers.

Finally, a China coffee cup has been used, to represent a turbid sample. A 2-D scan has been produced from the surface, and after having removed the coating and drilled on the surface, a second 2-D image was produced.

5.4.7 Industrial applications

Resins are widely used in composite processing industry. They harden on heating or on irradiation with a UV source. As they change state from liquid to solid, the RI changes too. Fresnel experiments have previously been used to monitor the degree of cure (Buggy et al. 2005).

The idea here is to carry out the same process and observe the curing process via the change of reflectivity at a resin-glass boundary. Having characterised the system response with the position of the MCS, the refractive index of the MCS can be found and, after a few droplets, the refractive index of the resin is found from the sensitivity

measurements. With the Fizeau-based OCT, it is proposed to investigate the possible application on the curing process of the resin.

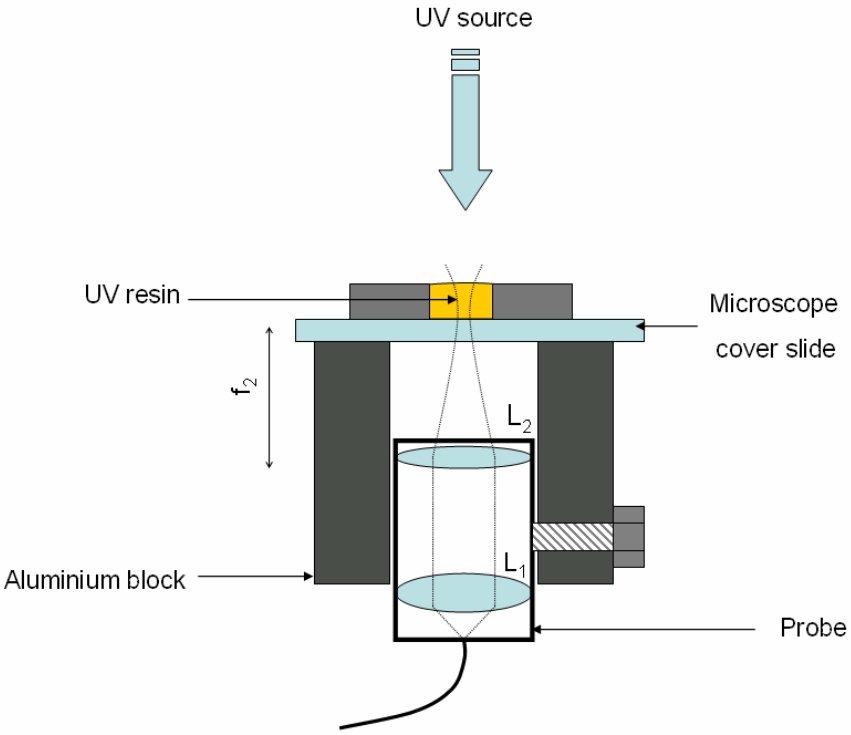

Figure 5-15: UV resin cure set-up

A clean MCS is positioned (as shown in figure 5-15) and before adding the resin, the Labview™ program is run. This allows carrying out several scans of the glass-air interface which is used as reference. The resin is then added and the UV lamp is switched on after a few scans. Several scans are carried out to monitor the 3 hours curing process.

The amplitude and the position of the peak are acquired for the entire duration of the process at a time interval of 2.5 s.

5.5 Summary

Preliminary experiments have been carried out on a single detector Fizeau configuration with an optical circulator.

The different steps of the Fizeau interferometer development have been explained. The systems have been applied to measurements on several samples. The evaluation of the instrumentation and its improvements has been carried out by means of the SNR study.

Transparent and non-transparent samples have been employed to investigate the feasibility. 2-D cross-sectional images have been obtained demonstrating the microstructures, and the results are shown in the next chapter.

Reference List

1. Bamford, K.J. (2000) An Investigation Of Optical Radar And Low Coherence Interferometry For The Detection Of Precancerous Tissues. *Ph. D., Cranfield University, School Of Engineering*

2. Brezinski, M.E. and Fujimoto, J.G. (1999) Optical Coherence Tomography: High-Resolution Imaging In Non-transparent Tissue. *IEEE Journal Of Selected Topics In Quantum Electronics* **5**, 1185-1192.

3. Buggy, S., James, S.W. and Tatam, R.P. (2005) Refractive Index Measurement Using LPGs For Cure Monitoring Applications. *Institute Of Physics, Optical Group, Photonex05*

4. Carmelo Rosa, C. and Podoleanu, A.Gh. (2004) Limitation Of The Achievable Signal-To-Noise Ratio In Optical Coherence Tomography Due To Mismatch Of The Balanced Receiver. *Applied Optics* **43**,

5. Ford, H.D., Beddows, R., Casaubieilh, P. and Tatam, R.P. (2005) Comparative Signal-To-Noise Analysis Of Fibre-Optic Based Optical Coherence Tomography systems. *Journal of Modern Optics* **52**, 1965-1979.

6. Hamamatsu photonics K. K., S.S.D. (2004) InGaAs PIN Photodiode G8376 Series Standard Type.

7. Melles Griot (1999) Gaussian Beam Optics. *The Practical Application Of Light*, pp. 2.1-2.12.

8. Rollins, A. and Izatt, J.A. (2000) SNR Analysis of Conventional and Optimal Fiber-Optic Low-Coherence Interferometer Topologies. *Proceedings of SPIE* **3915**, 60-67.

6 Results and Interpretations

6.1 Introduction

Chapter 5 established the different steps of the experimental investigation of the Fizeau interferometer.

Experimentally, it has been first proposed to set-up and get results from the configuration with the optical circulator and a single detector (chapter 5). The configuration was then modified to allow balanced detection. Finally it was proposed to add electronic demodulation.

This chapter presents the results from transparent and non-transparent samples that have been used in the development of the FI for OCT application.

6.2 Preliminary results

The results in this section were all obtained using the Fizeau configuration, employing an optical circulator and a single detector (figure 5-2).

A 1550 nm-wavelength source was used with a FWHM of 60 nm (Opto Speed, 2002). Figure (6-1-a) gives the measured optical spectrum, which provides a theoretical axial resolution of 21 μm in air. By placing a mirror at the focusing plane of the probe (figure (6-1-b)), the auto correlation of the source is found from which the axial resolution is found to be 21 ±0.002 μm. The axial resolution depends on the refractive index (RI) in a medium, e.g. in most of the literature, the tissue RI is considered equal to 1.4, implying an axial resolution of 15 μm in typical tissue samples.

The interferometric signal observed is a Gaussian modulated by fringes (figure (6-1-c)), which are due to the change of the optical path in the processing interferometer and the optical spectrum is Gaussian.

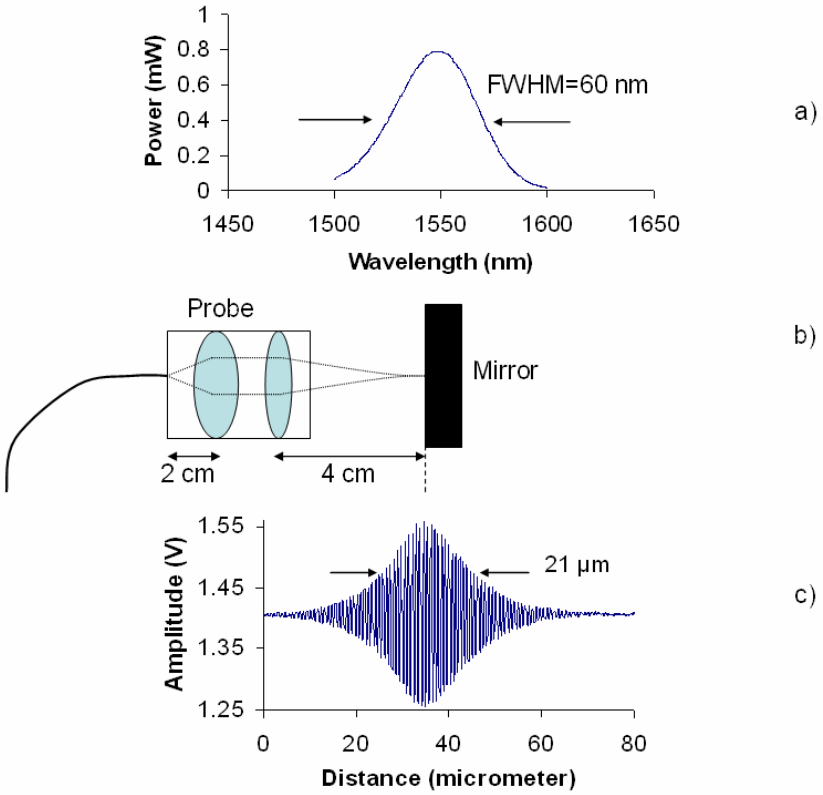

Figure 6-1: Source characterisation: a) optical spectrum of the SLD, b) experimental arrangement of the mirror placed at the focusing plane of the probe and c) the autocorrelation function of the reflection from the mirror

Due to the low-coherence property of the light source, it is expected that at boundaries, delimiting two areas with different optical properties (i.e. the refractive index), a Gaussian signal, modulated by interference fringes, are expected at each boundary. The peak amplitude of this Gaussian signal is dependent on the reflectivity at each boundary.

Several MS-air-MS samples were made (as described in figure 5-4) because it was not possible to remove the RI oil. The refractive index oils (RIO) were inserted in the gap. The sample is positioned to centre the beam focus in the gap, and the mirror in the MPI is scanned. An example of the results is shown in figure 6-2, for oil refractive indices (ORI) of 1.4, 1.5 and 1.7. The peak corresponding to the first air-MS interface is clearly visible, the second and third peaks for 1.4 and 1.7 ORI being the glass-oil interfaces; finally the last group of peaks is the glass-air interface (because there is an

air gap between the glass and the block) and the coatings on the surface on the block. Peaks of oil-glass interfaces were not observed for a range of RIO from 1.45 to 1.55.

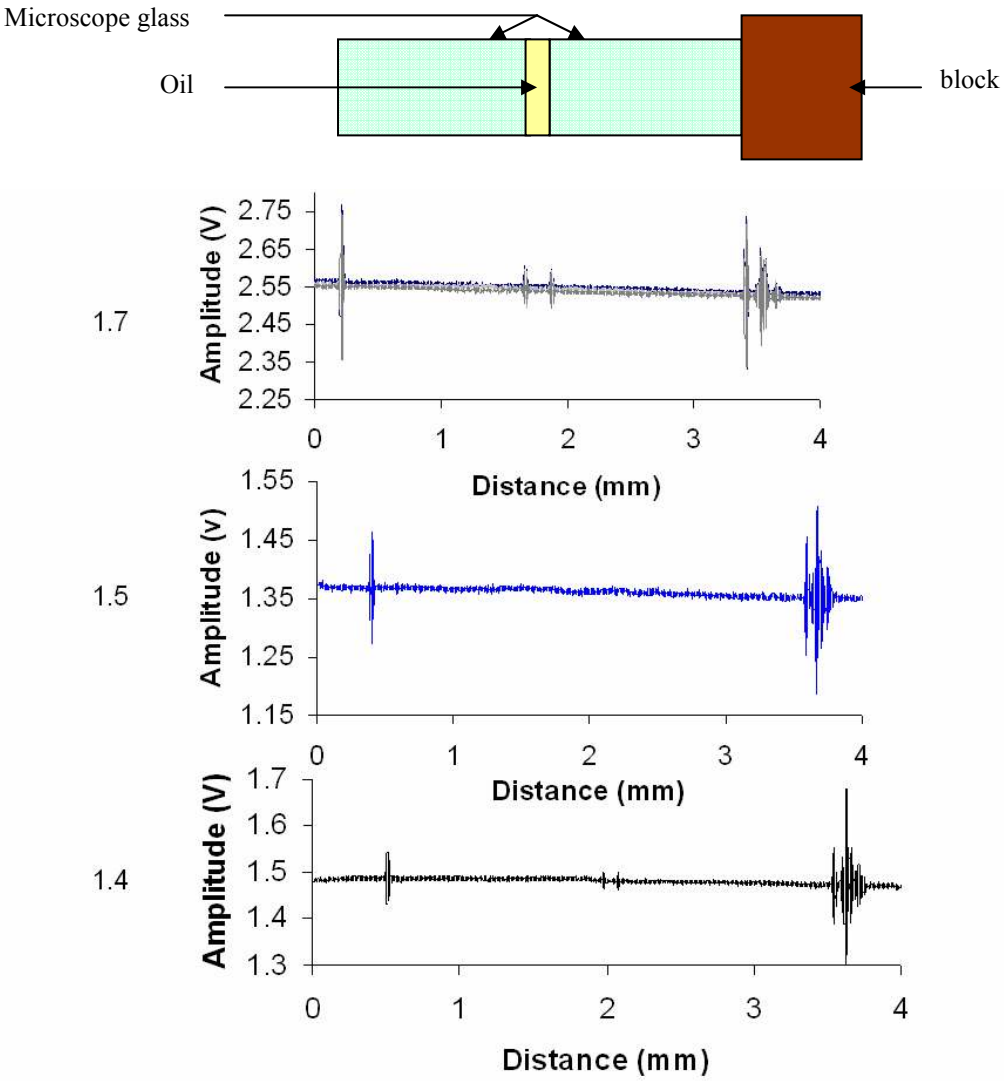

Figure 6-2: block and MS-RIO-MS sample and corresponding longitudinal scans for ORI = 1.7, 1.5 and 1.4

This is mainly due to the oil refractive index being close to the refractive index of the glass (1.502). Tearney *et al.* (Tearney et al. 1995) measured the refractive index of several tissues (dermis: 1.4 ± 0.007, left ventricular muscle: 1.382 ± 0.007, mesenteric adipose 1.467 ± 0.008) using OCT. These samples are scattering tissues and the refractive index difference between each tissue is small. This implies that the single detector FI with MPI has an insufficient SNR for medical applications.

However the results obtained still gave interesting information on the requirements for achieving OCT measurements with a FI. In figure (6-2-b), there is also a good repeatability of the peak position.

In chapter 4, the SNR of the Fizeau configuration was investigated and suggestions were made for possible improvements. In particular, the use of balanced detection was discussed which should improve significantly the SNR of the Fizeau configuration, and these results are provided later in this chapter.

Adding a LNA after the detector, applying the following settings: a gain of $5 \cdot 10^3$ and a filter frequency range of 100-300 Hz (the translation stage has a speed of 0.2 mms^{-1} and a 1 μm step is used between each measurement, this means the data acquisition rate is about 200 Hz), enables us to reduce strongly the noise and to obtain scans of a piece of onion, the side of a hand and a composite fibre coupon. The A-scans are shown in figure 6-3, figure 6-4 and figure 6-5 (an A-scan is a longitudinal scan). At each acquisition step, 10 sample values are taken and averaged.

The hand side has been used as a test sample for two reasons:

- The acquisition speed of the current system is slow: thus, to be able to carry out a proper acquisition, the sample should not move;
- The hand, like the bottom of the feet, has hard skin. Thus four tissue layers may be observed (the stratum corneum has to be taken in account). The interfaces between the layers are rough, which contribute to the scattering of the light.

The result of the acquisition of the hand side is shown in figure 6-3. The histology of the hand is not available, but compared to a general structure diagram of the skin, similarities are observed: the epidermis (with the stratum corneum) and the dermis layers are distinguished. The optical thicknesses are in concordance with values found in literature. The thickness of tissue is different for different people and also depends from which part of the body it is measured (table 6-1) (Brannon, 2005).

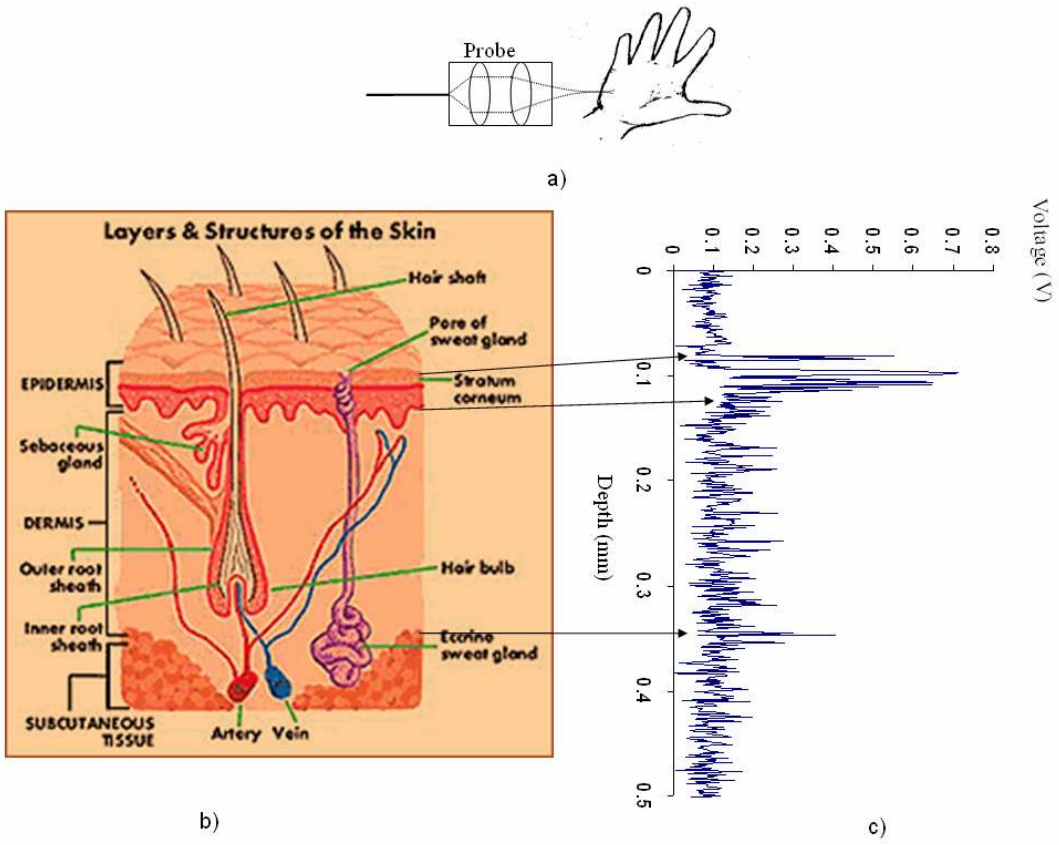

Figure 6-3: a) Position of the hand for the acquisition, b) cross-sectional image of the skin (University of Wisconsin, 2003) and c) the A-scan obtained from the hand side

Table 6-1: epidermis and dermis thicknesses

tissue	Thickness range
Epidermis	0.05 – 1.5 mm
dermis	0.1 – 3 mm

It is the thinnest on the eyelids at 0.05 mm and the thickest on the palms and soles at 1.5 mm. The dermis also varies in thickness depending on the location of the skin. It is 0.3 mm on the eyelid and 3.0 mm on the back.

The scans of the onion have been carried out over 0.8 mm (Figure 6-4). Four boundaries may be found delimiting potential layers or air gap. The onion skin is a transparent tissue. The small variation of refractive index of the boundaries is sufficient to be detected.

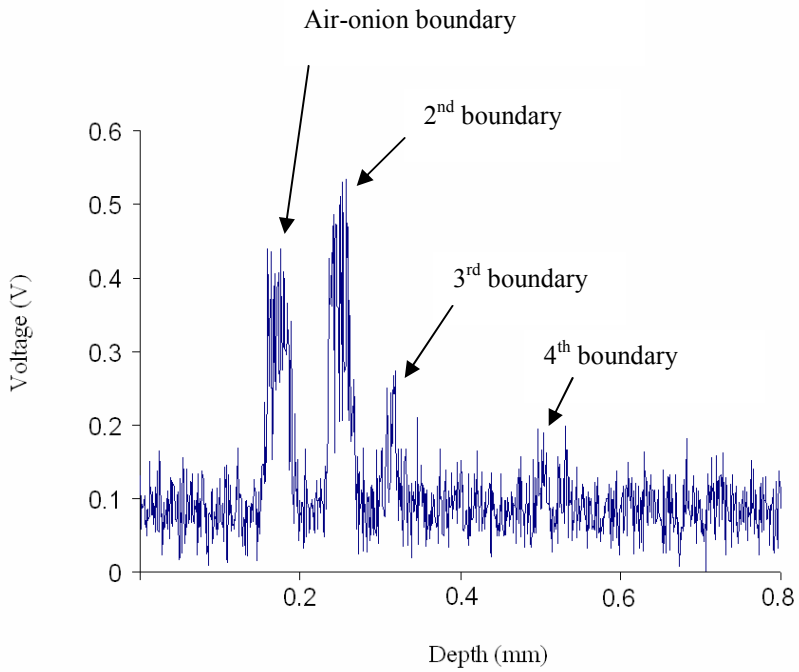

Figure 6-4: A-scan of the onion

The cured composite sample investigated is composed of 8 layers. An image of this sample is on figure (6-5-b). This time the acquisition is carried out every 1 µm to reduce the time of acquisition. The LNA has the sample characteristics as before. Figure (6-5-a) presents an A-scan of the fibre composite sample; this result shows some inhomogeneities inside the sample, represented by the peaks. They are due to local change in optical properties (e.g. RI) and air gaps (especially those with high amplitude).

The results have been obtained with a single InGaAs detector, limiting the sensitivity of observation of the RI change for sets of Refractive index oils. The detected signal, filtered via a LNA, enabled details to be obtained from less transparent, more turbid samples, giving interesting results.

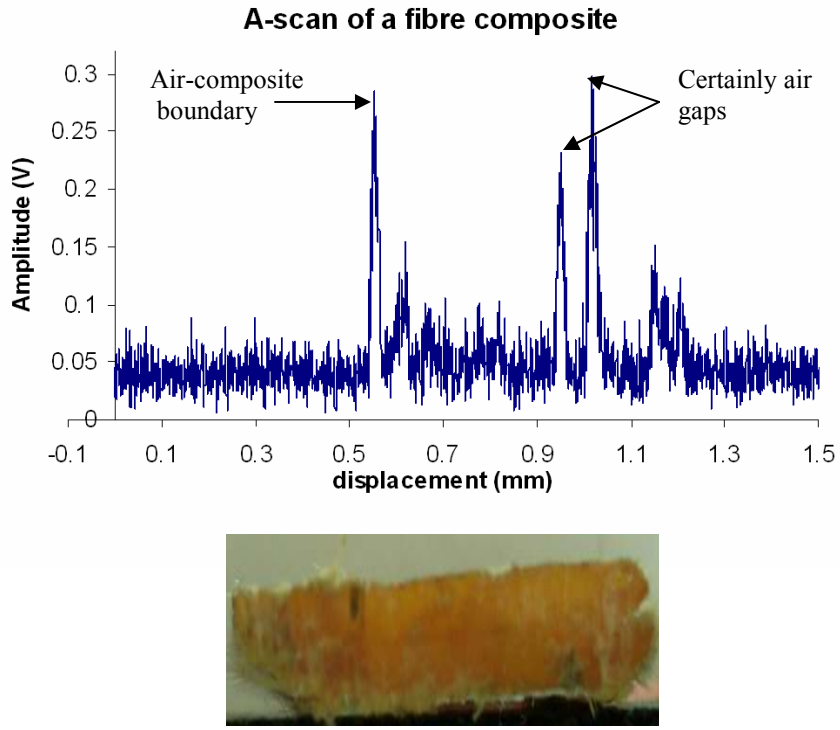

Figure 6-5: a) A-scan of fibre composite, b) fibre composite sample

6.2.1 Limitations

One of the main limitations in the signal is the saturation at the detector and in the acquisition card. It is due to the DC component which accompanies the wanted AC interferometric signal.

In the tests with MS-RIO-MS with several refractive indices, the DC component is expected to be different, due to the reflectivities at the glass-refractive index boundary contributing also to the DC signal which are changing.

For medical applications, the actual acquisition technique used here is very slow. An interesting alternative could be to carry out at the same time the movement of the stage and the acquisition of the signal. The stage could be then moved at a higher speed and the acquisition of the detected signal will be faster.

In chapter 4, it was shown that the SNR of the Fizeau interferometer is not significantly improved with a single detector compared to the standard configuration.

The next section presents the first result obtained from a "prototype" balanced Fizeau interferometer using an optical circulator and a MZPI made with standard optical bench components.

6.3 Balanced detection

The balanced Fizeau configuration using the Michelson processing interferometer and the fourth port of the optical circulator is not useful. It is practically very difficult to couple back all the light to the optical fibre to be sent to the fourth port of the circulator. This means that different spectral intensities reach both detectors which then does not allow to carry out a proper balanced detection. What's more, the excess noise cannot be neglected in both detectors. All noise sources, defined in chapter 4, contribute to reducing the SNR of the system.

The MZPI is investigated for the implementation of the balanced detection (figure 5-7). The balanced photoreceicer was a New Focus Nirvana auto-balanced detector (model: 125 kHz Auto-Balanced photoreceiver). The configuration has been tested on an air corner sample (figure (6-6-a)), and the result is presented in figure (6-6-b).

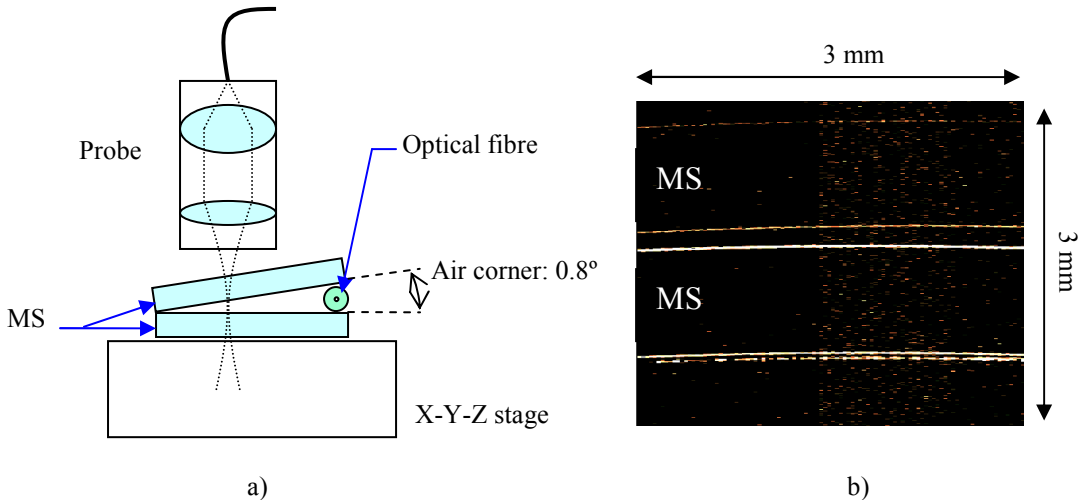

Figure 6-6: a) Sketch of the experimental sample, b) the 2-D scan across the air corner sample; MS: microscope slide

The different boundaries of the sample can be observed, in the air corner area where the probe was focused. The surface of the microscope slides being clean the light is essentially reflected. This is unlike a biological sample, where light from individual scatterers returns in the numerical aperture of the probe. The result enables to resolve the wedge.

This was an application on a transparent sample. Podoleanu *et al.* (Podoleanu et al. 2001) demonstrated that broadband components, having a non-constant spectral splitting ratio, limit the SNR of an OCT system. The cubic beam splitters are broadband optical components and the SNR of the system is not optimised.

As explained in the previous chapters, a balanced detector configuration carries out the subtraction of two signals in antiphase.

At the output of the third port of the optical circulator, a microscope objective was used, which has some antireflection coatings, not ideal for 1550 nm-wavelength; a more appropriate device is required in order to collimate the light and to improve the light efficiency coming back, such as a GRIN lens or a lens with a coating for 1550 nm.

6.4 Balanced detection efficiency

After having replaced the broadband components by 1550 nm-components (GRIN lens to collimate the light and plate beam splitter), the efficiency of the FI with MZPI has been investigated.

The smallest reflectivity that the system can detect gives information of the efficiency of the system and this was investigated. A microscope cover slide (MCS) has been used as a substrate. Before doing any sensitivity measurements, it is important to know the refractive index of the MCS. The physical thickness is found using vernier calipers and the optical thickness can be found carrying out an A-scan of the MCS. Twenty A-scans were carried out: the scan is obtained from a step-by-step acquisition every 84 nm (figure 6-7 provides the result). A good repeatability is found in terms of the amplitude of the peaks and their position. The OT is found equal to 0.24519 mm with an experimental deviation of $1.367 \cdot 10^{-6}$ mm and the physical thickness (T) measured with the vernier calliper is equal to 0.160 mm with an experimental standard deviation of $0.379 \cdot 10^{-6}$ m.

Then the refractive index or group index of the MCS (n_{MCS}) is determined:

$$n_{mes} = \frac{OT}{T} \qquad \textbf{(6-1)}$$

After substituting measured values,

$$n_{MCS} = 1.50 \pm 0.02$$

(in appendix B, the uncertainty calculation is provided).

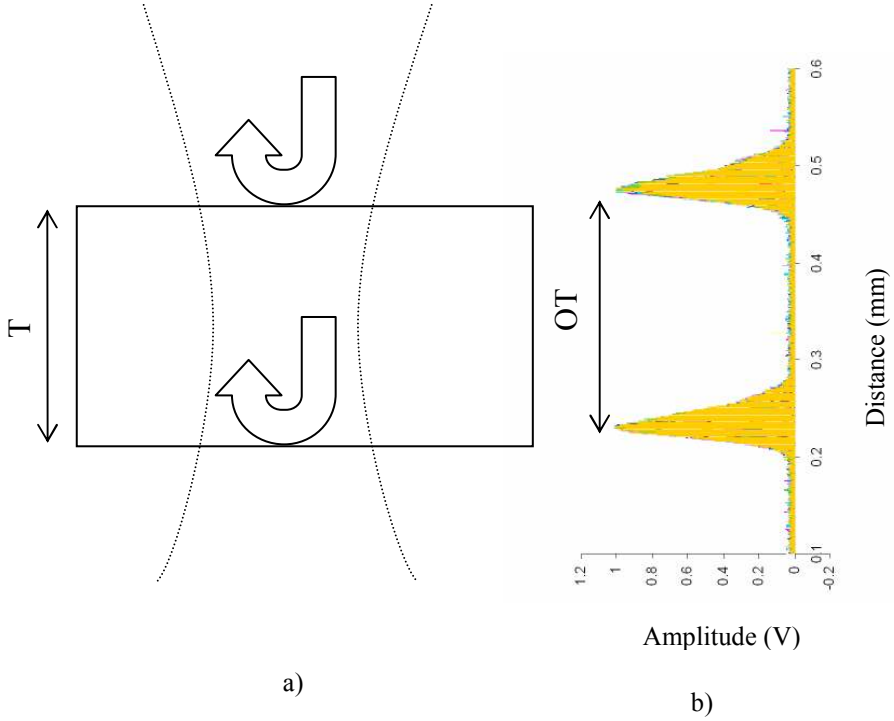

Figure 6-7: a) MCS sketch and b) 20 A-scans of the MCS

From the theory, in chapter 4, the SNR will fall quickly as the reflectivity of the sample tends to 0. To optimise the set-up, the sensitivity to the refractive index change (or reflectivity) at the boundaries of the system has been compared for different instrumentation. Employing the MCS, as a reference sample, and the Cargille Industry RIOs, the results obtained are shown in figures 6-8, 6-9 and 6-10.

To carry out the BD sensitivity measurements the maximum amplitude of the set of fringes is used and this is dependent on the scan rate of the acquisition; this could affect the measurement of the SNR.

When the Model-2017 and -1817 balanced photoreceivers (BP's) are used in the configuration, the SNR is much better with the former of these; it is in part due to a

reduced bandwidth (figure 6-8). It is also specified in model-1817 BP manual (NewFocus, 2003) that in order to detect weaker signal, the model-20X7 or a lock-in amplifier should be used.

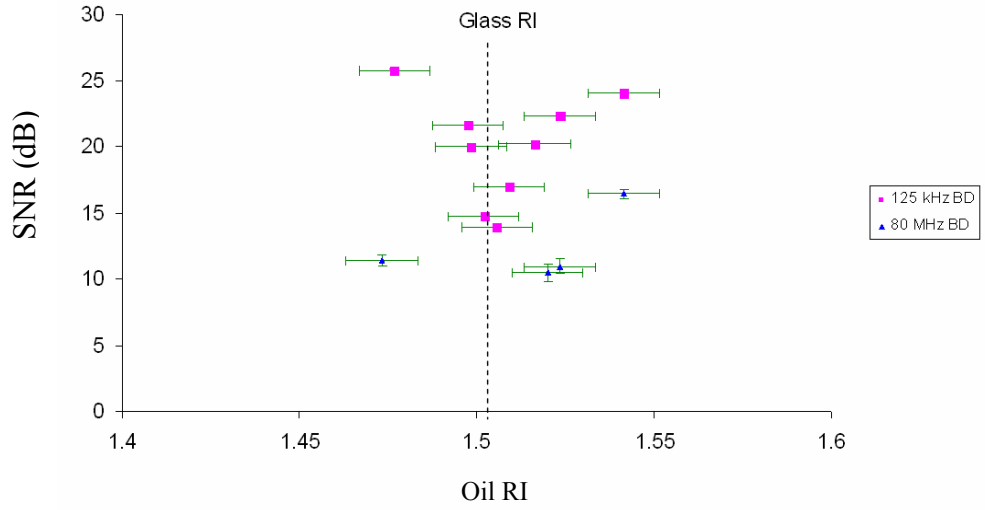

Figure 6-8: SNR evolution of the detected signal using the 125 kHz BD and the 80 MHz BD as a function of the refractive index. The RI error is taken from the data sheet given by Cargille oil manufacturers

Of course, the use of LNA, filtering and applying a gain, after the Model-1817 BP, improves significantly the SNR by about 10 to15 dB (figure 6-9).

The lock-in amplifier (LIA) system did not provide adequate sensitivity; considering the air-glass interface, the SNR was found equal to 25 dB, which is much lower than for the other techniques. Also the sensitivity of the LIA is dependent on the time constant setting: the SNR is better for a long time constant, requiring the acquisition to be carried out as slowly as possible. This implies that an A-scan will take much longer to be obtained. The LIA will not be considered for future application.

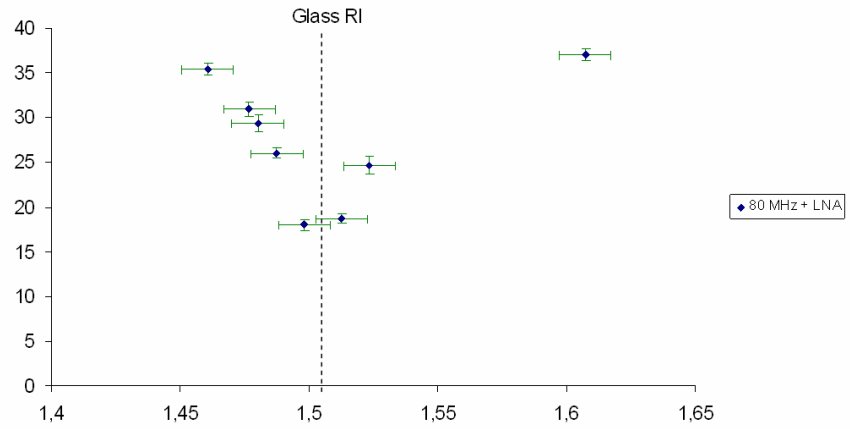

Figure 6-9: SNR evolution of the detected signal using the 80 MHz connected to the LNA

The rectifier based demodulation process described in chapter 5, is a good way to remove the fringes and to detect the maximum peak, making the detection process less dependent on a rapid sampling rate.

The demodulation process enabled the best results for the SNR sensitivity measurement (figure 6-10). Changes in sensitivities were observed for two gains applied in the demodulation. When a gain of 100 is used, the SNR decreased when the MCS-RIO boundary reflectivity decreased. It was difficult to obtain results from 1.404 to 1.600 because the signals were too low. By increasing the gain to 1000, lower reflectivities were detected, mainly when the ORI was near the refractive index of the MCS. A better sensitivity is obtained, however high reflectivities could not be considered due to the overload of the LNAs. For biomedical sample application RI changes are generally small (epidermis: $n_{epidermis} = 1.4$, $n_{dermis} = 1.36$ (Ding et al. 2006)) and the boundaries have rough surfaces, meaning that little light will be scattered and will be collected within the numerical aperture of the probe. The system now has sufficient SNR to make it suitable for turbid samples.

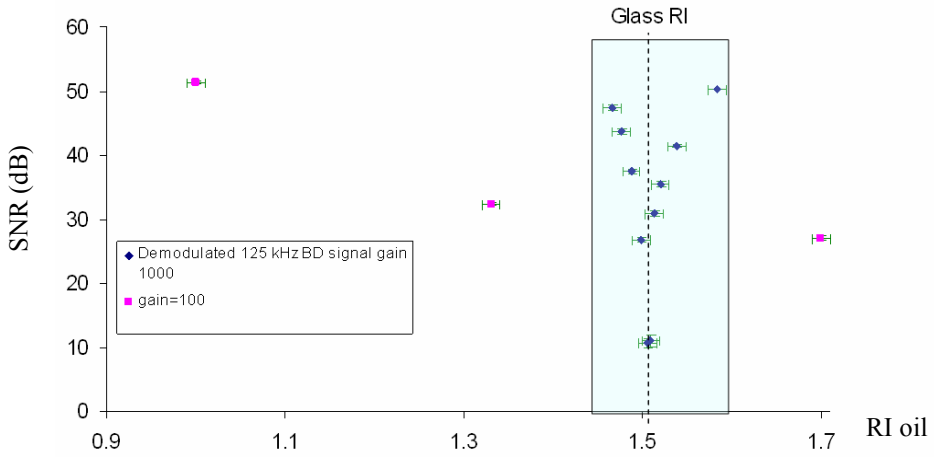

Figure 6-10: SNR of the detected signal from the rectifier based demodulation process with two gains using the 125 kHz BD

The minimum SNR is expected for Rs = 0, meaning when ORI tends to MCS-RI.

When the reflectivity at the glass-oil boundary is small: varying from 0 to 0.4% or 4% (if the air-glass interface is considered), as mentioned for the SNR (dB) graphs (figure 6-6), the change in the detected peak amplitude can be approximated by a linear relationship tending to 0, at the refractive index of the substrate. The results are shown in appendix C. By changing the substrate RI, the plots will be shifted along the RI axis, with a minimum always at the substrate RI.

Finally the reproducibility of the measurements was carried out on the detection of the air-MCS interface. The MCS is positioned at the focusing plane of the probe, scanned, repositioned, and so on. Fifty measurements were taken. The result is shown in figure 6-11.

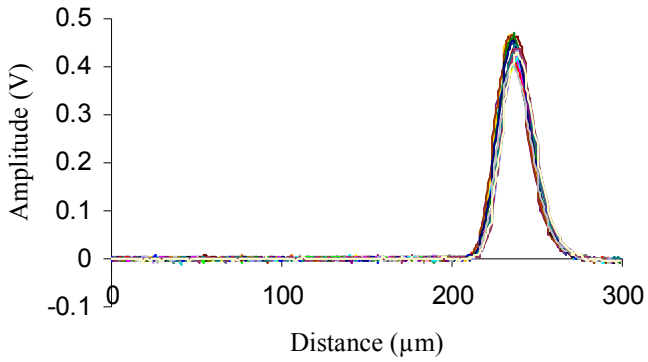

Figure 6-11: Reproducibility test on air-MCS interface

The peak position is at 236 ± 1 µm and the amplitude is 0.44 ± 0.02 V. Then there is a good reproducibility.

6.5 Demonstration of 2-D imaging

6.5.1 Probe efficiency

The arrangement of the MCS and air gaps shown in figure 6-12 was imaged by scanning the stage, as presented in figure (6-12-a), and the result is presented in a 2-D graph in figure (6-12-b). The step size is 30 µm. Figure (6-12-c) is an A-scan where peaks at boundaries can be detected. The 4-MCS sample was moved forward to the direction of the probe, then the position of the peaks moved too, explaining the lines observed at an angle on the OCT image. Figure (6-12-d) presents the evolution of the noise amplitude average for the different scans. Associating figure (6-12-b) and figure (6-12-d) there is a specific position for the focused beam (around the surface) for which several layers can be detected within the Rayleigh range of the beam. The reflection at each boundary has a contribution to the noise.

If many reflections at boundaries are detected, more noise is also detected (figure (6-12-d)). Of course, the biggest peak is for the first air-MCS interface which makes the largest contribution to the dc signal and then the noise. It is noted also that when the beam focus is moved into the sample, the amplitude of the first peak decreases

and more boundaries can be detected. OCT provides localised information, and the probe design enables a focus depth of about 5 mm in this transparent sample. Of course in medical samples and others, scattering and absorption limit the imaging depth.

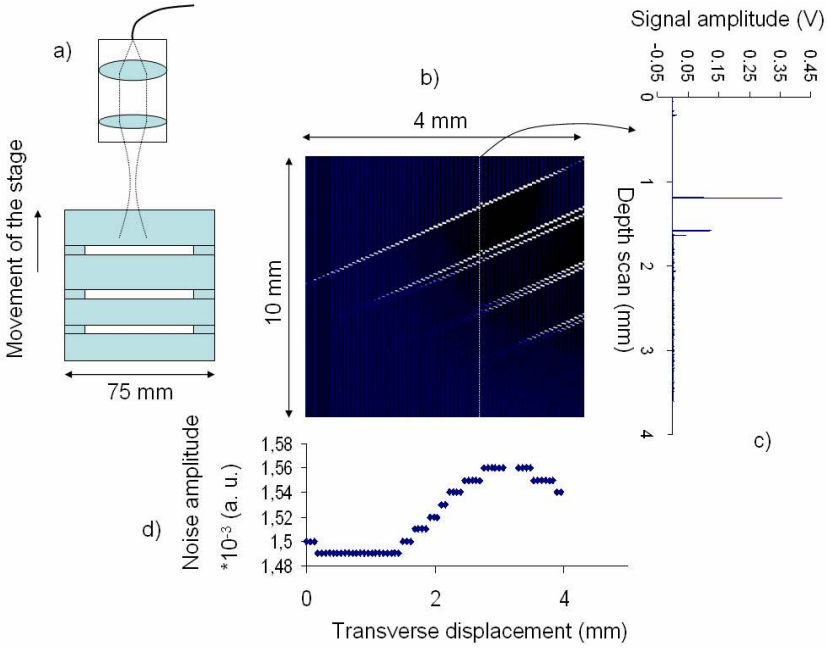

Figure 6-12: a) Sample of 4MCS with an air gap between them: a) sample arrangement, b) Images of the different scans, c) A-scan of the sample and d) noise amplitude in function of the position of the focusing

6.5.2 Cross-sectional images of samples

1-D scans provide depth information. Compiling many longitudinal scans taken for different transverse positions results in 2-D images providing cross-sectional structural details of sample surfaces. A result for the air corner sample has been presented previously. This showed some preliminary results of the balanced Fizeau configuration on a transparent sample.

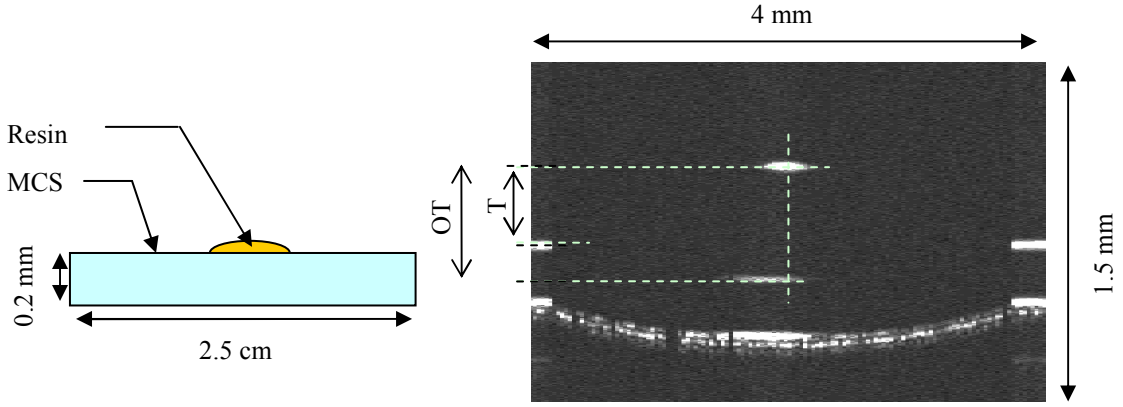

Figure 6-13: a) resin droplet sample and b) 2-D scan

A droplet of resin (OG 134) was deposited on the top surface of a MCS. After having scanned along this sample, the result is presented in figure (6-13-b).

The resin-air interface cannot be clearly distinguished and essentially only the central region of the upper surface is seen. This is due to specular reflections falling outside the numerical aperture of the probe.

The resin-glass boundary appears curved because OCT technology provides a measurement of optical path and not true physical path.

It is specified in chapter 2 that most of the OCT developments were originally carried out for ophthalmology. An example of such a development is the incorporation of adaptive optics, applied in telescopes to minimise atmosphere influences and distortion of the image. The eye is a good subject for this application and it was implemented to reduce distortions caused by the cornea (Zawadzki et al. 2005) on the observed OCT image. Other research groups have used a sample, e.g. tissue on the top of a plane reference surface (Tearney et al. 1995) to determine the refractive index of the tissue. The method could be applied to the OCT image in figure (6-13-b).

The refractive index n_r of the resin can be found by:

$$n_r = \frac{OT}{T} \qquad \textbf{(6-2)}$$

After numerical substitution it is found by this technique that the refractive index of the resin is equal to:

$$n_r = 1.41 \pm 0.08$$

The limitation with the resin droplet is that it is a transparent sample and the curvature of the droplet cannot be observed owing to the specular reflection.

However, the primary interest of OCT applications is for less transparent biological samples. The system has been applied to measurements on spring onion and red onion samples as these have layered structure.

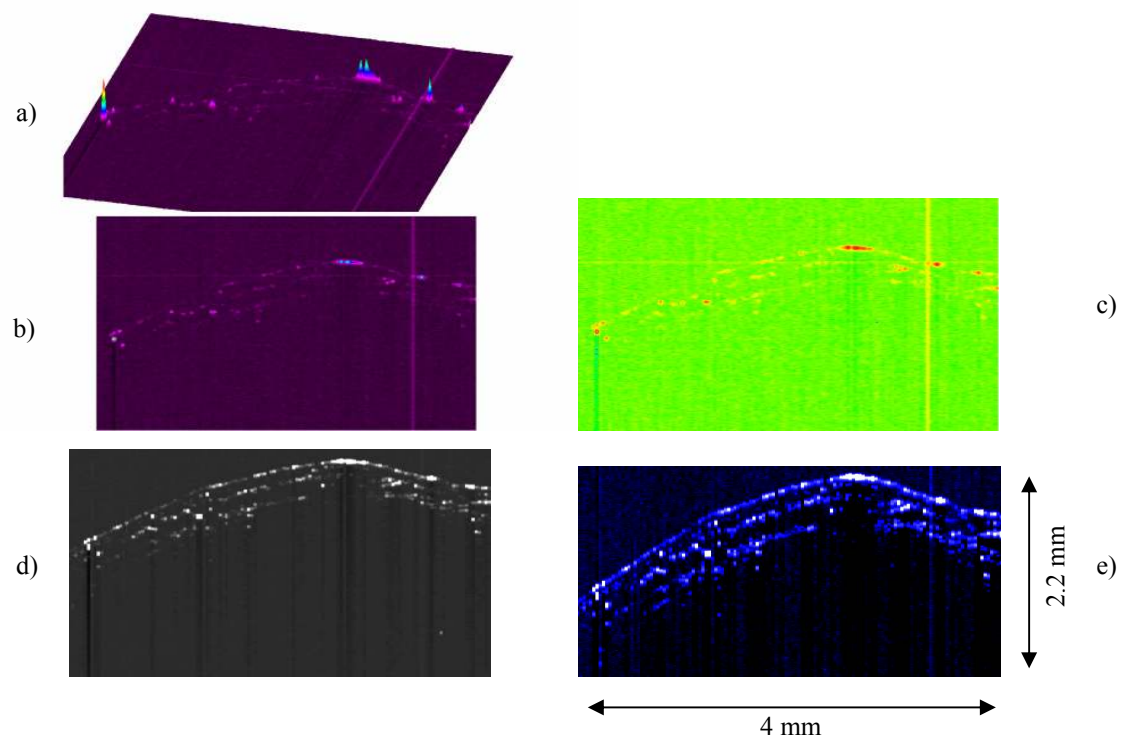

Figure 6-14: several possible presentation of the 2-D data from the spring onion scans; a) and b) obtained using "3-D plot surface plot.vi" (one of the Labview™ tools) in a tilted and in-face display; c) logarithmic display with spectral colour; d) and e) result in grey scale and from blue-white-black colour range

One hundred and thirty-three longitudinal scans have been carried out and compiled to produce the 2-D image. Figure 6-14 presents the results obtained from the spring onion displayed on different ways: figures (6-14-a) and (-b) were obtained from the "3-D surface plot.vi", with a) corresponding to the 3-D view (in relief) obtained by tilting the plane of view, b) corresponding to the 2-D plot from the front view; the spectral false

colour is used. Figure (6-14-c) was obtained by plotting the intensity in dB, employing the expression:

$$I_{dB} = 10 \log\left(\frac{I(z) - I_{min}}{I_{max}}\right) \quad \textbf{(6-3)}$$

Where I_{max}, I_{min} and I(z) are the maximum and minimum values, and the initial 2-D image.

Figure (6-14-e) is the 2-D graph plot obtained from Labview^{TM} (in blue-black-white grade colour) and d) the grey scale 2-D plot. More details are obtained from the grey scale plots and from the 2D blue-black-white grade scale. For comparison, the results are also shown in colour. The spring onion is composed of several thin layers and three layers can be observed.

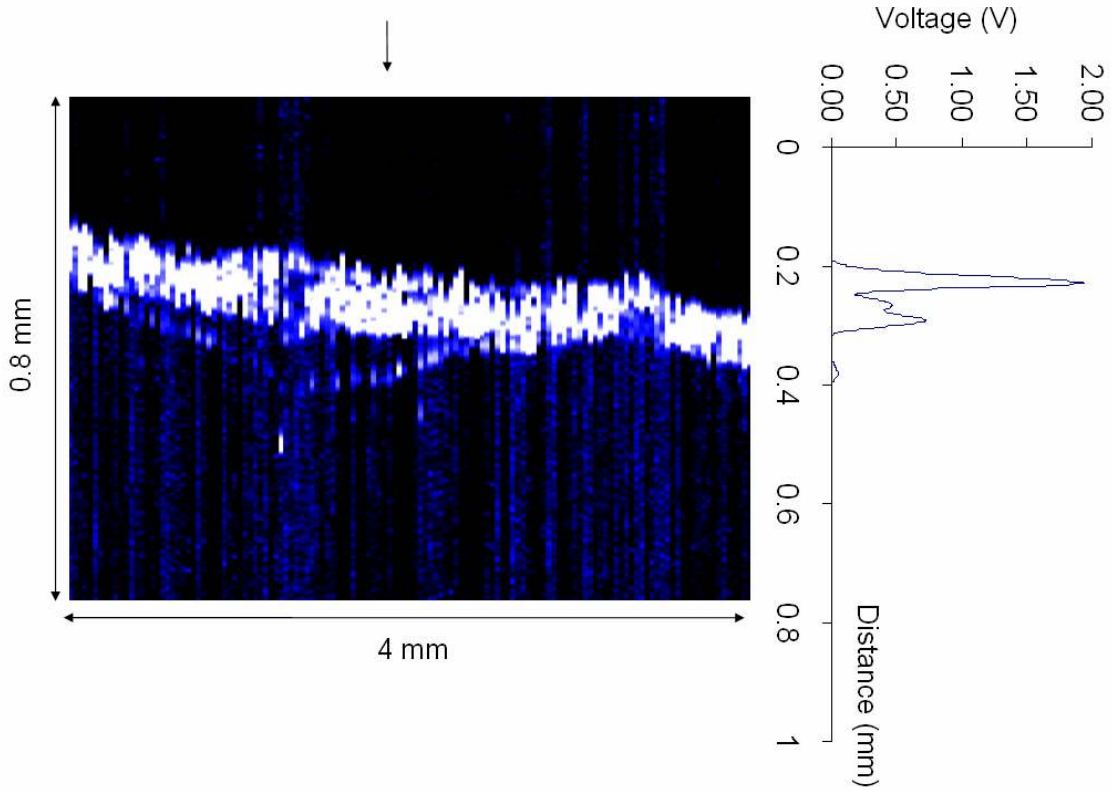

Figure 6-15: a) 2-D scan of red onion top surface and b) An A-scan

In contrast the red onion has thick internal layers, of about 2 to 3 mm-thickness. With this sample, it is not expected to see a full layer, because the onion skin layers are

thicker and less transparent. Figure 6-15 shows a few thin surface layers of the outside of the red onion.

The results obtained from the two fibre composites are shown in figures 6-16 and 6-17. The first result was on a compact fibre composite and few microstructures can be detected. The second result, figure 6-17, corresponds to the cross-sectional image of the edge of a thinner composite. Structures are detected that may be due to air gaps or fibre composite that has not completely cured on the edge.

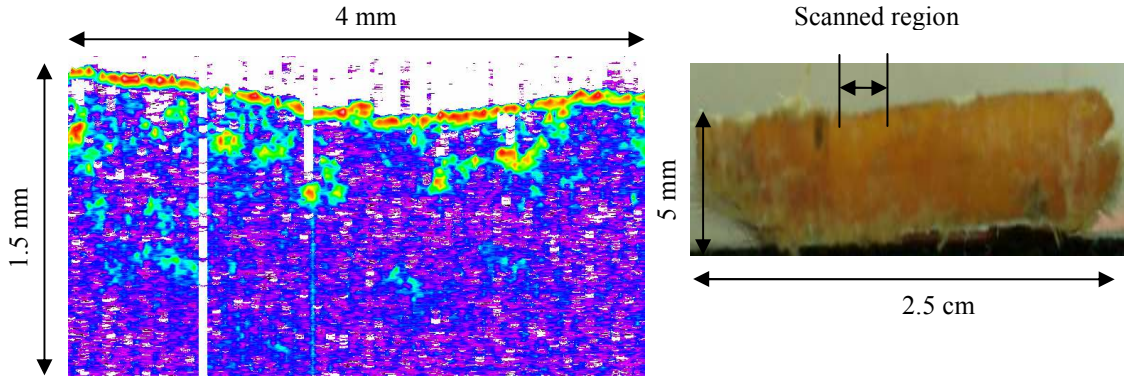

Figure 6-16: a) OCT image and b) photograph sample of composite

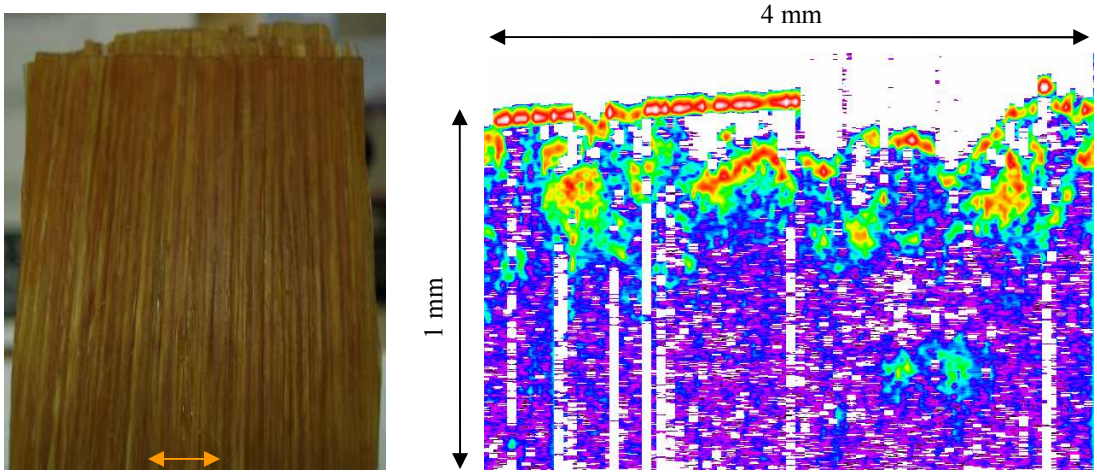

Figure 6-17: Fibre composite sample and its 2-D OCT image

This experiment shows that the Fizeau interferometer is potentially useful as a tool to detect defects in materials.

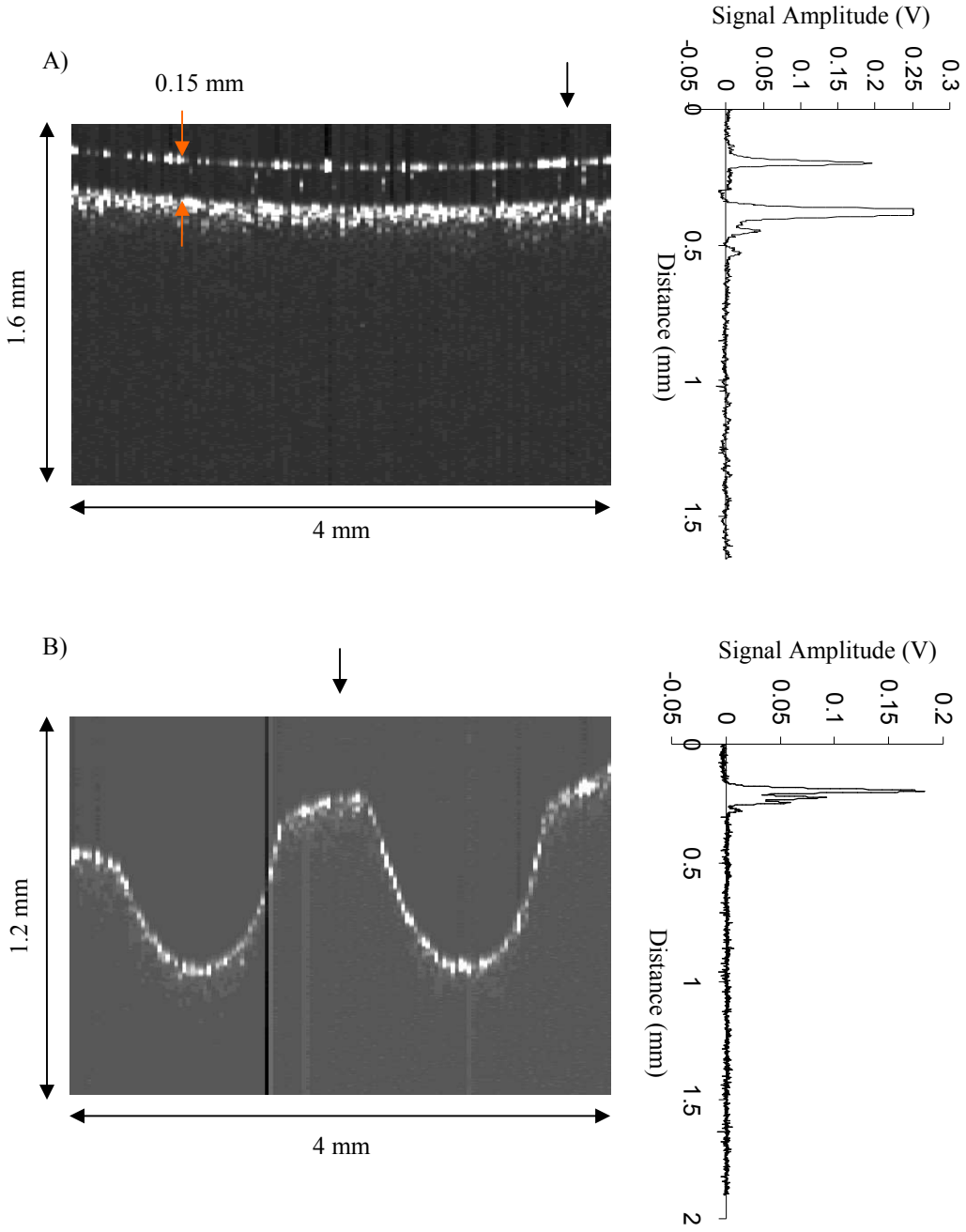

Figure 6-18: OCT image of a piece of a ceramic coffee cup A) with the glazing and B) the glazing or coating is removed and cavities are drilled

Finally the balanced FI has been used on a non-transparent Chinese cup. Figure (6-18-A) shows that the glazing (first surface) and microstructure can be well observed

at the beginning of the second layer due to the porous ceramic structure. On the A-scan, the second peak is truncated, not because of detector saturation, but because the acquisition was done for a reduced range of A/D voltage from -0.05 to 0.25 V to allow a good resolution. The first peak is not as high as might be expected, compared to the second, because the probe is focused on the second boundary. After having removed the coating and drilled holes in the ceramic (diameter ≈ 1 mm, depth ≈ 0.4 mm), the contour of the sample structure (figure (6-18-B)) is observed with visible microstructures below the surface. Of course with such a strongly non-transparent sample, it is not expected to detect deep microstructures, limiting the depth imaging to about 250 µm.

6.5.3 Resin curing

Figures 6-19 and 6-20 correspond to the curing process of a resin under UV irradiation as measured through the magnitude of the OCT signal obtained from the output of the balanced detector and after the demodulation process (experimental details were provided in chapter 5). As deduced from the sensitivity measurements, figure 6-19, the previously used gains of either 100 or 1000 are not suitable for the resin application because with the former it is not possible to detect around ORI = 1.4 and with the latter the system could suffer from overload at the LNAs. A gain of 200 enables us to monitor the entire cure process.

Figure 6-20 presents the curing process with just the balanced detection and without demodulation system. Figure (6-20-a) corresponds to the complete result where the first few minutes correspond to the initial arrangement with simply the air-MCS interface and the second section (a zoom is shown in figure (6-20-b)) corresponds to the reflectivity evolution following the moment where the resin is deposited on the glass and begins to cure.

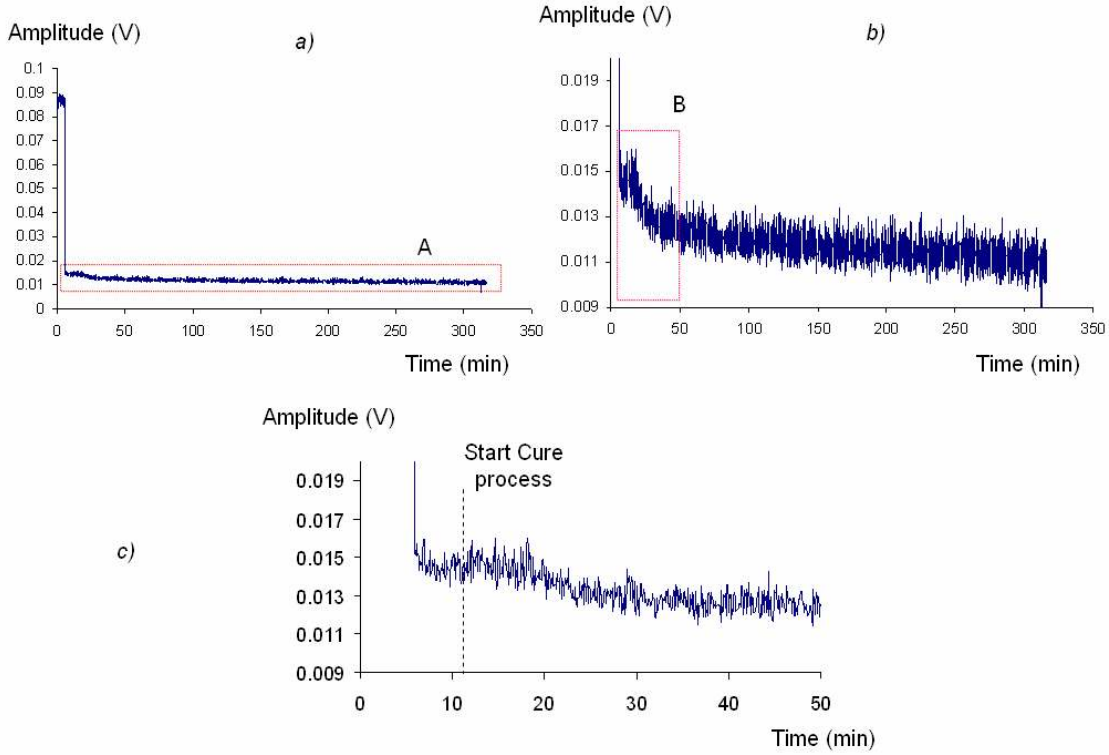

Figure 6-19: Monitoring curing process with just the balanced detection; a) Resin curing; b) Part A zoomed and c) part B zoomed

Figure 6-20 presents similar results, but this time with the demodulation process and the gain of 200. In figure (6-20-b), the power was first adjusted (part A'') to avoid overload from the LNAs. Part B'' is the transition where the resin is deposited on the surface of the glass. In part C'', the change is due to the power of the source that was increased to improve the sensitivity. Figure (6-20-c) is a zoom of the part B' (figure (6-20-a)).

The experimental results (figure 6-22) show a bigger sensitivity to the change in RI for the demodulated signal than for the balanced detection alone in the resin curing. Also, the reflectivity at the MCS-RIO boundary being small, as mentioned for the SNR results, the change in amplitude can be approximated as linear behaviour tending to 0 at the RI of the substrate. This is demonstrated theoretically by plotting the amplitude of the peak at the interface against the refractive index. By changing the substrate RI, the plots will shift with a minimum at the refractive index of the substrate RI. By analogy,

the SNR via ORI will behave in the same way, falling due to the refractive index of the substrate.

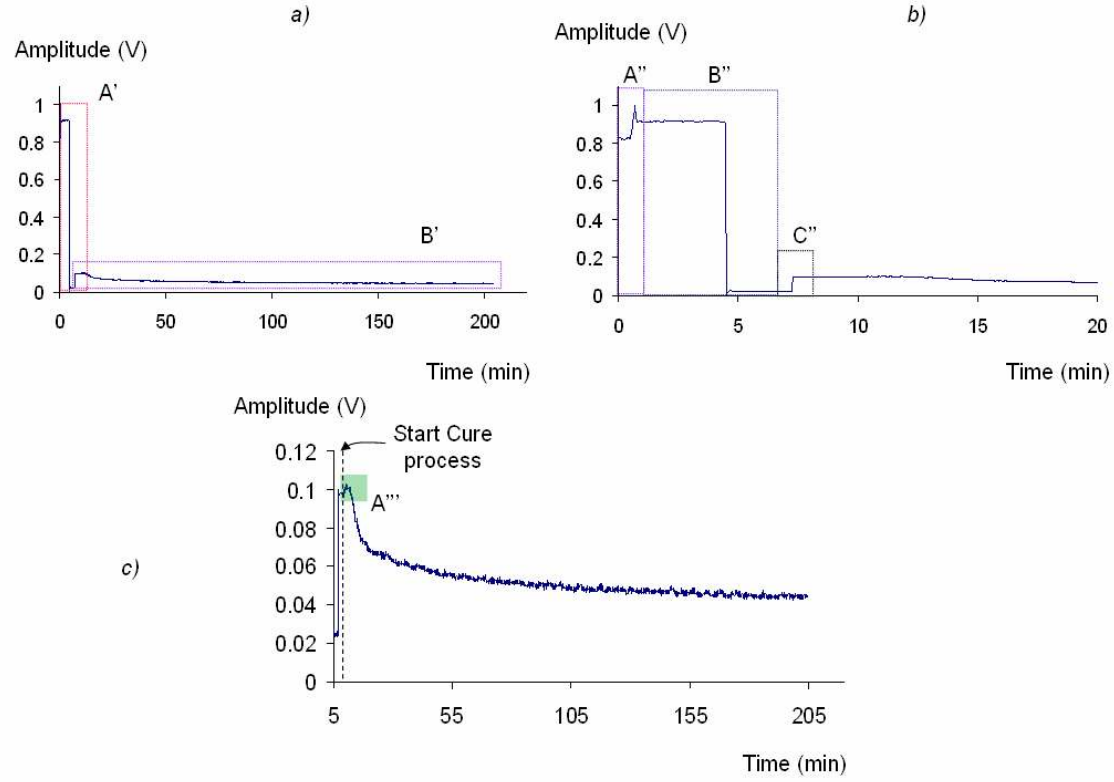

Figure 6-20: Resin curing process results with the balanced detector and the demodulation system; a) completed data set, b) part A' zoomed c) part B' zoomed; part A'': the power is adjusted, part B'': the resin is deposited on the MCS; part C'': the power of the source was increased; Gain = 200

Knowing the system response to ORI (figure 6-21) for the instrumentation used, by means of the equation of the curve, the refractive index of the sample can be found.

As was observed before with the SNR measurements, the rectifier-based demodulation causes a significant improvement in sensitivity (about 30 dB) to small changes of refractive index change and there is a faster response. Using the sensitivity results, the refractive index of the liquid resin is found (figure 6-21). The value is found to be in concordance with the information in the data sheet that was provided by resin manufacturers. Figure 6-22 presents the evolution of the RI of the resin via the time during the curing process. When the resin is completely cured, a lower RI is found for the end of the cure. This may be certainly explained because when the resin is cured, its state changes from liquid to solid, with a tendency to shrink. The top surface is

immediately cured when the UV source is On. During the curing process, two elements have been taken into consideration: the amplitude of interface peak and its position. Figure 6-23 corresponds to the plot of the position of the peak with the time. The peak position changed with time because of shrinking and the MCS was then deforming. The MCS may not be a suitable reference substrate, being too flexible, for measurement of the resin curing.

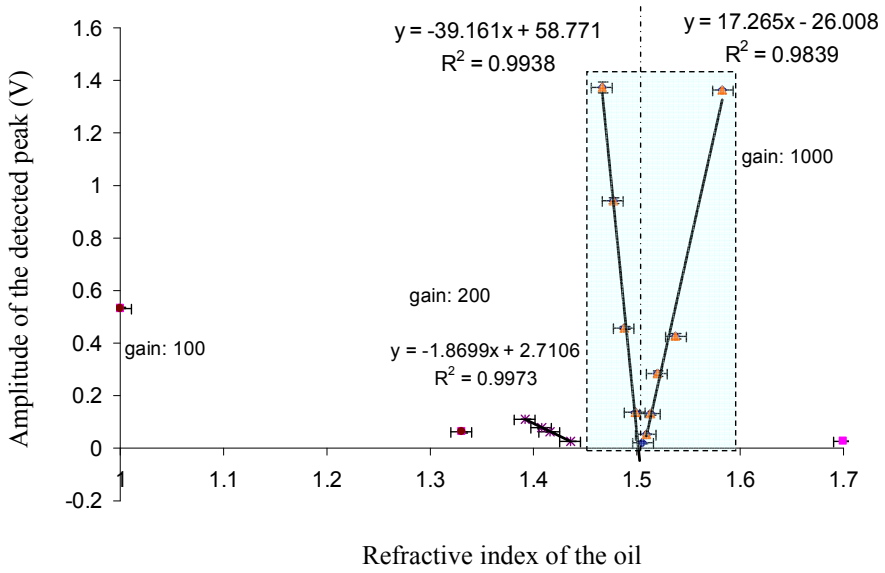

Figure 6-21: Sensitivity measurement for the balanced detection + demodulation for different gains

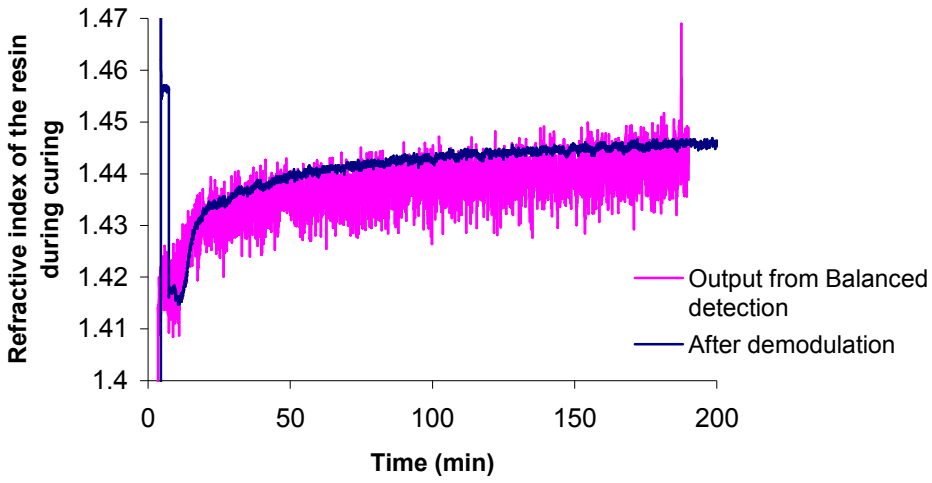

Figure 6-22: Refractive index measured during the cure

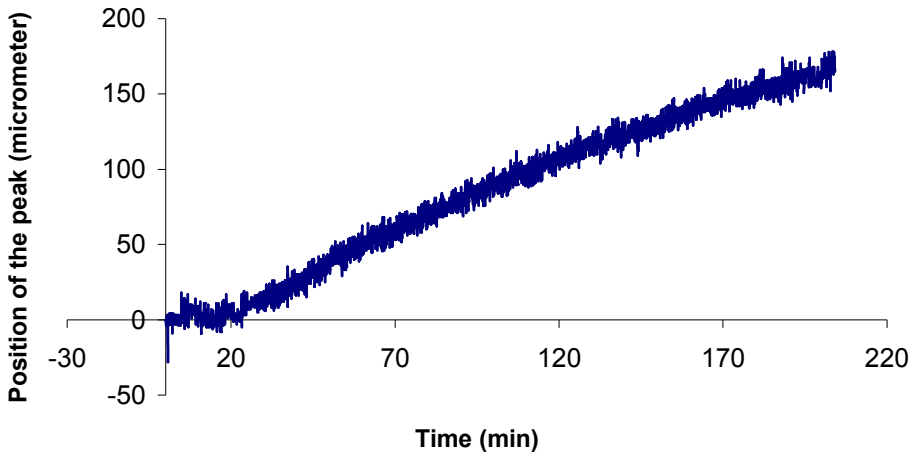

Figure 6-23: Peak position change during the cure

In both results, a lobe is observed following the start of the curing process (the UV source is On) due to the emitted heat. This was also viewed and checked by Buggy *et al.* in an independent RI measurement experiment using long period fibre gratings (Buggy et al. 2005).

6.6 Discussion

6.6.1 Samples considered

The first results from the system, with MPI and single detector, were obtained on transparent samples. This enabled some idea of the possible application of a single detector Fizeau interferometer development for biomedical or industrial applications. Previous results have been demonstrated on oesophagus epithelium layer (Bamford, 2000) without having provided the histology or an image of the sample, using the standard Fizeau configuration. A transparent sample is not the most representative that can be considered for a future medical system. On the other hand, it demonstrates interesting and promising results in terms of the potential of this system. From the samples assessed, the first medical application employing the Fizeau configuration

could be in ophthalmology, which is a medical area that had a lot of interest for OCT researchers.

Using a single detector alone has some inconveniences like the dc component that appears on the observed signal along with the ac signal. The dc component is dependent on the sample composition. It affects the production of 2D images. A high-pass filter could have been used to remove the dc components. By means of the LNA, a band-pass filter removed the dc component on the observed signal and reduced the noise, improving the SNR. It is important to understand that if a high-pass filter is used, the dc component is removed from the displayed signal, but the noise is still dependent on it. This was used on the side of the hand.

The efficiency of the system was even more improved by means of the balanced detection and the rectifier-based demodulation process which permitted depth information from turbid samples, e.g. the fibre composites or the coffee cup. However the modified or improved system was not tested on human tissue, because such sample requires authorisations and specific process.

The OCT system's sensitivity to detect sub-layers or refractive index mismatch sites is dependent on the coherence length of the source, the power, the optical properties of the sample under investigation, the optical components constituting the interferometer, the probe design and the detection process composing it. The microscope cover slide makes an ideal and cheap reference sample, to investigate the potential of a system and its improvements, that can be positioned in the focusing region of the probe. Of course this does not mean that it does not work with other samples like a 1 mm-thickness microscope slide. Lower SNRs are then expected, following the same trend, being improved by increasing the gain. It has to be noted that with the MCS, there are two reflections which contribute both to the dc component and then the noise, but just one interface was observed for the SNR study. This described a way to check the SNR efficiency of a system.

The PI C-843 card was much more efficient than the PI C-842 card, which did not enable continuous movement of the translation stage and data acquisition at the same time. 2-D imaging was achieved by translating a second stage (PI C-842 card was probably defective). The probe could be modified, as related in section 2-3-3, where two galvanometer mirrors are employed to produce en-face imaging. Of course in terms of

medical application, movement stages are not the fastest way to scan a sample, but 1 to 2 mm sample depths are scannable in few minutes. After having written the Labview™ program for the PI C-843 card to carry out a continuous acquisition, hysteresis was observed due to the logic in the program and the communication with the stage. The stage was driven for given distance and speed, and moved backward to the initial position. Therefore, in the logic, at the end of the stage movement a command was included requiring the stage to be stopped, which was achieved via the "wait for axis to stop.vi" added after the movement section; the hysteresis problem then disappeared.

6.6.2 Balanced detection

The use of balanced detection helped for two reasons: improving the SNR and, removing the dc component on the signal (similar to LNA incorporation). The system with balanced detection was applied on an air corner sample formed between two inclined glass surfaces.

The SNR of a system is affected by and strongly dependent on the difference of power reaching both detectors of the balanced detection. This is caused when components with spectral and polarisation dependence are employed. In order to reduce losses and improve the SNR (and efficiency) in a system incorporating the balanced detection, the microscope objective (designed for visible, with anti-reflection that may affect IR-wavelength region), and broad bandwidth beam splitters were replaced by a GRIN lens and by the plate BSs with anti-reflection coating on one of the surfaces, and this also helped to compact the final system which could be installed on a small optical bench to make it portable.

The choice of the processing interferometer may be crucial in terms of SNR. Incorporating a balanced detection, easily achieved building a MZPI, enhanced the SNR of the system. This was even more with the demodulation process, applied in much less transparent sample like the fibre composite block. This was also observed with the resin cure, due to the difference of sensitivity, the response to small change in refractive index is more sensitive with the demodulation process.

Reference List

1. Bamford, K.J. (2000) An Investigation Of Optical Radar And Low Coherence Interferometry For The Detection Of Precancerous Tissues. *Ph. D., Cranfield University, School Of Engineering*

2. Brannon, Heather. Skin Anatomy. 2005.

3. Buggy, S., James, S.W. and Tatam, R.P. (2005) Refractive Index Measurement Using LPGs For Cure Monitoring Applications. *Institute Of Physics, Optical Group, Photonex05*

4. Ding, H., Lu, J.Q., Wooden, W.A., Kragel, P.J. and Hu, X.-H. (2006) Refractive Indices Of Human Skin Tissues At Eight Wavelengths And Estimated Dispersion Relations Between 300 And 1600 nm . *Institute Of Physics Publishing, Physics In Medecine And Biology, Phys. Med. Biol.* **51**, 1479–1489

5. NewFocus (2003) User's Guide: 80-MHz Balanced Photoreceivers Model 18X7. 181710 Rev. A,

6. Opto Speed (2002) General Specifications: High Power 1550 nm Superluminescent LED SLED1550D5A.

7. Podoleanu, A.Gh., Rogers, J.A., Cucu, R.C. and Jackson, D.A. (2001) Simultaneous Low Coherence Interferometry Imaging At Two Depths Using An Integrated Optic Modulator. *Optics Communications* **191**, 21-30.

8. Tearney, G.J., Brezinski, M.E., Southern, J.F., Bouma, B.E., Hee, M.R. and Fujimoto, J.G. (1995) Determination Of The Refractive Index Of Highly Scattering Human Tissue By Optical Coherence Tomography. *Opt. Lett.* **20**, 2258-2260.

9. University of Wisconsin. Skin Cancer: Protecting Yourself At The Beach. 2003.

10. Zawadzki, R.J., Jones, S.M., Olivier, S.S., Zhao, M., Bower, B.A., Izatt, J.A.,

Choi, S., Laut, S. and Werner, J.S. (2005) Adaptive-Optics Optical Coherence Tomography For High-Resolution And High-Speed 3D Retinal In Vivo Imaging. *Optics Express* **13**, 8532-46.

7 Conclusions and Future Work

Since the initial paper demonstrated by Huang *et al.* (Huang et al. 1991), Optical Coherence Tomography (OCT) has proved to be a valuable and interesting imaging tool in its development for medical research.

OCT is a non-invasive and non-contact optical imaging technique enabling the production of cross sectional images of different samples. It has been demonstrated on several samples, e.g. eye, skin and gastro-intestine, as a potential diagnostic tool of malignant tissues (chapter 2). Research has been on the fast scanning techniques to reduce the acquisition time for the comfort of the customer. Most OCT previous developments have been carried out with the Michelson interferometer. It offers the advantage to be easy to implement, but it suffers from polarisation state fluctuations due to optical fibre stretching or temperature change. Several interferometers have been implemented and Bamford (Bamford, 2000) has shown that the standard Fizeau interferometer was possible for the application of OCT.

In this present thesis the Fizeau interferometer has been developed further to optimise its SNR and as a mitigating solution to the downlead sensitivity suffered by the Michelson interferometer.

7.1 Conclusions

Experimentally, a 1550-nm wavelength source was employed to improve the depth of penetration of light (this is a telecommunication wavelength for which optical components defined at this wavelength are readily available). The aims and goals of the project were divided into three parts:

- the SNR of various interferometer configuration had to be compared to investigate which configuration was suitable for OCT and its development;
- It is a necessity with medical imaging devices to acquire images in near real-time to improve the comfort of the patient; several scanning devices had to be investigated to improve the acquisition speed;

• the final system had to be portable in order to carry out possible tests in hospitals.

It was theoretically found that the use of optical circulator and a Michelson processing interferometer in the Fizeau interferometer does not improve the SNR of the standard Fizeau interferometer (46 dB) but is smaller than the Michelson interferometer by 10 dB. However the use of the optical circulator, the Mach-Zehnder processing interferometer and balanced detection led to an improvement in the SNR of the Fizeau interferometer (64 dB). This improvement is still 10 dB lower than the balanced Michelson interferometer. This difference should be negligible when compared to the benefits derived from the "downlead insensitivity" that the Fizeau interferometer provides.

Experimentally, the standard FI with a Michelson processing interferometer was applied to transparent samples, which was satisfying for a first set of results, but had poor sensitivity to small changes in refractive index. The use of a band-pass filter enabled the acquisition of A-scans from less transparent samples.

Balanced detection was first achieved, after comparison of the possible processing interferometers, employing a Mach-Zehnder processing interferometer, with standard optical components, which was used to produce a first 2-D image of an air corner made by two microscope slides. Such sample was used to check if the system was able to resolve the angle between the two glasses. As discussed in chapters 4, 5 and 6, the balanced detection is dependent on the power reaching both detectors. Deterioration of the SNR of the system (Carmelo Rosa and Podoleanu, 2004) could happen if the dc powers were not similar or if the optical component did not have the same wavelength splitting ratio. The replacement by proper components designed to operate in the 1550-nm wavelength region, coupled with micro-bench elements, enabled a much smaller and stable system, and to realise a proper balanced detection. Several detection systems were considered, e.g. the balanced detectors, and the best SNR was obtained with the New-Focus 2017-Model, having the smallest electronic bandwidth. The SNR of the systems have been investigated by means of a microscope cover glass, being a cheap reference substrate.

The best SNR has been then obtained by incorporating an electronic rectifier-based demodulation process (chapter 5) consisting essentially of a band-pass filter,

which allowed a reduction in the scan rate and the scan time, and then the size of the data in memory, and with an adjustable gain, different sensitivities were obtained defining different region of application. Adjustable gain enabled the demodulation technique to be applied to transparent and turbid samples (chapter 6). Several reference substrates may be used to try and achieve the maximum sensitivity, in terms of the rate of change of refractive index, especially around the refractive index of interest; this could be useful to obtain more sensitive measurement of the resin curing.

The final system had the size of 2 A4-format pages, making it transportable. This was possible using micro-bench components.

Some further work has been carried out with the implementation of the RSOD line in order to reduce the acquisition time. The configuration used is given in figure 7-1 and an initial result is given in figure 7-2 from a reflection at a mirror.

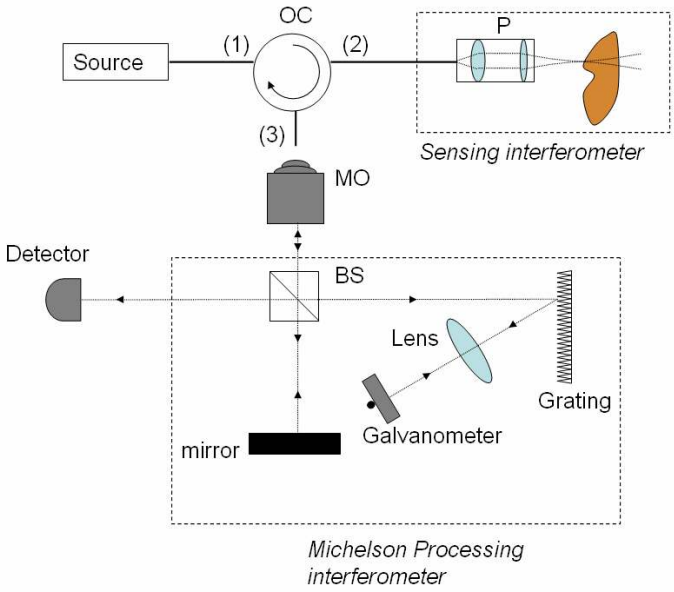

Figure 7-1: Single detector Fizeau configuration with a rapid scanning delay line

The measurement was done considering a mirror as a reference in the FI with a Michelson Processing interferometer. A RSOD line is set-up in the processing interferometer and the observed signal is shown in figure 7-2.

Fringes were observed because the optical path difference in the Michelson processing interferometer was matched to the optical path difference in the sensing interferometer. The top of the oscillations cannot be observed due to the saturation at

the acquisition card, limited to 10 V. The position of the galvanometer was shifted to observe the carrier fringes. The intensity decreases (after 0.2 s) because the angle of the mirror mounted on the galvanometer does not enable the reflection of the light to be detected. This demonstrates that the principle of the RSOD works on the Fizeau interferometer. It has not been developed further and may be of interest in the future.

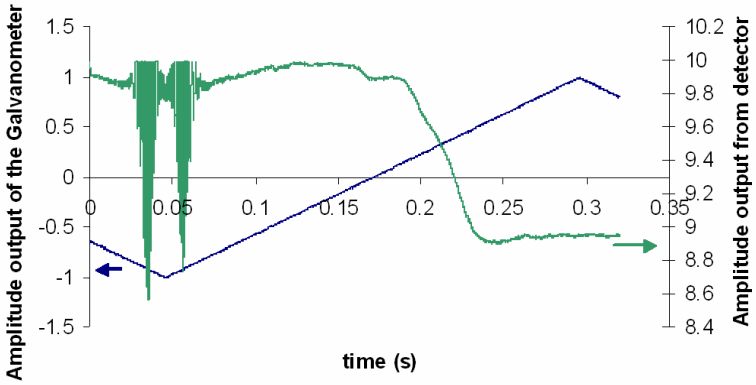

Figure 7-2: Signal Obtained from the RSOD line applied in the MPI from a mirror as a sample

The main concern being the application of balanced detection, the RSOD line has been implemented in the MZPI but without interesting success when both broadband and wavelength-specific components were used. Fringes of poor visibility were observed due to a non-properly aligned system. The difficulty arises from the fact that the three components (the grating, the lens and the galvanometer) have to be aligned in a totally free-space processing interferometer set-up having the output beam from the RSOD line passing through a different path from that of the input beam. The three optical components have to be moved together to carry out a proper alignment.

The RSOD line, having to be set-up in-free space, is not easy and convenient to implement, but the idea should work. From the literature, almost all researchers use this system with in-fibre interferometers.

7.2 Future work

Most of the aims and objectives have been achieved to completeness. A near real-time OCT system was not achieved because the stepper motor used to move the stage for scanning purposes was slow; however this was sufficient to produce an OCT image in a reasonably short time. It was not possible to obtain good alignment of the RSOD line in the Mach-Zehnder processing interferometer because of the reasons explained before.

The Fizeau interferometer may be developed further with the RSOD line in the Michelson processing interferometer (figure 7-1). A low noise amplifier could be used to improve the SNR and a rectifier-based demodulation could also be implemented.

Fourier-domain OCT may be more appropriate and researchers tend to implement this technique which does not require scanning any mechanical devices. This could also enable a reduction in the size of the system. As with the RSOD line, if the spectrometer is "home made", the alignment can be critical and it is not so easy to find CCD cameras operating in the 1550-nm wavelength region as they are not commercially prevalent; however, as laser makers develop efficient tuneable sources, they could be of particular interest in the future for swept-source Fourier-domain systems. Future work will certainly require development of such a system by replacing the SLD with a swept source to facilitate real-time imaging.

The SNR's and sensitivities of the systems have been investigated by means of a microscope cover slide (MCS), being a cheap reference substrate. The inconvenience comes when a resin is cured; the MCS is flexible and suffers from stress during the curing process. Use of other glass materials that are harder would be appropriate for the resin curing process.

Longitudinal scans were obtained by mounting a right angle prism on a stage controlled by a stepper motor. This is a slow method, but efficient, stable and repeatable.

The demodulation process required two low-noise amplifiers (LNA's), making a bulky demodulation system, dedicated LNA's can be built that can be used at the required cut-off frequencies.

OCT has been extended for polarisation-sensitive and spectral measurements which provide additional characterisation of the sample under study. The systems were applied using the Michelson interferometer, like most of the new technologies applied for the development of OCT. Interest could be given to the extensions of OCT to obtain e.g. birefringence or flow information, by developing a PS-OCT or a DOCT based on the Fizeau interferometer.

7.2.1 Endoscopic OCT development

The in-fibre Michelson interferometer is used primarily for ease of alignment and for requiring few components. OCT systems that are suitable for development into medical devices will have to be applicable in diverse situations, like accessing in-vivo gastrointestinal tract or arteries and get information on the state of the organs. This can be achieved via an endoscope and was demonstrated with a Michelson interferometer. This interferometer has reference and sample arms separated which do not suffer from the same temperature and polarisation changes, which make it less suitable for *in-vivo* applications, but can be overcome with the Fizeau interferometer.

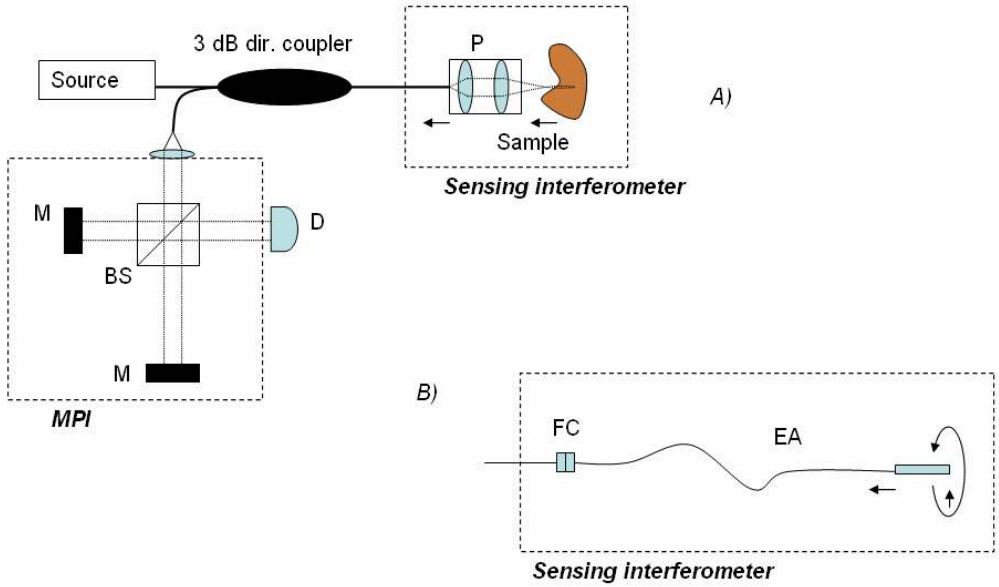

Figure 7-3: A) Standard Fizeau interferometer and B) the sensing interferometer for the endoscope implementation; P: probe, MPI: Michelson processing interferometer, M: mirror, BS: beamsplitter, FC: fibre connector, EA endoscope arm

As for the Fizeau application (figure (7-3-A)), the probe is replaced by the endoscope. The endoscope head will require a polished fibre unlike the MI that requires an angle-cleaved fibre. This is because the Fizeau interferometer requires the reflection at the end of the fibre (figure (7-3-B)).

Care in the design of the endoscope will have to be taken to avoid unwanted reflected light that could contribute to increase the beat and excess noise.

Finally, Optical Coherence Tomography is an optical imaging technique offering 1-3 mm depth information, which is sufficient to detect early stage development of cancers. It is a much cheaper medical system compared to other diagnostic imaging systems found in hospitals.

After investigations, the use of the Fizeau interferometer, with an optical circulator and a Mach-Zehnder processing interferometer has been demonstrated for several applications and transparent and turbid samples, giving rise to good potential for

endoscopic studies. The development of flexible fibre bundles offers great possibilities in the development of *en-face* imaging and could be applied to endocopic applications. *En-face* imaging will be beneficial to produce 3-D image of sample.

The originality of this research comes from a theoretical approach that was first carried out on the SNR of numerous configurations that helped in defining which configurations were more suitable and was then experimentally demonstrated. A simple experimental arrangement was made to carry out sensitivity measurements. Other researchers could conduct similar experiments to investigate the efficiency of their configurations. The rectifier-based demodulation electronic circuit enabled to achieve the best SNR and to increase the acquisition speed of the scans to produce the OCT image. The feasibility of the Fizeau interferometer has been demonstrated through (non-transparent and turbid) samples available in the lab.

Reference List

1. Bamford, K.J. (2000) An Investigation Of Optical Radar And Low Coherence Interferometry For The Detection Of Precancerous Tissues. *Ph. D., Cranfield University, School Of Engineering*

2. Carmelo Rosa, C. and Podoleanu, A.Gh. (2004) Limitation Of The Achievable Signal-To-Noise Ratio In Optical Coherence Tomography Due To Mismatch Of The Balanced Receiver. *Applied Optics* **43**.

3. Huang, D., Swanson, E.A. and Lin, P.C. (1991) Optical Coherence Tomography. *Science* 1178-1181.

4. Tearney, G., Bouma, B.E. and Fujimoto, J.G. inventors Massachusetts Institute Of Technology, (Aug 28, 2001) Grating Based Phase Control Optical Delay Line. US 6,421,164 B2.

Appendix A: Explanation of the Labview™ program

Two PI cards (C-842.20 and C-843.20) have been used during the PhD project to control the movement of stepper motors. The main improvement having been done with the C-843.20 PI card, the Labview™ program is explained for this card.

The function of the Labview™ program is to enable a continuous acquisition of the signal with the movement of the stage on which a mirror is positioned to carry out the scans. The logic diagram is shown in figure A-1.

Before running the program, a configuration set-up program is required, which has to be still open when the scanning program runs. The configuration set-up program essentially requires to specify the number of ports connected to motors and to provide the reference name of the different motors. The other step deals with moving the stage and acquiring the data continuously and finally displaying the results.

A.1 User Interface

In the main program, the device number and the channel number where the detector is connected are given. The velocity and the scan depth are also specified. The data acquisition time has to be the same as the duration of the scan. The program could slow down and not work properly if the time was different. The number of samples and the sample rate have to be chosen to match the scan time. A display indicates the number of longitudinal scans that have been carried out.

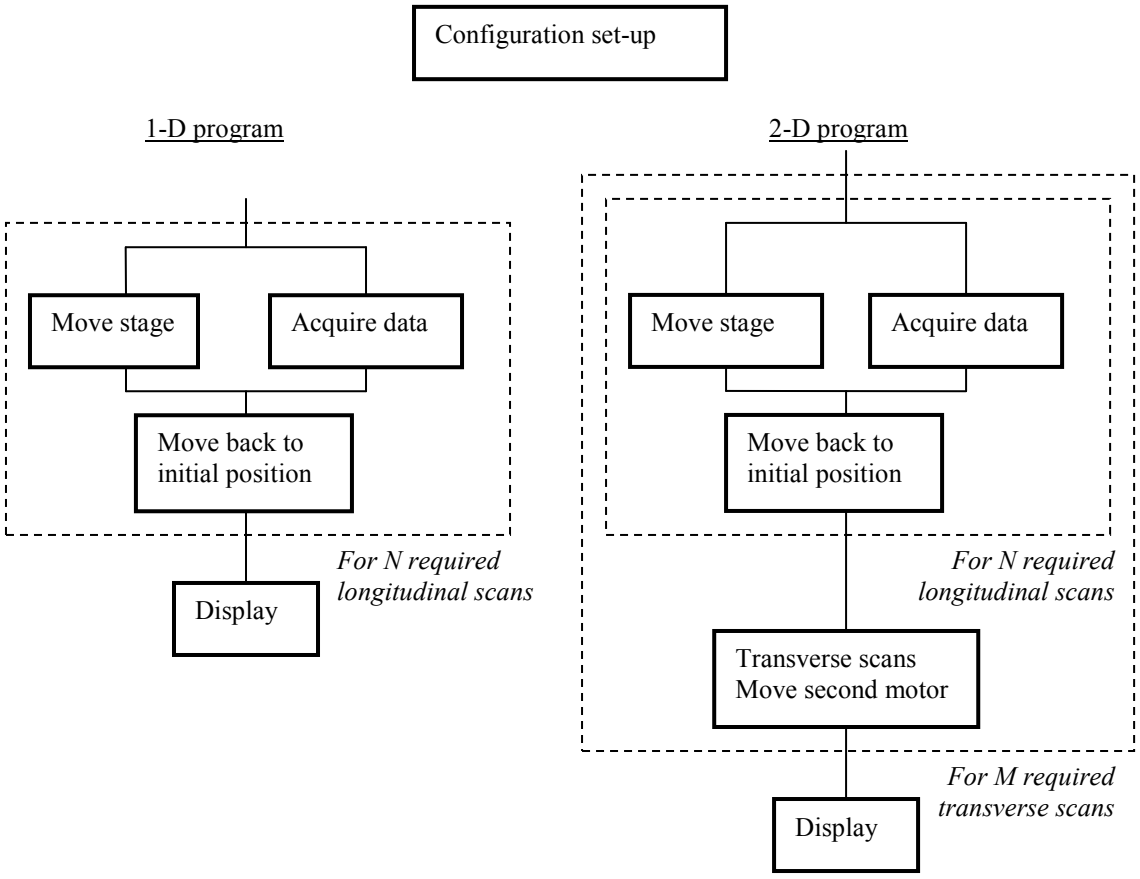

Figure A-1: logic diagram corresponding to the Labview™ program for the C-843.20 PI card

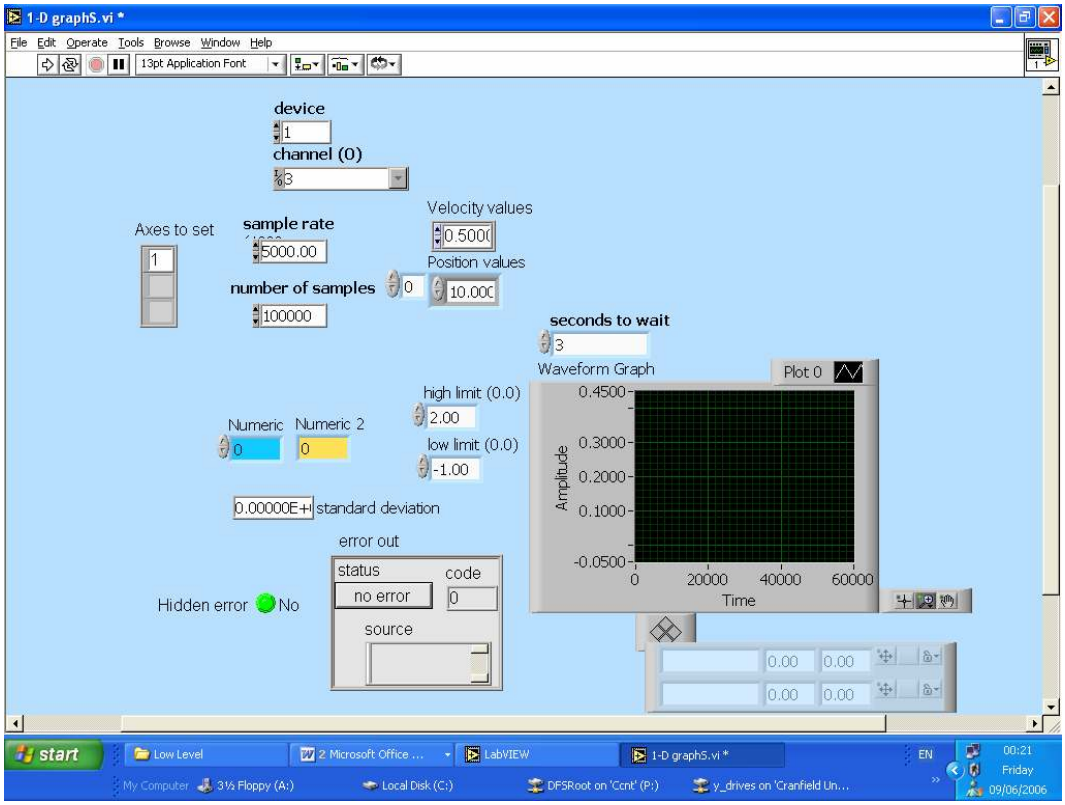

Figure A-2: User interface

A.2 Diagram

The Labview™ diagram follows the logic given in the logic diagram.

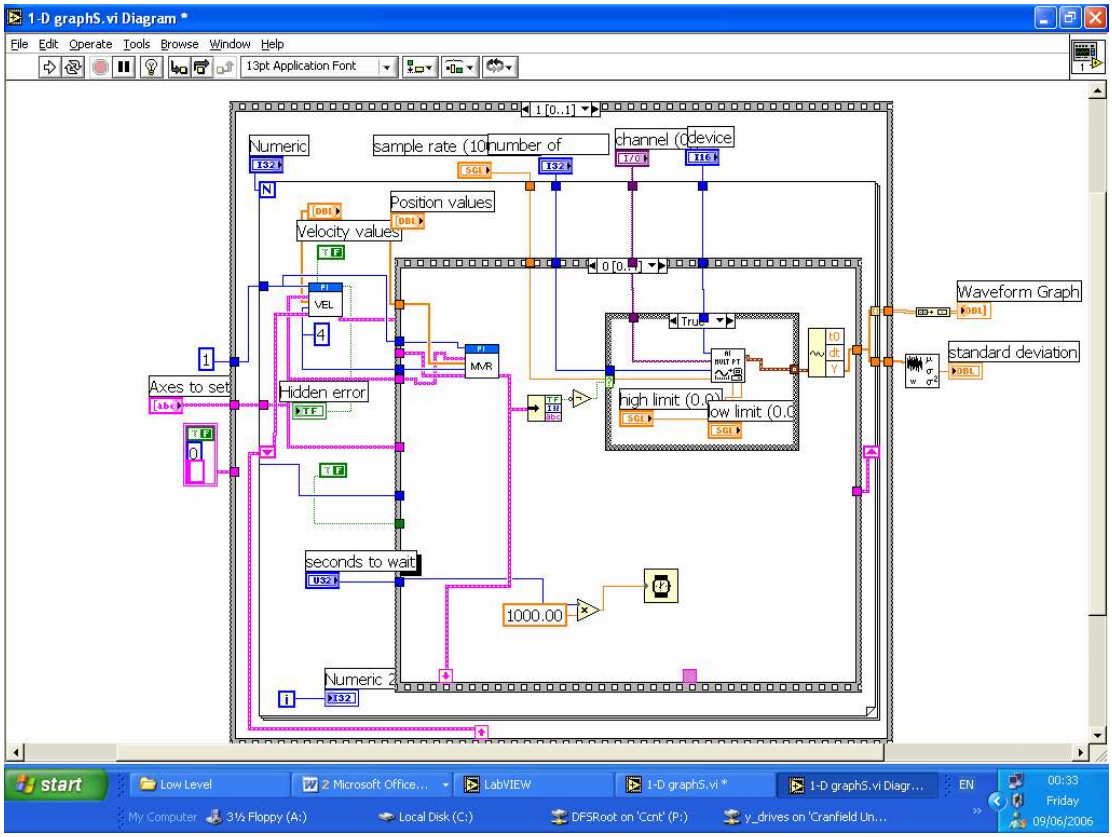

Figure A-3: Main diagram

A.3 2-D imaging

OCT images are produced compiling several longitudinal scans taken at different transverse position. The transverse scans are monitored with another stepper motor. Then the Labview™ program works in the same way as for the 1-D display and requires the number of transverse scans to carry out, the displacement and the speed.

The logic is similar to the 1-D program with a second action being the transverse displacement (figure A-1). The user interface has been modified to take the number of transverse scans, the distance between each transverse scan and the speed of the movement of the stage. The user interface is shown in figure A-4.

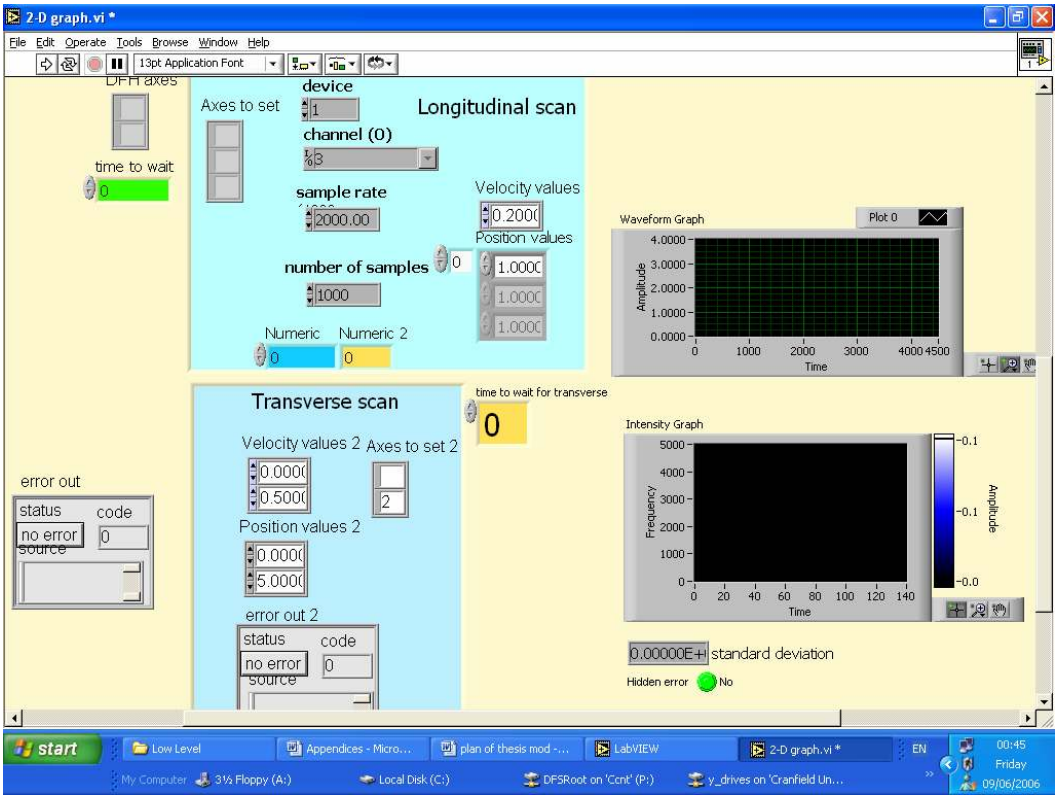

Figure A-4: User interface of 2-D plot program

Appendix B: Refractive index uncertainty calculations

B.1 RI measurement from the microscope cover slide (MCS)

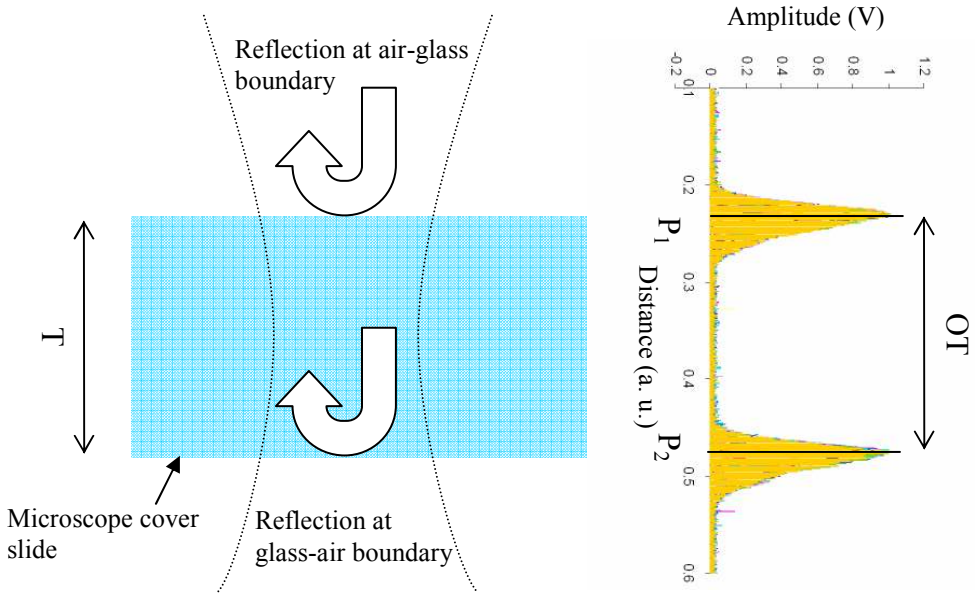

Figure B-1: repeatability longitudinal scans on MCS. T: MCS thickness, OT: optical thickness

The MCS RI is given by:

$$n = \frac{OT}{T} = \frac{P_2 - P_1}{T} \qquad \textbf{(B-1)}$$

where OT is the optical thickness, P_1 and P_2 are the positions of the maxima corresponding to the air-glass and glass-air interfaces. The uncertainty $u_c(y)$ of the quantity y is defined as:

$$u_c^2(y) = \sum \left(\frac{\partial}{\partial x_i}(y) \right)^2 u_c^2(x_i), \qquad \textbf{(B-2)}$$

where x_i corresponds to the individual variables, $\frac{\partial}{\partial x_i}$ is the partial differentiation

Applying (A-2) to n:

$$\begin{aligned} u_c^2(n) &= \sum\left(\frac{\partial}{\partial x_i}(n)\right)^2 u_c^2(x_i) \\ &= \left(\frac{\partial}{\partial P_2}(n)\right)^2 u_c^2(P_2) + \left(\frac{\partial}{\partial P_1}(n)\right)^2 u_c^2(P_1) + \left(\frac{\partial}{\partial T}(n)\right)^2 u_c^2(T) \\ &= 2\cdot\left(\frac{1}{T}\right)^2 u_c^2(P) + \left(-\frac{OT}{T^2}\right)^2 u_c^2(T) \end{aligned} \quad \textbf{(B-3)}$$

OT is measured by means of the Labview^{TM} program and this depends on the accuracy of the motor used and the acquisition scan rate (to determine the maximums positions), then:

$$u_c^2(OT) = u_{rep}^2(OT) + u_{read}^2(OT) + u_{cal}^2(OT), \quad \textbf{(B-4)}$$

where u_{rep} is the repeatability uncertainty of the measurement, found by applying to OT:

$$u_{rep}^2 = \sqrt{\frac{1}{n(n-1)}\sum_{i=1}^{n}\left(x_i - \bar{x}\right)^2} \quad \textbf{(B-5)}$$

and is equal to $1.367\cdot10^{-6}$ mm. u_{read} and u_{cal} are the reading and calibration uncertainties and both depends on the scan rate and the accuracy of the motor which controls the movement of the stage and the accuracy of the motor correspond to 1 count, which is equal to $8.432\cdot10^{-9}$ m (Physik Instrumente, 1999).

$$\begin{aligned} u_c^2(OT) &= u_{rep}^2 + 2\left(u_{scan\ rate}^2 + u_{motor}^2\right) \\ u_c^2(OT) &= \left(1.376\cdot10^{-6}\right)^2 + 2\left(\left(+\frac{8.432\cdot10^{-9}}{\sqrt{3}}\right)^2\right) \\ &= 1.893\cdot10^{-12}\ \text{mm}^2 \end{aligned} \quad \textbf{(B-6)}$$

T being measured by means of a vernier (model from Mitutoyo: 0 – 25 mm, 0.001 mm), which the reading can be done to ± 0.001 mm with a repeatability uncertainty of 0.000379 mm; then similarly to OT, the uncertainty on T can be expressed as:

$$\begin{aligned} u_c^2(T) &= u_{rep}^2(T) + u_{read}^2(T) + u_{cal}^2(T) \\ &= u_{rep}^2(T) + 2\, u_{read}^2(T) \\ &= (0.00012)^2 + 2\left(\frac{0.001}{2\sqrt{3}}\right)^2 \\ &= 2.27 \cdot 10^{-8}\ \text{mm}^2 \end{aligned} \quad \textbf{(B-7)}$$

Then u_r^2 and u_{cal}^2 are equal to:

$u_{read}^2 = u_{cal}^2 = 0.001$

Finally, the MCS RI uncertainty can be found:

$$\begin{aligned} u_c^2(n) &= 2 \cdot \left(\frac{1}{T}\right)^2 u_c^2(OT) + \left(-\frac{OT}{T^2}\right)^2 u_c^2(T) \\ &= 2\left(\frac{1}{0.160}\right)^2 1.893 \cdot 10^{-12} + \left(\frac{0.24519}{0.160^2}\right)^2 2.27 \cdot 10^{-8} \\ &= 2.08 \cdot 10^{-6} \end{aligned} \quad \textbf{(B-8)}$$

$u_c(n) = 0.00144$

Finally, the refractive index of the MCS is found equal to:

MCS-RI = 1.504 ± 0.003

B.2 Refractive index measurement of the resin

This is done for the droplet of the resin deposed on the MCS.

$$r_r = \frac{Y}{X} \quad \textbf{(B-9)}$$

X and Y are obtained by selecting the two boundaries. The resolution of OCT images is defined as the coherence length of the source.

$$u_c^2(X) = u_c^2(Y) = 2\left(\frac{21}{2\sqrt{3}}\right)^2 \mu\text{m}^2 \quad \textbf{(B-10)}$$

$$u_c^2(r_r) = \left(\frac{1}{X}\right)^2 u_c^2(Y) + \left(\frac{Y}{X^2}\right)^2 u_c^2(X)$$
$$= \left(\frac{1}{0.345} + \left(\frac{0.487}{0.345^2}\right)^2\right) 2\left(\frac{21}{2\sqrt{3}}\right)^2 \quad \textbf{(B-11)}$$
$$= 1.85 \cdot 10^{-9}$$

Then the resin of the resin is found equal to:

$$\boxed{r_r = 1.4116 \pm 0.0001}$$

Appendix C: Sensitivity of the measurements

The maximum of the interferometric signal is proportional to the root square of the reflectivity at the boundary, which is the reflectance:

$$r = \sqrt{R_b} = \sqrt{\left(\frac{n_g - n_{oil}}{n_g + n_{oil}}\right)^2} = \left|\frac{n_g - n_{oil}}{n_g + n_{oil}}\right| \quad \textbf{(C-1)}$$

($|...|$ denotes the absolute value). Experimentally, it is expected to have a curve with a negative slop for $n_{oil} < n_g$ and a positive slop for $n_g < n_{oil}$.

In the experimental results of the RI change sensitivity measurements, this response is observed in figures C-1, C-2, C-3 and C-4.

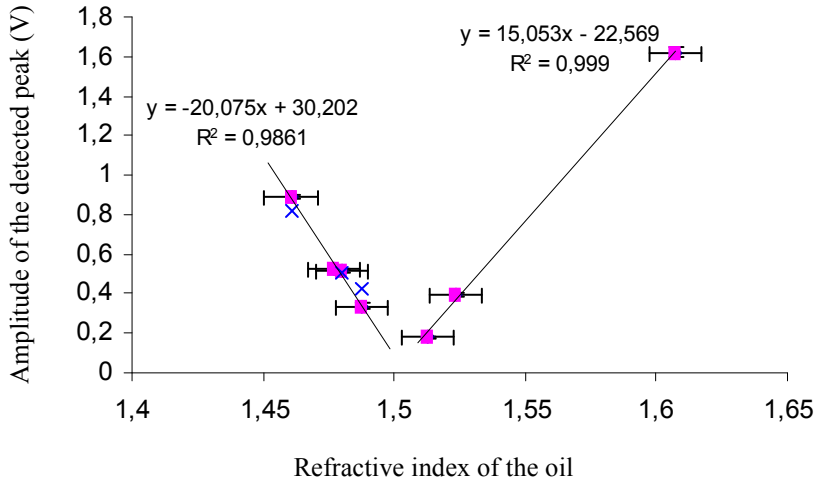

Figure C-1: Sensitivity to change in refractive index for the 80 MHz NewFocus balanced detector

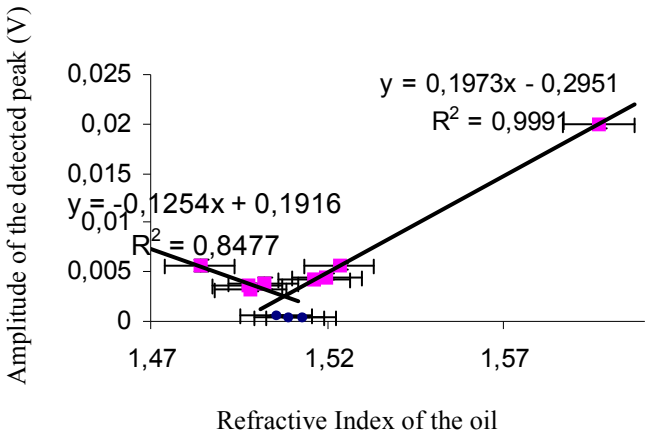

Figure C-2: Sensitivity to change in refractive index of the balanced detection carried out with the standard detectors connected to the LNA

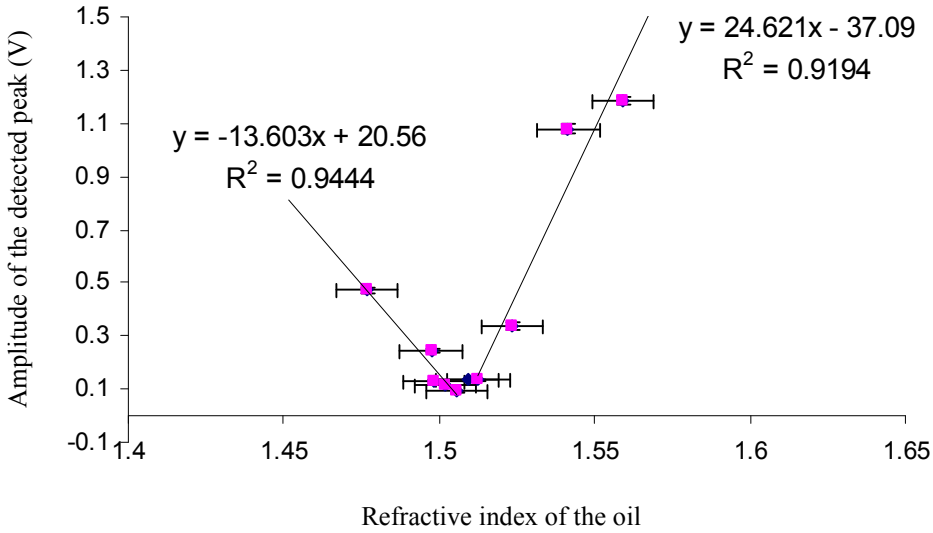

Figure C-3: Sensitivity to change in refractive index for the 125 kHz NewFocus balanced detector

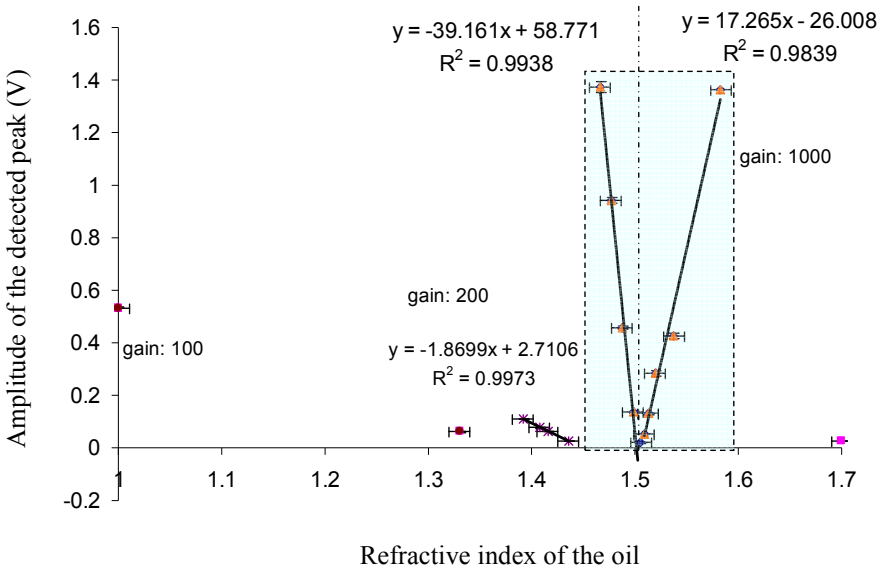

Figure C-4: Sensitivity measurement for the balanced detection + demodulation for different gains

From the measurements obtained, it can be concluded that the sensitivity is not only dependent on the detector, but also to the electronic bandwidth of the detection system. The importance of the electric rectifier-based demodulation process is that it identifies several areas of application depending on the gain applied.

Reference List

1. Physik Instrumente (1999) Operating Manual MP 32E: M-100 Series, Linear Positioning Stages.

List of publications arising from this work

1. Casaubieilh, P., Ford, H.D. and Tatam, R.P. (2004a) Optical-Fibre-Based Fizeau Interferometer For Optical Coherence Tomography (OCT). *Optical Techniques In Biomedical Instrumentation, The Institute Of Physics*

2. Casaubieilh, P., Ford, H.D. and Tatam, R.P. (2004b) Optical Fibre Fizeau-Based OCT. *Second European Workshop On Optical Fibre Sensors, Santander* **5502**, 338-341.

3. Casaubieilh, P., Ford, H.D. and Tatam, R.P. (2004c) Optical Coherence Tomography Based On Fizeau Interferometer Configurations. *PHOTON'04: QEP-16, Glasgow, SPIE*

4. Casaubieilh, P., Ford, H.D. and Tatam, R.P. (2004d) In-Fibre Optical Coherence Tomography Based On Fizeau Interferometer Configurations . *SPIE Int. Soc. Opt. Eng.,ALT'03 International Conference On advanced Laser Technologies: Biomedical Optics, Silsoe, 09/2003* **5486**, 112-122.

5. Casaubieilh, P., Ford, H.D. and Tatam., R.P. (2005) Optical Coherence Tomography With A Fizeau Interferometer Configuration. *SPIE: European Conference On Biomedical Optics, Munich, Germany* **5858**,

6. Ford, H.D., Beddows, R., Casaubieilh, P. and Tatam, R.P. (2005) Comparative Signal-To-Noise Analysis Of Fibre-Optic Based Optical Coherence Tomography systems. *Journal of Modern Optics* **52**, 1965-1979.

7. Ford, H.D., Casaubieilh, P. and Tatam, R.P. (2004) New Optical Fibre Configurations For Optical Coherence Tomography. *SET 2004: Presentations By Britain's Top Younger Researchers At The House Of Commons*